Optimization Techniques for Reconfigurable Intelligent Surfaces Assisted Wireless Networks

Abdelhamed Mohamed

université
PARIS-SACLAY

Optimization Techniques for Reconfigurable Intelligent Surfaces Assisted Wireless Networks

Techniques d'optimisation des communications sans fil assistées par des surfaces intelligentes reconfigurables

Thèse de doctorat de l'université Paris-Saclay

École doctorale n° 580, Sciences et technologies de l'information et de la communication (STIC)
Spécialité de doctorat: Réseaux, Information et Communications
Graduate School : Sciences de l'ingénieur et des systèmes
Référent : Faculté des sciences d'Orsay

Thèse préparée au **Laboratoire des signaux et systèmes** (Université Paris-Saclay, CNRS, CentraleSupélec), sous la direction de **Marco DI RENZO**, Directeur de recherche

Thèse soutenue à Paris-Saclay, le 24 Novembre 2022, par

Abdelhamed MOHAMED

Composition du Jury

Membres du jury avec voix délibérative

Michel KIEFFER Professeur, Paris-Saclay University, France	Président
Kai Kit WONG Professeur, University College London, UK	Rapporteur & Examinateur
Ana García ARMADA Professeure, University Carlos III Madrid, Spain	Rapportrice & Examinatrice
Boya DI Professeur Associé, Peking University, China	Examinatrice
Ioannis KIRKIDIS Professeur, University of Cyprus, Cyprus	Examinateur

Thèse de doctorat

NNT: 2022UPAST137

université PARIS-SACLAY

ÉCOLE DOCTORALE
Sciences et technologies de l'information et de la communication (STIC)

Titre: Techniques d'optimisation des communications sans fil assistées par des surfaces intelligentes reconfigurables

Mots clés: Communications sans fil, surfaces intelligentes reconfigurables, techniques d'optimisation, SWIPT, traitement du signal

Résumé: Récemment, l'émergence des surfaces intelligentes reconfigurables (RIS) a suscité une vive attention de l'industrie et du monde universitaire. Un RIS est une surface plane constituée d'un grand nombre d'éléments réfléchissants passifs à faible coût. En ajustant soigneusement les déphasages des éléments réfléchissants, un RIS peut remodeler l'environnement sans fil pour une meilleure communication. En général, cette thèse fournit des contributions sur : (i) les performances des RIS basées sur des modèles de rayonnement électromagnétique précis et réalistes. De plus, elle fournit des cadres d'optimisation pour améliorer la performance des systèmes de communication dans les deux cas d'utilisation suivants : (i) Améliorer conjointement le taux d'information et la quantité de puissance récoltée dans un réseau sans fil multi-utilisateurs MISO descendant assisté par les RIS. (ii) améliorer l'efficacité spectrale pour un grand nombre d'utilisateurs situés en bordure de cellule ou de l'autre côté du RIS en utilisant des omni-surfaces intelligentes (IOS).

Le chapitre 1 présente les défis à relever pour répondre aux exigences des réseaux 6G, le concept d'environnements radio intelligents et les RIS, qui constituent l'une des technologies habilitantes. Dans les communications futures, les RIS sont une technique clé qui aura des applications potentielles permettant d'obtenir une connectivité sans faille tout en consommant moins d'énergie.

Le chapitre 2 présente les systèmes de communication assistés par RIS. Le principe de réflexion, le problème d'estimation de canal et le problème de conception du système sont présentés en détail. Les recherches de pointe sur les problèmes d'estimation de canal et de conception de système sont passées en revue.

Le chapitre 3 étudie l'impact de modèles de reradiation réalistes pour les RIS en fonction de l'inter-distance sub-longueur d'onde entre les éléments proches du RIS, les niveaux de quantification des coefficients de réflexion, l'interaction entre l'amplitude et la phase des coefficients de réflexion, et la présence d'interférences électromagnétiques. En conclusion, notre étude montre que, en raison de contraintes de conception, telles que la nécessité d'utiliser des coefficients de réflexion quantifiés ou l'interaction inhérente entre la phase et l'amplitude des coefficients de réflexion, un RIS peut reradir la puissance vers des directions non désirées qui dépendent des ondes électromagnétiques prévues et interférentes.

Le chapitre 4 aborde le problème de l'optimisation simultanée du taux d'information et de la puissance récoltée dans un réseau sans fil multi-utilisateurs MISO en liaison descendante avec surface intelligente reconfigurable (RIS) et transfert simultané d'information et de puissance sans fil (SWIPT). Un algorithme pratique est développé par une interaction entre l'optimisation alternée, l'optimisation séquentielle et les méthodes basées sur les prix.

Le chapitre 5 propose un algorithme d'optimisation qui a un taux de convergence rapide en quelques itérations pour maximiser le taux de somme dans les canaux de diffusion MIMO assistés par IOS, qui peut être exploité pour servir l'utilisateur de bord de cellule et améliorer la couverture du réseau. La particularité de ce travail est de considérer que les coefficients de réflexion et de transmission d'un IOS sont étroitement couplés.

Enfin, le chapitre 6 résume les principales conclusions de la thèse et discute des orientations futures possibles qui méritent d'être étudiées pour libérer tout le potentiel des RIS et les mettre en pratique .

université PARIS-SACLAY

ÉCOLE DOCTORALE
Sciences et technologies de l'information et de la communication (STIC)

Title: Optimization Techniques for Reconfigurable Intelligent Surfaces Assisted Wireless Networks

Keywords: Wireless communications, reconfigurable intelligent surfaces, Optimization techniques, SWIPT, signal processing

Abstract: Recently, the emergence of reconfigurable intelligent surface (RIS) has attracted heated attention from both industry and academia. An RIS is a planar surface that consists of a large number of low-cost passive reflecting elements. By carefully adjusting the phase shifts of the reflecting elements, an RIS can reshape the wireless environment for better communication. In general, this thesis provides contributions on: (i) the performance of RISs based on accurate and realistic electromagnetic reradiation models. Moreover, it provides some of optimization frameworks for enhancing the communication system performance on the following two use case: (i) To jointly improves the information rate and the amount of harvested power in a RIS-aided MISO downlink multiuser wireless network. (ii) enhancing spectral efficiency for large number of users located on cell edge or on the other side of the RIS by utilizing the intelligent omni-surfaces (IOSs).

Chapter 1 introduces the challenges of fulfilling the requirements of of 6G networks, the concept of smart radio environments and RIS as it is one of the enabling technologies. In future communications, RIS is a key technique that will have potential applications which will achieve seamless connectivity and less energy consumption at the same time.

Chapter 2 also introduces the state-of-art optimization techniques developed for RIS-aided systems. Firstly, it introduces the system models of RIS-aided MIMO systems and then investigates the reflection principle of RISs. In addition, it introduces the Optimization techniques challenges of RIS-assisted systems. Also, The proposed optimization techniques for designing the continuous and discrete phase shifts are presented in detail.

Chapter 3 studies the impact of realistic reradiation models for RISs as a function of the sub-wavelength inter-distance between nearby elements of the RIS, the quantization levels of the reflection coefficients, the interplay between the amplitude and phase of the reflection coefficients, and the presence of electromagnetic interference. In conclusion, our study shows that, due to design constraints, such as the need to use quantized reflection coefficients or the inherent interplay between the phase and the amplitude of the reflection coefficients, a RIS may reradiate power towards unwanted directions that depend on the intended and interfering electromagnetic waves.

Chapter 4 considers the problem of simultaneously optimizing the information rate and the harvested power in a reconfigurable intelligent surface (RIS)-aided MISO downlink multiuser wireless network with simultaneous wireless information, and power transfer (SWIPT) is addressed. A practical algorithm is developed through an interplay of alternating optimization, sequential optimization, and pricing-based methods.

Chapter 5 proposes an optimization algorithm that has a rapid convergence rate in a few iterations for maximizing the sum rate in IOS-aided MIMO broadcast channels, which can be exploited to serve the cell-edge user and enhance network coverage. This work's distinguishable feature lies in considering that the reflection and transmission coefficients of an IOS are tightly coupled.

Finally, Chapter 6 summarizes the main findings of the thesis and discusses possible future directions that are worth investigating to unlock the full potential of RIS and bring it into practice.

Acknowledgements

First and foremost, I would like to thank my supervisor, Prof. Marco Di Renzo, for his invaluable advice, continuous support, and patience during my Ph.D. Also, I'd like to express my thanks Prof. Alessio Zappone for His assistance, insightful comments and suggestions. I would also like to thank all the members of my thesis committee for their valuable comments.

Doing a PhD. in a new country has always been difficult without support from friends. Therefore, I would like to thank all the current and former lab colleagues in L2S, CentraleSupelec: Dr. Xuewen Qian, Dr. Fadil Habib,and Dr.Jiang Liu, Arzhang Shahbazi, Dr. Alexis Aravanis, Dr. Kishor Chandra Joshi, and Dr. Farshad Shams. They have been very helpful to my research by sharing their insightful advice and being friends these past few years.

I would like to thank the European Commission for generously supporting my research under the auspices of the H2020 PAINLESS project. Thanks to this project, I got to know a lot of excellent researchers and fellow Ph.D. students from across Europe and had ample opportunities to participate in professional training that would benefit me in the future.

Last but not least, I would like to thank my family: my father Mohamed sayed, my mother Zakia Tawfik, my siblings, and my Mother-in-law Fatima Ibrahim. Their prayers and moral support from Egypt are what encourage me to finish my Ph.D. journey. Finally, a unique token of gratefulness goes to my wife, Ghada Mohsen, and my two wonderful angels, Shahd and Raghad, for their unconditional love and support during the highs and lows of my life in Paris. This thesis would not have been there without them.

CentaleSupelec, 24 November 2022 Abdelhamed Mohamed

Synthèse en français

En général, cette thèse fournit des contributions sur : (i) les performances des RIS basées sur des modèles de reradiation modèles de rayonnement électromagnétique précis et réalistes. De plus, elle fournit des cadres d'optimisation d'optimisation pour améliorer la performance des systèmes de communication dans les deux cas d'utilisation suivants : (i) Améliorer conjointement le taux d'information et la quantité de puissance récoltée dans un système descendant MISO assisté par RIS. (i) Améliorer conjointement le taux d'information et la quantité de puissance récoltée dans un réseau sans fil multi-utilisateurs MISO en liaison descendante assisté par RIS. (ii) améliorer l'efficacité spectrale pour un grand nombre d'utilisateurs situés en bordure de cellule ou de l'autre côté du RIS en utilisant les omni-surfaces intelligentes (IOS).

La thèse commence par présenter, dans le chapitre 1, les défis à relever pour répondre aux exigences strictes des réseaux 6G. Pour aller plus loin, elle présente le concept d'environnements radio intelligents (SRE) et les RIS comme l'une des technologies habilitantes, en soulignant ses propriétés, ses propriétés, ses fonctionnalités et ses avantages par rapport aux technologies existantes. Ensuite, il résume certaines des applications potentielles des RIS dans les réseaux 6G.

Le chapitre 2 présente également les techniques d'optimisation de pointe développées pour les systèmes assistés par les RIS. systèmes assistés par les SRI. Il présente tout d'abord les modèles de systèmes MIMO assistés par les RIS, puis étudie le principe de réflexion des RIS. En outre, il présente les techniques d'optimisation les défis des systèmes assistés par les RIS. Enfin, les techniques d'optimisation proposées pour concevoir les déphasages continus et discrets sont présentées en détail.

Le chapitre 3 étudie l'impact de modèles de rayonnement réalistes pour les RIS en fonction de l'inter-distance sub-longueur d'onde. de l'inter-distance sub-longueur d'onde entre les éléments proches du RIS, des niveaux de quantification des coefficients de réflexion, de l'interplay et de l'inter-distance. de quantification des coefficients de réflexion, de l'interaction entre l'amplitude et la phase des coefficients de réflexion et de la présence d'électrons. et la présence d'interférences électromagnétiques. En outre, il étudie les deux études de cas sur les régions de champ lointain et de champ proche d'un RIS. En conclusion, notre étude montre que, en raison des contraintes de conception, telles que la nécessité d'utiliser des coefficients de réflexion quantifiés ou l'interaction inhérente entre la phase et l'amplitude des coefficients de réflexion, un RIS peut reradier de la puissance vers des directions non désirées qui dépendent des ondes électromagnétiques et des ondes électromagnétiques

interférentes. En outre, nous avons montré que le pic proéminent du motif reradié peut ne pas être parfaitement orienté vers la direction nominale de reradiation pour de grands angles d'inclinaison. pour de grands angles de déviation. Par conséquent, il est, en général, essentiel d'optimiser un RIS en prenant en compte la totalité du rayonnement. un RIS en prenant en compte l'ensemble du diagramme de rayonnement lors de la conception afin de maximiser maximiser la puissance rayonnée vers les directions de rayonnement souhaitées tout en limitant la puissance rayonnée vers d'autres directions non souhaitées. puissance rayonnée vers les directions de rayonnement souhaitées tout en maintenant la puissance rayonnée vers d'autres directions non souhaitées à un niveau faible. Parmi les conceptions envisagées pour les RIS, notre étude montre qu'un RIS 2 bits à commande numérique avec une amplitude de réflexion presque constante en fonction de la phase appliquée. en fonction du déphasage appliqué, et dont les éléments de diffusion ont une taille et une inter-distance comprises entre (1,5) et (2). et une inter-distance comprise entre (1/8)-ième et (1/4)-ième de la longueur d'onde du signal peut constituer un bon entre les performances, la complexité de mise en œuvre et le coût.

Le chapitre 4 aborde le problème de l'optimisation simultanée du débit d'information et de la puissance récoltée dans un réseau sans fil multi-utilisateurs à entrées multiples et à sortie unique en liaison descendante, assisté par une surface intelligente reconfigurable, avec transfert simultané d'information et de puissance sans fil (SWIPT). Les vecteurs de formation de faisceaux, les coefficients de réflexion RIS et les rapports de répartition de la puissance sont optimisés conjointement en fonction de contraintes de puissance maximale, de contraintes de puissance maximale, de puissance récoltée minimale et de contraintes réalistes sur les coefficients de réflexion RIS. A algorithme pratique est développé par une interaction entre l'optimisation alternée, l'optimisation séquentielle et les méthodes basées sur les prix. séquentielle et de méthodes basées sur les prix. De plus, il considère le cas réaliste dans lequel une fonction déterministe couple les phases et les modules des coefficients de réflexion RIS. Sur En outre, l'optimisation du rapport de division de puissance au niveau du récepteur, qui constitue une nouveauté par rapport à la plupart des travaux connexes sur les systèmes RIS-aéroport. par rapport à la plupart des travaux connexes sur les systèmes RIS et SWIPT.

Le chapitre 5 propose un algorithme d'optimisation qui a un taux de convergence rapide en quelques itérations pour maximiser le taux de somme dans les canaux de diffusion MIMO assistés par le RIS, qui peut être exploité pour servir l'utilisateur de bord de cellule et améliorer la couverture du réseau. L'algorithme d'optimisation est appliqué pour optimiser la matrice de covariance au niveau de la station de base, la matrice des coefficients de réflexion et de transmission au niveau de l'IOS, et la quantité de puissance qui est réfléchie et réfractée par l'IOS. La particularité de ce travail est de considérer que les coefficients de réflexion et de transmission d'un IOS sont étroitement couplés.

Enfin, le chapitre 6 résume les principaux résultats de la thèse et discute des orientations futures possibles qui méritent d'être étudiées pour libérer tout le potentiel des RIS et les mettre en pratique. En outre, nous devons considérer que les résultats présentés dans le chapitre 3, sont faits sous certaines hypothèses qui doivent être modifiées pour étudier une

considération et des contraintes plus pratiques telles que le couplage mutuel entre les éléments réfléchissants, en particulier pour une plus petite inter-distance entre les éléments RIS (c'est-à-dire (1/32)ème de la longueur d'onde).
En résumé, dans le contexte général des communications sans fil, les résultats obtenus dans cette thèse révèlent qu'il faut toujours concevoir des techniques d'optimisation en tenant compte non seulement des modèles de rayonnement réalistes, mais aussi des contraintes de conception du matériel.

Contents

Acronyms

ADMM Alternating Direction Method of Multipliers

AI Artificial Intelligence

AmBC AambientBackscattering Communications

AO alternating optimization

APGM alternating projected gradient method

APM accelerated proximal gradient method

ASP antenna separation product

AWGN additive white Gaussian noise

APG Accelerated Projected Gradient

BER Bit-Error-Ratio

PIN positive intrinsic

BC broadcast channel

BCM block coordinate maximization

BEP bit error probability

BF-MIMO beamforming MIMO

BF beamforming

BS base station

bpcu bits per channel use

CG Conjugate Gradient

CPU Central Processing Unit

CR Cognitive Radio

CSI Channel State Information

CP cyclic prefix

CSI channel state information

CSIR channel state information at RX

SSK space shift keying

CSIT channel state information at TX

DCMC discrete-input continuous-output memoryless channel

DFT discrete Fourier transform

DL-TR-GSM dual-layered transmit-receive **GSM!**

DLT dual-layered transmission

DPC dirty paper coding

DoF Degree of Freedom

DC direct-current

DoA Direction of arrival

ELPC Extremely Low-Power Communications

ERLLC Extremely Reliable and Low-Latency Communications

URLLC Ultra-reliable and low latency communication

EGC equal gain combining

EM electromagnetic

EVD eigenvalue decomposition

eMBB enhanced Mobile Broadband

FeMBB Further-enhanced Mobile Broadband

FSPL free space path loss

FFT fast Fourier transform

FDE frequency domain equalization

mMTC massive machine-type communications

FPGA field-programmable gate array

INR Interference-to-Noise-Ratio

IOSs intelligent omni-surfaces

IoT Internet-of-Things

IRS Intelligent Reflecting Surface

IFFT invserse fast Fourier transform

ICI inter-channel interference

i.i.d. independent and identically distributed

IOS intelligent omni-surface

IQ in-phase and quadrature

ISI intersymbol interference

ISI-free intersymbol interference free

KKT Karush-Kuhn-Tucker

KPI Key performance indicator

LOS line-of-sight

LR LOS fading

LS Least Squares

LIS large intelligent surface

MC Monte Carlo

MT mobile terminal

MEC Mobile Edge Computing

MEMS Microelectromechanical System

MIMO Multiple Input Multiple Output

MISO Multiple Input Single Output

ML Maximum Likelihood

MMSE Minimum Mean Square Error

mmWave millimeter-wave

MAC multiple-access channel

MUSIC MUltiple SIgnal Classification

NOMA Non-Orthogonal Multiple Access

NLOS non-LOS

OFDM orthogonal frequency division multiplexing

OFDMA orthogonal frequency division multiple access

QoS quality-of-service

RAWC RIS-Aided Wireless Communication

RBIT RIS Based Information Transmission

RE Reflective Element

RF Radio Frequency

RIS Reconfigurable Intelligent Surface

RR Rayleigh Fading

RV Random Variable

RX receiver

RAN radio access network

SCI Soft Interference Cancellation

SDR SemiDefinite Relaxation

SIMO Single Input Multiple Output

SINR Signal-to-Interference-plus-Noise Ratio

SNR Signal-to-Noise Ratio

SPC Short Packet Communications

SR Symbiotic Radio

SRE Smart Radio Environments

SSK Space Shift Keying

SWIPT Simultaneous Wireless Information and Power Transfer

SER symbol error rate

SIC successive interference cancellation

SISO single-input single-output

SVD singular value decomposition

THz Terahertz

TX transmitter

UE User Equipment

ULA uniform linear array

URA uniform rectangular array

UAVs Unmanned aerial vehicles

VLC Visible Light Communications

ZF Zero-Forcing

ZMCG zero-mean complex Gaussian

Notation

The following notation is used throughout this thesis.

$\mathbf{x}$	a vector
$\mathbf{x}_n$	the nth vector
$\|\mathbf{x}\|$	the norm of $\mathbf{x}$
$\mathbf{X}$	a matrix
$\mathbf{X}_n$	the nth matrix
s_i	the ith symbol
$\overset{d}{=}$, $\sim$	Equivalent in distribution, distributed as
$\overset{N\gg1}{=}$, $\overset{N\gg1}{\approx}$, $\overset{N\gg1}{\propto}$	Equality, approximation and scaling law if $N \gg 1$
diag($\mathbf{x}$)	a diagonal matrix with diagonal given by vector $\mathbf{x}$
$\arg(x)$	the angle of the complex variable x.
$\mathbb{E}$, $\mathbb{V}$, cov	Expectation, variance, covariance
Re, Im	Real part, imaginary part
$(\cdot)^H$, $\mathbf{1}(\cdot)$	Hermitian operator, indicator function
$\|\cdot\|$, $\|\cdot\|$	Absolute value, norm of a vector
$\mathbf{0}_{A\times B}$	$A \times B$ matrix with all zero entries
$\mathbf{1}_{A\times B}$	$A \times B$ matrix with all one entries
$\operatorname{sinc}(x)$	Normalized sampling function ($\sin(\pi x)$ / (πx))
$\mathcal{O}(\cdot)$	Big O (asymptotic) notation
$\mathcal{N}\left(m,\sigma^2\right)$	Gaussian random variable ($\mathbb{E} = m$, $\mathbb{V} = \sigma^2$)
$\mathcal{CN}\left(m,\sigma^2\right)$	Complex Gaussian random variable ($\mathbb{E} = m$, $\mathbb{V} = \sigma^2$)
$\mathcal{U}(a,b)$	Uniform random variable in $[a,b]$
Rayleigh(σ)	Rayleigh random variable with scale σ

List of Figures

List of Tables

1 Introduction

This chapter begins with *Section 1.1* which introduces the challenges of 6G networks and the concept of smart radio environments (SRE). *Section 1.2* introduces reconfigurable intelligent surface (RIS) and illustrates the working principle of RIS. In *Section 1.3*, we introduce merits of RIS by summarizing potential applications of RIS in 6G networks. *Section 1.4* highlights the major contributions in this thesis work and the organization of the thesis. *Section 1.5* provides lists of publications produced during the Ph.D. thesis.

1.1 Background

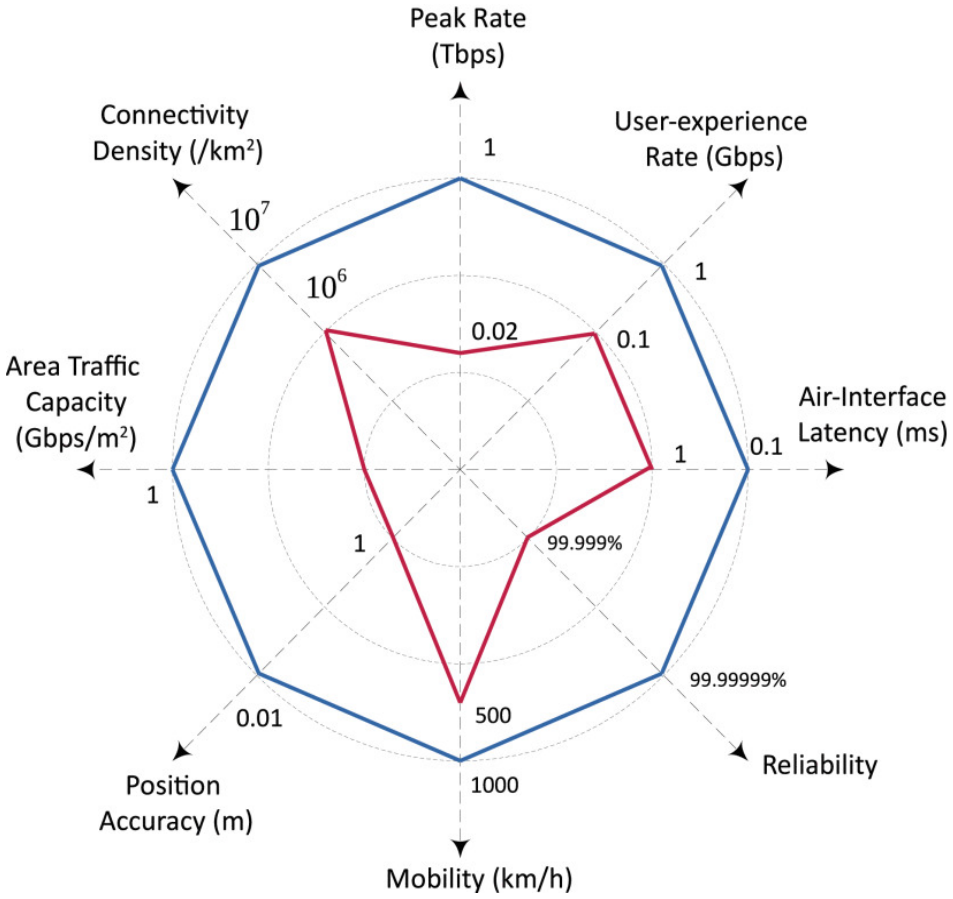

Figure 1.1: Quantitative comparison of the technical requirements between 5G and 6G w.r.t eight representative KPIs [1].

The next-generation wireless and mobile communication systems are expected to support the tremendous demand on the higher date rates, which is estimated to increase every year by more than 50 %, generated not only due to the huge increase in the number of the smart connected devices but also the new disruptive services and applications on the horizon. Moreover, it is also driven by the permanent need to continuously enhance network efficiencies, namely cost efficiency, energy efficiency, spectrum efficiency, and operational efficiency. Seeking to better fulfill the increased requirement for the current services and to offer the possibilities for novel services and applications, the communication communities push more efforts to explore the most advanced technologies such as Artificial Intelligence (AI), Terra-Hertz (THz), and large-scale satellite constellations, and to be able to evolve towards a more powerful and more efficient system.

The 5G system is designed to satisfy more diverse quality-of-service (QoS) requirements stemming from a huge variety of applications and services. Nowadays, with the development of technologies, the 5G system is able to define different use cases such as [1],

- enhanced Mobile Broadband (eMBB) addresses the human-centric applications for providing a high-data-rate access to mobile services, multi-media content, and data in addition to a better latency for newer applications. It emphasizes wide-area coverage to provide seamless access and high capacity in hot spots.
- Ultra-reliable and low latency communication (URLLC) opens the possibility for mission-critical connectivity for new applications such as automatic vehicles, Smart Grid, and Industry 4.0, which have stringent requirements on reliability, latency, and availability. According to the 3GPP standard, the end-to-end delay of 5G communications is required to be less than 1 ms, which is about 1/200 of delay requirement for 4G, and the target reliability must be as high as 10^{-2} to 10^{-7} .
- massive machine-type communications (mMTC) supports dense connectivity with a very large number of connected devices typically deployed in IoT scenarios. The devices such as sensors are low-cost, low-power consumption but typically transmitting a low volume of delay-tolerate data.

The eight technical Key performance indicator (KPI) presented in Fig. 1.1 are used to quantify the difference between the 5G and 6G objectives. As visualised in the figure, the expected device connectivity density is larger than 10^7 devices/km^2; the reliability should be higher than 99.9999% and the latency should be smaller than 0.1 ms [12]; the peak data rate should be at least 1 Tb/s and the user-experienced data rate should be higher than 1 Gb/s; the energy efficiency should be ten or hundred times of 5G.

Various advanced technologies on transmission, networking, and computing are being studied to fulfill these typical stringent requirements to then applied in the 6G system. Those advanced technologies can be classified into several groups: new spectrum consisting of mmWave, Terahertz (THz) communications, new networking that covers softwarization and virtualization, radio access network (RAN) slicing, O-RAN, and post-quantum security, new air interface including massive MIMO, Reconfigurable Intelligent surfaces (RISs), cell-free massive MIMO, and new modulation techniques.

Since the beginning of the wireless communication era, the propagation channel and the physical objects are always regard as sources for performance deficiency, as it is always have a negative effect on the propagated signals due to the interaction between the electromagnetic waves and the environment objects. in addition, the designer of wireless communication system always adhere to the postulates that the environment between communicating devices (i) cannot be modified as it is controlled by nature, (ii) we can only compensate it negative effect through the design of sophisticated transmission and reception schemes.

Reconfigurable Intelligent Surface (RIS), or Intelligent Reflecting Surface (IRS) introduced in the new air interface attracted the attention from the wireless community for its capability to configure Smart Radio Environments (SRE) where the wireless propagation conditions are designed to improve wireless communication [2].

A novel view of the wireless environment is now exist with the deployment of the RISs elements in the propagation channel. Since RISs are capable of shaping the wavefront of the radio waves throughout the network, thus, the wireless environment can be in theory customized to suit the system requirements as depicted in Fig (1.2). The authors in [2] defined an SRE as a smart reconfigurable radio environment that plays actively in transferring and processing information and that enhances the reliability of data exchange between transmitters and receivers.

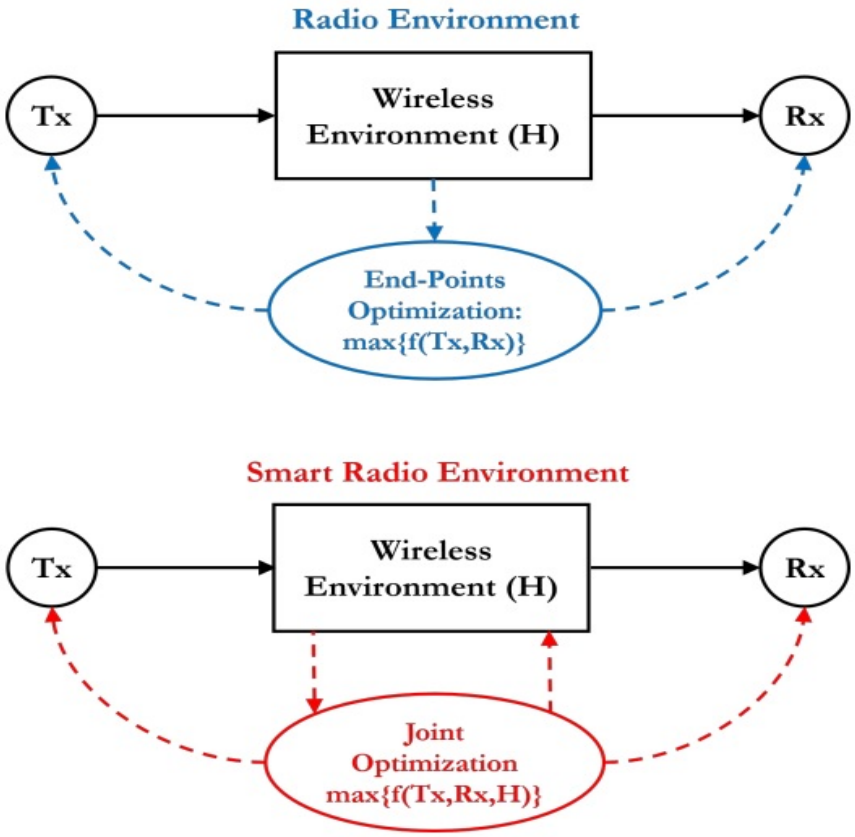

Figure 1.2: Radio environments vs. smart radio environments [2].

1.2 Reconfigurable intelligent surface

Recently, Reconfigurable Intelligent Surfaces (RIS) [13],[14] and reference therein, have been emerged as one of the auspicious solutions to to achieve SRE through customizing the uncontrolled propagation environment. RIS is an array of low-cost and lightweight passive antenna elements (reflecting elements), easily deployed/mounted on different propagation environment objects such as building facades and walls. RIS's power consumption is negligible compared to the immense energy required for the RF chains of Massive MIMO antennas arrays. The RIS has capability of reconfiguring the propagation environment relies on the physical

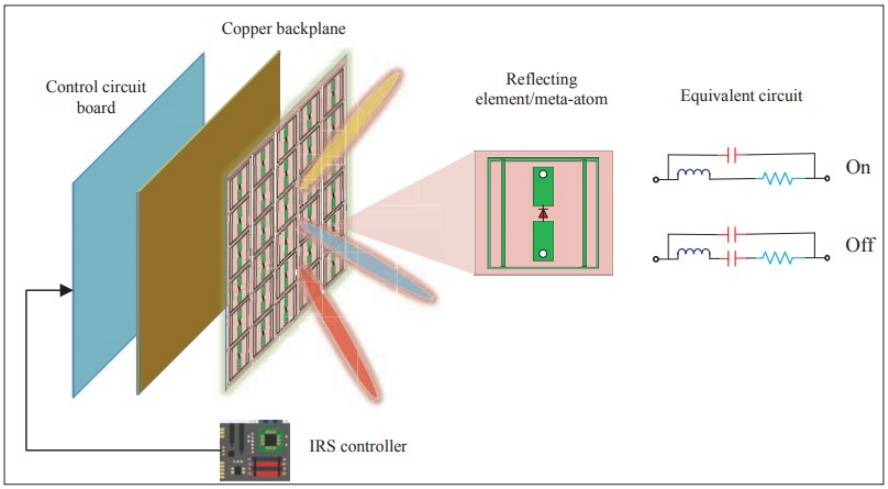

Figure 1.3: Architecture of RIS [3].

properties of its Meta-Materials building blocks. A large number of these building blocks often referred to as unit-cells or meta-atoms, are assembled into a planner surface. Each reflecting element is designed and controlled to reconstruct the characteristics of the electromagnetic waves impinging upon its surfaces, such as amplitude, phase, and polarization. Therefore, RIS adds a new Degree of Freedom (DoF) to improve the radios environment further. Based on the available channel state information (CSI) at the Base Station base station (BS), network operators have full access to control and reconfigure each reflecting element of RIS through a dedicated wireless control channel and a RIS integrated software controller.

A simple and typical RIS architecture is presented in Fig(1.3). The RIS consists of three layers and a smart controller. In the outer layer, a huge number of metallic patches (elements) are printed on a dielectric substrate to directly interact with incident signals. The layer in between is a copper plate to be utilized to prevent the signal energy leakage. The Last (the inner) layer represents a control circuit board that is responsible for configuring the reflection amplitude/phase shift of each element, triggered by a smart controller attached to the RIS. In practice, the RIS controller is implemented by implementing a field-programmable gate array (FPGA) , which also acts as a gateway to communicate and coordinate with other network components (e.g., BSs, APs, and user terminals) through separate wireless links for low-rate information exchange with them. The figure also shows the structure and the equivalent electrical circuit for an individual element , where a positive intrinsic (PIN) diode is embedded in each element. By controlling its biasing voltage via a direct-current (DC) feeding line, the states of the PIN diode can be switched between “On” and “Off” states as shown in the equivalent circuits, there by generating a phase-shift difference. In addition, a variable resistor load can be applied in the element design and by changing the values of resistors in each element, different portions of the incident signal’s energy are dissipated, thus achieving controllable reflection amplitude in [0, 1].

By adopting RIS as an aided object to control and customize the wireless channel.The func-

tions of the proposed RIS technology can be different. By its capability of amplifying and performing signal processing operations on the impinging radio wave, they are classified into active and passive surfaces, for example, the punch of the received signals at the receiving side can be combined constructively or destructively [15], [16]. Therefore, an enhanced data rate can be delivered if the RIS is programmed to combine the received signals constructively at one or more designated receivers. A high energy harvesting can be achieved if the RIS allows the received signals to be combined destructively, which creates a free-interference zone at unintended receivers without implementing any interference cancellation and management techniques. For more details about State-of-art of Smart radio environment or RIS, its abundant potential application for Beyond 5G networks, open research challenges, the interested readers are referred to [4, 13, 14, 17, 18, 19, 20, 21].

1.2.1 The working principle of RIS

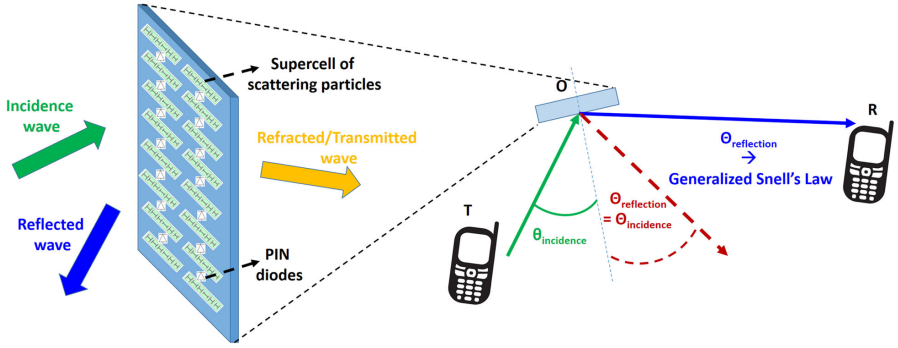

Figure 1.4: Working principle of RIS [2].

The working principle of a RIS can be explained with the help of Fig.1.4. Once An incident electromagnetic radio wave reaches the RIS , it is divided into two parts: the reflected and transmitted (or refracted) radio wave. The reflected and transmitted radio waves can be reconfigured with specific arrangements of the scattering particles on the RIS [22], which is achieved by using PIN diodes in this example. The RIS is capable of shaping the radio waves by the generalized Snell's laws of reflection and refraction [23], which makes the angle of reflection radio waves controllable. Typically, the intelligent reconfiguration is achieved with the aid of sensors embedded at the RIS and a feedback link connected to a Central Processing Unit (CPU) controller.

1.2.2 Illustrative Example of RIS use cases for Smart Radio Environment

An example of smart radio environment is sketched in Fig. (1.5), where four application scenarios are identified [4].

- **Signal engineering**: Assume that small cell 1 wishes to communicate with mobile terminal (MT) 1, but the line-of-sight (LOS) link is blocked by an object. In this case,

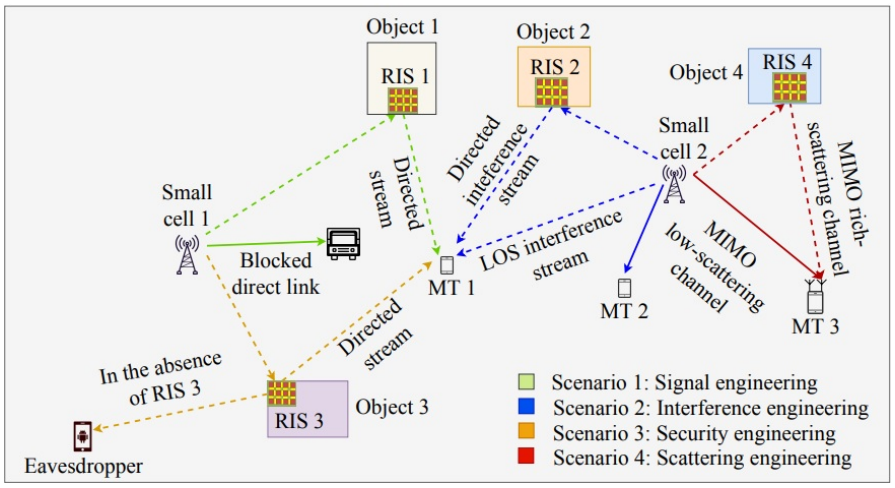

Figure 1.5: Example of smart radio environment[4].

small cell 1 redirects the transmitted beam towards RIS 1 that coats object 1, and assists the communication by shaping the incident wave towards MT 1 so that the received signal strength is maximized.

- **Interference engineering**: While small cell 1 communicates with MT 1, small cell 2 communicates with MT 2. Thus, an interfering signal reaches MT 1 from small cell 2. To suppress it at MT 1, RIS 2 is programmed to shape the impinging radio wave from small cell 2 towards MT 1 in a way that the two signals are destructively combined at MT 1.

- **Security engineering**: In the absence of RIS 3, the signal emitted by small cell 1 and intended to MT 1 is reflected from object 3 towards a malicious user that overhears it. To avoid this, RIS 3 is programmed to shape the reflection towards MT 1 so that it is steered away from the malicious user while being decoded more reliably, via diversity combining, at MT 1.

- **Scattering engineering**: The multiple-antenna small cell 2 wishes to convey information to the multiple-antenna MT 3 with the aid of multiple-input multiple-output transmission. The channel between small cell 2 and MT 3 has, however, a low rank (low scattering environment), which negatively affects the attainable data rate. To avoid this issue, small cell 2 directs the signal intended to MT 3 towards RIS 4, which appropriately shapes it so as to create a rich-scattering environment (high rank channel) for high data rate transmission.

1.3 Potential applications in 5G/6G networks

Upcoming beyond fifth generation (5G) communications systems goal at further enhancing key performance indicators and fully supporting brand-new use cases by embracing emerging techniques, e.g., reconfigurable intelligent surface (RIS), integrated communica-

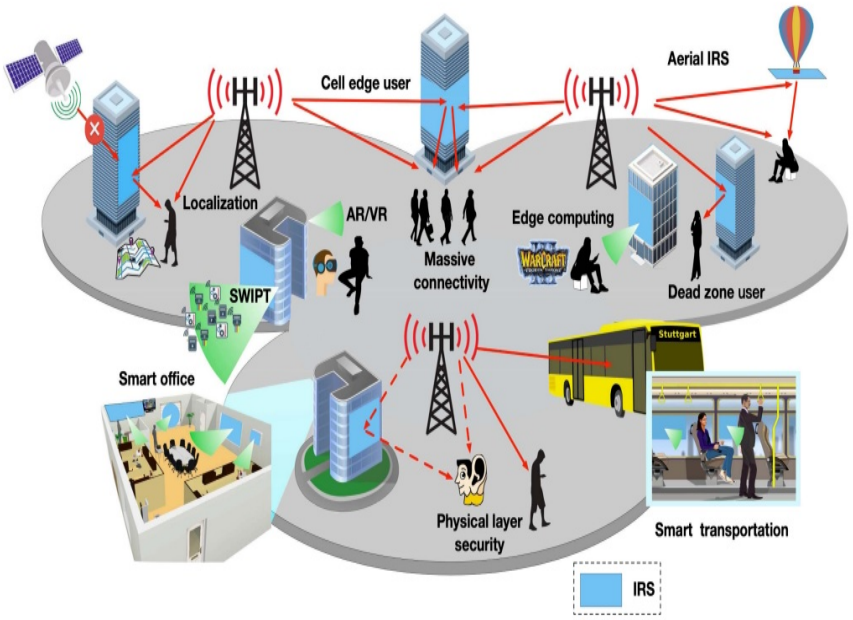

Figure 1.6: Illustration of RIS applications in future wireless network [5].

tion, localization, and sensing, mmWave/THz communications, visible light communications (VLC), mobile edge computing (MEC) and simultaneous wireless information and power transfer (SWIPT) have been proposed. Moreover, RIS can be jointly designed with these technologies and brings additional degrees of freedom for improving communication systems performances.

Creating a smart radio environment without increasing energy consumption and hardware cost is one of the appealing features of the RIS,thus, RIS is a neat sequel to these technologies to realize beyond fifth generation (5G) communications systems. In the following, we list some potential applications of RIS in 5G/6G networks.

1.3.1 Massive connectivity communications

In addition to enhanced mobile broadband (eMBB) and ultra-reliable low-latency communication (uRLLC), Massive connectivity, also known as massive machine type communication (mMTC), has been regarded as one of the three typical use cases of the fifth-generation (5G) wireless networks due to the popularity of the Internet of Things (IoT). A primary challenge of mMTC is to support sporadic short-packet communications between the base station (BS) and a massive number of IoT devices to ensure the connectivity. Usually, the IoT devices are located in a location called "dead zone", where the line-of-sight communication may not be available. Consequently, the signals received from the IoT devices are usually precarious, thus, accurate device detection is a challenging task for the BS. On the other hand, poor channel

conditions in the dead zones also reduce the link reliability for data transmissions between the active devices and the BS [24]. RIS can be employed for overcoming these challenges. In [24], the RIS-related activity detection and channel estimation problem in the RIS-assisted massive IoT network is studied. A modeled the RIS-to-BS channel as a sparse channel due to limited scattering between the RIS and the BS was proposed. Where a sparse matrix factorization problem is modeled by simultaneously exploiting the sparsity of both sporadic transmissions in massive connectivity and the RIS-to-BS channels.The authors proposed an AMP-based algorithm to jointly detect active devices and estimate two separated channels of the RIS-to-BS link and the RIS-to-device link relying on the Bayesian inference framework to solve these problems.

1.3.2 THz communications

Radio spectrum is always a tightly regulated resource. Recently, THz communications operating between 100 GHz and 10 THz is considered as a key enabler for FeMBB in the next generation of wireless communication. Because high-frequency signals are much likely blocked due to high penetration loss and reduced diffraction effects, RIS is needed THz communications to solve the problem. In [25], a joint hybrid precoding strategy was proposed to maximize the sum-rate for RIS-aided THz MIMO communication systems. Then, the hierarchical search codebook design was proposed in [26] to reduce the complexity of channel estimation and data transmission. In [27], the theoretical error rate of the system was analyzed where the RIS was mounted on a satellite to enable signal propagation in low earth orbit satellite networks with THz communications.

1.3.3 Localization, Positioning, and Sensing

The emerging location-aware applications such as virtual reality, robot navigation, autonomous driving are among the requirements of the future wireless communication networks. These applications oblige more strict requirements on both the communication and sensing performance of today's wireless systems, such as ultra-high data rate, ubiquitous and seamless coverage, extremely-high reliability and ultra-low latency, as well as high-precision/resolution sensing. To meet the high demands of future 6G systems in terms of both communication and sensing, In [28] a new RIS-self-sensing system is proposed, where the RIS controller is implemented to transmit probing signals, and dedicated sensors are installed at the RIS for location/angle estimation based on the reflected signals by the target with and without the RIS reflection. The MUSIC algorithm was applied to estimate the DOA of the target in the RIS's vicinity with high accuracy, without the involvement of either the BS or any mobile device.

1.3.4 Wireless Power Transfer and SWIPT

Enhancing energy efficiency is one of the major pillars of future wireless systems. Simultaneous wireless information and power transfer (SWIPT) is a technology for transferring information and power form the source (transmitter) to a destination (receiver) at the same time. To improve the efficiency of simultaneous wireless information and power transfer (SWIPT) from the AP to wireless devices in e.g., smart office/home, the large aperture of IRS can be leveraged to compensate for the significant power loss over long distance via reflect beamforming to its nearby devices. In indoor communication

In [29], the authors consider the downlink of a MISO system in which a base station sends information and energy signals to a set of receivers and an RIS is used to aid the information and energy transfer. In this setup, the base station beamformer and the RIS phase shifts are alternatively optimized with the aim of maximizing the minimum power received at all the energy-harvesting receivers, by fulfilling individual SINR constraints for the information receivers and a maximum transmit power constraint for the base station. The resulting optimization problem is tackled by using alternating optimization and semi-definite relaxation, thus obtaining a sub-optimal but efficient algorithm.

1.3.5 Mobile edge computing

Edge computing, as one of the key technologies in 6G networks to support low-latency services with high-performance, establishes a distributed computing environment by deploying computation and storage resources in proximity to end users. However, the potential advantages of MEC systems are restricted by the long-distance offloading link. This problem can be hacked by deploying an RIS to amplify the signal transmission by passive beamforming. RIS-aided MEC systems were considered in [30, 31], where joint design of the active and passive beamformers, RIS deployment, communications, and computing resource allocation of RIS-aided MEC systems is investigated to further enhance the uplink offloading performance and system performance.

1.3.6 Air-ground communications

Recently, the communication community exert a huge effort in bringing resilience and agility to advanced wireless networks that depends on flying access points, namely air-to-ground networks. Unmanned aerial vehicles (UAVs) will be, soon, a part of our lives by improving the way we work, e.g., package delivery and to extend the safety and security of our society. In [32], the RIS was implemented into the air-ground communications with multiple aerial/terrestrial users, the active and passive beamformers besides the RIS locations are jointly designed. Furthermore, in [33], the aerial user trajectory was further considered in the above system to achieve a higher spectrum and energy efficiency.

1.4 Thesis Overview and Major Contributions

A huge portion of this thesis work revolves around paving the way for further research into the performance of RISs based on accurate and realistic electromagnetic reradiation models, in addition to developing optimization frameworks for enhancing the communication system performance on two main use case: (i) To jointly improves the information rate and the amount of harvested power in a RIS-aided MISO downlink multiuser wireless network. (ii) To investigate the intelligent omni-surfaces (IOSs) for enhancing spectral efficiency for large number of users located on cell edge or on the other side of the RIS.

The main contributions of this thesis are the following:

i) This thesis shown that the size and the inter-distance between the RIS reconfigurable elements, and the quantization of the amplitudes and phases of the reflection coefficients both determine the quality of the reradiated pattern. Furthermore, we have shown that the main peak of the reradiated pattern may not be perfectly steered towards the nominal direction of reradiation for large angles of deflection. Moreover, this thesis shown that an RIS inherently filters out the interference towards the desired direction of reradiation, provided that the interfering electromagnetic waves originate from directions that are sufficiently different from the direction of incidence of the intended user (chapter3).

ii) This thesis proposed the novel bi-objective function that simultaneously maximize the information rate and harvested power, subject to minimum downlink rate, minimum harvested power, and maximum transmit power constraints. it provided an optimization framework, with affordable complexity, rely on alternating maximization, sequential optimization, and penalty-based methods. Also, it considered the realistic case in which the phases and moduli of the RIS reflection coefficients are coupled by a deterministic function, in addition to, the optimization of the power split ratio at receiver, which is a novel feature compared to most related works on RIS-aided and SWIPT-based systems (chapter4).

iii) This thesis proposed an optimization algorithms, that has a rapid convergence rate in a few iterations, for maximizing the sum-rate in IOS-aided MIMO broadcast channels which can be exploited for serving cell-edge user and for enhancing network coverage, Also, it analyzed the case studies with continuous-valued and discrete-valued phase shifts for the reflection and transmission coefficients, that are assumed to be dependent of each other (chapter5).

1.5 Publications

Journal Paper The following is the journal publication produced from the research outcomes of this thesis.

(*J*1) **Abdelhamed. Mohamed**, A. Zappone and M. D. Renzo, "Bi-objective Optimization of Information Rate and Harvested Power in RIS-aided SWIPT Systems," in *IEEE Wireless Communications Letters*, 2022, doi: 10.1109/LWC.2022.3196906.
Abstract: The problem of simultaneously optimizing the information rate and the harvested power in a reconfigurable intelligent surface (RIS)-aided multiple-input single-output downlink multiuser wireless network with simultaneous wireless information and power transfer (SWIPT) is addressed. The beamforming vectors, RIS reflection coefficients, and power split ratios are jointly optimized subject to maximum power constraints, minimum harvested power constraints, and realistic constraints on the RIS reflection coefficients. A practical algorithm is developed through an interplay of alternating optimization, sequential optimization, and pricing-based methods. Numerical results show that the deployment of RISs jointly improves the information rate and the amount of harvested power.

Conference Paper The following is the conference paper produced from the research outcomes of this thesis.

(*C*1) **Abdelhamed. Mohamed**, N. S. Perović and M. Di Renzo, "Intelligent Omni-Surfaces (IOSs) for the MIMO Broadcast Channel," *IEEE 23rd International Workshop on Signal Processing Advances in Wireless Communication (SPAWC)*, 2022, pp. 1-5, doi: 10.1109/SPAWC51304.2022.9833922.
Abstract: Reconfigurable intelligent surfaces (RISs) are regarded as an emerging technology for the next generation of wireless communications. In this paper, we consider intelligent omni-surfaces (IOSs), which are capable of simultaneously reflecting and refracting electromagnetic waves. We focus our attention on the multiple-input multiple-output (MIMO) broadcast channel, and we introduce an algorithm for jointly optimizing the covariance matrix at the base station, the matrix of reflection and transmission coefficients at the IOS, and the amount of power that is reflected and refracted from the IOS. The distinguishable feature of this work lies in taking into account that the reflection and transmission coefficients of an IOS are tightly coupled. Simulation results are illustrated to show the convergence of the proposed algorithm and the benefits of using surfaces with simultaneous reflection and refraction capabilities.

Book Chapter The following is the book chapter produced from the research outcomes of this thesis.

($B1$) Marco Di Renzo, **Abdelhamed. Mohamed**, Alessio Zappone, Vincenzo Galdi, Gabriele Gradoni, Massimo Moccia, and Giuseppe Castaldi. "Digital Reconfigurable Intelligent Surfaces: On the Impact of Realistic Reradiation Models.",2022, arXiv preprint arXiv:2205.09799.

Abstract: Reconfigurable intelligent surface (RIS) is an emerging technology that is under investigation for different applications in wireless communications. RISs are often analyzed and optimized by considering simplified electromagnetic reradiation models. Also, the existence of possible electromagnetic waves that are reradiated towards directions different from the desired ones are often ignored. Recently, some testbed platforms have been implemented, and experimentally validated reradiation models for RISs have been reported in the literature. In this chapter, we aim to study the impact of realistic reradiation models for RISs as a function of the sub-wavelength inter-distance between nearby elements of the RIS, the quantization levels of the reflection coefficients, the interplay between the amplitude and phase of the reflection coefficients, and the presence of electromagnetic interference. Furthermore, we consider both case studies in which the users may be located in the far-field and near-field regions of an RIS. Our study shows that, due to design constraints, such as the need of using quantized reflection coefficients or the inherent interplay between the phase and the amplitude of the reflection coefficients, an RIS may reradiate power towards unwanted directions that depend on the intended and interfering electromagnetic waves. Therefore, it is in general important to optimize an RIS by taking into account the entire reradiation pattern by design, in order to maximize the reradiated power towards the desired directions of reradiation while keeping the power reradiated towards other unwanted directions at a low level. Among the considered designs for RISs, our study shows that a 2-bit digitally controllable RIS with an almost constant reflection amplitude as a function of the applied phase shift, and whose scattering elements have a size and an inter-distance between $(1/8)$-th and $(1/4)$-th of the signal wavelength may be a good trade-off between performance, implementation complexity and cost. However, the presented results are preliminary and pave the way for further research into the performance of RISs based on accurate and realistic electromagnetic reradiation models.

2 Optimization techniques for Reconfigurable Intelligent Surfaces- aided wireless communication systems- An Introduction

Chapter 2. Optimization techniques for Reconfigurable Intelligent Surfaces- aided wireless communication systems- An Introduction

In this chapter, the state-of-art of the optimization techniques developed for RIS-aided systems are introduced. This chapter is organized as follows. In *Section 2.1*, we introduce the system models of RIS-aided MIMO systems and then investigate the reflection principle of RISs. In *Section 2.2*, we introduce the Optimization techniques challenges of RIS-assisted systems. In *Section 2.3*, we present the proposed optimization techniques for the design of the continuous phase shifts and *Section 2.4*, the optimization of RISs subject to discrete-valued phase shifts, which leads to an NP-hard optimization problem, are presented.

As highlighted in Chapter 1, RIS is considered as a nearly-passive device that needs to utilize the radio waves to operate its function. And, by utilizing this revolutionary idea of reconfigurable intelligent surfaces (RISs), which are capable of configuring the wireless propagation environment into a more desirable transmission medium, we can gain a huge performance gain compared to the traditional network design without RISs. However, in order to unleash the full potential of RISs, we are in a need to understand their behavior in the context of communication systems. Besides, the practical challenges related to the design RISs hardware and how to optimize its parameters (i.e., amplitude, and phase shift) under different considerations. Also, advanced optimization techniques should be developed to optimize the performance of an RIS for given performance target.

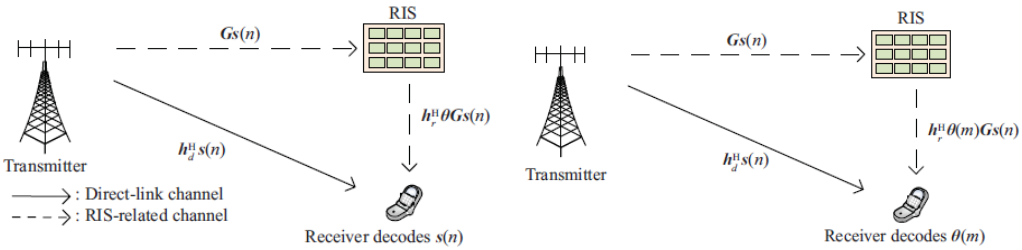

(a) RAWC (b) RBIT

Figure 2.1: Two communication paradigms of RIS [6].

2.1 RIS-aided communication systems

The RISs can be exploited to perform two functionalities in the communication system based on the purpose of the RISs reflection as shown in Fig. 2.1. RISs can be utilized for information transmission and for improve communication link quality. The former is called RIS based information transmission (RBIT), and the RIS adapt its reflection coefficient matrix θ to assist the transmitter according to the CSI, thus more channel diversity are provided. The latter is called RIS-aided wireless communications (RAWC) [6], the RIS proactively adjust its reflection coefficient matrix $\theta(\mathbf{m})$ to delivers its own message to the receiver. Specifically, in (RBIT), the generated messages at the transmitter $s(n)$ are encoded in $s(n)$ or $\theta(\mathbf{m})$, or both as shown in Fig. 2.1(b). In (RAWC), the information message $s(n)$ aren't changed by the reflection coefficient matrix of the RIS via the RIS-related channel, thus, the messages are only encoded in $s(n)$ as shown in Fig. 2.1(a),.

In this thesis, we focus on the latter scenario, where the RISs is implemented to improve the communication link quality as a virtual line-of-sigh.

2.1.1 System models

For the purpose of exposition, we introduce an RIS-assisted multi-user multiple input single output (MISO) for downlink communication system. The baseband channels from the BS to the RIS, from the RIS to user k, and from the BS to user k are denoted by $\mathbf{H}^{\mathrm{H}} \in \mathbb{C}^{M\times N}$, $\mathbf{h}_{r,k}^{\mathrm{H}} \in \mathbb{C}^{1\times M}$ and $\mathbf{h}_{d,k}^{\mathrm{H}} \in \mathbb{C}^{1\times N}$, respectively [34]. The transmitted data symbols for user k is denoted by s_k with $\mathbb{E}\{s_k\} = 0$ and $\mathbb{E}\{s_k^2\} = 1$. The beamforming vector for user k is $\mathbf{w}_k \in \mathbb{C}^{N\times 1}$. Then, the transmitted data at the BS is given by $\mathbf{x} = \sum_{j=1}^{K} \mathbf{w}_j s_j$, and the received signal at user k is expressed as

$$y_k = \left(\mathbf{h}_{d,k}^{\mathrm{H}} + \mathbf{h}_{r,k}^{\mathrm{H}} \Theta \mathbf{H}^{\mathrm{H}}\right) \sum_{j=1}^{K} \mathbf{w}_j s_j + n_k, \tag{2.1}$$

where $n_k \sim \mathscr{CN}\left(0, \sigma_k^2\right)$ is the AWGN at user k and Θ is the reflection coefficient matrix given by $\Theta = \mathrm{diag}\,(\boldsymbol{\theta})$, where $\boldsymbol{\theta} = [\theta_1, \cdots, \theta_M]^{\mathrm{T}}$ is the corresponding reflection coefficient vector at the RIS with $\theta_m = \alpha_m e^{j\varphi_m}$ being the reflection coefficient corresponding to the m-th reflecting element. Using the signal-to-interference-plus-noise-ratio (SINR) at user k is given by

$$\mathrm{SINR}_k = \frac{\left|\left(\mathbf{h}_{d,k}^{\mathrm{H}} + \boldsymbol{\theta}^{\mathrm{T}} \mathbf{G}_k^{\mathrm{H}}\right) \mathbf{w}_k\right|^2}{\sum_{i=1, i\neq k}^{K} \left|\left(\mathbf{h}_{d,k}^{\mathrm{H}} + \boldsymbol{\theta}^{\mathrm{T}} \mathbf{G}_k^{\mathrm{H}}\right) \mathbf{w}_i\right|^2 + \sigma_k^2}. \tag{2.2}$$

Hence, it is observed from (2.2) that the cascaded channel $\mathbf{G}_k^{\mathrm{H}}$ along with the direct channel $\mathbf{h}_{d,k}^{\mathrm{H}}$ are sufficient for designing the transmission of the BS and the RIS. The data rate of user k is $R_k = \log_2(1 + \mathrm{SINR}_k)$.

2.1.2 Reflection principle

It is apparent that RIS-based communications rely on the design of the reflection coefficients, which is a defining issue in practical hardware implementations.

In order to realize the smart radio environment, we should be able to control each reflecting element and reconfigure its characteristic. The reconfigurability lies in adjusted independently the reflection coefficient of each reflecting element by a designed control signal. The reflection coefficient is defined as a parameter that describes how much of a wave is reflected by an impedance discontinuity in the transmission medium.

The reflection coefficient of the m-th reflecting element as θ_m, can be expressed as

$$\theta_m = \alpha_m e^{j\varphi_m} \tag{2.3}$$

where α_m and φ_m represent the controllable amplitude and phase shift of the m-th reflecting element, respectively.

Form the EM point-of-view, the reflection coefficient θ_m can be expressed as

$$\theta_m = \frac{\tilde{E}(m)}{E(m)} \tag{2.4}$$

where $\tilde{E}(m)$ and $E(m)$ be the electromagnetic (EM) wave impinging on the m-th reflecting element,and the EM wave reflected from the m-th reflecting element. Furthermore, let Z_0 and $Z(m)$ denote the impedance towards the source in the air and the equivalent load impedance of the m-th reflecting element, the reflection coefficient θ_m can be written as [35]

$$\theta_m = \frac{Z(m) - Z_0}{Z(m) + Z_0} \tag{2.5}$$

Therefore, the amplitude and the phase of the reflection coefficient can be written as

$$\alpha_m = \left| \frac{Z(m) - Z_0}{Z(m) + Z_0} \right| \tag{2.6}$$

and

$$\varphi_m = \arctan\left(\frac{\mathrm{Im}\left(\frac{Z(m)-Z_0}{Z(m)+Z_0}\right)}{\mathrm{Re}\left(\frac{Z(m)-Z_0}{Z(m)+Z_0}\right)} \right) \tag{2.7}$$

The equivalent circuit model for a reflecting element is shown in Fig. 2.2, with L_1, L_2, $C(m)$, $R(m)$ and ω denoting the bottom/inner layer inductance, top/outer layer inductance, effective capacitance, effective resistance, and angular frequency of the incident signal [7], respectively. The impedance of the m-th element is denoted as a function of C_m and R_m as follow

$$Z_m(C_m, R_m) = \frac{j\omega L_1 \left(j\omega L_2 + \frac{1}{j\omega C_m} + R_m \right)}{j\omega L_1 + j\omega L_2 + \frac{1}{j\omega C_m} + R_m} \tag{2.8}$$

Investigating carefully eq. (2.8), it is observed that $Z(m)$ is a function of the effective resistance R_m and the effective capacitance C_m, where R_m determines the amount of power dissipation due to the losses in the devices and C_m denotes the charge accumulation related to the semiconductor device. Moreover, the amplitude and the phase of the reflection coefficient can be carefully tuned, theoretically, by varying the impedance $Z(m)$ using a control signal based on eqs. (2.6) and (2.7). For additional illustration, the Fig.2.3 visualize the behavior of the experimental amplitude and the phase shifts of the reflection coefficient.

The RISs are classified into two categories, continuous reflection amplitude and phase shift and discrete reflection amplitude and phase shift.

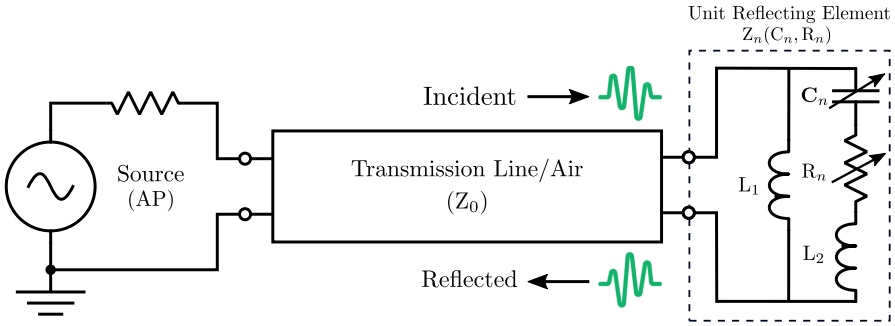

Figure 2.2: Transmission line model of an reflecting element [7].

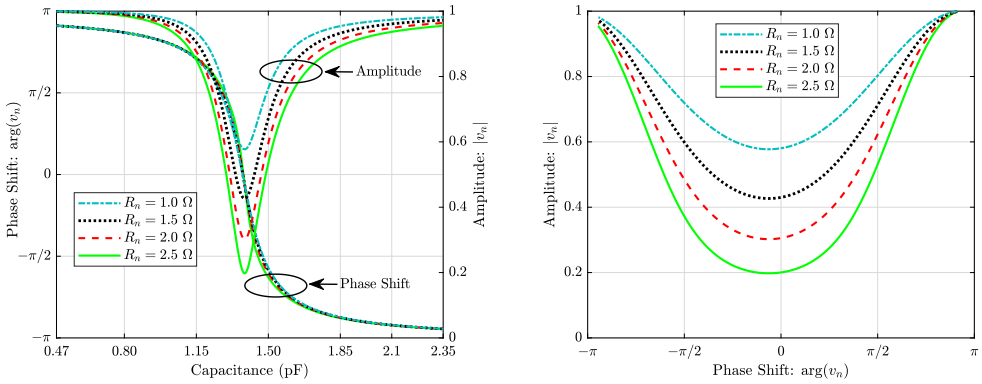

(a) Phase shift and amplitude versus the effective capacitance C_n and the effective resistance R_n.

(b) Amplitude versus phase shifts.

Figure 2.3: Reflection coefficient of an reflecting element [7].

Continuous reflection amplitude and phase shift

Under this assumption, the RIS reflection amplitude and phase shift per element can be independently and continuously tuned, thus yielding their following respective feasible sets: $\alpha_m \in [0,1]$ and $\varphi_m \in [-\pi,\pi)$. To obtain the ideal phase shift control, where $\alpha_m = 1$ and $\varphi_m \in [-\pi,\pi)$, each element should dissipate zero energy dissipation for reflection. However, this is impossible in practical hardware. In addition, the majority of research works on RIS are mainly based on the ideal model where the phase shifts can be adjusted continuously and independently from the reflection amplitudes . However, this ideal feasible sets for RIS reflecting elements usually lead to theoretical performance limits of RIS-aided wireless communication systems under practical reflection models [5].

Discrete reflection amplitude and phase shift

The continuous tuning of the reflection coefficient is beneficial for optimizing the communication performance, it is practically difficult not only due to the increased cost but also more

complex hardware design. For practical RISs, it is more cost-effective to implement only discrete and finite amplitude/phase-shift levels that require only a small number of control bits for each element, e.g., two-level (reflecting or absorbing) amplitude control, and/or two-level (0 or π) phase-shift control.

In general, let b_α and b_φ denote the number of bits for controlling the corresponding number of reflection amplitude and phase-shift levels denoted by K_α and K_φ, respectively, where $K_\alpha = 2^{b_\alpha}$ and $K_\varphi = 2^{b_\varphi}$. Then the sets of discrete reflection amplitudes and phase shifts at each element of RIS can be respectively expressed as

$$\mathscr{F}'_\alpha = \{\bar{\alpha}_1, \cdots, \bar{\alpha}_{K_\alpha}\}, \tag{2.9}$$

$$\mathscr{F}'_\varphi = \{\bar{\varphi}_1, \cdots, \bar{\varphi}_{K_\varphi}\}, \tag{2.10}$$

where $0 \le \bar{\alpha}_m < \bar{\alpha}_{m'} \le 1$ for $1 \le m < m' \le K_\alpha$ and $0 \le \bar{\varphi}_l < \bar{\varphi}_{l'} < 2\pi$ for $1 \le l < l' \le K_\varphi$.

In practice, to further reduce the hardware cost and design complexity, only discrete phase-shift control or discrete amplitude control may be implemented, thus leading to the following two special cases of the above discrete models [5], namely,

- RIS with discrete phase-shift control only, where for each reflecting element, only the phase shift can be tuned while the reflection amplitude is set to its maximum value of one, i.e., $\mathscr{F}'_\alpha = \{\alpha | \alpha = 1\}$ and $\mathscr{F}'_\varphi = \{0, \Delta\varphi, \cdots, (K_\varphi - 1)\Delta\varphi\}$;
- RIS with discrete amplitude control only, where for each reflecting element, only the reflection amplitude can be tuned while the phase shift is set to be a constant (say, zero without loss of generality), i.e., $\mathscr{F}'_\alpha = \{0, \Delta\alpha, \cdots, (K_\alpha - 1)\Delta\alpha\}$ and $\mathscr{F}'_\varphi = \{\varphi | \varphi = 0\}$.

Generally speaking, phase-shift control (or phase beamforming) is of higher cost to implement as compared to amplitude control (or amplitude beamforming) for RIS [5].

Coupled Reflection Amplitude and Phase Shift

Recently, a practical reflection model for RIS was proposed in [7] to provide a maximum design flexibility by modelling each reflecting element as a resonant circuit with certain inductance, capacitance, and resistance. It is observed that the phase shifts and amplitudes are strongly non-linearly coupled which thus are not independently adjustable. Specifically, as shown in Fig. 2.3(b), the reflection amplitude typically reaches its minimum value at the zero phase shift, but monotonically increases and asymptotically approaches the maximum value of one as the phase shift tends to π or $-\pi$. Since the reflection amplitude and phase-shift coupling has a huge influence on the optimal reflection coefficient design of RIS reflecting elements, as it requires to achieve an optimal balance between the signal amplitude and phase reflected by each element such that the reflected signals by all RIS elements are combined at the receiver with maximum power. An analytical model for the phase shift which describe the non-linear

coupling between the phase shifts and amplitudes is proposed in [7]. The amplitude is a function of the phase shifts, which is given as

$$\alpha_m\left(\varphi_m\right) = (1-\alpha_{\min})\left(\frac{\sin\left(\varphi_m-\phi\right)+1}{2}\right)^{\beta}+\alpha_{\min} \tag{2.11}$$

where $\alpha_{\min} \geq 0$, $\phi \geq 0$ and $\beta \geq 0$ are the constants related to specific circuit implementation.

2.2 Optimization techniques challenges

After introducing the practical hardware challenges and constraints related to the manufacturing of the RISs. There still other challenges to be solved due to the deployment of RISs in the propagation environment. In this section, we introduce the Optimization techniques challenges of RIS-assisted systems. To illustrate this point, let us introduce the following general optimization problem, where only the phase shifts of the reflecting elements are optimized, that has been utilized in the vast majority of the existing transmission design as follow [34]:

$$\begin{aligned} &\min_{\mathbf{W},\Theta} \; f\left(\mathbf{W},\Theta\right) \\ &\text{s.t.} \quad \text{C1}: g_i\left(\mathbf{W},\Theta\right) \geq D_i, i=1,\cdots,I, \\ &\qquad \text{C2}: \theta_m \in \mathscr{S}_1 \text{ or } \mathscr{S}_2, \forall\, m=1,2,\ldots,M, \end{aligned} \tag{2.12}$$

where $\mathbf{W}=[\mathbf{w}_1,\cdots,\mathbf{w}_K]$ is the collection of all beamforming vectors. The $f\left(\mathbf{W},\Theta\right)$ and $g_i\left(\mathbf{W},\Theta\right)$ can be any functions that depend on $\mathbf{W}$ and Θ, and I denotes the number of constraints in C1. In constraint C2, $\mathscr{S}_1$ and $\mathscr{S}_2$ denote the set of continuous and discrete phase shifts respectively, which are given by

$$\mathscr{S}_1 = \left\{\theta \middle| \theta = e^{j\varphi}, \varphi \in [0,2\pi)\right\}, \tag{2.13}$$

$$\mathscr{S}_2 = \left\{\theta \middle| \theta = e^{j(l-1)\Delta\varphi}, l=1,\cdots,L\right\}, \tag{2.14}$$

where $L=2^b$ with b being the number of bits used to quantize the continuous phase shifts, and $\Delta\varphi = 2\pi/L$. Optimization frameworks are introduced for optimizing both the phase shifts and the amplitudes of the reflecting elements subject to the constraint $|\theta_m| \leq 1, \forall\, m$ in [36, 37, 38]. It is worth noting that some works considered practical RIS reflection models with phase-dependent amplitude [39, 40, 41]. As discussed earlier simultaneous optimization of both the phase shifts and the amplitudes leads to a more complex hardware design.

Basically, there are two main challenges in solving the optimization problem in (2.12):

- The phase shifts and the system parameters represented here by the beamforming vectors are coupled as shown in the SINR expression in (2.2).
- The optimization problem is non-convex/NP-hard due to the unit modulus constraint

or the discrete-valued phase shifts.

In the following, we discuss the four major challenges to design an efficient optimization techniques for RISs-aided communication systems based on the coupling between phase shift vector Θ and other system parameters,i.e., represented in our basic example by $\mathbf{W}$ [42]:

1. **challenge 1:** the phase shift vector Θ and the system parameter $\mathbf{W}$ are coupled in the objective function although they are independent in constraints.
2. **challenge 2:** the system parameter $\mathbf{W}$ Only exists in the objective function, while Θ and $\mathbf{W}$ are coupled in constraints.
3. **challenge 3:** Only Θ exists in the objective function, while Θ and $\mathbf{W}$ are coupled in constraints.
4. **challenge 4:** Θ and $\mathbf{W}$ are coupled in both objective function and constraints.

It is observed that if one of the optimization variable is fixed, the problem reduced to a feasibility check problem, which indicated in challenge 2 and 3, and to find an efficient solution, a new objective function needs to be reformulated [43, 44].

The major difference between challenge 1 and 4 is that challenge 4 has non-convex constraints which are more challenging to handle due to the coupling and results in difficulty of finding the stationary point.

Consequently, finding a highly efficient and locally optimal solutions with low computational complexity is targeted by the outsmart of the current research works since obtaining a globally optimal solution is challenging.

The alternating optimization (AO) algorithms are usually applied in the most of the works. The main idea behind utilizing the AO algorithm is that we can easily use the previously developed optimization algorithms for the conventional system, if the phase shifts vector of the RISs are known. Under this assumption, the optimization problem reduces to a conventional design problem, which has been extensively studied in the literature and the AO algorithm can be applied to decouple the optimization variables

Moreover, Some tricks are applied to reformulate the original intractable problem into a new tractable but approximated problem. The fractional programming (FP) [45] or the weighted minimum mean-square error (WMMSE) algorithm [46] techniques are often used for this purpose. Then, the existing optimization techniques methods are implemented to optimize the other different system parameters at the BS.

Therefore, The optimization techniques applied for optimizing the phase shifts of the RIS is discussed in the following according to the set over which the phase shift vectors are optimized (,i.e.,the continuous-valued phase shifts or the discrete-valued phase shifts).

2.3 Optimization Techniques for Continuous Phase Shifts.

In this section, we present the current proposed optimization techniques in the literature, for the design of the continuous phase shifts that can be classified into the following categories[34].

2.3.1 *Relaxation and projection*

The idea of this technique is first to relax the non-convex constraint, the unit modulus of the phase shift, $\mathscr{S}_1 = \{\theta \,||\theta| = 1, \theta \in \mathbb{C}\}$ to the convex constraint $\tilde{\mathscr{S}}_1 = \{\theta \,||\theta| \leq 1, \theta \in \mathbb{C}\}$. And obtain a solution for the new formulated problem and then project the obtained solution onto the unit-modulus constraint $\mathscr{S}_1$. Accordingly, having the solution θ_m of the relaxed problem, the final solution is $\theta_m^\star = e^{j\varphi_m}$, where φ_m is the phase of θ_m as applied in [47, 48, 49].

2.3.2 *Element-wise block coordinate descent (BCD)*

The idea of the element-wise BCD algorithm is to update only one variable at each iteration while all the remaining variables are fixed with a given values. Specifically, this technique can be explained as follow, at the m-th iteration, one reflection coefficient θ_m is optimized by keeping fixed the other reflecting coefficients $\theta_{m'}, m' \neq m, m = 1, \cdots, M$, as indicated in [50, 51, 52, 53]. The algorithm ends after M iterations when all the reflection coefficients are optimized one-by-one while keeping the other fixed. The element-wise BCD algorithm is quiet simple since it is not difficult to optimize a single variable rather than optimizing M variables simultaneously. On the other hand, the complexity may be high when the number of reflecting elements is large.

2.3.3 *Semidefinite relaxation (SDR)*

The SDR method is the most common method for optimizing the phase shifts under constraint $\mathscr{S}_1$, i.e., for continuous phase shifts. The unit modulus constraint with $\mathscr{S}_1$, can be reformulated into a rank one form that can be easily solved. The unit modulus constraint can be equivalently written as $\mathbf{V} \succ \mathbf{0}$ and $\text{rank}(\mathbf{V}) = 1$, given that $\mathbf{V} = \boldsymbol{\theta}\boldsymbol{\theta}^{\text{H}}$. However, the reformulated problem is still non-convex due to the rank one constraint [54, 55, 56, 57, 58, 59, 60]. Nevertheless, by applying the SDR method, the non-convex rank one constraint is relaxed. The obtained relaxed problem is a convex semidefinite program (SDP), which can be readily solved by using CVX [61]. In general, the Gaussian randomization method [62] is utilized to obtain a rank-one solution since the obtained relaxed problem is not a rank-one solution, i.e., $\text{rank}(\mathbf{V}) \neq 1$.

2.3.4 *Rank-one equivalents*

The idea of this technique is to transform the rank one constraint into an equivalent form. The rank one constraint represented in the unit modulus constraint can be written as $\mathbf{V} \succ \mathbf{0}$

and rank$(\mathbf{V}) = 1$ [63, 64], given that $\mathbf{V} = \boldsymbol{\theta}\boldsymbol{\theta}^{\mathrm{H}}$. The rank-one constraint can be equivalently transformed to

$$\mathrm{tr}(\mathbf{V}) - \|\mathbf{V}\|_2 = 0. \tag{2.15}$$

Also, $\mathrm{tr}(\mathbf{V}) = \sum_{m=1}^{M} \lambda_m$ and $\|\mathbf{V}\|_2 = \lambda_1$, where λ_m denotes the m-th largest singular value of $\mathbf{V}$. Since $\mathbf{V} \succ \mathbf{0}$ and $\mathbf{V}$ is a non-zero matrix, the equality $\mathrm{tr}(\mathbf{V}) - \|\mathbf{V}\|_2 = 0$ holds only when $\lambda_1 > 0$ and $\lambda_m = 0, m = 2, \cdots, M$. However, the new constraints is still non-convex, thus, a first order approximation method is usually applied. Specifically, at the $(t+1)$-th iteration of the iterative algorithm, a lower-bound for $\|\mathbf{V}\|_2$ at the point $\mathbf{V}^t$ can be derived as

$$\|\mathbf{V}\|_2 \geq \left\|\mathbf{V}^t\right\|_2 + \left\langle \left(\mathbf{V} - \mathbf{V}^t\right), \partial_{\mathbf{V}} \|\mathbf{V}\|_2|_{\mathbf{V}=\mathbf{V}^t} \right\rangle \triangleq f\left(\mathbf{V}; \mathbf{V}^t\right), \tag{2.16}$$

where $\partial_{\mathbf{V}} \|\mathbf{V}\|_2|_{\mathbf{V}=\mathbf{V}^t}$ is a subgradient of $\|\mathbf{V}\|_2$ with respect to $\mathbf{V}$ at $\mathbf{V} = \mathbf{V}^t$, which is equal to $\mathbf{u}_1\mathbf{u}_1^{\mathrm{H}}$ with $\mathbf{u}_1$ denoting the eigenvector that corresponds to the largest singular value of $\mathbf{V}^t$.

Based on (2.16), the constraint in (2.15) can be approximated with the following convex constraint

$$\mathrm{tr}(\mathbf{V}) - f\left(\mathbf{V}; \mathbf{V}^t\right) \leq \varepsilon, \tag{2.17}$$

where ε is a very small positive constant. Then, when ε tends to zero, $\mathrm{tr}(\mathbf{V})$ will approach $\|\mathbf{V}\|_2$, which ensures that the rank-one constraint is fulfilled.

2.3.5 *Majorization-Minimization (MM) algorithm*

The MM algorithm is another widely used technique for optimizing the phase shifts of the RIS [65, 66, 67, 68, 69, 70]. The MM algorithm is an iterative optimization method that approximates a difficult problem as a series of more tractable subproblems that are solved iteratively. Assume that the solution of the subproblem at the t-th iteration is $\boldsymbol{\theta}^t$ and the corresponding objective function is $f(\boldsymbol{\theta}^t)$. Based on the MM algorithm, a surrogate objective function $\tilde{f}\left(\boldsymbol{\theta}|\boldsymbol{\theta}^t\right)$ is constructed, which fulfills the following three conditions:

1) $\tilde{f}\left(\boldsymbol{\theta}^t\middle|\boldsymbol{\theta}^t\right) = f\left(\boldsymbol{\theta}^t\right)$;
2) $\nabla_{\boldsymbol{\theta}} \tilde{f}\left(\boldsymbol{\theta}|\boldsymbol{\theta}^t\right)\big|_{\boldsymbol{\theta}=\boldsymbol{\theta}^t} = \nabla_{\boldsymbol{\theta}} f\left(\boldsymbol{\theta}^t\right)\big|_{\boldsymbol{\theta}=\boldsymbol{\theta}^t}$;
3) $\tilde{f}\left(\boldsymbol{\theta}|\boldsymbol{\theta}^t\right) \geq f(\boldsymbol{\theta})$.

The convergence of this sequence of the solutions of each subproblem is guaranteed if these conditions are fulfilled. For further explanation, the original objective function is replaced with the surrogate objective function $\tilde{f}\left(\boldsymbol{\theta}|\boldsymbol{\theta}^t\right)$, the subproblem to be solved in each iteration , after removing the constant terms, is given by

$$\max_{\boldsymbol{\theta}} \ \mathrm{Re}\left\{\boldsymbol{\theta}^{\mathrm{H}}\mathbf{q}^t\right\} \tag{2.18a}$$

$$\text{s.t.} \quad |\theta_m| = 1, m = 1, \cdots, M, \tag{2.18b}$$

where $\mathbf{q}^t$ is a constant complex vector at the t-th iteration. The optimal solution to the optimization problem in (2.18) is

$$\boldsymbol{\theta}^{t+1} = e^{j \arg(\mathbf{q}^t)}. \tag{2.19}$$

This procedure is repeated until convergence. The pricing-based method can be utilized [69], if the phase shifts of the RIS is existed in the constraints of the optimization problem.

2.3.6 *Manifold approach*

There exist different kinds of manifold methods. the complex circle manifold (CCM) method [71] is one of the most used methods [71, 72, 73, 74, 75]. The main idea of the CCM method is to derive the gradient descent algorithm based on the manifold space given in (2.20). The constraint space in $\mathscr{S}_1$ can be regarded as the product of M complex circles, which is a sub-manifold of $\mathbb{C}^M$ given by

$$\mathscr{S}^M \triangleq \left\{ \mathbf{x} \in \mathbb{C}^M : |x_l| = 1, l = 1, 2, \cdots, M \right\}, \tag{2.20}$$

where x_l is the l-th element of vector $\mathbf{x}$. The optimization problem aims at optimizing the phase shifts to minimize the objective function $\hat{f}(\boldsymbol{\theta})$.

2.3.7 *Alternating direction method of multipliers (ADMM) based algorithm*

The idea of the Alternating direction method of multipliers (ADMM) based algorithm [76, 77, 54], is to introduce an auxiliary variable $\boldsymbol{\omega}$ such that $\boldsymbol{\omega} = \boldsymbol{\theta}$, which can be regarded as a copy of $\boldsymbol{\theta}$. In addition, reformulate the feasible region of constraint C1 is denoted by $\mathscr{B}$, by the indicator function as follows,

$$\mathbb{I}_{\mathscr{B}}(\mathbf{W}, \boldsymbol{\theta}) = \begin{cases} f(\mathbf{W}, \boldsymbol{\theta}), & \text{if } \{\mathbf{W}, \boldsymbol{\theta}\} \in \mathscr{B} \\ \infty, & \text{otherwise.} \end{cases} \tag{2.21}$$

Similarly, the feasible region that corresponds to constraint C2, i.e., $\mathscr{S}_1$ can be written as follows

$$\mathbb{I}_{\mathscr{S}_1}(\boldsymbol{\omega}) = \begin{cases} 0, & \text{if } \boldsymbol{\omega} \in \mathscr{S}_1 \\ \infty, & \text{otherwise.} \end{cases} \tag{2.22}$$

Then, the equivalent ADMM reformulation for the optimization problem in (2.12) is

$$\begin{aligned} &\min_{\mathbf{W}, \boldsymbol{\theta}, \boldsymbol{\omega}} \ \mathbb{I}_{\mathscr{B}}(\mathbf{W}, \boldsymbol{\theta}) + \mathbb{I}_{\mathscr{S}_1}(\boldsymbol{\omega}) \\ &\text{s.t.} \quad \boldsymbol{\omega} = \boldsymbol{\theta}. \end{aligned} \tag{2.23}$$

The augmented Lagrangian of the optimization problem in (2.23) is

$$\mathscr{L}_{\xi} = \mathbb{I}_{\mathscr{B}}(\mathbf{W}, \boldsymbol{\theta}) + \mathbb{I}_{\mathscr{S}_1}(\boldsymbol{\omega}) + \frac{\xi}{2} \|\boldsymbol{\theta} - \boldsymbol{\omega} + \boldsymbol{\lambda}\|_2^2, \tag{2.24}$$

where $\xi > 0$ is a constant penalty parameter, and $\boldsymbol{\lambda} = [\lambda_1, \cdots, \lambda_M]^T$ is the dual variable vector of the constraint $\boldsymbol{\omega} = \boldsymbol{\theta}$. Based on the ADMM algorithm, the variables $\mathbf{W}, \boldsymbol{\theta}$ and $\boldsymbol{\omega}$ are alternately optimized.

The ADMM algorithm is an iterative approach. In the t-th iteration, given $\mathbf{W}^t, \boldsymbol{\theta}^t$ and $\boldsymbol{\omega}^t$, the variables are updated as follows.

(a) Updating $\boldsymbol{\theta}$: The subproblem for updating $\boldsymbol{\theta}$ is

$$\begin{aligned} &\min_{\boldsymbol{\theta}} \ f(\boldsymbol{\theta}) + \frac{\xi}{2} \left\|\boldsymbol{\theta} - \boldsymbol{\omega}^t + \boldsymbol{\lambda}^t\right\|_2^2 \\ &\text{s.t.} \quad g_i(\boldsymbol{\theta}) \geq D_i, i = 1, \cdots, I. \end{aligned} \tag{2.25}$$

Note that the unit-modulus constraint for $\boldsymbol{\theta}$ is not included in this subproblem, which significantly reduces the complexity of computing $\boldsymbol{\theta}$.

(b) Updating $\mathbf{W}$: The subproblem for updating $\mathbf{W}$ is

$$\begin{aligned} &\min_{\mathbf{W}} \ f(\mathbf{W}) \\ &\text{s.t.} \quad g_i(\mathbf{W}) \geq D_i, i = 1, \cdots, I. \end{aligned} \tag{2.26}$$

(c) Updating $\boldsymbol{\omega}$: The subproblem for updating $\boldsymbol{\omega}$ is

$$\boldsymbol{\omega}^{t+1} = \arg\min_{\boldsymbol{\omega} \in \mathscr{S}_1} \left\|\boldsymbol{\theta}^{t+1} + \boldsymbol{\lambda}^t - \boldsymbol{\omega}\right\|_2^2. \tag{2.27}$$

The objective of the optimization problem in (2.27) is to project $\boldsymbol{\theta}^{t+1} + \boldsymbol{\lambda}^t$ onto the feasible set $\mathscr{S}_1$, whose solution is $\boldsymbol{\omega}^{t+1} = e^{j \arg(\boldsymbol{\theta}^{t+1} + \boldsymbol{\lambda}^t)}$.

(d) Updating $\boldsymbol{\lambda}$: The update of $\boldsymbol{\lambda}$ is $\boldsymbol{\lambda}^{t+1} = \boldsymbol{\lambda}^t + \boldsymbol{\theta}^{t+1} - \boldsymbol{\omega}^{t+1}$.

2.3.8 *Penalty convex-concave procedure (CCP)*

Th idea of the Penalty convex-concave procedure (CCP) is to reformulate the unit modulus constraint as $1 \leq |\theta_m|^2 \leq 1, \forall m$. since the reformulated constraint is still non-convex, the successive convex approximation (SCA) method is applied. Thus, the non-convex constraint $1 \leq |\theta_m|^2$ can be converted into a series of convex constraints, i.e., $1 \leq 2\text{Re}(\theta_m^* \theta_m^t) - \left|\theta_m^t\right|^2$, where θ_m^t is the solution in the t-th iteration. The phase shift optimization problem can be

rewritten as

$$\begin{aligned} &\min_{\boldsymbol{\theta},\mathbf{b}\geq\mathbf{0}} f(\boldsymbol{\theta}) - \lambda^t \textstyle\sum_{m=1}^{2M} b_m \\ &\text{s.t.} \quad g_i(\boldsymbol{\theta}) \geq D_i, i = 1,\cdots,I, \\ &\qquad \left|\theta_m^t\right|^2 - 2\mathrm{Re}(\theta_m^* \theta_m^t) \leq b_m - 1, \forall m, \\ &\qquad |\theta_m|^2 \leq 1 + b_{m+M}, \forall m, \end{aligned} \tag{2.28}$$

where λ^t is the regularization factor to control the feasibility of the constraints in the t-th iteration and $\mathbf{b} = [b_1, \cdots, b_{2M}]$ is a $2M$ slack variables. After some mathematical manipulations, the optimization problem in (2.28) can be solved by CVX, as indicated in references [78, 79, 80]

2.3.9 *Barrier function penalty*

Th idea of the barrier function penalty, firstly, is to reformulate the unit modulus constraint as $\mathrm{tr}\left(\boldsymbol{\theta}\boldsymbol{\theta}^{\mathrm{H}}\right) = M$ and $\|\boldsymbol{\theta}\|_\infty \leq 1$. Then, the l_p norm with large p can be used to approximate $\|\boldsymbol{\theta}\|_\infty$ Since it is non-differentiable, i.e., $\|\boldsymbol{\theta}\|_\infty = \lim_{p\to\infty} \|\boldsymbol{\theta}\|_p$. To deal with the constraint $\|\boldsymbol{\theta}\|_p \leq 1$, the logarithmic barrier function $F(x)$ can be used to approximate the penalty of violating the l_p constraint, as

$$F(x) = \begin{cases} -\frac{1}{\kappa}\ln(x), & x > 0, \\ \infty, & x \leq 0, \end{cases} \tag{2.29}$$

where $\kappa > 0$ is the barrier function penalty factor. Accordingly, the phase shift optimization problem can be reformulated as

$$\begin{aligned} &\min_{\boldsymbol{\theta}} G(\boldsymbol{\theta}) = f(\boldsymbol{\theta}) + F\left(1 - \|\boldsymbol{\theta}\|_p\right) \\ &\text{s.t.} \quad \mathrm{tr}\left(\boldsymbol{\theta}\boldsymbol{\theta}^{\mathrm{H}}\right) = M. \end{aligned} \tag{2.30}$$

Due to the non-convex constraint, the optimization problem in (2.30) is still non-convex. A possible solution is to utilize the gradient and projection method, which provides a low complexity but sub-optimal solution,[81, 82].

2.3.10 *Gradient descent approach*

The gradient descent method is an iterative approach that is utilized to find a sub-optimal solution for the optimization problem When the objective function $f(\boldsymbol{\theta})$ is differentiable. Specifically, let $\boldsymbol{\theta}^t$ be the phase shift vector at the t-th iteration. Then, the optimization variable $\boldsymbol{\theta}$ at the $(t+1)$-th iteration is updated as

$$\boldsymbol{\theta}^{t+1} = \exp\left(j \arg\left(\boldsymbol{\theta}^t - \mu \nabla_{\boldsymbol{\theta}} f(\boldsymbol{\theta})\big|_{\boldsymbol{\theta}=\boldsymbol{\theta}^t}\right)\right), \tag{2.31}$$

where μ is the step size and the arg operator is used for satisfying the unit-modulus constraint[83, 84, 65, 85].

2.3.11 *Accelerated projected gradient (APG)*

Th idea of the Accelerated projected gradient (APG) is to define a projection operator $\mathbb{P}_{\mathscr{S}_1}$ defined as [86, 87, 88, 89, 90]

$$\hat{\boldsymbol{\theta}} = \mathbb{P}_{\mathscr{S}_1}(\boldsymbol{\theta}) \Leftrightarrow \hat{\theta}_m = \begin{cases} \theta_m/|\theta_m|, \text{if } \theta_m \neq 0 \\ 1, \qquad \text{otherwise.} \end{cases} \tag{2.32}$$

The Accelerated projected gradient (APG) is introduced to speed up the convergence rate of the gradient method by utilizing an extrapolation points at each iteration. Thus, the update of the phase shifts in the $(i+1)$-th iteration is given by

$$\boldsymbol{\theta}_{i+1} = \mathbb{P}_{\mathscr{S}_1}\left(\mathbf{z}_i - \frac{1}{\gamma_i}\nabla_{\boldsymbol{\theta}} f(\boldsymbol{\theta})\big|_{\boldsymbol{\theta}=\mathbf{z}_i}\right), \tag{2.33}$$

where $\mathbf{z}_i = \boldsymbol{\theta}_i + \alpha_i(\boldsymbol{\theta}_i - \boldsymbol{\theta}_{i-1})$, and α_i is updated as

$$\alpha_i = \frac{\xi_{i-1}-1}{\xi_i}, \xi_i = \frac{1+\sqrt{1+4\xi_{i-1}^2}}{2}. \tag{2.34}$$

In (2.33), γ_i is obtained by using the backtracking line search method [91].

2.3.12 *Heuristic methods*

When the objective function is analytically involving, the above-mentioned algorithms may not be applicable or the computation of the gradient may be time-consuming. Possible solutions to wrapping this issue include the use of heuristic methods such the genetic algorithms (GA) or the particle swarm optimization (PSO) methods. More details can be found in [92, 93, 94, 95].

2.3.13 *Deep reinforcement learning*

Machine learning methods can also be applied to optimize the phase shifts of the RIS. A suitable approach is the use of deep reinforcement learning. In fact, deep reinforcement learning based methods do not need a large number of training labels and can learn and operate in an online manner. Some examples of application of deep reinforcement learning to the optimization of RIS-aided communications can be found in [96, 97, 98].

2.4 Optimization Techniques for Discrete Phase Shifts

In this section the optimization of RISs subject to discrete-valued phase shifts, which leads to an NP-hard optimization problem, are presented. The existing works in this area can be classified into the following categories [34].

2.4.1 *Rounding method*

The main idea of this method is first to obtain a continuous solution that fulfills the unit modulus constraint [47, 99, 100, 101, 76]. The obtained solution can be donated as $\hat{\theta}_m, \forall m$. Then, we rounded the obtained solution to the nearest discrete value in $\mathscr{S}_2$ as follow

$$\theta_m^\star = \arg\min_{\phi\in\mathscr{S}_2} \left|\hat{\theta}_m - \phi\right|, \forall m. \tag{2.35}$$

2.4.2 *Binary mode selection method*

The main idea of this method is first to transform the original optimization problem into a binary variable optimization problem, and the branch and bound (BnB) method can be utilized to obtain the globally optimal solution [99].

Specifically, the objective function of the optimization problem is transformed into a function of φ_m, $\cos(\varphi_m)$ and $\sin(\varphi_m)$ [99, 102]. A binary vector $\mathbf{x}_m = \left[x_{1,m}, \cdots, x_{L,m}\right]^T$ is introduced such that $\sum_{l=1}^{L} x_{l,m} = 1, x_{l,m} \in \{0,1\}$, for each reflecting element m. Hence, $\mathbf{x}_m$ can be regarded as a mode selection vector. Define $\mathbf{a} = \left[0, \Delta\varphi, \cdots, (L-1)\Delta\varphi\right]^T$, $\mathbf{b} = \left[1, \cos\left(\Delta\varphi\right), \cdots, \cos\left((L-1)\Delta\varphi\right)\right]^T$ and $\mathbf{c} = \left[0, \sin\left(\Delta\varphi\right), \cdots, \sin\left((L-1)\Delta\varphi\right)\right]^T$. Then, we have

$$\varphi_m = \mathbf{a}^T\mathbf{x}_m, \cos\left(\varphi_m\right) = \mathbf{b}^T\mathbf{x}_m, \sin\left(\varphi_m\right) = \mathbf{c}^T\mathbf{x}_m. \tag{2.36}$$

Based on (2.36), the BnB method can be applied. However, the BnB method has an exponential computational complexity. To reduce the complexity, the authors of [102] proposed to apply the SCA method. Specifically, the binary constraint on $x_{l,m}$ can be equivalently transformed into the following two continuous constraints:

$$x_{l,m} - x_{l,m}^2 \leq 0, 0 \leq x_{l,m} \leq 1. \tag{2.37}$$

The first constraint in (2.37) is the difference between two convex functions, and the SCA method can be used.

2.4.3 *Negative square penalty (NSP)*

The main idea of this method is first to add a negative penalty term to the objective function, and solve the optimization problem over the convex hull of the discrete set. The NSP method

[103] was adopted to solve the discrete phase shift in [104]. Specifically, the discrete phase shift optimization problem can be expressed as

$$\min_{\boldsymbol{\theta}\in\tilde{\mathscr{S}}_2} f(\boldsymbol{\theta}) \tag{2.38}$$

where $\tilde{\mathscr{S}}_2 = \left\{\theta | \theta = e^{j\left(\frac{2\pi}{L}l+\frac{\pi}{L}\right)}, l = 0,\cdots,L-1\right\}$. Based on the NSP methods, we introduce the following problem

$$\min_{\boldsymbol{\theta}\in\tilde{\mathscr{S}}_2} F(\boldsymbol{\theta}) \triangleq f(\boldsymbol{\theta}) - \lambda\|\boldsymbol{\theta}\|^2 \tag{2.39}$$

where $\bar{\mathscr{S}}_2 = \text{conv}\tilde{\mathscr{S}}_2$ is the convex hull of $\tilde{\mathscr{S}}_2$, and λ is a penalty parameter.

The purpose of the penalty term $\lambda\|\boldsymbol{\theta}\|^2$ is to pushes each θ_m to an extreme point of $\bar{\mathscr{S}}_2$. It is important to note that the constraint of the optimization in (2.39) is convex, which is easier to handle than the original problem formulation in (2.38). The authors of [103] provided the conditions on λ for the problem in (2.39) to be equivalent to the original problem in (2.38). The MM method is utilized to solve the reformulated problem in (2.39). Let $\boldsymbol{\theta}^i$ denote the value of $\boldsymbol{\theta}$ at the i-th iteration. Then, for any $\boldsymbol{\theta}$, we have

$$F(\boldsymbol{\theta}) \leq f(\boldsymbol{\theta}) + \lambda\left\|\boldsymbol{\theta}^i\right\|^2 - 2\text{Re}\left\{\boldsymbol{\theta}^{\text{H}}\boldsymbol{\theta}^i\right\} \triangleq G\left(\boldsymbol{\theta}|\boldsymbol{\theta}^i\right). \tag{2.40}$$

Then, at the i-th iteration, the optimization problem is reformulated as follows

$$\min_{\boldsymbol{\theta}\in\tilde{\mathscr{S}}_2} G\left(\boldsymbol{\theta}|\boldsymbol{\theta}^i\right). \tag{2.41}$$

The optimization problem in (2.41) can be tackled by using the APG method, which can be written as

$$\boldsymbol{\theta}^{i+1} = \mathbb{P}_{\tilde{\mathscr{S}}_2}\left(\mathbf{z}^i - \frac{1}{\beta_i}\nabla_{\boldsymbol{\theta}} G\left(\boldsymbol{\theta}|\boldsymbol{\theta}^i\right)\Big|_{\boldsymbol{\theta}=\boldsymbol{\theta}^i}\right), \tag{2.42}$$

where the same notation as for the APG method introduced for the case of continuous phase shifts is used. Specifically, the projection onto the convex set $\bar{\mathscr{S}}_2$ is denoted by $\mathbb{P}_{\bar{\mathscr{S}}_2}(u)$ whose closed-form expression is [103]

$$\mathbb{P}_{\bar{\mathscr{S}}_2}(u) = e^{j\frac{2\pi l}{L}}\left([\text{Re}(\tilde{u})]_0^{\cos(\pi/L)} + j\,[\text{Im}(\tilde{u})]_{-\sin(\pi/L)}^{\sin(\pi/L)}\right),$$

where

$$n = \left\lfloor \frac{\angle u + \pi/L}{2\pi/L} \right\rfloor, \tilde{u} = ue^{-j\frac{2\pi n}{L}}.$$

2.4.4 *Heuristic methods*

It is observed that the application of some heuristic methods such as the PSO are effective methods to tackle the discrete phase shift optimization problem [95].

2.5 Conclusion

In this chapter, the RIS-aided wireless communication and RIS based information transmission systems are introduced, respectively. Then, the related practical hardware design challenges were investigated. Moreover, the challenges related to the design of optimization techniques were presented in some details. Afterwards, the state-of-the-art research on optimization techniques utilized for the system design was introduced in details With the ability to achieve a reconfigurable and controllable environment, RIS is a promising technique in the future communications.

3 Digital Reconfigurable Intelligent Surfaces: On the Impact of Realistic Reradiation Models

Chapter 3. Digital Reconfigurable Intelligent Surfaces: On the Impact of Realistic Reradiation Models

Reconfigurable intelligent surface (RIS) is an emerging technology that is under investigation for different applications in wireless communications. RISs are often analyzed and optimized by considering simplified electromagnetic reradiation models. Also, the existence of possible electromagnetic waves that are reradiated towards directions different from the desired ones are often ignored. Recently, some testbed platforms have been implemented, and experimentally validated reradiation models for RISs have been reported in the literature. In this chapter, we aim to study the impact of realistic reradiation models for RISs as a function of the sub-wavelength inter-distance between nearby elements of the RIS, the quantization levels of the reflection coefficients, the interplay between the amplitude and phase of the reflection coefficients, and the presence of electromagnetic interference. Furthermore, we consider both case studies in which the users may be located in the far-field and near-field regions of an RIS. Our study shows that, due to design constraints, such as the need of using quantized reflection coefficients or the inherent interplay between the phase and the amplitude of the reflection coefficients, an RIS may reradiate power towards unwanted directions that depend on the intended and interfering electromagnetic waves. Therefore, it is in general important to optimize an RIS by taking into account the entire reradiation pattern by design, in order to maximize the reradiated power towards the desired directions of reradiation while keeping the power reradiated towards other unwanted directions at a low level. Among the considered designs for RISs, our study shows that a 2-bit digitally controllable RIS with an almost constant reflection amplitude as a function of the applied phase shift, and whose scattering elements have a size and an inter-distance between (1/8)th and (1/4)th of the signal wavelength may be a good tradeoff between performance, implementation complexity and cost. However, the presented results are preliminary and pave the way for further research into the performance of RISs based on accurate and realistic electromagnetic reradiation models.

3.1 Introduction

3.1.1 Reconfigurable Intelligent Surfaces and Holographic Surfaces

In the last few years, intelligent surfaces have been the subject of extensive research activities in the context of wireless communications and networks [2], [105], [106], [107], [108]. A recent roadmap can be found in [109]. In essence, an intelligent surface is a dynamic metasurface, which shapes the reradiated electromagnetic waves as desired, thanks to a careful design of elementary scattering elements and to an appropriate optimization of simple electronic circuits [110]. In wireless communications, intelligent surfaces have been researched for several applications, and mainly for two possible uses:

1. **Nearly-passive reconfigurable devices** that are capable of shaping the electromagnetic waves that impinge upon them [111]. Two typical examples are surfaces that reflect or refract, e.g., smart windows, the electromagnetic waves towards non-specular directions. These surfaces are usually referred to as reconfigurable intelligent surfaces (RISs) [112].

2. **Low-complexity active transceivers** that are capable of realizing extremely massive multiple-input multiple-output communications [113]. These surfaces are usually referred to as dynamic metasurface antennas (DMA) [114] or holographic surfaces (HoloS) [115].

The main advantage of an RIS consists of controlling the propagation environment besides the end points of a transmission link, i.e., transmitters and receivers, without the need of requiring power amplifiers, radio frequency chains, and digital signal processors. An RIS operates in the analog domain directly on the electromagnetic waves. The main advantage of a HoloS consists of being equipped with a very large number of reconfigurable metamaterial elements (like an RIS) but with a limited number of radio frequency chains. This feature is highly desirable, since it reduces the number of radio frequency chains while offering higher beamforming and spatial multiplexing gains [114]. Notably, these surfaces, if sufficiently large in size, may provide spatial multiplexing gains, i.e., multiple orthogonal communication modes, even in free-space line-of-sight propagation environments [116], [117], [118]. In wireless communication systems and networks, RIS and HoloS are jointly deployed in the environment to boost the communication performance. An illustration of this emerging communication scenario is shown in Fig. 3.1.

Specifically, thanks to their expected large electrical size, RIS and HoloS may bring fundamentally new challenges to the design and optimization of wireless networks. One of them is the need of engineering and optimizing wireless communication networks whose devices may likely operate in the near-field of each other and, therefore, the electromagnetic waves can no longer be assumed to be characterized by a planar wavefront, but a spherical wavefront needs to be accounted for at the design stage [34]. Also, the possibility of packing on an intelligent surface hundreds or thousands of radiating elements at sub-wavelength inter-distances re-

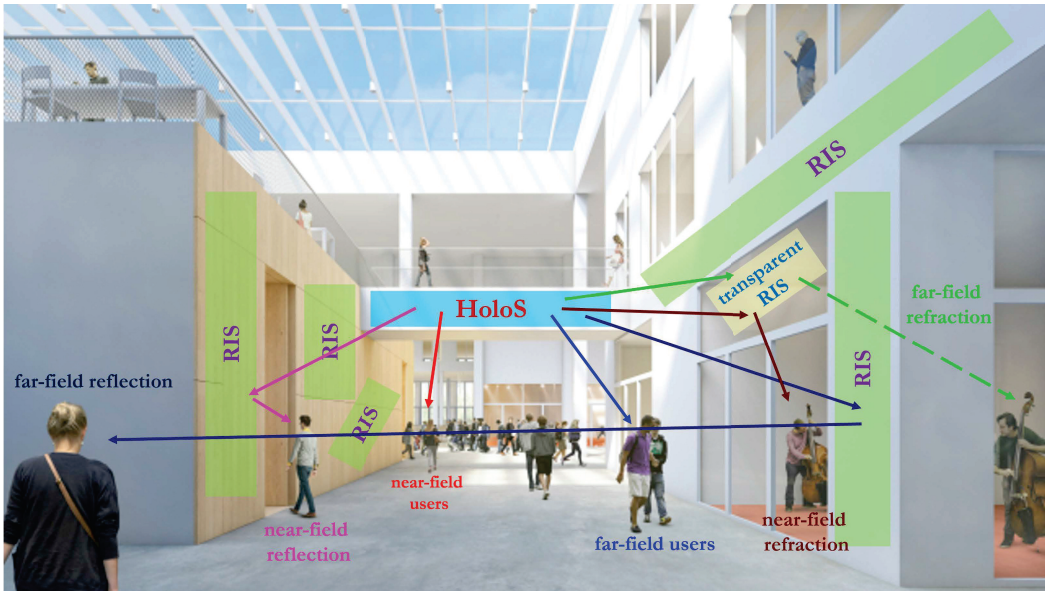

Figure 3.1: Emerging wireless communication scenario with far-field and near-field users.

quires new communication models that account, at the optimization stage, for the mutual coupling among the elements [119], [120], [121], [122].

3.1.2 Electromagnetically Consistent Modeling of Reconfigurable Intelligent Surfaces

In this chapter, we focus our attention on RISs. The deployment and optimization of RISs in wireless networks need several challenges to be tackled. Interested readers can consult, e.g., [108], [111] for a comprehensive discussion. One of the major and open research challenges in RIS-aided wireless communications lies in developing and utilizing electromagnetically-consistent models that account for the practical implementation of RISs. A comprehensive summary of the communication models most widely utilized in wireless communications for RISs is reported in [123]. From the overview in [123], it is apparent that three main communication models are typically utilized:

1. The locally periodic discrete model;
2. The mutually coupled antenna-elements model;
3. The inhomogeneous sheets of surface impedance model.

Interested readers are referred to [123] for a comprehensive discussion of the main characteristics, strengths, and limitations of these models. In this contribution, we focus our attention on the **locally periodic discrete model**, since it is the most widely used model in wireless communications and in the field of **digital metasurfaces** [124]. According to this model, an RIS is modeled as an ensemble of reconfigurable elements that can be configured in a finite number

of states. From an implementation standpoint, each RIS reconfigurable element is made of one or several engineered scattering elements and some electronic circuits. From a signal and system (or communication) standpoint, each RIS reconfigurable element is associated with a discrete-valued alphabet, sometimes referred to as lookup table or codebook, which determines the finite number of wave manipulations that each RIS reconfigurable element can apply to the incident electromagnetic waves.

According to [123], each value of the alphabet (or state of the RIS) can be interpreted as the (electric field) reflection coefficient of an infinite and homogeneous surface whose constituent elements are all configured to the same state. This definition and characterization of the alphabet of each RIS reconfigurable element introduces some limitations on the applicability of the locally periodic discrete model: The model may not be accurate if the desired wave transformation is not "slowly-varying" at the scale of the wavelength of the electromagnetic waves. In other words, the model can be applied if a "not-too-small" number of neighboring RIS reconfigurable elements is configured to the same state, so as to ensure that, locally, each RIS reconfigurable element "sees" other RIS reconfigurable elements configured to the same value of the alphabet. This "slowly-varying" or "locally periodic" condition needs to be carefully evaluated when utilizing this communication model for RISs.

3.1.3 Realistic Scattering Models for Reconfigurable Intelligent Surfaces

The numerical results in [123] show, in addition, that the presence of imperfections (non-ideal effects), with respect to the theoretically optimum, of the RIS configuration that is required to realize the desired wave transformations may result in the existence of higher-order harmonics (or grating lobes in antenna theory) towards undesired directions. Also, any periodic RIS that is illuminated by a plane wave may reradiate several electromagnetic waves according to Floquet's theorem, whose intensity depends on how the RIS surface impedance is engineered [125], [126]. In the context of the locally periodic discrete model, inaccuracies in the design of the alphabet of the RIS scattering elements, i.e., the use of a non-ideal alphabet, with respect to the theoretically optimum, may result in the presence of reradiated but undesired electromagnetic waves. Specifically, three major practical issues can be identified when engineering the RIS reconfigurable elements (which encompass the scattering elements and the electronic circuits):

1. *The phases of the complex-valued elements of the alphabet of the RIS reconfigurable elements are not exactly the same as those identified at the design stage.* Assume, for example, that one wants to realize a three-bit digitally controllable RIS. In theory, the phase difference between the complex-valued elements of the alphabet should be an integer multiple of 45 degrees. However, it may not be possible to realize eight different phases with this constraint [127]. Also, it may not be possible to realize any phase shifts, i.e., the range of admissible phase shifts may be smaller than 360 degrees.

2. *The amplitudes of the complex-valued elements of the alphabet of the RIS reconfigurable*

elements are not exactly unitary and they are not independent of the corresponding phases of the complex-valued elements of the alphabet. For example, if one wants to apply a given phase shift to an incident electromagnetic wave, the corresponding amplitude may be much smaller than one. This results in a phase-dependent signal attenuation [128], [11].

3. *Due to the implementation and power constraints associated with any electronic circuit, it may be possible to realize alphabets for the RIS reconfigurable elements with only a finite number of complex-valued elements, i.e., the number of RIS states is finite.* An often convenient implementation, due to the ease of realization, reduced cost, and limited power consumption, is the design of binary surfaces whose elements can only take two possible states and whose nominal phase shifts differ by 180 degrees. Recent results have shown that these extremely quantized surfaces may result in far-field reradiatiated beams towards undesired directions, e.g., towards the direction that is symmetrical with respect to the desired direction of radiation for the case study of anomalous reflectors [129].

3.1.4 Modeling Reconfigurable Intelligent Surfaces in Wireless Communications

In wireless communications, in spite of these considerations, the typical assumptions made on the complex-valued elements of the alphabet of the RIS reconfigurable elements (usually referred to as the RIS reflection coefficients in wireless communications) when considering the locally periodic discrete model for RIS are the following [5]:

1. The amplitudes of the RIS reflection coefficients are assumed to be unitary or constant as a function of the corresponding phases;
2. The phase shifts of the RIS reflection coefficients are either assumed to be continuous-valued variables or discrete-valued variables with equal phase differences;
3. In some cases, the amplitudes and phases of the RIS reflection coefficients are assumed to be optimized independently of one another.

Most probably, however, **the main assumption made in the context of wireless communications lies in optimizing a utility function at particular locations of one or multiple receivers, while disregarding the reradiation pattern of an RIS towards other directions**. Inherently, therefore, the presence and impact of undesired reradiated beams are not explicitly investigated. The presence of unwanted reradiations may, however, not be negligible if realistic alphabets (reflection coefficients) for the RIS reconfigurable elements are utilized. The existence of these undesired beams has, in particular, two major and negative consequences on a communication system:

1. Some power is directed towards directions that are different from the nominal ones. This implies that the power efficiency of an RIS towards the target directions is reduced.

Since an RIS does not usually amplify the incident signals, this may further limit the transmission coverage;

2. The unwanted beams result in interference that an RIS injects into the network, which may negatively affect the performance of other network users.

3.1.5 Chapter Contribution

Motivated by these considerations, we evince that it is necessary to comprehensively study the reradiation pattern of an RIS when practical reflection models (alphabets) are utilized, according to the assumption of the locally periodic discrete model. The aim of the present chapter is to study this open issue, which, to the best of our understanding, is not sufficiently understood by the wireless community. More precisely, we consider some recently reported alphabets for RISs that operate at different frequencies and study the reradiation pattern of each of them. Special focus is put on comparing currently available RIS alphabets based on existing hardware prototypes against "ideal" alphabets whose elements have unit amplitudes and evenly spaced phases, as is often assumed in wireless communications. Our numerical results show that major differences in the reradiation pattern of an RIS usually exist, especially either when binary RIS reconfigurable elements are utilized, or when the amplitudes and phases of the reflection coefficients are not independent of one another and the variations of the amplitudes with the phases are not negligible.

3.1.6 Chapter Organization

The rest of this chapter is organized as follows. In Section 3.2, the considered system model is described. To focus our attention on the main contribution of the chapter, i.e., the impact of practical alphabets of the RIS reconfigurable elements, the canonical system model with a single transmit and a single receive antenna is considered. In Section 3.3, we describe the algorithm that is utilized for optimizing an RIS under the assumption that each RIS reconfigurabale element is characterized by complex-valued elements (alphabet) whose amplitudes and phases are not necessarily independent of one another. In Section 3.4, several numerical results are illustrated by utilizing experimentally validated alphabets for RISs. In Section 3.5, finally, we provide concluding remarks.

3.2 System Model

We consider a single-user system in which a single-antenna transmitter and a single-antenna receiver communicate through an RIS. For simplicity, we assume that no direct link between the transmitter and the receiver exists. We denote by $\mathbf{H}$ and $\mathbf{G}$ the channel matrices from the transmitter to the RIS and from the RIS to the receiver, respectively.

As far as the RIS is concerned, we model it as a uniform planar array with NM RIS reconfig-

urable elements that are arranged and are equally spaced on N rows and M columns. The RIS is assumed to be centered at the origin and to lie in the xy plane (i.e., $z = 0$). The inter-distance between the RIS reconfigurable elements on each row and column is denoted by d_x and d_y, respectively. The inter-distances d_x and d_y are referred to as the geometric periods of the RIS in the context of dynamic metasurfaces. The surface area of each RIS reconfigurable element is $d_x d_y$, and it encompasses one or multiple scattering elements and the associated tuning circuits. For simplicity, we can assume that each RIS reconfigurable element is made of a single radiating element and one or more positive-intrinsic-negative (PIN) diodes [8] or varactors [11]. Each RIS reconfigurable element can be optimized independently of the others.

As mentioned in Section 3.1, we adopt the locally periodic discrete model for an RIS [123]. Accordingly, each RIS reconfigurable element is associated with a set of L complex-valued coefficients (the RIS alphabet) denoted by Γ_1, Γ_2, ..., Γ_L. Each element of the alphabet is obtained by appropriately configuring the electronic circuits of the RIS reconfigurable element. For ease of description, we assume that the RIS operates as a reflecting surface. From the physical standpoint, therefore, the complex-valued coefficient Γ_l has the meaning of a reflection coefficient, i.e., the ratio between the reflected electric field and the incident electric field, of an infinite RIS whose elements are all configured to the same state. Therefore, the corresponding equivalent structure is a homogeneous surface that realizes specular reflection. According to this definition, each RIS reconfigurable element is characterized by means of locally periodic boundary conditions, and, since an RIS is not endowed with power amplifiers, the reflection coefficients Γ_l for $l = 1, 2, \ldots, L$ have an amplitude that is, by definition, less than one, i.e., $|\Gamma_l| \leq 1$ for $l = 1, 2, \ldots, L$. However, this neither necessarily implies that the amplitude of Γ_l is a constant independent of the phase of Γ_l nor that the amplitude and the phase of Γ_l can be optimized independently of one another.

Examples of alphabets that can be found in the literature and that correspond to available hardware platforms, i.e., are experimentally validated, can be found in Table 3.1 and Table 3.2, which were originally reported in [123]. As far as the RIS prototype introduced in [9] is concerned, we have reported only the reflection coefficients in Table 3.1 and have ignored the transmission coefficients, since they are of no interest for our study. The reflection coefficients in Table 3.1 and Table 3.2 are utilized in Section 3.4 to obtain the numerical results. It is worth mentioning that the "typical" model utilized in wireless communications for a reflecting-type RIS assumes that (i) either $|\Gamma_l| = 1$ for any possible phase of Γ_l and that the phase of Γ_l can be adjusted to any continuous values or (ii) $|\Gamma_l| = 1$ for any possible phase of Γ_l and that the phase of Γ_l can be adjusted to a finite number of phase shifts that are evenly spaced within the range $0 - 360$ degrees. Further details are provided in Section 3.4.

Under the considered modeling assumptions, the achievable rate per unit bandwidth can be formulated as follows:

$$R = \log_2 \left(1 + \frac{p}{\sigma^2} \left| \sum_{n=1}^{N} \sum_{m=1}^{M} g_{nm} \gamma_{nm} h_{nm} \right|^2 \right) \tag{3.1}$$

Table 3.1: Examples of reflection coefficients for an RIS with discrete-valued phase shifts (two-state and four-state RIS elements). f and λ denote the frequency and the wavelength, respectively.

Reference	Size of the unit cell	Reflection Coefficient
[10] ($f = 33$ GHz)	$0.418\lambda \times 0.418\lambda$	$\lvert\Gamma_1\rvert = 0.8, \quad \angle\Gamma_1 = 150^\circ$ $\lvert\Gamma_2\rvert = 0.8, \quad \angle\Gamma_2 = 0^\circ$
[10] ($f = 27$ GHz)	$0.126\lambda \times 0.252\lambda$	$\lvert\Gamma_1\rvert = 0.9, \quad \angle\Gamma_1 = 165^\circ$ $\lvert\Gamma_2\rvert = 0.7, \quad \angle\Gamma_2 = 0^\circ$
[9] ($f = 3.6$ GHz)	$0.345\lambda \times 0.170\lambda$	$\lvert\Gamma_1\rvert = 0.46, \quad \angle\Gamma_1 = 20^\circ$ $\lvert\Gamma_2\rvert = 0.55, \quad \angle\Gamma_2 = 215^\circ$
[8] ($f = 2.3$ GHz)	$0.286\lambda \times 0.286\lambda$	$\lvert\Gamma_1\rvert = -1.2\,\text{dB}, \quad \angle\Gamma_1 = -205.5^\circ$ $\lvert\Gamma_2\rvert = -1.2\,\text{dB}, \quad \angle\Gamma_2 = -383.2^\circ$ $\lvert\Gamma_3\rvert = -0.8\,\text{dB}, \quad \angle\Gamma_3 = -290.2^\circ$ $\lvert\Gamma_4\rvert = -0.7\,\text{dB}, \quad \angle\Gamma_4 = -110.3^\circ$

Table 3.2: Example of reflection coefficient for an RIS with continuous-valued phase shifts [11]. The operating frequency is 5.15 – 5.75 GHz and the size of the unit cells is approximately a quarter of the signal wavelength.

Voltage	Reflection coefficient amplitude ($\lvert\Gamma\rvert$)	Reflection coefficient phase ($\angle\Gamma$)
0 V	-1.517 dB	32.798°
0.25 V	-1.807 dB	40.854°
0.5 V	-3.156 dB	46.807°
0.75 V	-5.59 dB	53.543°
1 V	-9.576 dB	70.32°
1.25 V	-20.563 dB	-167.158°
1.5 V	-6.615 dB	-73.171°
1.75 V	-3.029 dB	-49.627°
2 V	-1.959 dB	-35.908°
2.5 V	-0.874 dB	-23.263°
3 V	-0.749 dB	-16.087°
3.5 V	-0.469 dB	-12.663°
4 V	-0.528 dB	-9.925°
5 V	-0.439 dB	-6.906°

where p is the transmitted power, σ^2 it the noise power at the receiver, g_{nm} is the (n,m)th entry of the channel matrix $\mathbf{G}$, h_{nm} is the (n,m)th entry of the channel matrix $\mathbf{H}$, and γ_{nm} is the value of the reflection coefficient of the (n,m)th RIS reconfigurable element, with $\gamma_{nm} \in \{\Gamma_1, \Gamma_2, \ldots, \Gamma_L\}$ for $n = 1,2,\ldots,N$ and $m = 1,2,\ldots,M$.

Since we are interested in characterizing the reradiation pattern of an RIS as a function of the alphabet of the RIS reconfigurable elements, we focus our attention on free-space propagation. Accordingly, it was recently proved in [10], [130] that the power received at the generic location

$\mathbf{r}^{(\mathrm{rx})} = \left(x_{\mathrm{rx}}, y_{\mathrm{rx}}, z_{\mathrm{rx}}\right)$ can be formulated as follows:

$$p_{\mathrm{rx}}\left(\mathbf{r}^{(\mathrm{rx})}\right) = \frac{p}{16\pi^2}\left|\sum_{n=1}^{N}\sum_{m=1}^{M}\gamma_{nm}\begin{bmatrix}\sqrt{G_{\mathrm{tx}}\left(\theta_{nm}^{(\mathrm{tx})}\right)}\left(\frac{z_{\mathrm{tx}}}{|\mathbf{r}_{nm}^{(\mathrm{tx})}|}\frac{\exp\left(-jk|\mathbf{r}_{nm}^{(\mathrm{tx})}|\right)}{|\mathbf{r}_{nm}^{(\mathrm{tx})}|}\right)\\ \sqrt{G_{\mathrm{rx}}\left(\theta_{nm}^{(\mathrm{rx})}\right)}\left(\frac{z_{\mathrm{rx}}}{|\mathbf{r}_{nm}^{(\mathrm{rx})}|}\frac{\exp\left(-jk|\mathbf{r}_{nm}^{(\mathrm{rx})}|\right)}{|\mathbf{r}_{nm}^{(\mathrm{rx})}|}\right)\\ \left(d_x\mathrm{sinc}\left(k\left(\frac{(x_{\mathrm{rx}}-x_n)}{|\mathbf{r}_{nm}^{(\mathrm{rx})}|}+\frac{(x_{\mathrm{tx}}-x_n)}{|\mathbf{r}_{nm}^{(\mathrm{tx})}|}\right)\frac{d_x}{2}\right)\right)\\ \left(d_y\mathrm{sinc}\left(k\left(\frac{(y_{\mathrm{rx}}-y_m)}{|\mathbf{r}_{nm}^{(\mathrm{rx})}|}+\frac{(y_{\mathrm{tx}}-y_m)}{|\mathbf{r}_{nm}^{(\mathrm{tx})}|}\right)\frac{d_y}{2}\right)\right)\end{bmatrix}\right|^2 \tag{3.2}$$

where the following notation is used:

- $j = \sqrt{-1}$ is the imaginary unit, $\mathrm{sinc}(x) = \sin(x)/x$, and $k = 2\pi/\lambda$ where λ is the wavelength;
- $(x_{\mathrm{tx}}, y_{\mathrm{tx}}, z_{\mathrm{tx}})$ is the location of the transmitter;
- (x_n, y_m) is the center point of the (n,m)th RIS reconfigurable element;
- $p_{\mathrm{rx}}\left(\mathbf{r}^{(\mathrm{rx})}\right)$ is the received power at $\mathbf{r}^{(\mathrm{rx})}$;
- $G_{\mathrm{tx}}\left(\theta_{nm}^{(\mathrm{tx})}\right)$ and $G_{\mathrm{rx}}\left(\theta_{nm}^{(\mathrm{rx})}\right)$ are the antenna gains of the transmitter and receiver, respectively, where $\theta_{nm}^{(\mathrm{tx})}$ is the angle between the transmitter and the center point of the (n,m)th RIS reconfigurable element and $\theta_{nm}^{(\mathrm{rx})}$ is the angle between the receiver and the center point of the (n,m)th RIS reconfigurable element;
- $\left|\mathbf{r}_{nm}^{(\mathrm{tx})}\right|$ is the distance between the transmitter and the center point of the (n,m)th RIS reconfigurable element;
- $\left|\mathbf{r}_{nm}^{(\mathrm{rx})}\right|$ is the distance between the center point of the (m,n)th RIS reconfigurable element and the receiver.

In the next section, based on this signal model, we propose a simple algorithm for optimizing the link rate in (3.1). It is worth mentioning that the proposed optimization algorithm can be applied to any channel model, and that the free-space model is considered only for illustration and because we are interested in characterizing the reradiation pattern of an RIS.

3.3 Optimization Algorithm

Let $\mathbf{\Gamma}$ be the $N \times M$ matrix of complex values γ_{nm} and let $\mathscr{A} = \{\Gamma_1, \Gamma_2, \ldots, \Gamma_L\}$ denote the alphabet of each RIS reconfigurable element, i.e., $\mathscr{A}$ is the feasible set of γ_{nm} for $n = 1,2,\ldots,N$ and $m = 1,2,\ldots,M$. The maximization of the rate R in (3.1) in a free-space channel model is equivalent to the following constrained optimization problem:

$$\max_{\mathbf{\Gamma}} p_{\mathrm{rx}}\left(\mathbf{r}^{(\mathrm{rx})}\right) = p\left|\sum_{n=1}^{N}\sum_{m=1}^{M} g_{nm}\gamma_{nm}h_{nm}\right|^2 \tag{3.3a}$$

$$\text{s.t. } \gamma_{nm} \in \mathscr{A}, \quad \forall\ n = 1,2,\ldots,N,\ m = 1,2,\ldots,M \tag{3.3b}$$

where the following two identities hold:

$$\begin{aligned} g_{nm} = \frac{1}{4\pi}\sqrt{G_{\text{tx}}\left(\theta_{nm}^{(\text{tx})}\right)}\left(\frac{z_{\text{tx}}}{\left|\mathbf{r}_{nm}^{(\text{tx})}\right|}\frac{\exp\left(-jk\left|\mathbf{r}_{nm}^{(\text{tx})}\right|\right)}{\left|\mathbf{r}_{nm}^{(\text{tx})}\right|}\right) \\ \times\left(d_x \text{sinc}\left(k\left(\frac{(x_{\text{rx}}-x_n)}{\left|\mathbf{r}_{nm}^{(\text{rx})}\right|}+\frac{(x_{\text{tx}}-x_n)}{\left|\mathbf{r}_{nm}^{(\text{tx})}\right|}\right)\frac{d_x}{2}\right)\right) \end{aligned} \tag{3.4}$$

$$\begin{aligned} h_{nm} = \frac{1}{4\pi}\sqrt{G_{\text{rx}}\left(\theta_{nm}^{(\text{rx})}\right)}\left(\frac{z_{\text{rx}}}{\left|\mathbf{r}_{nm}^{(\text{rx})}\right|}\frac{\exp\left(-jk\left|\mathbf{r}_{nm}^{(\text{rx})}\right|\right)}{\left|\mathbf{r}_{nm}^{(\text{rx})}\right|}\right) \\ \times\left(d_y \text{sinc}\left(k\left(\frac{(y_{\text{rx}}-y_m)}{\left|\mathbf{r}_{nm}^{(\text{rx})}\right|}+\frac{(y_{\text{tx}}-y_m)}{\left|\mathbf{r}_{nm}^{(\text{tx})}\right|}\right)\frac{d_y}{2}\right)\right) \end{aligned} \tag{3.5}$$

The formulated optimization problem in (3.3) is characterized by the optimization variables γ_{nm} that can only take discrete values, which prevents us from using gradient-based optimization methods. Moreover, the discrete values in the set $\mathscr{A}$ do not possess any specific structure that can be exploited for optimization purposes: They are generic complex numbers. Finally, the fact that only discrete-valued phase shifts can be applied by an RIS that is characterized by the feasible set $\mathscr{A}$ makes it impossible to perfectly compensate the phases of the channels g_{nm} and h_{nm} for any $n = 1,2,\ldots,N$ and $m = 1,2,\ldots,M$. In principle, given the discrete nature of the feasible set, it is always possible to resort to an exhaustive search over the set $\mathscr{A}^{NM}$. However, this would require searching over $(NM)^L$ configurations of the matrix $\mathbf{\Gamma}$, which is computationally infeasible for practical values of (N,M) and L. In fact, typical values for NM are of the order of hundreds or thousands, while L is of the order of units. This motivates us to develop optimization algorithms with a complexity that is linear in NM, i.e., with the total number of RIS reconfigurable elements.

The approach that we propose to solve the formulated optimization problem in (3.3) is based on the alternating optimization principle, i.e., the NM reflection coefficients are optimized sequentially one at a time. To elaborate, the optimization of the generic reflection coefficient γ_{qp}, while all other reflection coefficients are kept fixed, is stated as follows:

$$\max_{\gamma_{qp}} \left| g_{qp}\gamma_{qp}h_{qp} + \sum_{n=1\neq q}^{N}\sum_{m=1\neq p}^{M} g_{nm}\gamma_{nm}h_{nm}\right|^2 \tag{3.6a}$$

$$\text{s.t. } \gamma_{qp} \in \mathscr{A} \tag{3.6b}$$

Algorithm 1 Algorithm to solve the optimization problem in (3.3)

Initialize $\boldsymbol{\Gamma}$ to a feasible value $\boldsymbol{\Gamma}_0$; $k=0$; $F^{(k)}=F(\boldsymbol{\Gamma}_0)$, $F^{(k-1)}=0$;
Set a convergence tolerance $0\leq\varepsilon\leq F^{(0)}$;
while $\left|F^{(k)}-F^{(k-1)}\right|>\varepsilon$ **do**
  for $q=1,2,\ldots,N$ **do**
    for $p=1,2,\ldots,M$ **do**
      Set γ_{qp} as the maximizer of (3.7);
    end for
  end for
  $k=k+1$; $F^{(k-1)}=F^{(k)}$, $F^{(k)}=F(\boldsymbol{\Gamma})$;
end while
return $\boldsymbol{\Gamma}$.

Defining $\alpha_{qp}=\sum_{n=1\neq q}^{N}\sum_{m=1\neq p}^{M}g_{nm}\gamma_{nm}h_{nm}$, the objective function in (3.6) can be expanded as follows:

$$\left|g_{qp}\gamma_{qp}h_{qp}+\alpha_{qp}\right|^2=\left|\gamma_{qp}\right|^2\left|g_{qp}h_{qp}\right|^2+2\Re\left\{\gamma_{qp}g_{qp}h_{qp}\alpha_{qp}^*\right\}+\left|\alpha_{qp}\right|^2 \tag{3.7}$$

where $\Re$ denotes the real part of a complex number and $(\cdot)^*$ denote the complex conjugate operator.

Since the third addend in (3.7) is independent of the optimization variable γ_{qp}, the objective function is maximized by searching among the L elements of the set $\mathscr{A}$ and by selecting the element of the set that provides the largest value of $\left|\gamma_{qp}\right|$ whose phase is the closest to the term $g_{qp}h_{qp}\alpha_{qp}^*$. The complete iterative algorithm for solving the formulated optimization problem in (3.3) is reported in Algorithm 1. Specifically, the function $F^{(k)}$ denotes the objective function in (3.6) at the kth iteration of the algorithm and the maximizer of (3.7) is obtained through a simple exhaustive search over the L elements of $\mathscr{A}$.

By direct inspection, we see that the complexity of Algorithm 1 scales linearly with NM, since the NM reflection coefficients of the RIS are optimized sequentially. Therefore, Algorithm 1 can be considered to be a low-complexity optimization solution. Specifically, the overall complexity of Algorithm 1 is $\mathscr{O}(I_\varepsilon NML)$, where I_ε is the number of iterations required to reach the convergence tolerance ε. As far as the quality of the solution obtained by Algorithm 1 is concerned, the discrete nature of the optimization problem in (3.3) prevents us from making any formal claim. It is known, however, that alternating optimization methods converge to a first-order optimal solution when the objective function and the constraint functions are differentiable, and the constraints are decoupled in the optimization variables, which is the case of the problem in (3.3) [131]. Thus, we can claim that Algorithm 1 converges to a first-order optimal point of the optimization problem that is obtained by relaxing the optimization variables in (3.3) to the continuous set $\left\{\gamma_{nm}\in\mathbb{C}:\left|\gamma_{nm}\right|\leq 1,\forall n=1,2,\ldots,N \text{ and } m=1,2,\ldots,M\right\}$.

3.4 Numerical Results

In this section, we illustrate several numerical results in order to show the impact that realistic alphabets of the RIS reconfigurable elements may have in wireless communications. To this end, we consider the following canonical setup unless stated otherwise:

- The direct link between the transmitter and the receiver is assumed to be sufficiently weak and is ignored to focus on the role of the RIS;
- The RIS is assumed to be in the far field region of both the transmitter and the receiver, and, therefore, the electromagnetic waves have a planar wavefront across the RIS and at the receiver;
- The electromagnetic wave emitted by the transmitter impinges normally upon the RIS (normal incidence), which is consistent with the alphabets reported in Table 3.1 and Table 3.2 that are obtained for normal incidence;
- The RIS is assumed to be a square surface, which is centered at the origin and that lies in the xy plane at $z = 0$, whose size is $Nd_x = Md_y = 1$ meter;
- The inter-distances along the rows and the columns of the RIS are assumed to be identical, i.e., $d_x = d_y = d$. Specifically, we consider different values of $d \leq \lambda/2$ in order to analyze the impact of sub-wavelength implementations;
- Two desired angles of reflection are considered: 45 degrees and 75 degrees. This choice allows us to analyze the impact of moderate and large angles of reflection with respect to the incident electromagnetic wave (whose angle of incidence is equal to zero degrees).

As far as the parametric study as a function of d is concerned, the following remarks are in order. The RIS alphabets reported in Table 3.1 and Table 3.2 are obtained for normal incidence (i.e., the angle of incidence is zero degrees) and the corresponding reflection coefficients are obtained for a given size of the RIS reconfigurable elements. Therefore, rigorously, these alphabets should be utilized only for the sizes given in Table 3.1 and Table 3.2. In this chapter, however, we are interested in analyzing how *qualitatively* the reradiation capabilities of an RIS change as a function of the size of the RIS reconfigurable elements, while assuming that their reflection characteristics are kept unchanged as their size changes (either shrinks or increases). This provides us with an indication of how the spatial sampling affects the reradiation pattern of an RIS while keeping fixed the quantization of the phase shift and the relation between the amplitude and the phase shift of the reflection coefficient. It needs to be emphasized that it may sometimes be difficult to design RIS reconfigurable elements with a very small size (e.g., 16 or 32 times smaller than the wavelength) while ensuring that they can realize a wide range of phase shifts. If the number of quantization bits, i.e., the cardinality L of the RIS alphabet, is limited to one or two as in Table 3.1, this may, in general, be easier to be obtained in practice.

In order to evaluate the impact of realistic alphabets for the RIS reconfigurables elements, the following optimization criteria are considered:

- **Unit Amplitude and Continuous Phase (UACP)**. Based on this optimization criterion, which is usually considered in wireless communications, the reflection coefficient γ_{nm} in (3.3) is set as follows:

$$\begin{aligned} &|\gamma_{nm}| = 1 \\ &\angle\gamma_{nm} = -\angle g_{nm} - \angle h_{nm} \end{aligned} \tag{3.8}$$

- **Unit Amplitude and Discrete Evenly-Spaced Phase (UADP)**. Based on this optimization criterion, which is usually considered in wireless communications, the reflection coefficient γ_{nm} in (3.3) is set as follows:

$$\begin{aligned} &|\gamma_{nm}| = 1 \\ &\angle\gamma_{nm} = \underset{\phi\in\mathscr{P}(L)}{\arg\min}\left\{\left|\phi - \left(\angle g_{nm} + \angle h_{nm}\right)\right|\right\} \end{aligned} \tag{3.9}$$

  where $\mathscr{P}(L)$ is the set of L evenly-spaced phases as follows:

$$\mathscr{P}(L) = \left\{\phi : \frac{2\pi}{L}n, \quad n = 0, 1, \ldots, L-1\right\} \tag{3.10}$$

- **Unit Amplitude and Experimental Phase (UAEP)**. Based on this optimization criterion, the reflection coefficients γ_{nm} in (3.3) are set as follows:

$$\begin{aligned} &|\gamma_{nm}| = 1 \\ &\angle\gamma_{nm} = \underset{\phi\in\mathscr{A}}{\arg\min}\left\{\left|\phi - \left(\angle g_{nm} + \angle h_{nm}\right)\right|\right\} \end{aligned} \tag{3.11}$$

  where the set $\mathscr{A}$ is the actual alphabet in Table 3.1 and Table 3.2.

- **Experimental Alphabet (Alphabet)**. This corresponds to the case of interest, in which the actual reflection coefficients, in amplitude and phase, in Table 3.1 and Table 3.2 are considered.

In order to analyze the reradiation pattern of an RIS, we plot the received power in (3.2) as a function of the angle of observation (elevation) $\theta_{\text{obs}} \in [-90, 90]$ for the four case studies "UACP", "UADP", "UAEP", and "Alphabet". As far as the UADP case study is concerned, we indicate the number L of evenly-spaced phases as well. Due to the large number of configuration setups that can be considered, we are not able to show all the simulation results. As an example, therefore, we report all the considered case studies only for the RIS alphabet in [8], and we then show a subset of figures for the other considered RIS alphabets in order to highlight differences and similarities.

The numerical results that correspond to the RIS alphabet in [8], which is reported in Table

3.1, are illustrated in Figs. 3.2-3.49. For illustrative purposes, we report the color maps that correspond to the optimal configuration of the RIS reconfigurable elements and the corresponding received power as a function of the angle of observation. From the analysis of the color maps, we evince that the design of an RIS with sub-wavelength RIS reconfigurable elements allows us to better approximate the ideal (i.e., continuous-valued) phase profile, which results in an RIS reradiation pattern with fewer and smaller sidelobes. We observe, however, a typical diminishing return law: Reducing the size of the RIS reconfigurable elements from (1/8)th of the wavelength to (1/32)th of the wavelength does not offer any substantial gains in the considered case studies. Considering the difficulty of realizing RIS reconfigurable elements that are electrically small while ensuring reconfigurability and 360 degrees of phase modulation, this constitutes a good performance tradeoff.

By analyzing the curves that correspond to case study "UADP ($L = 2$)" with those of the alphabet in [8] where $L = 4$, we note a significantly different performance trend: The curves that correspond to the case study "UADP ($L = 2$)" show an undesired beam towards a direction that is symmetrical with respect to the desired direction, i.e., towards -45 degrees and -75 degrees for the considered case studies. This is related to the fact that an anomalous reflector with $L = 2$ reduces to a beam splitter. This is apparent from the corresponding color maps while the inter-distance between the RIS reconfigurable elements is kept the same. In other words, regardless of how fine the spatial resolution of an RIS is, an extreme quantization of the phase shift of the RIS reconfigurable elements introduces some fundamental limitations in the reradiation pattern. In addition, this occurs regardless of the practical implementation of an RIS, since the "UADP ($L = 2$)" case study is a mathematical abstraction. By considering that many available RISs are designed based on binary RIS reconfigurable elements, i.e., $L = 2$, this is an important takeaway message, especially because RISs with four-state reconfigurable elements almost completely solve this issue at a reasonable implementation complexity. It needs to be emphasized, in particular, that the undesired beam towards the direction that is symmetrical with respect to the desired direction and the desired beam have the same amplitude, which results in low reradiation performance towards the direction of interest (i.e., the total reradiated power is fixed).

By analyzing the different figures, we observe that there is a major gain by reducing the size and the inter-distance of the RIS reconfigurable elements from half (1/2) of the wavelength to (1/4)th (or smaller) of the wavelength: The radiation pattern has fewer and smaller side lobes. This is especially visible when the angle of reradiation (deflection) is very different from the angle of incidence, i.e., if the angle of reflection is 75 degrees for the considered case studies. If the RIS reconfigurable elements are smaller than (1/8)th of the wavelength, the differences are negligible for the considered case studies. As far as the case study for the desired angle of reflection equal to 75 degrees is concerned, we see that the peak of the desired beam is not exactly steered towards 75 degrees. This is due to the fact that the channels g_{nm} and h_{nm} in (3.3) are angle-dependent, and the main beam is not perfectly symmetric for large angles of deflection. This issue may be alleviated by designing an RIS based on a global design criterion [123].

The reradiated power as a function of the angle of observation for other RIS alphabets is reported in Figs. 3.50-3.73. The general trends observed for the RIS alphabet in [8] still hold, but some additional comments are in order. We see that the "UADP" case study provides a radiation pattern that does not usually result in undesired beams towards the specular direction, i.e., zero degrees. On the other hand, the "UAEP" and "Alphabet" case studies do. This is attributed to the perfect symmetry of the "UADP" alphabet both in amplitude and phase. A special comment is needed for the RIS prototype in [11]. In this case, we note a strong reradiated beam towards the specular direction (zero degrees). This is attributed to the intertwinement between the amplitude and the phase of the reflection coefficient in Table 3.2, and, more specifically, to the large attenuation for some values of the phase shift. This remark is confirmed by noting that the reradiated pattern of the "UAEP" case study does not have any beam towards the specular direction, since in this case the amplitude of the reflection coefficient is assumed to be equal to one for any phase.

In the considered case studies, we have noted that an RIS with $L = 2$ usually provides a radiation pattern with an unwanted reradiated beam towards the direction that is symmetrical with respect to the desired direction of reradiation. These conclusions were drawn under the assumption that the receiver and the transmitter are located in the far-field region of the RIS. Therefore, it is interesting to analyze the reradiated electromagnetic field when the receiver is in the near-field region of the RIS, while the transmitter is still kept in the far-field region of the RIS. This corresponds to the case in which the RIS is located close to the receiver. This case study is illustrated in Figs. 3.74-3.79 for the RIS alphabet in [9]. We note that the unwanted beams still exist but they are less strong towards the undesired direction of reradiation. Therefore, there exist differences between the reradiated power in the near-field and far-field regions of an RIS, and the use of binary RISs may be acceptable in the near-field region. We observe, however, that the peak of the reradiated power is still not exactly centered towards the desired direction of reradiation, if the angle of deflection is large. The most important observation from the considered case study is that the unwanted reradiated beam towards the direction that is symmetrical with respect to the desired direction of reradiation has a much smaller intensity as compared with the desired beam. Their difference is more than 5 dB if the desired angle of reradiation is 45 degrees and approximately 4 dB if the desired angle of reradiation is 75 degrees. In the far-field scenario, on the other hand, the two beam have almost the same intensity. A similar trend can be observed in Figs. 3.80-3.85 where the RIS alphabet in [11] is considered. In this case, we note that the unwanted beam towards the specular direction is significantly attenuated compared with the corresponding setup in the far-field region. However, we note that the beam towards the specular direction has a smaller amplitude than the desired beam if the inter-distance between the RIS reconfiguable elements is smaller than $d = \lambda/2$ and if the angle of reflection is not too large compared with the angle of incidence. In fact, we observe that a non-negligible specular beam still exists if the desired angle of reradiation is 75 degrees. This was somehow expected, since the RIS in [11] was designed to operate for angles that lie in the range $[-45, 45]$ degrees. The main reason for the presence of a strong beam towards the specular direction can be understood

by direct inspection of Table 3.2. For ease of discussion, the reflection coefficient in Table 3.2 is illustrated in Figs. 3.86, 3.87, 3.88. We note that the phase shifts that can be realized lie in the range [30,350] degrees, and, more important, the attenuation for the phases that lie in the range [90,270] degrees is much higher than the attenuation for the phases that lie in the range [−90,90] degrees. This results in a non-negligible unbalance of the amplitudes between the values of the reflection coefficient with a positive and negative real part, as illustrated in Fig. 3.88. As a result, the reflection coefficient is not centered around the origin, and this leads to a non-negligible specular reflection for any angle of incidence. A possible solution to alleviate this issue is to reduce the attenuation for the phases in the range [90,270]. Based on the full-wave simulations reported in [11], the attenuation for this range of phases was expected to be much smaller than that obtained from the experimental measurements. In the near-field region, nevertheless, we note that the beam towards the desired direction of radiation is 1.44 dB and 1.74 dB higher than the beam towards the specular direction for $d = \lambda/4$ and $d = \lambda/8$, respectively, and the desired angle of reradiation is 45 degrees.

The results illustrated so far assume that an RIS is designed and optimized for reradiating an electromagnetic wave that impinges upon the surface from a known direction towards another direction that is known as well. It is important to analyze, however, the reradiation properties of an optimized RIS when it is illuminated by unknown electromagnetic waves that originate from directions that are different from that of design. In wireless communications, this is the typical case study in which an optimized RIS operates in the presence of electromagnetic interference. This case study is illustrated in Figs. 3.89-3.96 by considering the RIS alphabet in [8]. More specifically, it is assumed that the RIS is first optimized in order to reradiate an electromagnetic wave from the normal direction towards a given direction of reradiation. Then, the optimized RIS is illuminated by an interfering electromagnetic wave from the direction $\theta_{\text{inc}} \neq 0$. It needs to be mentioned that the RIS alphabets in Table 3.1 and Table 3.2 are obtained by assuming normal incidence. Usually, however, an RIS alphabet is angle-dependent. Therefore, it changes with the angle of incidence. In our qualitative study this dependency is not considered, since the angle-dependency of the RIS alphabets in Table 3.1 and Table 3.2 is not available. For comparison, in addition, we report the reradiation patterns that correspond to two surfaces that operate as a specular reflector and as a diffuser. In the first case, the reflection coefficients γ_{nm} are set equal to one, and in the second case the reflection coefficients γ_{nm} have unit amplitude and a random phase. The figures show that the RIS reradiates the interfering signal towards a direction that is different from the location of the intended receiver. Therefore, an interfering electromagnetic wave may not be harmful for the intended receiver. However, the RIS may produce reradiated beams towards other directions that depend on the angle of incidence of the interfering electromagnetic wave and the phase modulation applied by the RIS. More specifically, the results illustrated in Figs. 3.95 and 3.96 show that an interfering electromagnetic wave results in a small interference towards the desired direction of reradiation if the angle of incidence is sufficiently different from the nominal angle of incidence. The example illustrated in Figs. 3.95 and 3.96 shows that, given the width of the obtained reradiated beam, an interfering electromagnetic wave that illuminates

the RIS from a direction that is at least five degrees different from the nominal direction of reradiation does not interfere with the intended receiver. However, it generates interference towards nearby locations, which need to be accounted for in the context of network-level analysis and optimization. This behavior is inherently due to the phase modulation applied by the RIS.

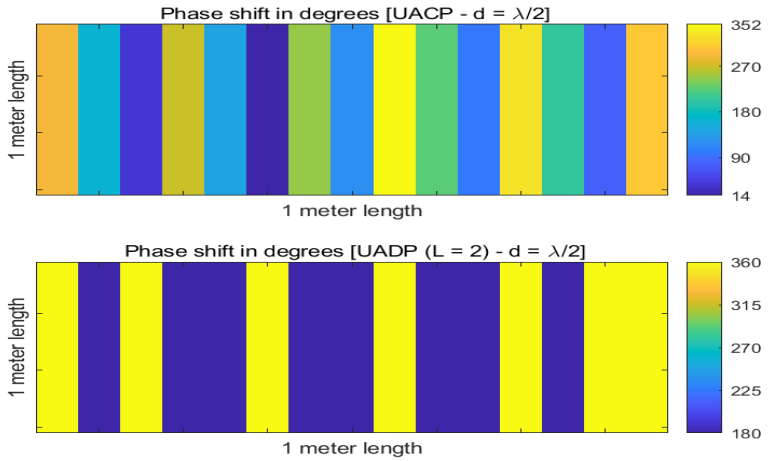

Figure 3.2: Color map representation of $\mathbf{\Gamma}$ corresponding to the UACP and UADP ($L = 2$) case studies. The desired angle of reflection is 45 degrees and the inter-distance is $d = \lambda/2$.

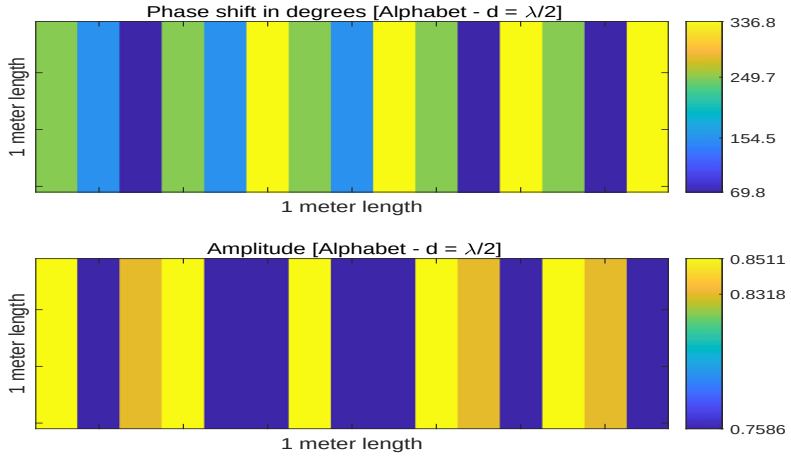

Figure 3.3: Color map representation of $\mathbf{\Gamma}$ corresponding to the RIS alphabet in [8]. The desired angle of reflection is 45 degrees and the inter-distance is $d = \lambda/2$.

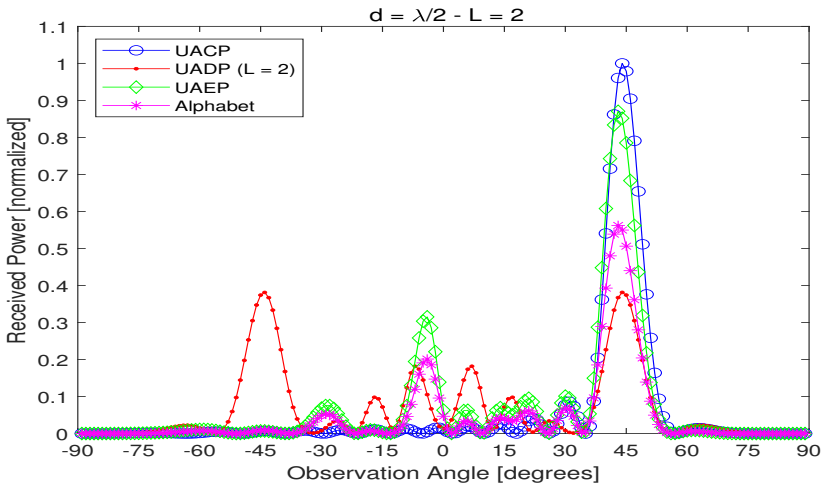

Figure 3.4: Received power as a function of the angle of observation. The RIS alphabet is [8], the desired angle of reflection is 45 degrees, and the inter-distance is $d = \lambda/2$.

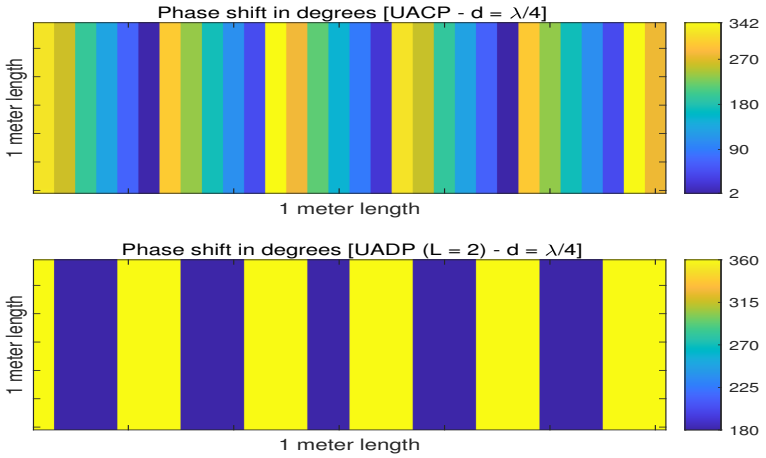

Figure 3.5: Color map representation of $\mathbf{\Gamma}$ corresponding to the UACP and UADP ($L = 2$) case studies. The desired angle of reflection is 45 degrees and the inter-distance is $d = \lambda/4$.

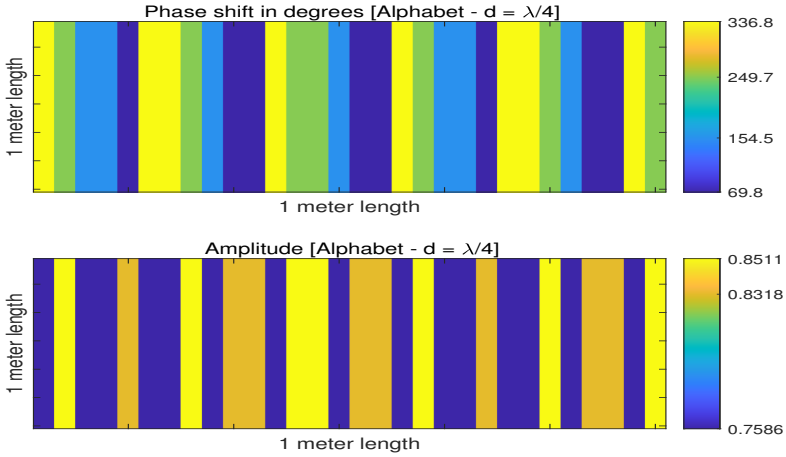

Figure 3.6: Color map representation of $\mathbf{\Gamma}$ corresponding to the RIS alphabet in [8]. The desired angle of reflection is 45 degrees and the inter-distance is $d = \lambda/4$.

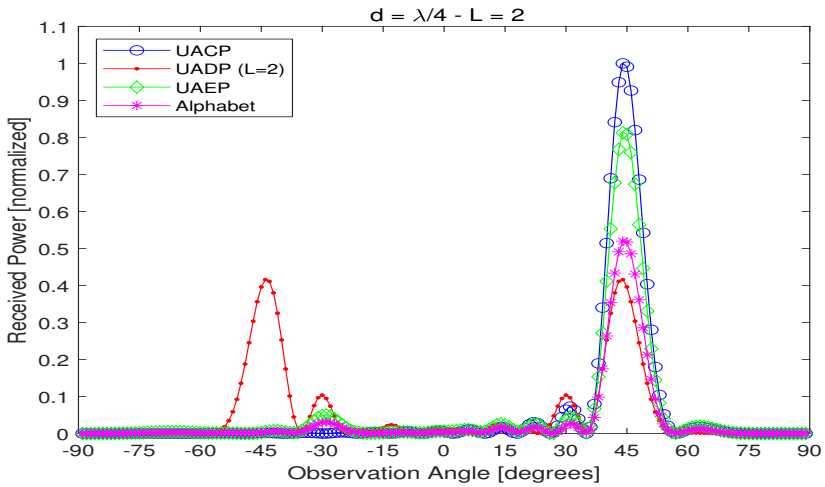

Figure 3.7: Received power as a function of the angle of observation. The RIS alphabet is [8], the desired angle of reflection is 45 degrees, and the inter-distance is $d = \lambda/4$.

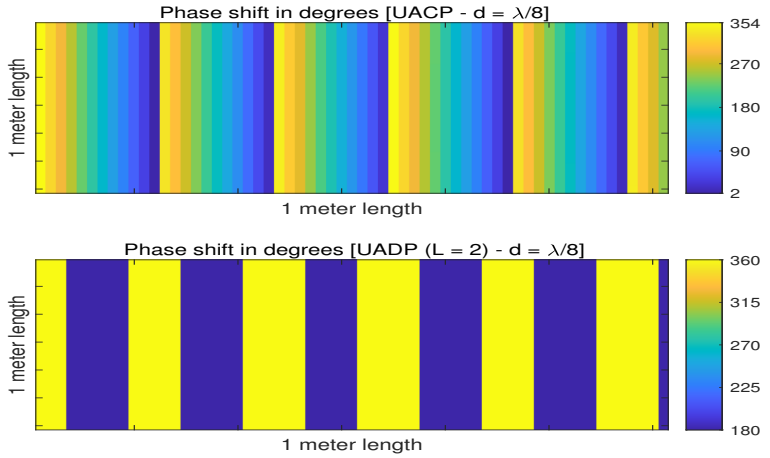

Figure 3.8: Color map representation of $\mathbf{\Gamma}$ corresponding to the UACP and UADP ($L = 2$) case studies. The desired angle of reflection is 45 degrees and the inter-distance is $d = \lambda/8$.

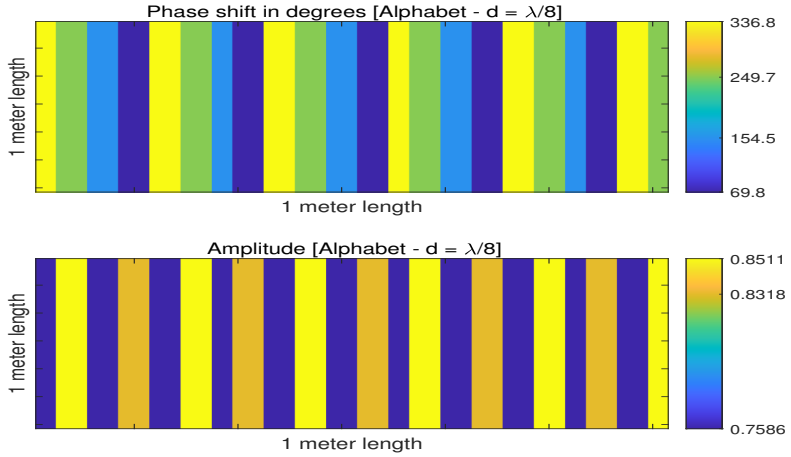

Figure 3.9: Color map representation of $\mathbf{\Gamma}$ corresponding to the RIS alphabet in [8]. The desired angle of reflection is 45 degrees and the inter-distance is $d = \lambda/8$.

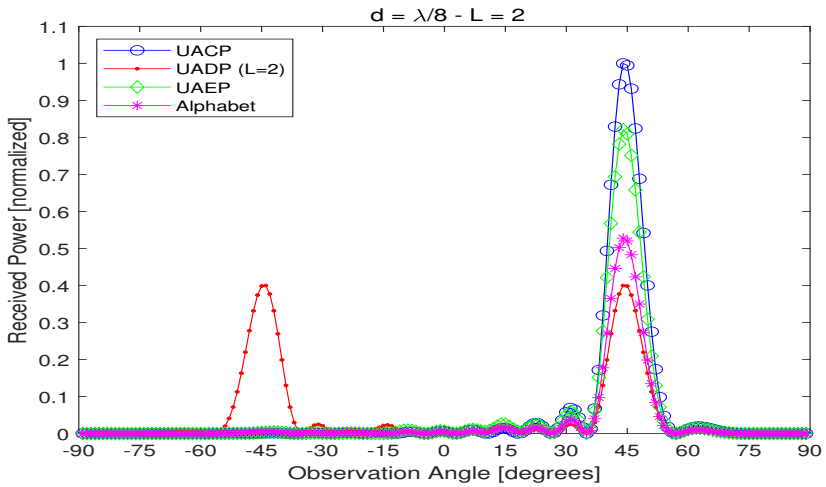

Figure 3.10: Received power as a function of the angle of observation. The RIS alphabet is [8], the desired angle of reflection is 45 degrees, and the inter-distance is $d = \lambda/8$.

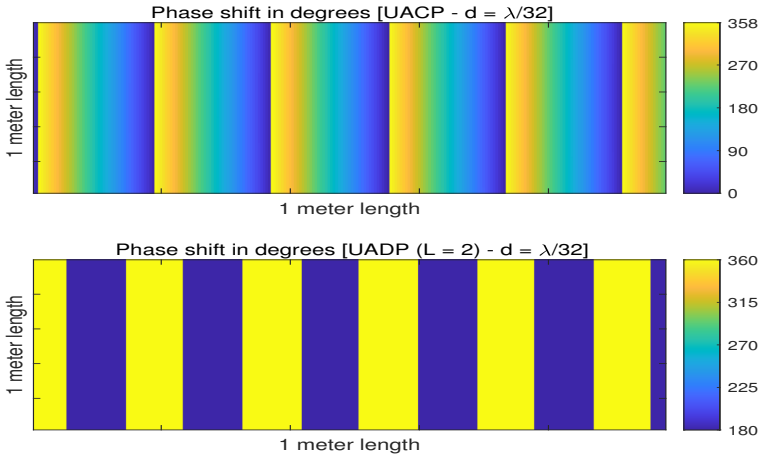

Figure 3.11: Color map representation of $\mathbf{\Gamma}$ corresponding to the UACP and UADP ($L = 2$) case studies. The desired angle of reflection is 45 degrees and the inter-distance is $d = \lambda/32$.

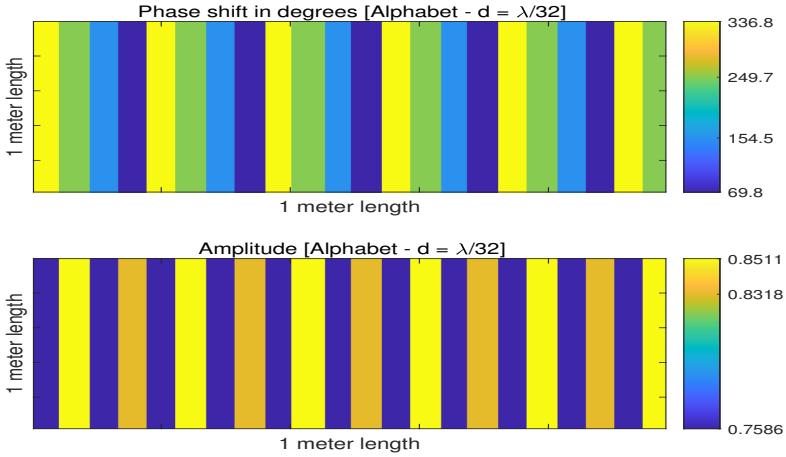

Figure 3.12: Color map representation of $\mathbf{\Gamma}$ corresponding to the RIS alphabet in [8]. The desired angle of reflection is 45 degrees and the inter-distance is $d = \lambda/32$.

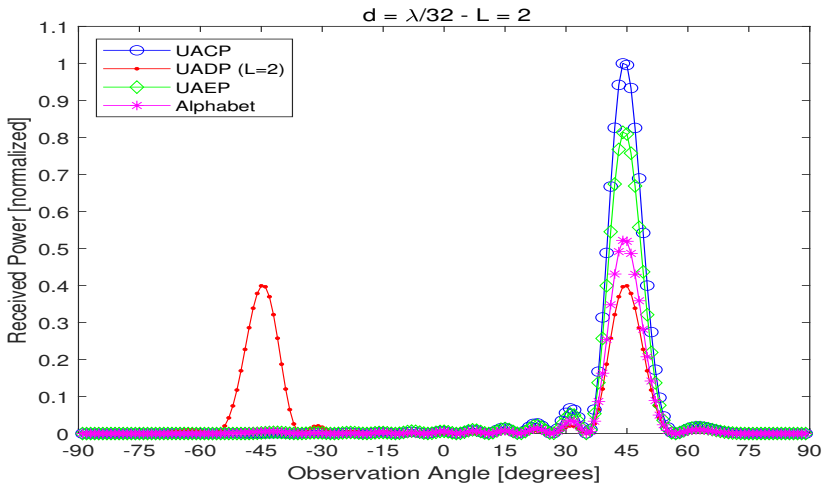

Figure 3.13: Received power as a function of the angle of observation. The RIS alphabet is [8], the desired angle of reflection is 45 degrees, and the inter-distance is $d = \lambda/32$.

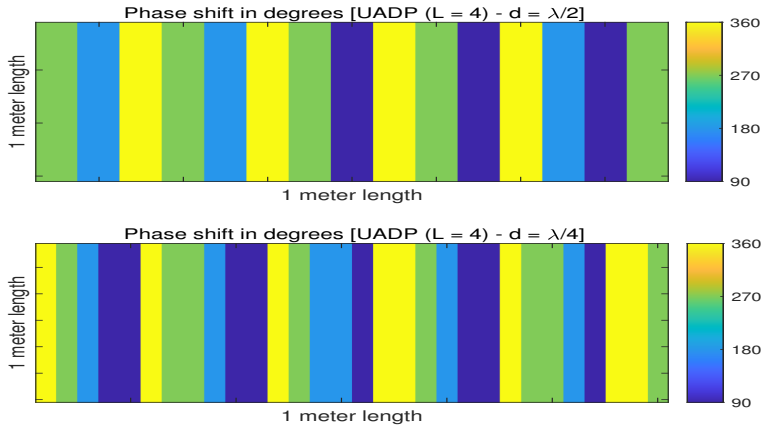

Figure 3.14: Color map representation of $\mathbf{\Gamma}$ corresponding to the UADP ($L = 4$) case study. The desired angle of reflection is 45 degrees and the inter-distance is $d = \lambda/2$ and $d = \lambda/4$.

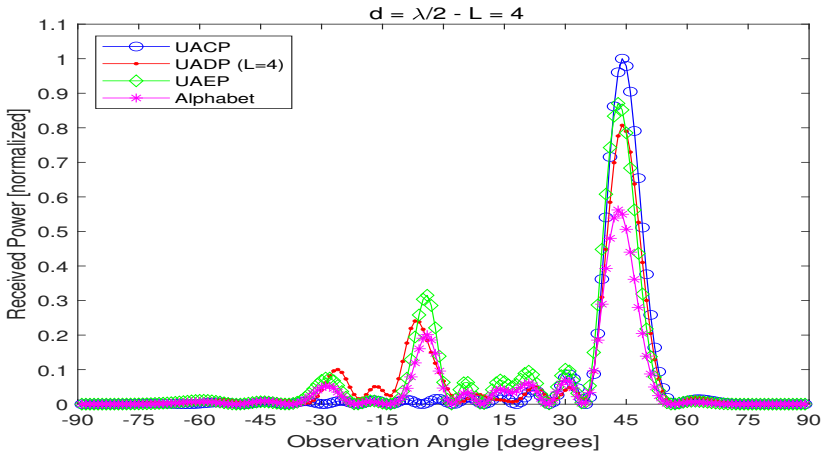

Figure 3.15: Received power as a function of the angle of observation. The RIS alphabet is [8], the desired angle of reflection is 45 degrees, and the inter-distance is $d = \lambda/2$.

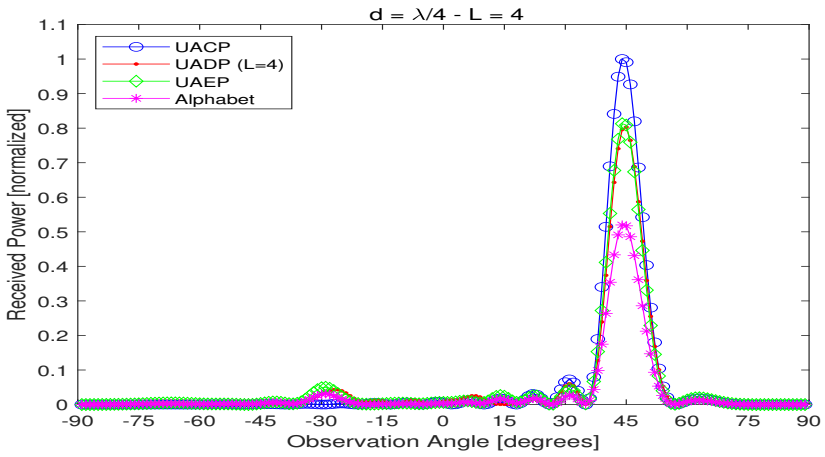

Figure 3.16: Received power as a function of the angle of observation. The RIS alphabet is [8], the desired angle of reflection is 45 degrees, and the inter-distance is $d = \lambda/4$.

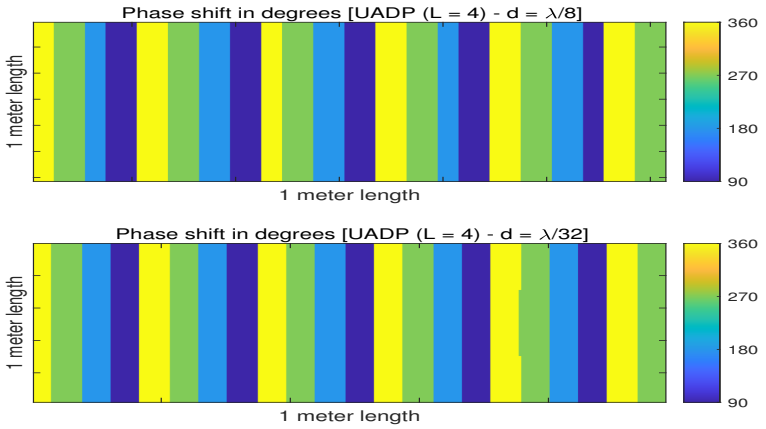

Figure 3.17: Color map representation of $\mathbf{\Gamma}$ corresponding to the UADP ($L = 4$) case study. The desired angle of reflection is 45 degrees and the inter-distance is $d = \lambda/8$ and $d = \lambda/32$.

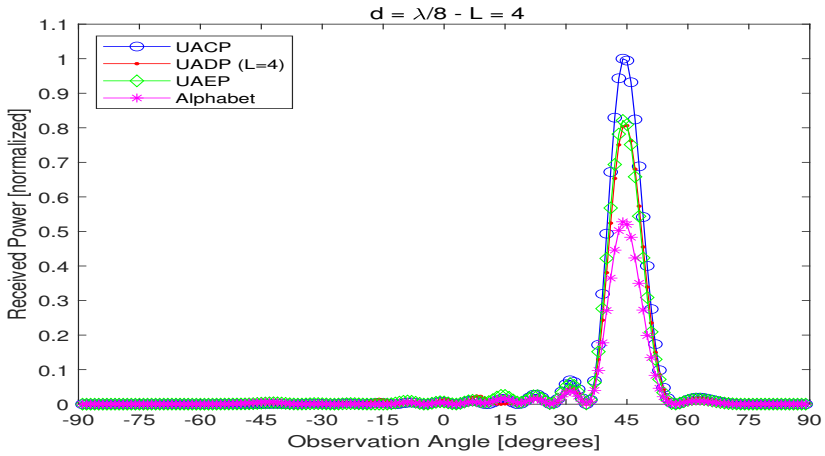

Figure 3.18: Received power as a function of the angle of observation. The RIS alphabet is [8], the desired angle of reflection is 45 degrees, and the inter-distance is $d = \lambda/8$.

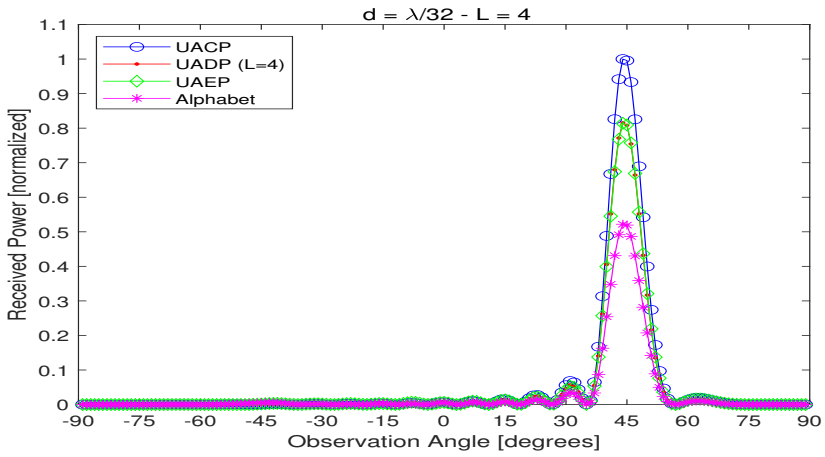

Figure 3.19: Received power as a function of the angle of observation. The RIS alphabet is [8], the desired angle of reflection is 45 degrees, and the inter-distance is $d = \lambda/32$.

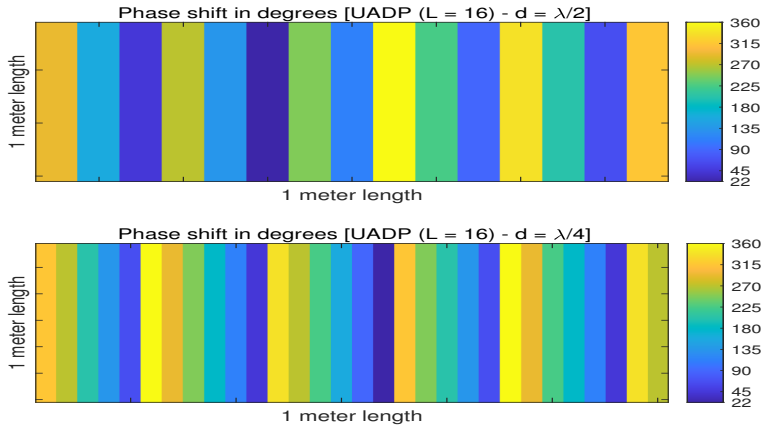

Figure 3.20: Color map representation of $\mathbf{\Gamma}$ corresponding to the UADP ($L = 16$) case study. The desired angle of reflection is 45 degrees and the inter-distance is $d = \lambda/2$ and $d = \lambda/4$.

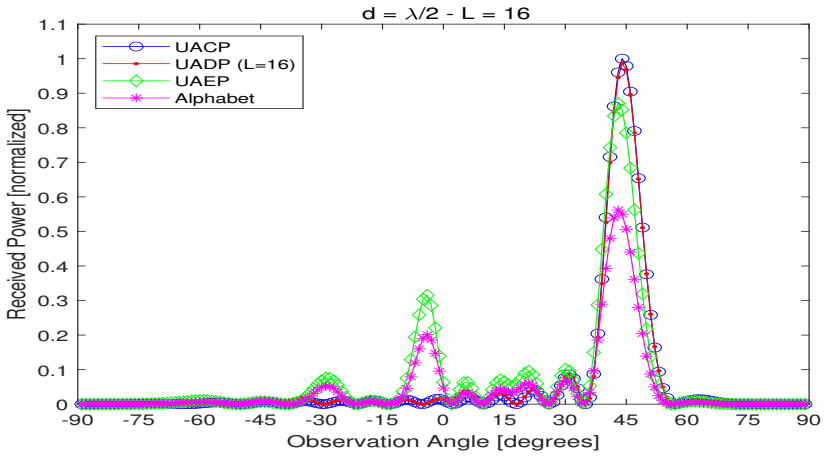

Figure 3.21: Received power as a function of the angle of observation. The RIS alphabet is [8], the desired angle of reflection is 45 degrees, and the inter-distance is $d = \lambda/2$.

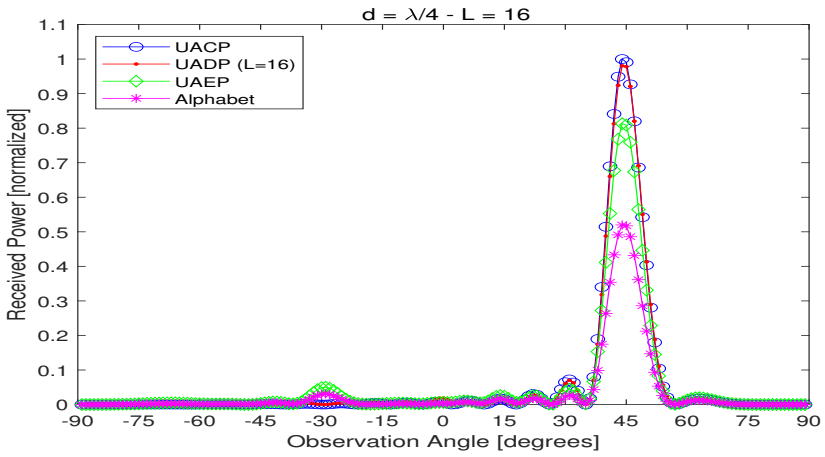

Figure 3.22: Received power as a function of the angle of observation. The RIS alphabet is [8], the desired angle of reflection is 45 degrees, and the inter-distance is $d = \lambda/4$.

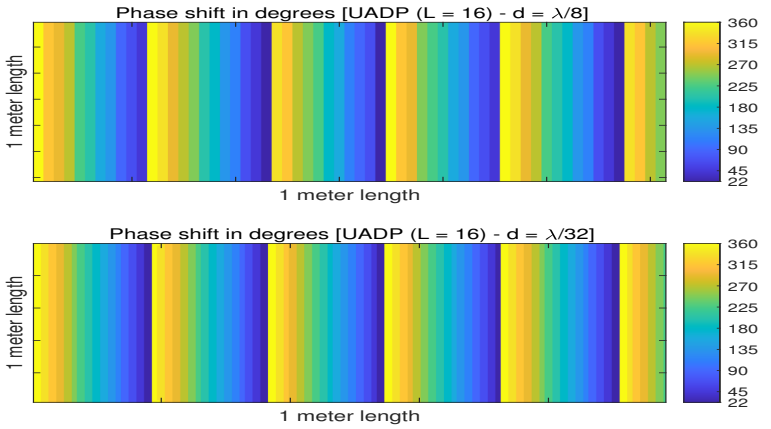

Figure 3.23: Color map representation of $\mathbf{\Gamma}$ corresponding to the UADP ($L = 16$) case study. The desired angle of reflection is 45 degrees and the inter-distance is $d = \lambda/8$ and $d = \lambda/32$.

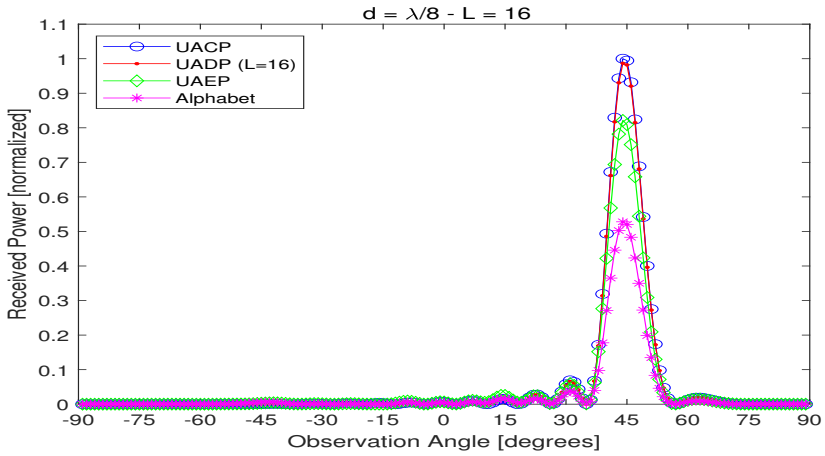

Figure 3.24: Received power as a function of the angle of observation. The RIS alphabet is [8], the desired angle of reflection is 45 degrees, and the inter-distance is $d = \lambda/8$.

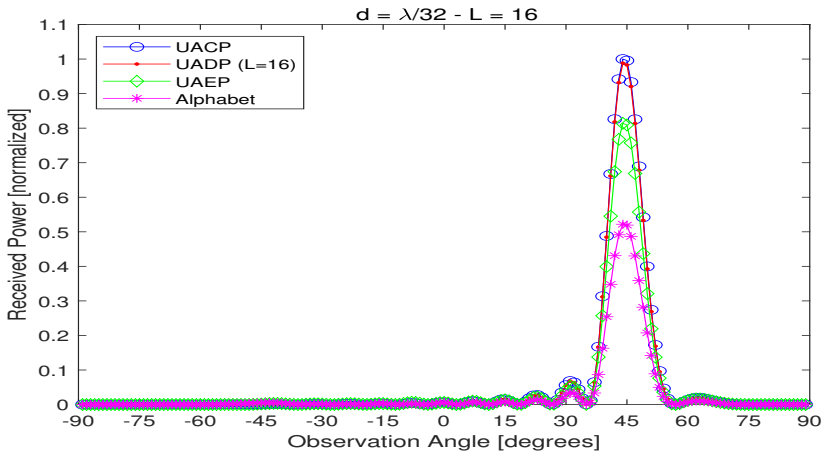

Figure 3.25: Received power as a function of the angle of observation. The RIS alphabet is [8], the desired angle of reflection is 45 degrees, and the inter-distance is $d = \lambda/32$.

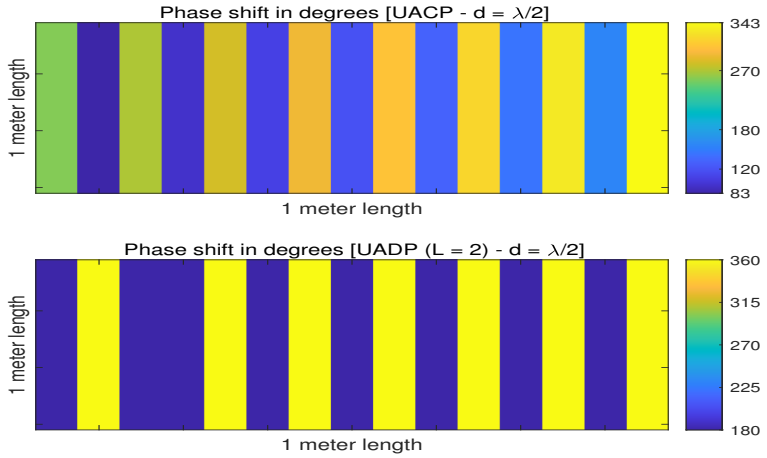

Figure 3.26: Color map representation of $\mathbf{\Gamma}$ corresponding to the UACP and UADP ($L = 2$) case studies. The desired angle of reflection is 75 degrees and the inter-distance is $d = \lambda/2$.

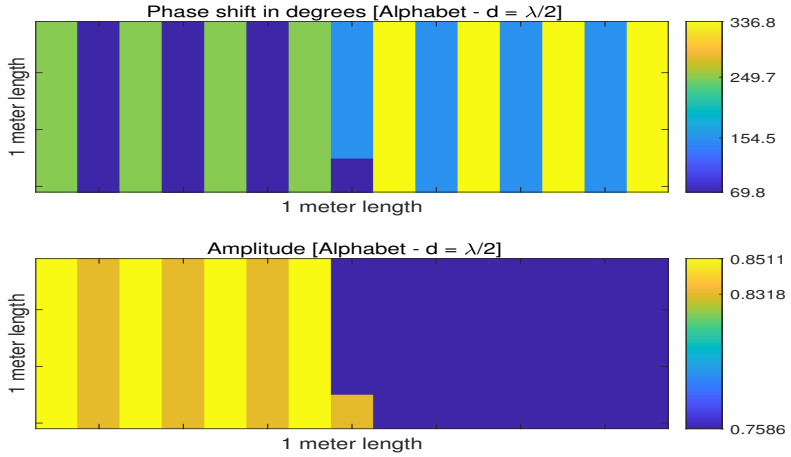

Figure 3.27: Color map representation of $\mathbf{\Gamma}$ corresponding to the RIS alphabet in [8]. The desired angle of reflection is 75 degrees and the inter-distance is $d = \lambda/2$.

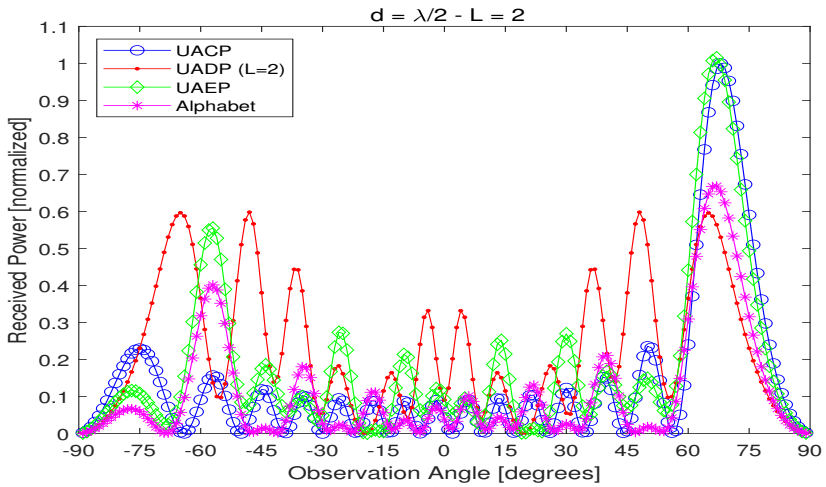

Figure 3.28: Received power as a function of the angle of observation. The RIS alphabet is [8], the desired angle of reflection is 75 degrees, and the inter-distance is $d = \lambda/2$.

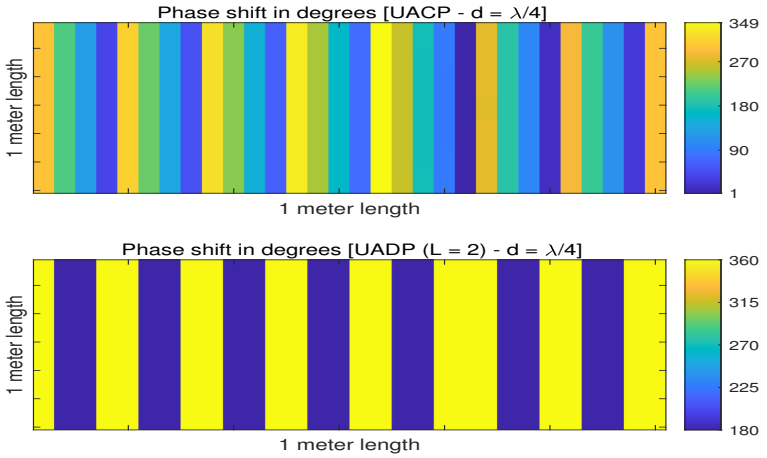

Figure 3.29: Color map representation of $\mathbf{\Gamma}$ corresponding to the UACP and UADP ($L = 2$) case studies. The desired angle of reflection is 75 degrees and the inter-distance is $d = \lambda/4$.

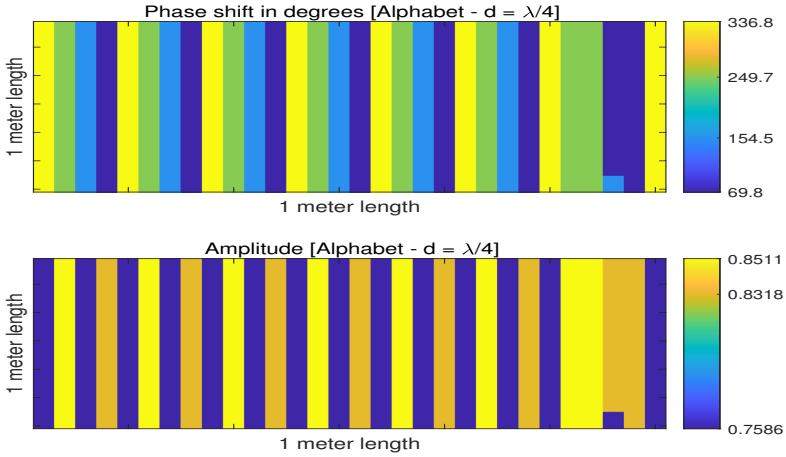

Figure 3.30: Color map representation of $\mathbf{\Gamma}$ corresponding to the RIS alphabet in [8]. The desired angle of reflection is 75 degrees and the inter-distance is $d = \lambda/4$.

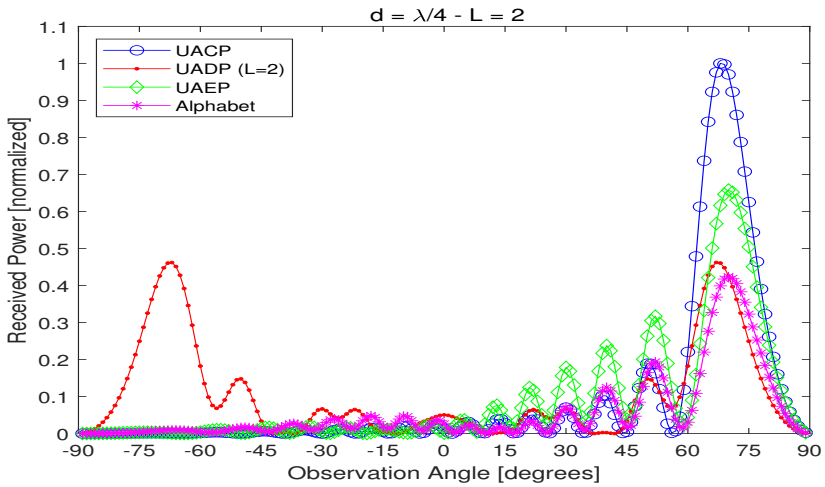

Figure 3.31: Received power as a function of the angle of observation. The RIS alphabet is [8], the desired angle of reflection is 75 degrees, and the inter-distance is $d = \lambda/4$.

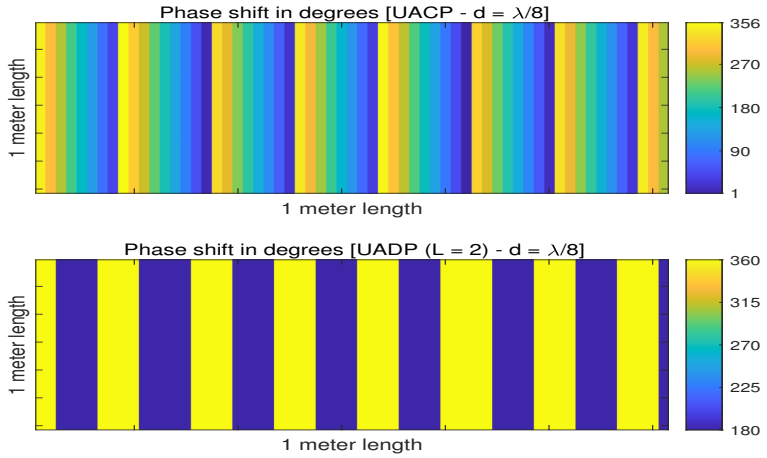

Figure 3.32: Color map representation of $\mathbf{\Gamma}$ corresponding to the UACP and UADP ($L = 2$) case studies. The desired angle of reflection is 75 degrees and the inter-distance is $d = \lambda/8$.

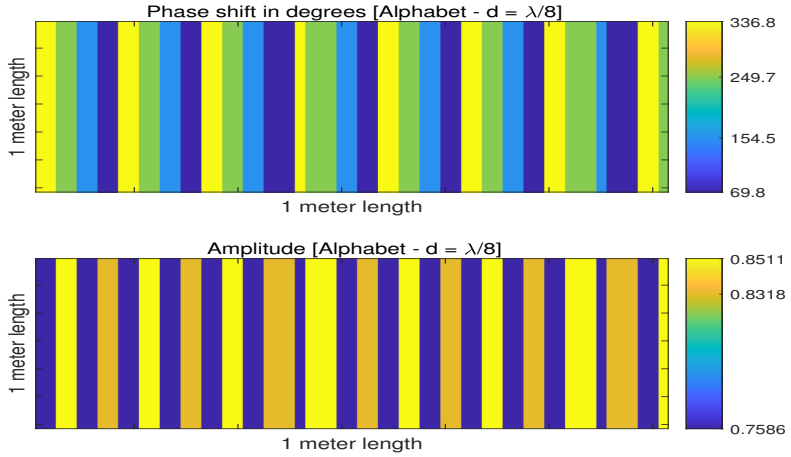

Figure 3.33: Color map representation of $\mathbf{\Gamma}$ corresponding to the RIS alphabet in [8]. The desired angle of reflection is 75 degrees and the inter-distance is $d = \lambda/8$.

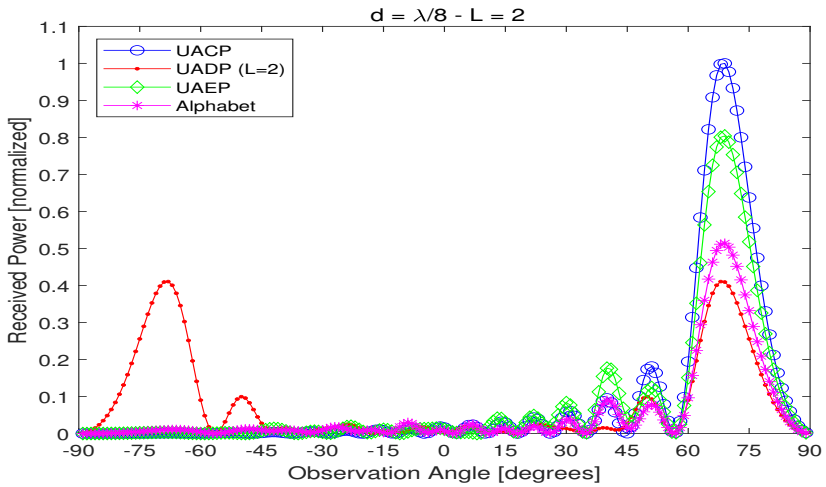

Figure 3.34: Received power as a function of the angle of observation. The RIS alphabet is [8], the desired angle of reflection is 75 degrees, and the inter-distance is $d = \lambda/8$.

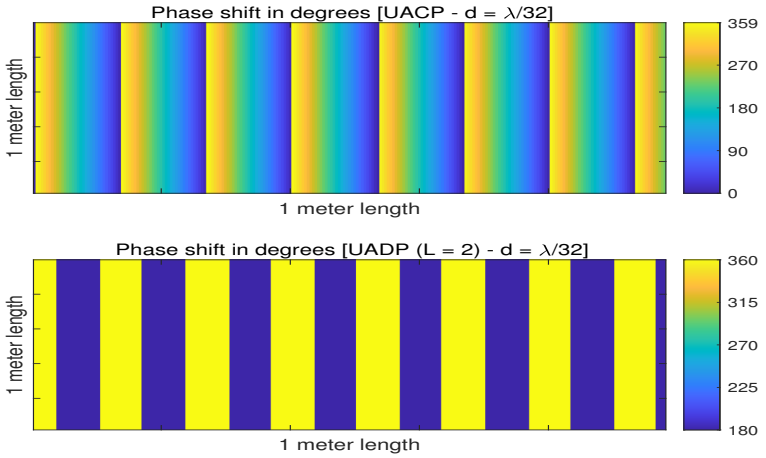

Figure 3.35: Color map representation of $\mathbf{\Gamma}$ corresponding to the UACP and UADP ($L = 2$) case studies. The desired angle of reflection is 75 degrees and the inter-distance is $d = \lambda/32$.

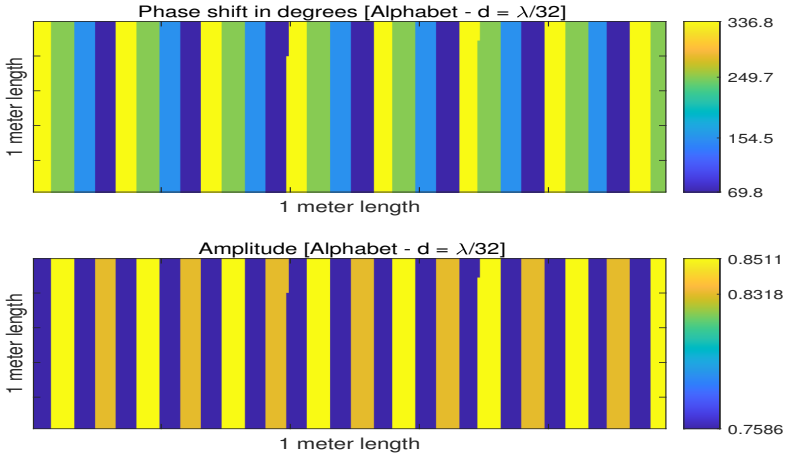

Figure 3.36: Color map representation of $\mathbf{\Gamma}$ corresponding to the RIS alphabet in [8]. The desired angle of reflection is 75 degrees and the inter-distance is $d = \lambda/32$.

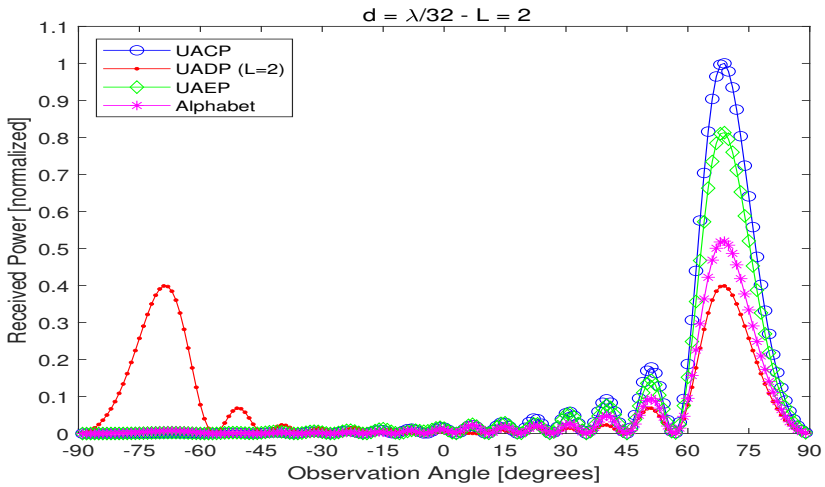

Figure 3.37: Received power as a function of the angle of observation. The RIS alphabet is [8], the desired angle of reflection is 75 degrees, and the inter-distance is $d = \lambda/32$.

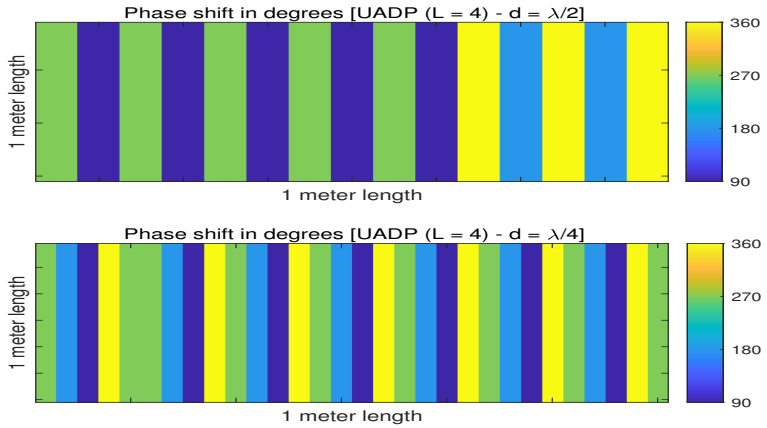

Figure 3.38: Color map representation of $\mathbf{\Gamma}$ corresponding to the UADP ($L = 4$) case study. The desired angle of reflection is 75 degrees and the inter-distance is $d = \lambda/2$ and $d = \lambda/4$.

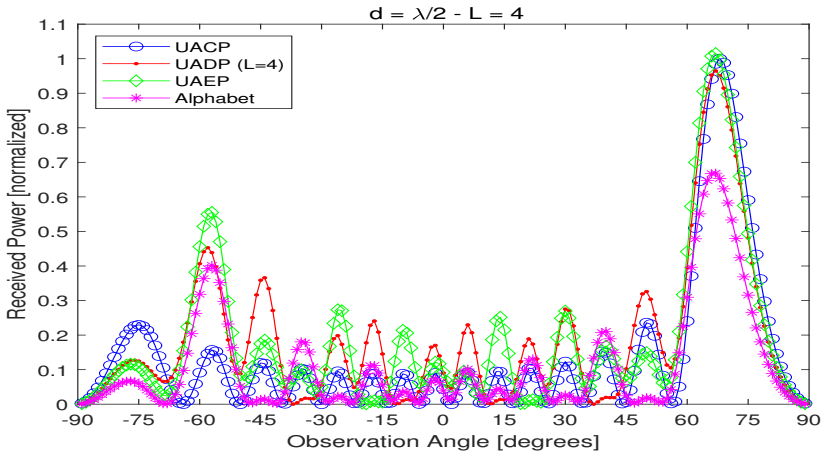

Figure 3.39: Received power as a function of the angle of observation. The RIS alphabet is [8], the desired angle of reflection is 75 degrees, and the inter-distance is $d = \lambda/2$.

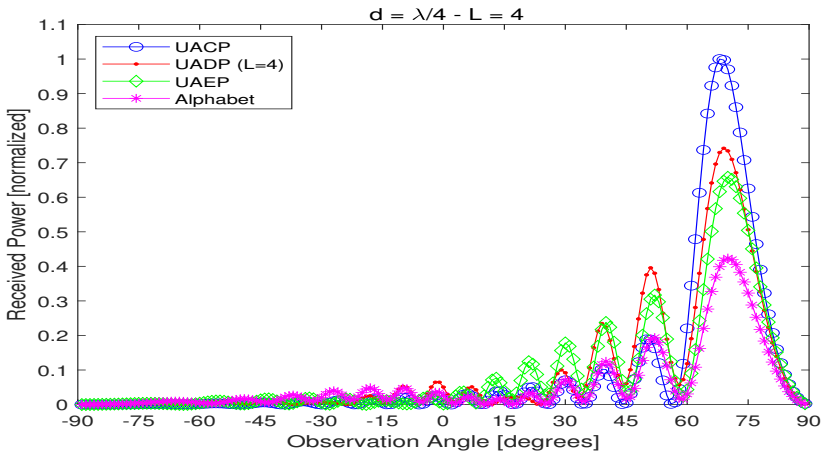

Figure 3.40: Received power as a function of the angle of observation. The RIS alphabet is [8], the desired angle of reflection is 75 degrees, and the inter-distance is $d = \lambda/4$.

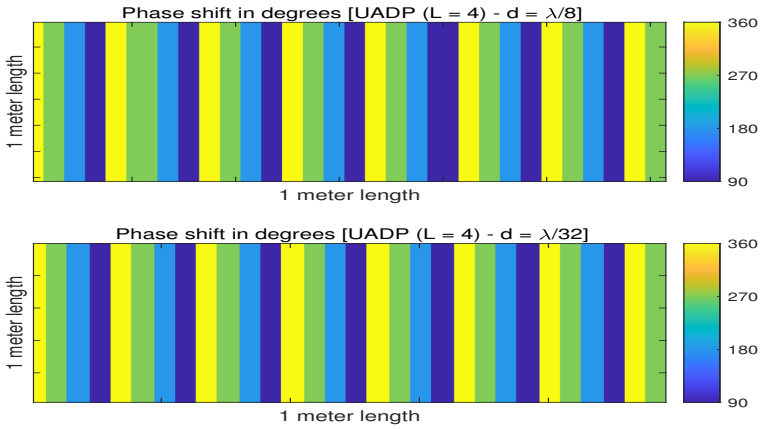

Figure 3.41: Color map representation of $\mathbf{\Gamma}$ corresponding to the UADP ($L = 4$) case study. The desired angle of reflection is 75 degrees and the inter-distance is $d = \lambda/8$ and $d = \lambda/32$.

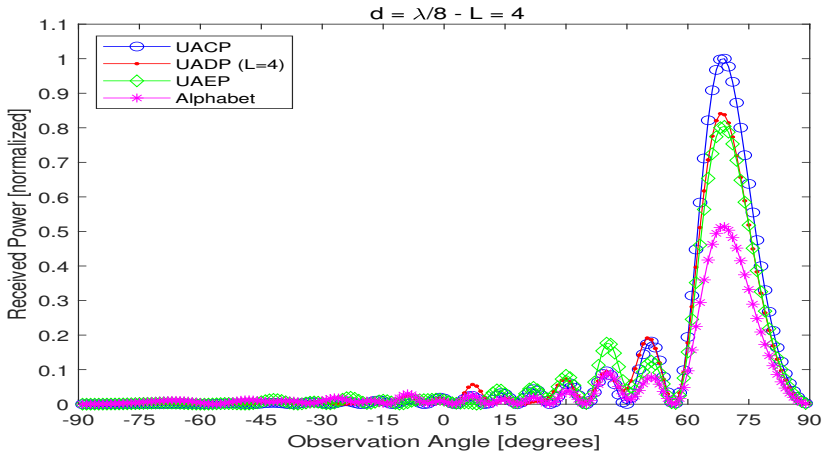

Figure 3.42: Received power as a function of the angle of observation. The RIS alphabet is [8], the desired angle of reflection is 75 degrees, and the inter-distance is $d = \lambda/8$.

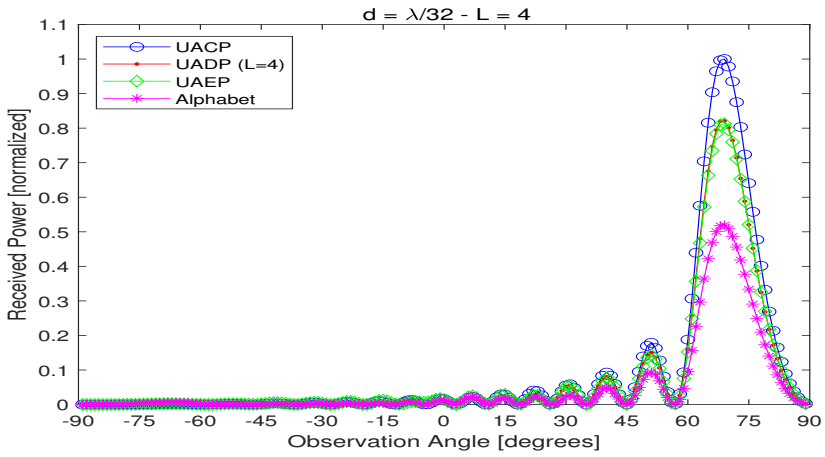

Figure 3.43: Received power as a function of the angle of observation. The RIS alphabet is [8], the desired angle of reflection is 75 degrees, and the inter-distance is $d = \lambda/32$.

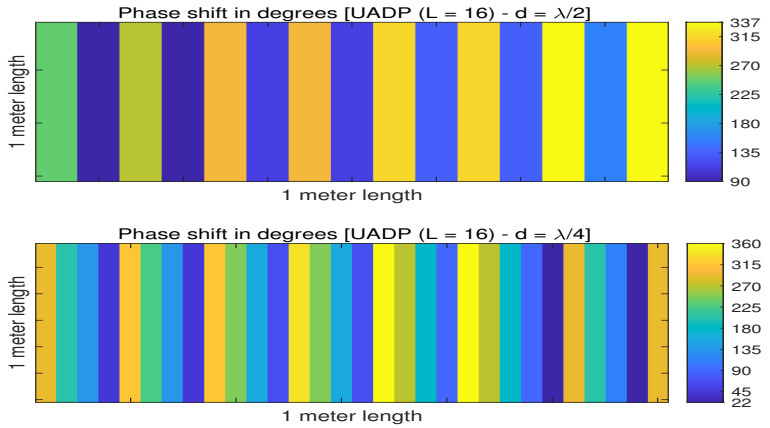

Figure 3.44: Color map representation of $\mathbf{\Gamma}$ corresponding to the UADP ($L = 16$) case study. The desired angle of reflection is 75 degrees and the inter-distance is $d = \lambda/2$ and $d = \lambda/4$.

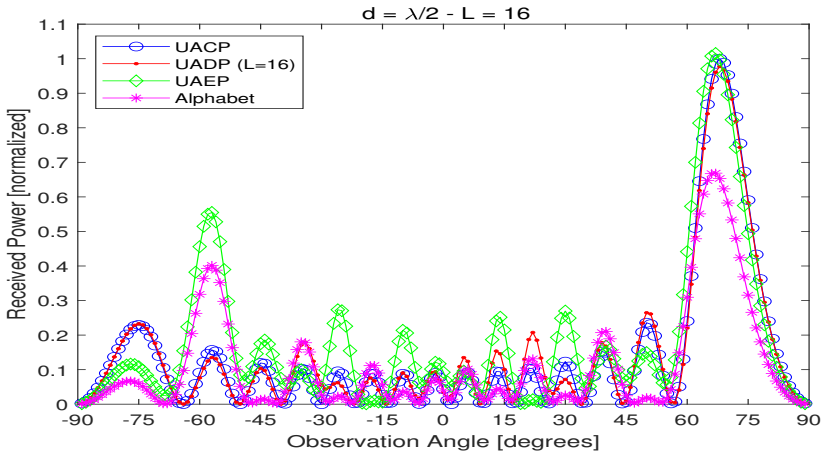

Figure 3.45: Received power as a function of the angle of observation. The RIS alphabet is [8], the desired angle of reflection is 75 degrees, and the inter-distance is $d = \lambda/2$.

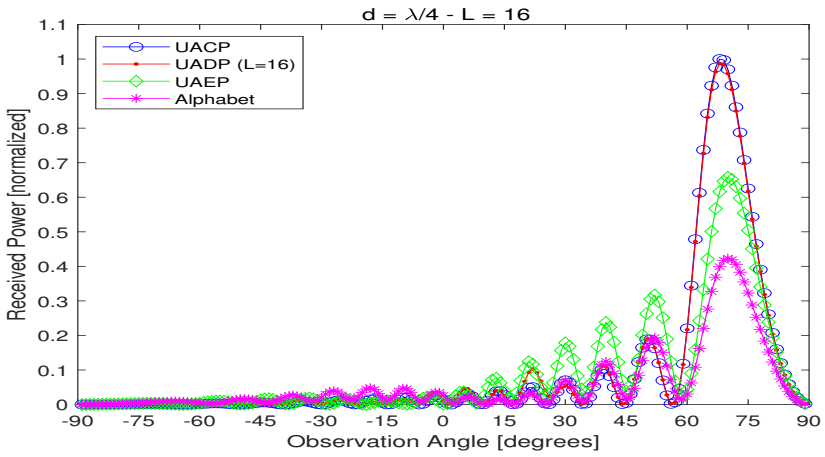

Figure 3.46: Received power as a function of the angle of observation. The RIS alphabet is [8], the desired angle of reflection is 75 degrees, and the inter-distance is $d = \lambda/4$.

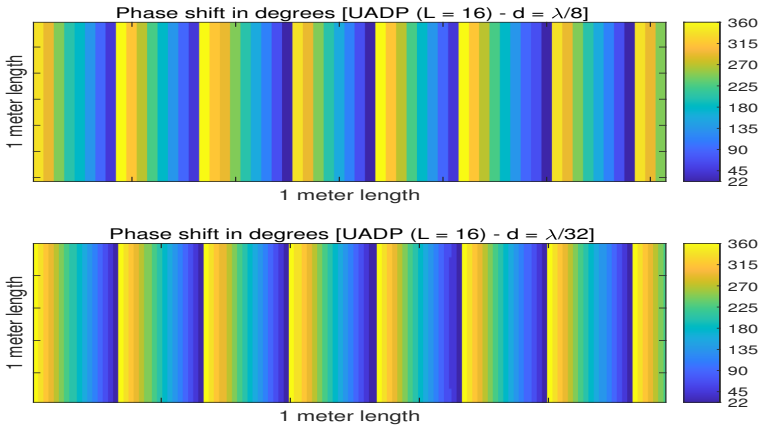

Figure 3.47: Color map representation of $\mathbf{\Gamma}$ corresponding to the UADP ($L = 16$) case study. The desired angle of reflection is 75 degrees and the inter-distance is $d = \lambda/8$ and $d = \lambda/32$.

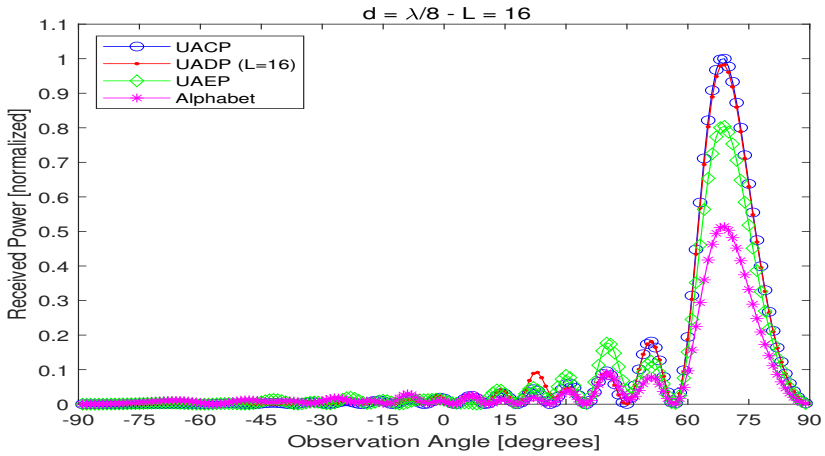

Figure 3.48: Received power as a function of the angle of observation. The RIS alphabet is [8], the desired angle of reflection is 75 degrees, and the inter-distance is $d = \lambda/8$.

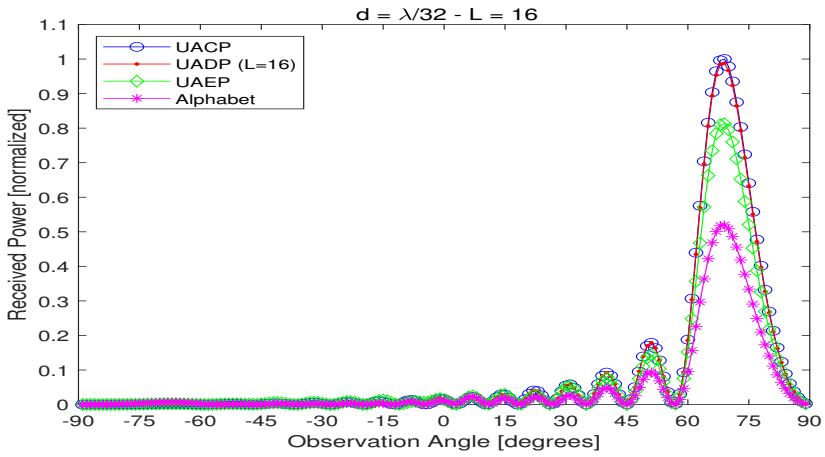

Figure 3.49: Received power as a function of the angle of observation. The RIS alphabet is [8], the desired angle of reflection is 75 degrees, and the inter-distance is $d = \lambda/32$.

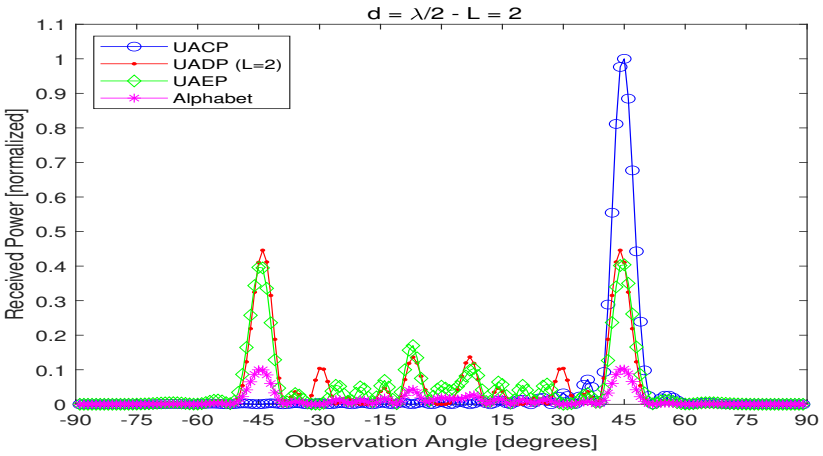

Figure 3.50: Received power as a function of the angle of observation. The RIS alphabet is [9], the desired angle of reflection is 45 degrees, and the inter-distance is $d = \lambda/2$.

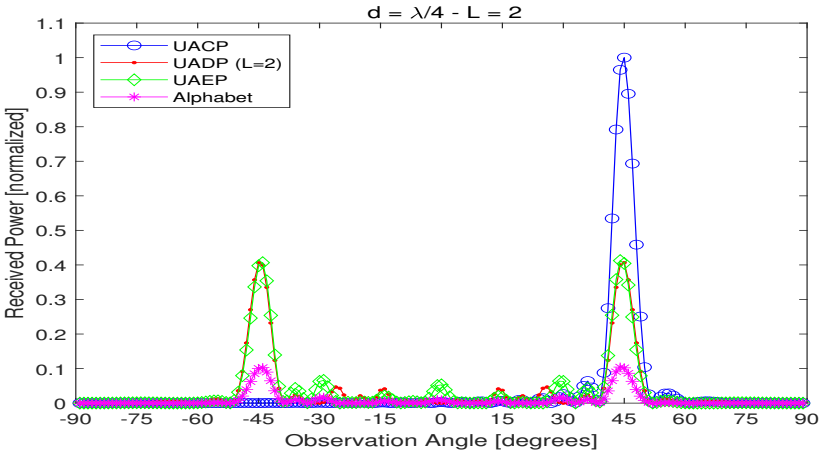

Figure 3.51: Received power as a function of the angle of observation. The RIS alphabet is [9], the desired angle of reflection is 45 degrees, and the inter-distance is $d = \lambda/4$.

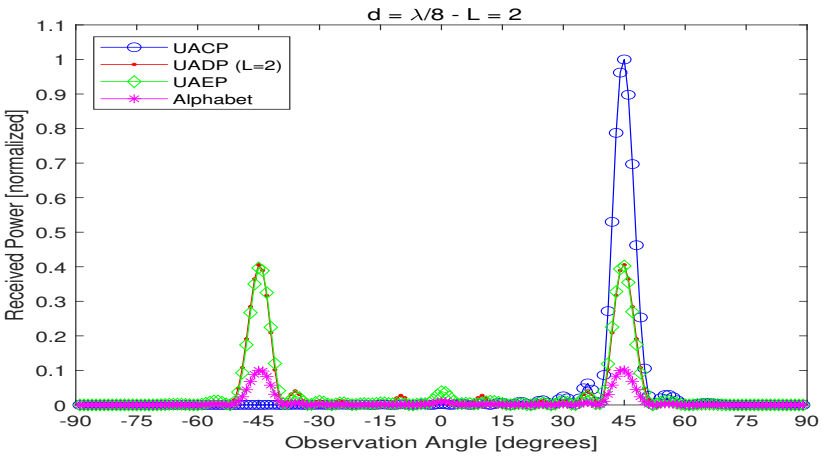

Figure 3.52: Received power as a function of the angle of observation. The RIS alphabet is [9], the desired angle of reflection is 45 degrees, and the inter-distance is $d = \lambda/8$.

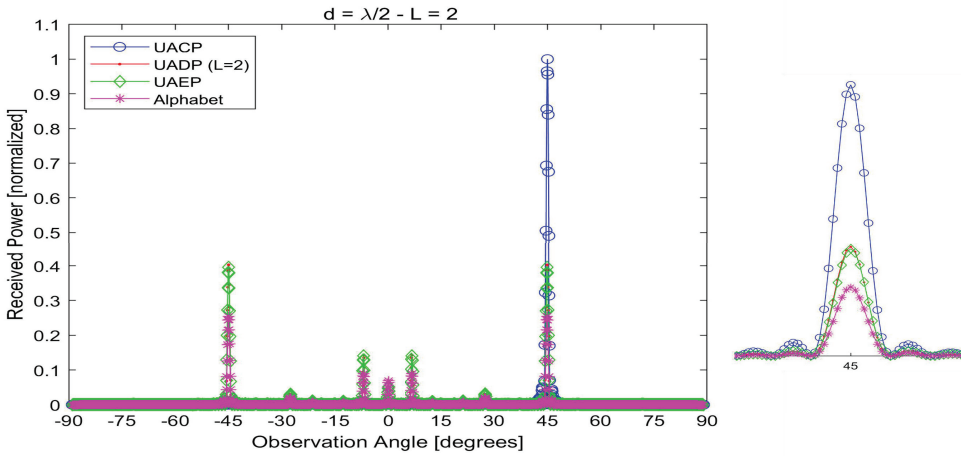

Figure 3.53: Received power as a function of the angle of observation. The RIS alphabet is [10] ($f = 27$ GHz), the desired angle of reflection is 45 degrees, and the inter-distance is $d = \lambda/2$.

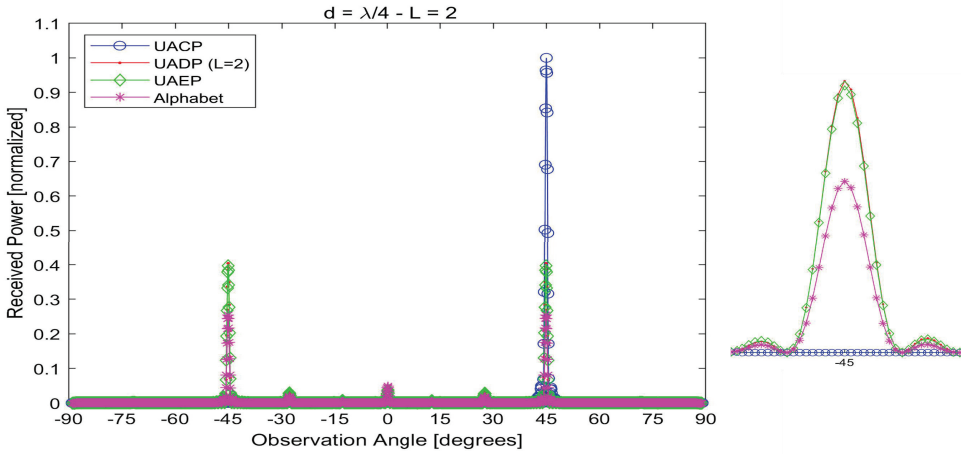

Figure 3.54: Received power as a function of the angle of observation. The RIS alphabet is [10] ($f = 27$ GHz), the desired angle of reflection is 45 degrees, and the inter-distance is $d = \lambda/4$.

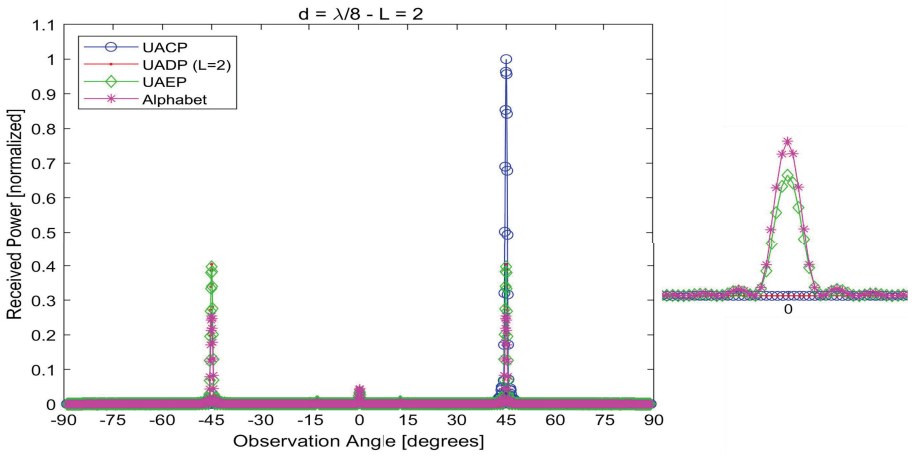

Figure 3.55: Received power as a function of the angle of observation. The RIS alphabet is [10] ($f = 27$ GHz), the desired angle of reflection is 45 degrees, and the inter-distance is $d = \lambda/8$.

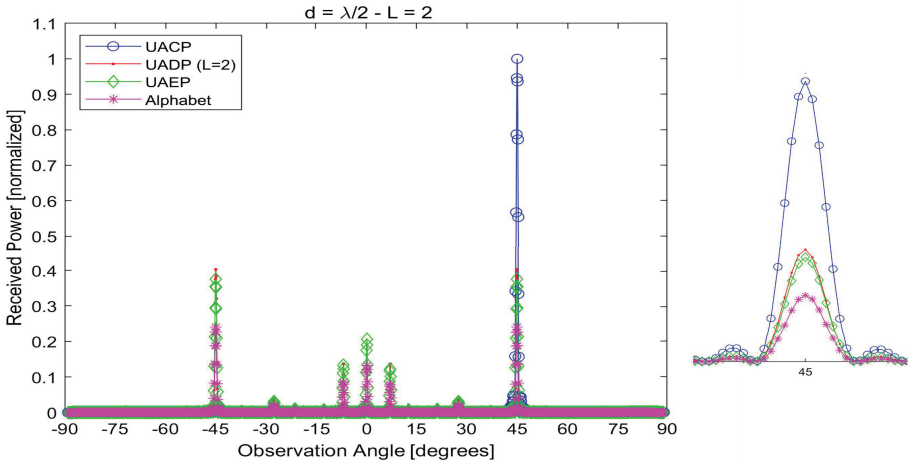

Figure 3.56: Received power as a function of the angle of observation. The RIS alphabet is [10] ($f = 33$ GHz), the desired angle of reflection is 45 degrees, and the inter-distance is $d = \lambda/2$.

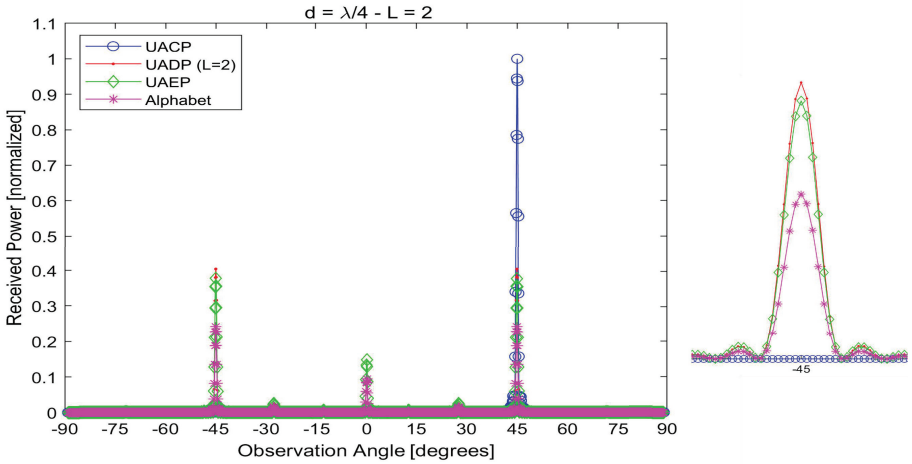

Figure 3.57: Received power as a function of the angle of observation. The RIS alphabet is [10] ($f = 33$ GHz), the desired angle of reflection is 45 degrees, and the inter-distance is $d = \lambda/4$.

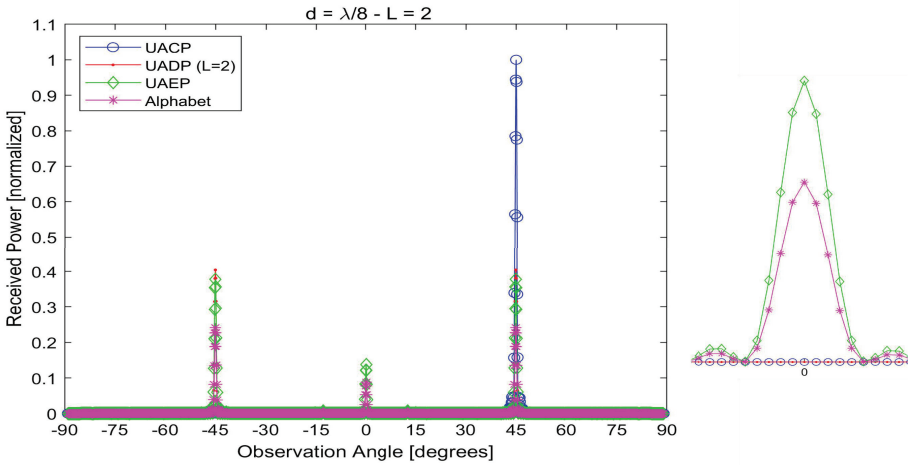

Figure 3.58: Received power as a function of the angle of observation. The RIS alphabet is [10] ($f = 33$ GHz), the desired angle of reflection is 45 degrees, and the inter-distance is $d = \lambda/8$.

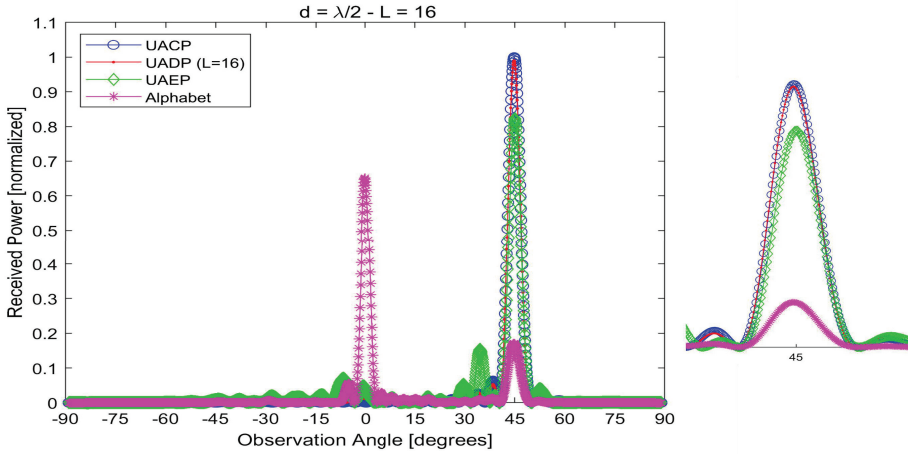

Figure 3.59: Received power as a function of the angle of observation. The RIS alphabet is [11], the desired angle of reflection is 45 degrees, and the inter-distance is $d = \lambda/2$.

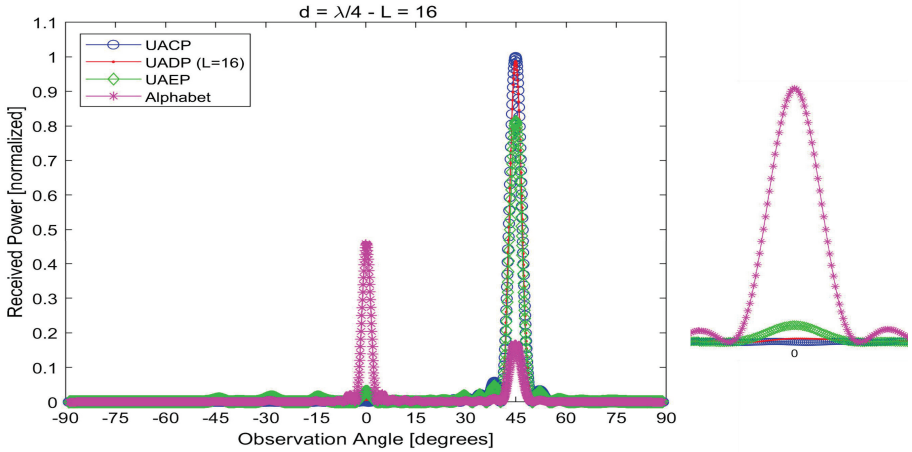

Figure 3.60: Received power as a function of the angle of observation. The RIS alphabet is [11], the desired angle of reflection is 45 degrees, and the inter-distance is $d = \lambda/4$.

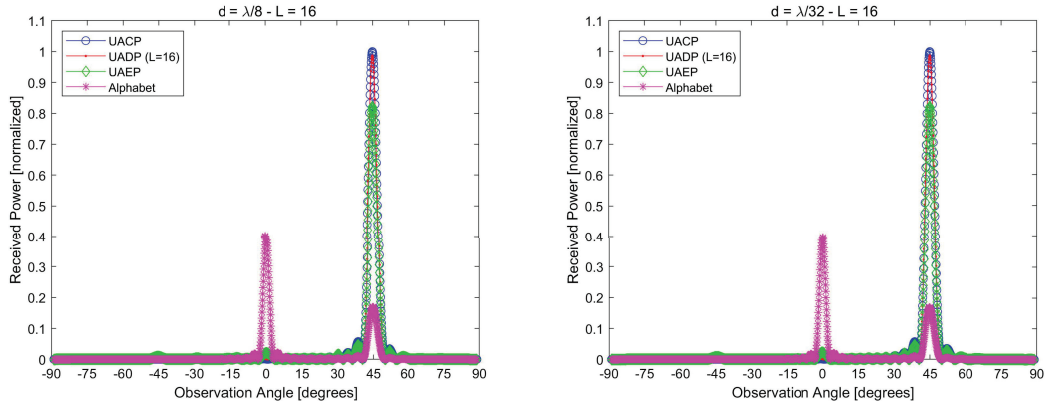

Figure 3.61: Received power as a function of the angle of observation. The RIS alphabet is [11], the desired angle of reflection is 45 degrees, and the inter-distance is $d = \lambda/8$ and $d = \lambda/32$.

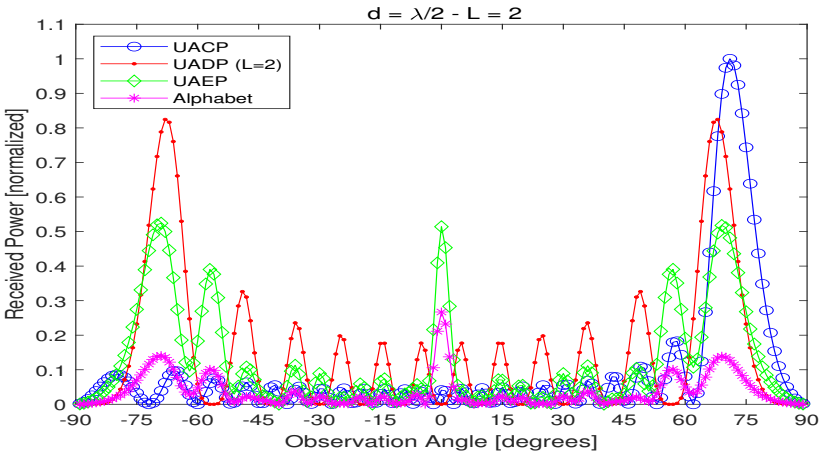

Figure 3.62: Received power as a function of the angle of observation. The RIS alphabet is [9], the desired angle of reflection is 75 degrees, and the inter-distance is $d = \lambda/2$.

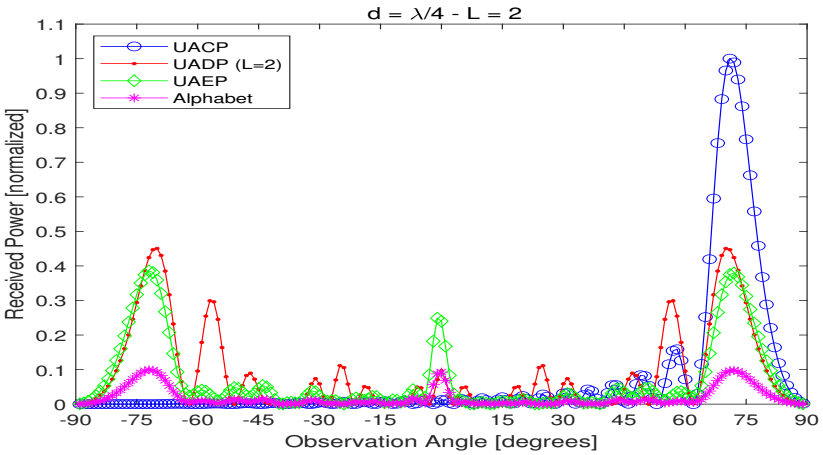

Figure 3.63: Received power as a function of the angle of observation. The RIS alphabet is [9], the desired angle of reflection is 75 degrees, and the inter-distance is $d = \lambda/4$.

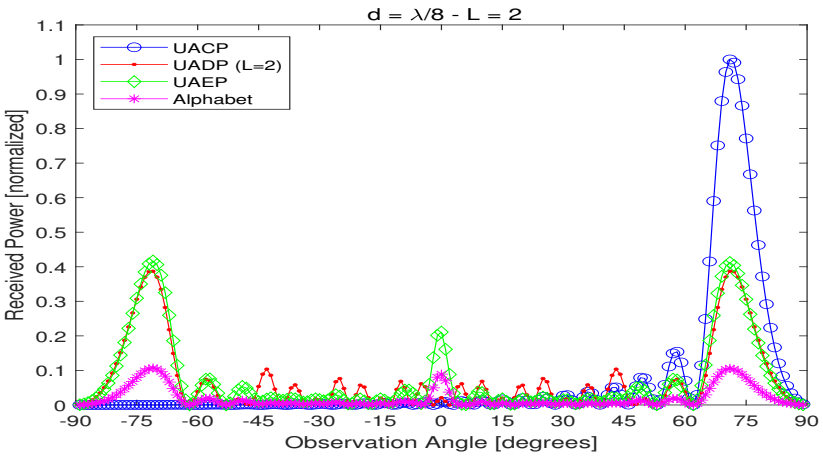

Figure 3.64: Received power as a function of the angle of observation. The RIS alphabet is [9], the desired angle of reflection is 75 degrees, and the inter-distance is $d = \lambda/8$.

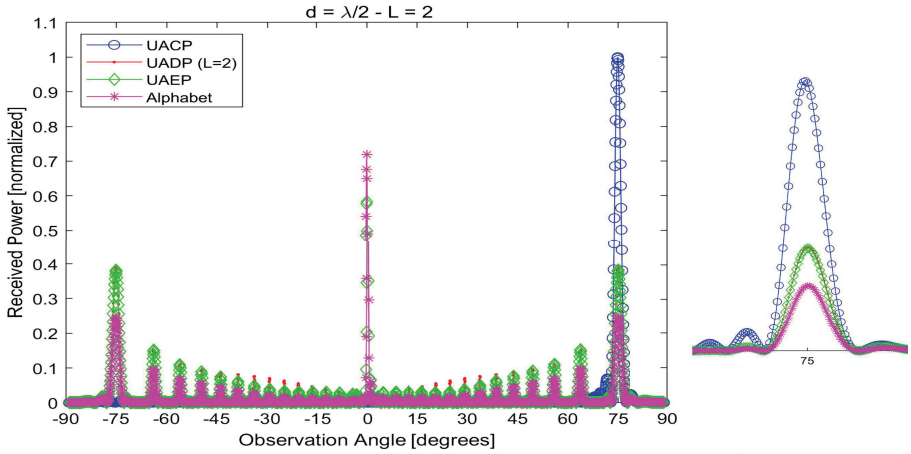

Figure 3.65: Received power as a function of the angle of observation. The RIS alphabet is [10] ($f = 27$ GHz), the desired angle of reflection is 75 degrees, and the inter-distance is $d = \lambda/2$.

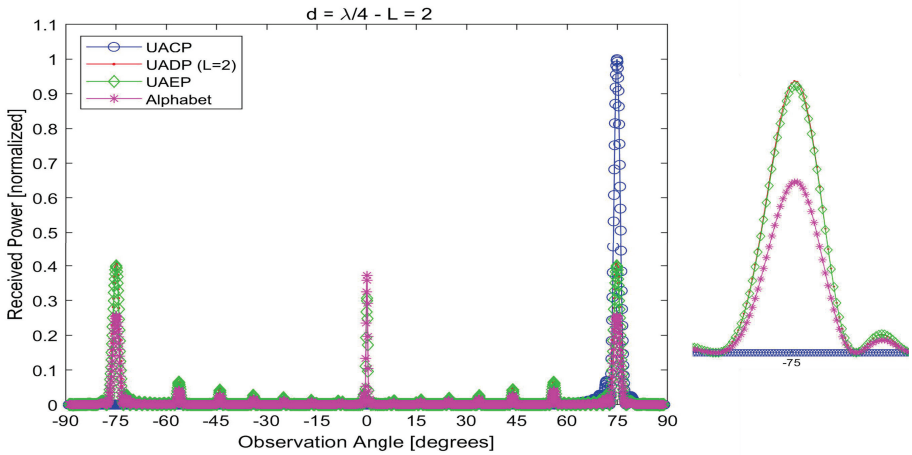

Figure 3.66: Received power as a function of the angle of observation. The RIS alphabet is [10] ($f = 27$ GHz), the desired angle of reflection is 75 degrees, and the inter-distance is $d = \lambda/4$.

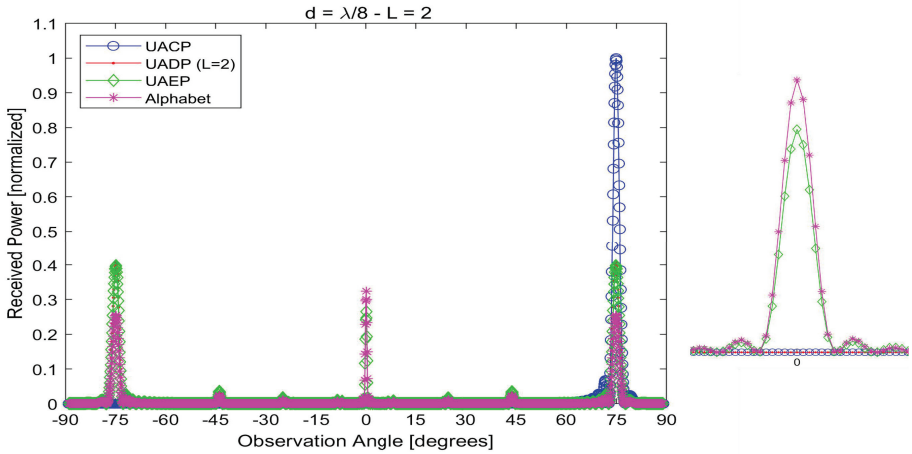

Figure 3.67: Received power as a function of the angle of observation. The RIS alphabet is [10] ($f = 27$ GHz), the desired angle of reflection is 75 degrees, and the inter-distance is $d = \lambda/8$.

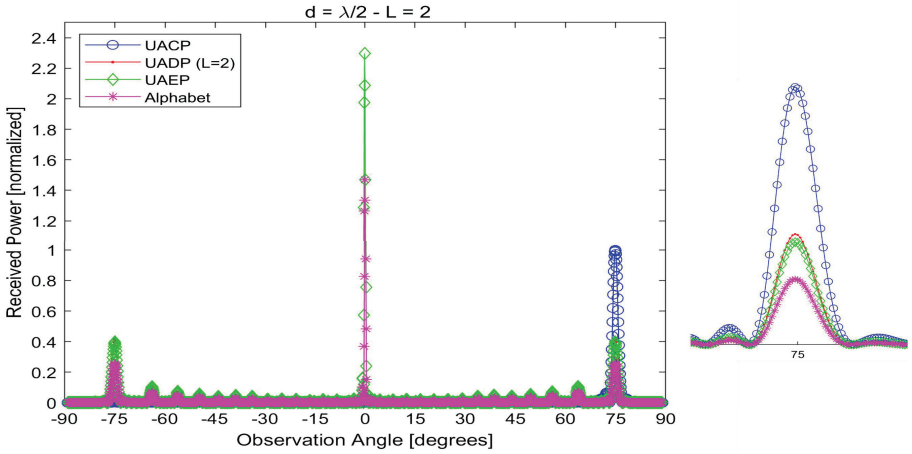

Figure 3.68: Received power as a function of the angle of observation. The RIS alphabet is [10] ($f = 33$ GHz), the desired angle of reflection is 75 degrees, and the inter-distance is $d = \lambda/2$.

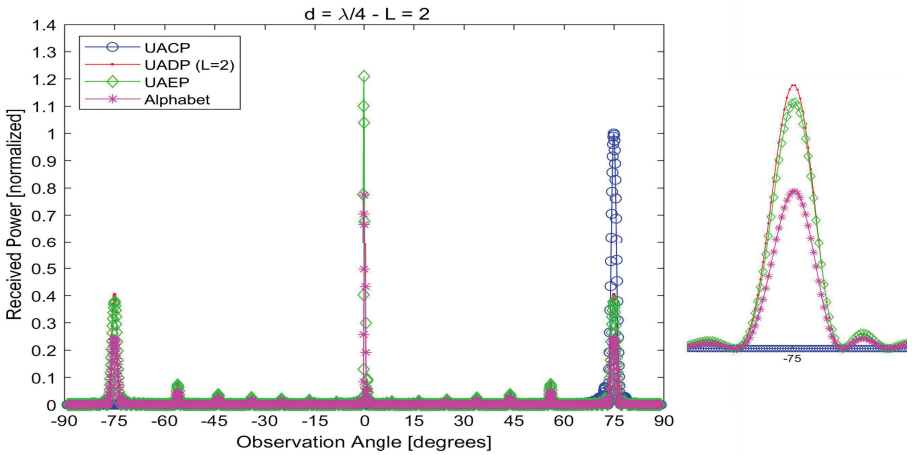

Figure 3.69: Received power as a function of the angle of observation. The RIS alphabet is [10] ($f = 33$ GHz), the desired angle of reflection is 75 degrees, and the inter-distance is $d = \lambda/4$.

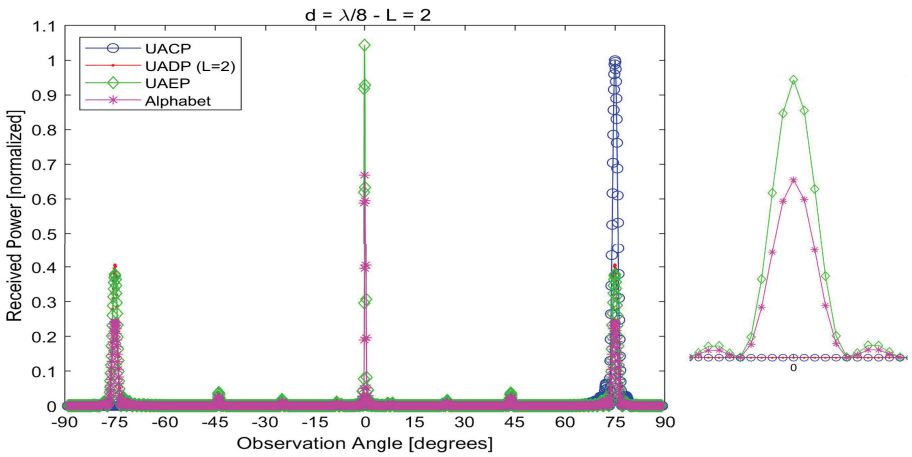

Figure 3.70: Received power as a function of the angle of observation. The RIS alphabet is [10] ($f = 33$ GHz), the desired angle of reflection is 75 degrees, and the inter-distance is $d = \lambda/8$.

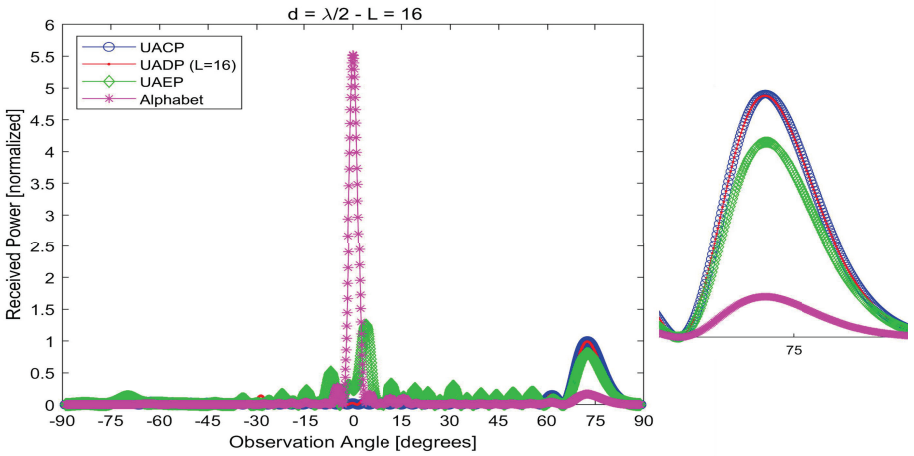

Figure 3.71: Received power as a function of the angle of observation. The RIS alphabet is [11], the desired angle of reflection is 75 degrees, and the inter-distance is $d = \lambda/2$.

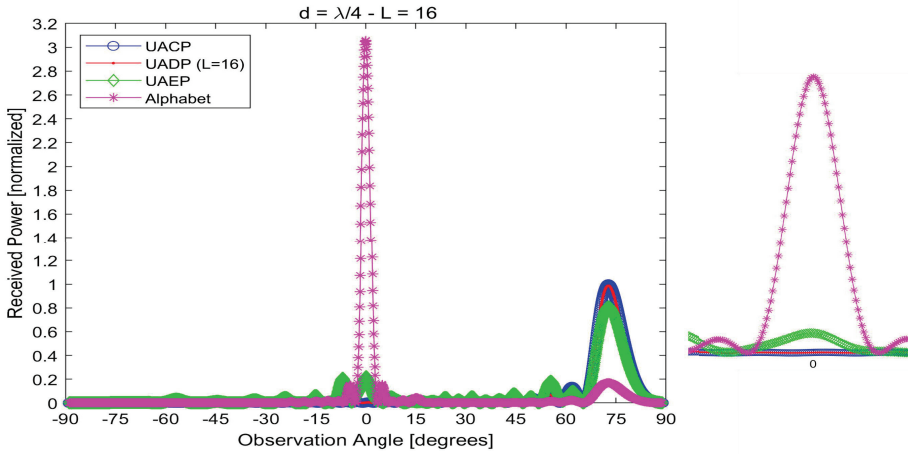

Figure 3.72: Received power as a function of the angle of observation. The RIS alphabet is [11], the desired angle of reflection is 75 degrees, and the inter-distance is $d = \lambda/4$.

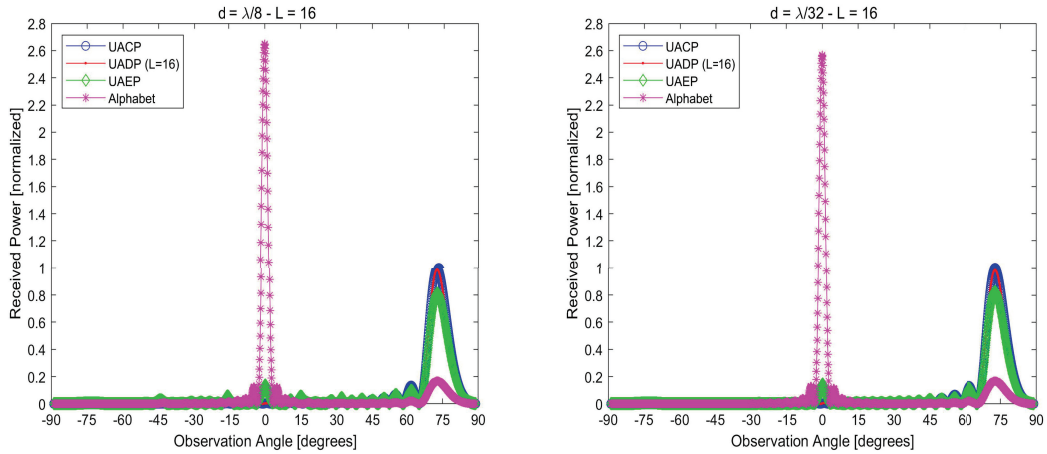

Figure 3.73: Received power as a function of the angle of observation. The RIS alphabet is [11], the desired angle of reflection is 75 degrees, and the inter-distance is $d = \lambda/8$ and $d = \lambda/32$.

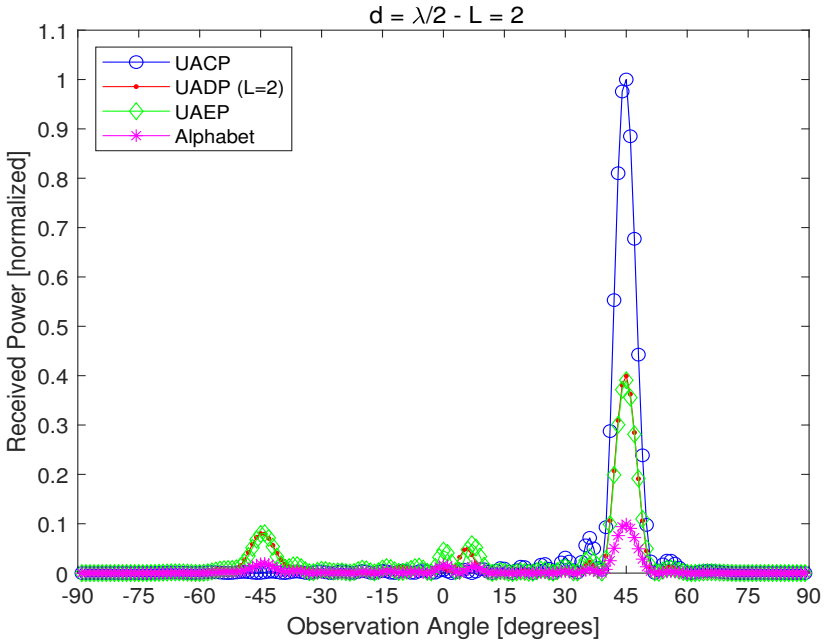

Figure 3.74: Received power as a function of the angle of observation (near-field case with the receiver located 5 meters far from the RIS). The RIS alphabet is [9], the desired angle of reflection is 45 degrees, and the inter-distance is $d = \lambda/2$.

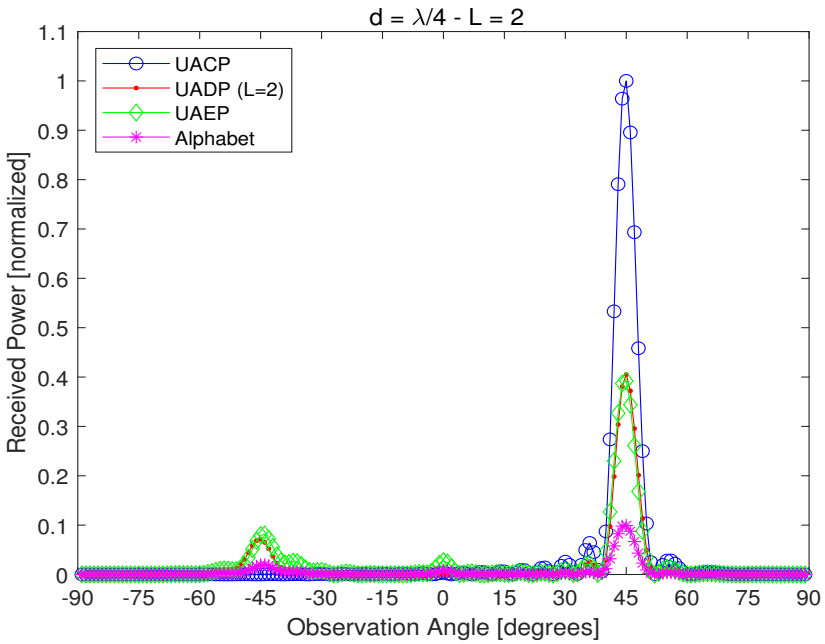

Figure 3.75: Received power as a function of the angle of observation (near-field case with the receiver located 5 meters far from the RIS). The RIS alphabet is [9], the desired angle of reflection is 45 degrees, and the inter-distance is $d = \lambda/4$.

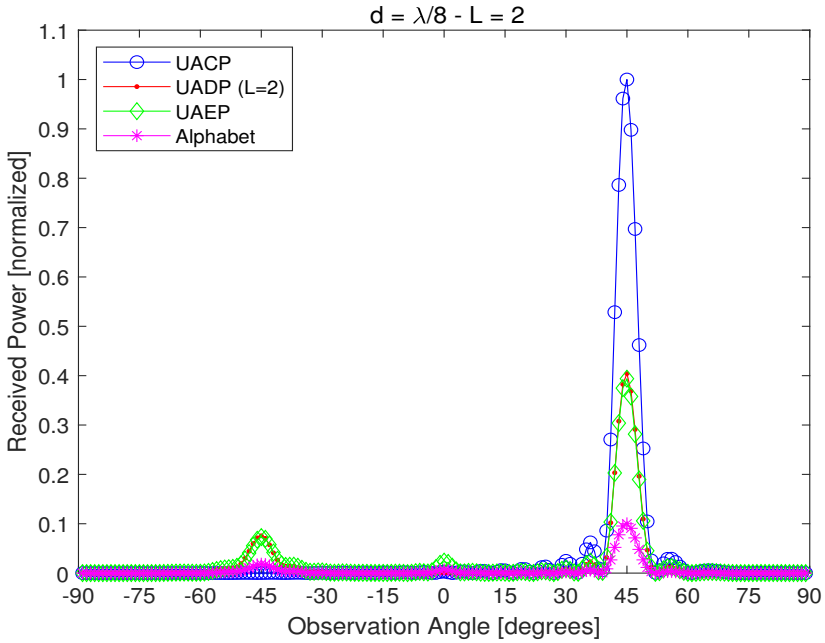

Figure 3.76: Received power as a function of the angle of observation (near-field case with the receiver located 5 meters far from the RIS). The RIS alphabet is [9], the desired angle of reflection is 45 degrees, and the inter-distance is $d = \lambda/8$.

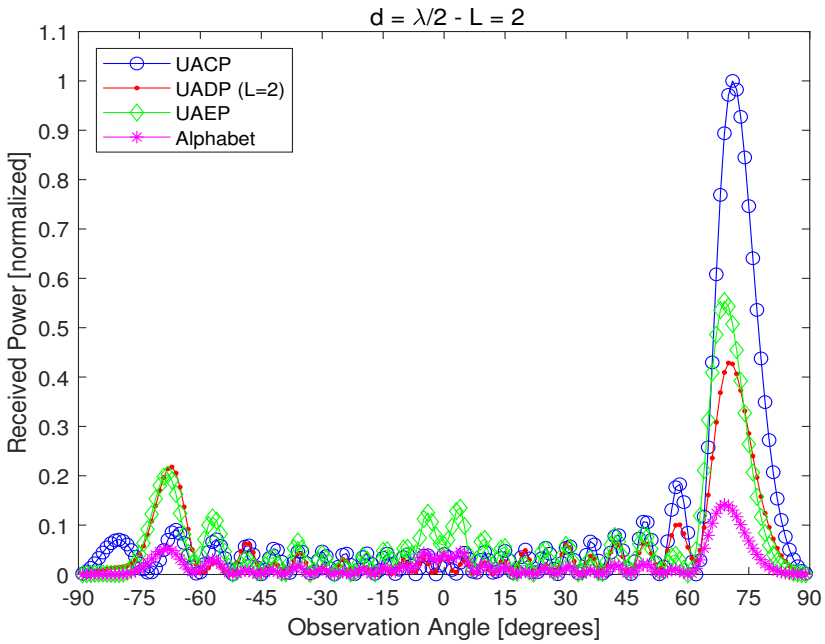

Figure 3.77: Received power as a function of the angle of observation (near-field case with the receiver located 5 meters far from the RIS). The RIS alphabet is [9], the desired angle of reflection is 75 degrees, and the inter-distance is $d = \lambda/2$.

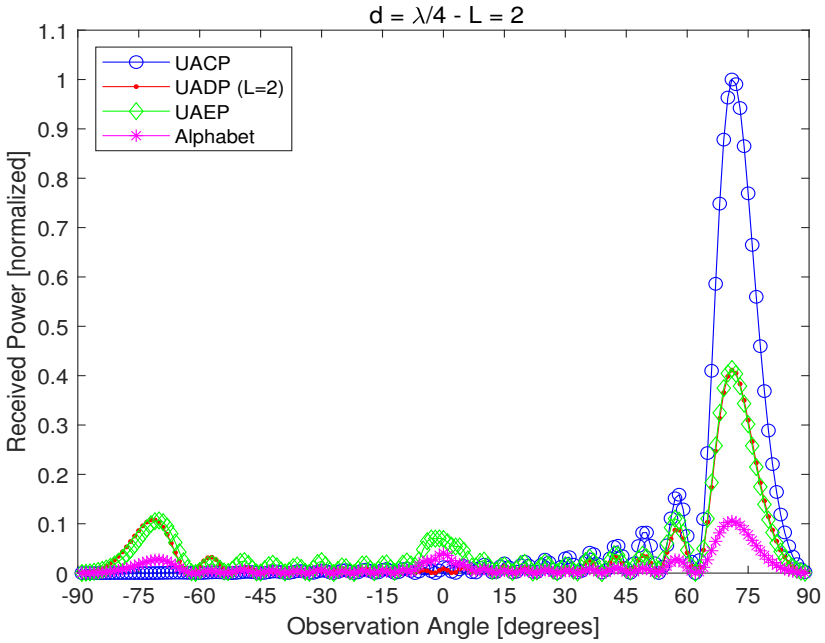

Figure 3.78: Received power as a function of the angle of observation (near-field case with the receiver located 5 meters far from the RIS). The RIS alphabet is [9], the desired angle of reflection is 75 degrees, and the inter-distance is $d = \lambda/4$.

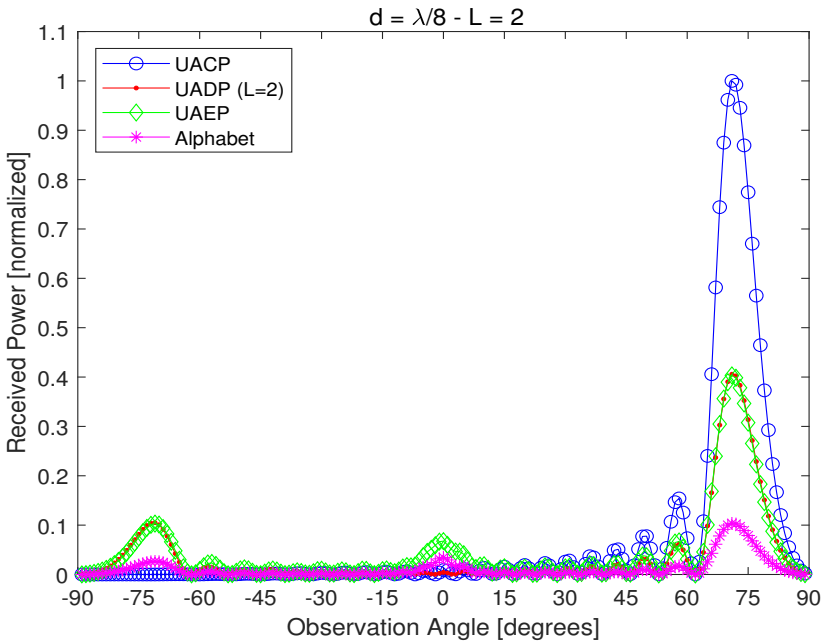

Figure 3.79: Received power as a function of the angle of observation (near-field case with the receiver located 5 meters far from the RIS). The RIS alphabet is [9], the desired angle of reflection is 75 degrees, and the inter-distance is $d = \lambda/8$.

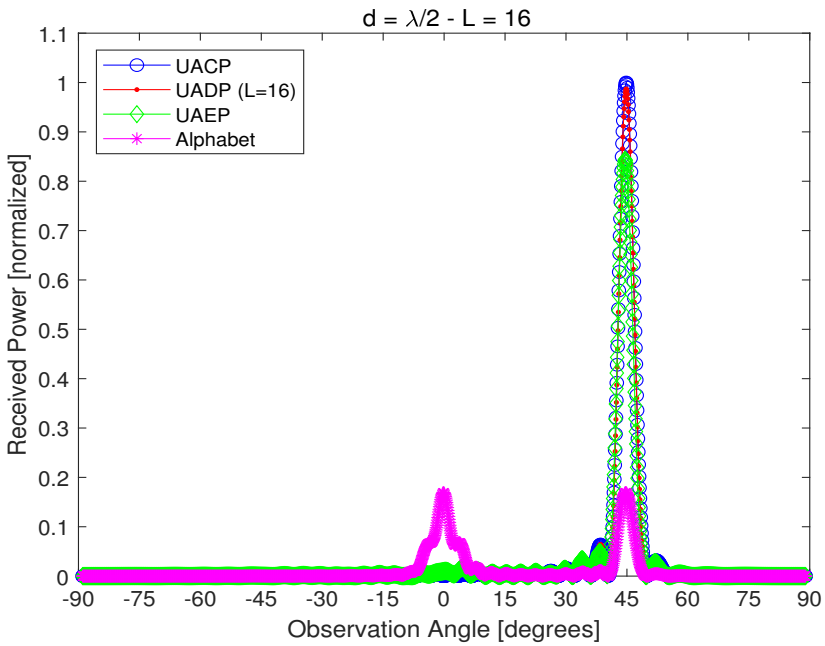

Figure 3.80: Received power as a function of the angle of observation (near-field case with the receiver located 5 meters far from the RIS). The RIS alphabet is [11], the desired angle of reflection is 45 degrees, and the inter-distance is $d = \lambda/2$.

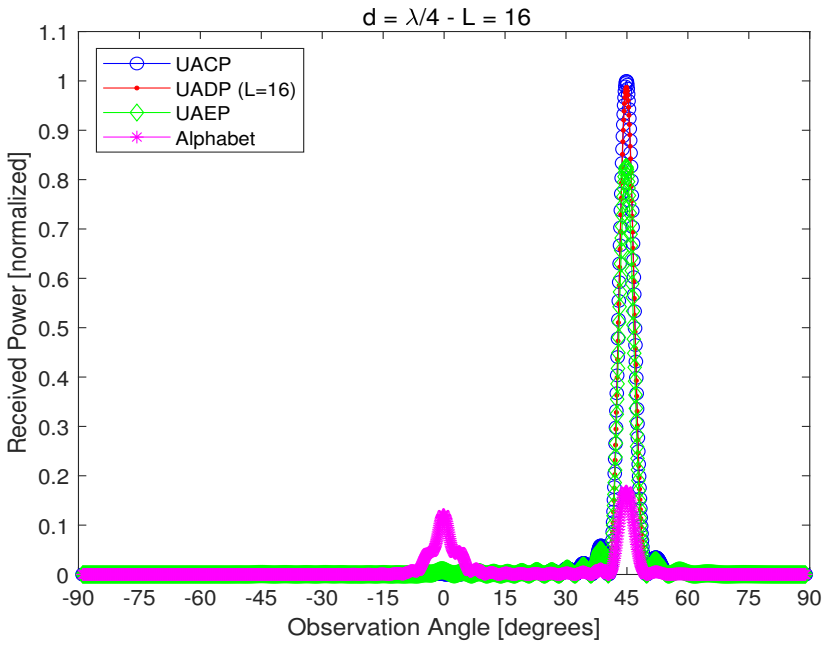

Figure 3.81: Received power as a function of the angle of observation (near-field case with the receiver located 5 meters far from the RIS). The RIS alphabet is [11], the desired angle of reflection is 45 degrees, and the inter-distance is $d = \lambda/4$.

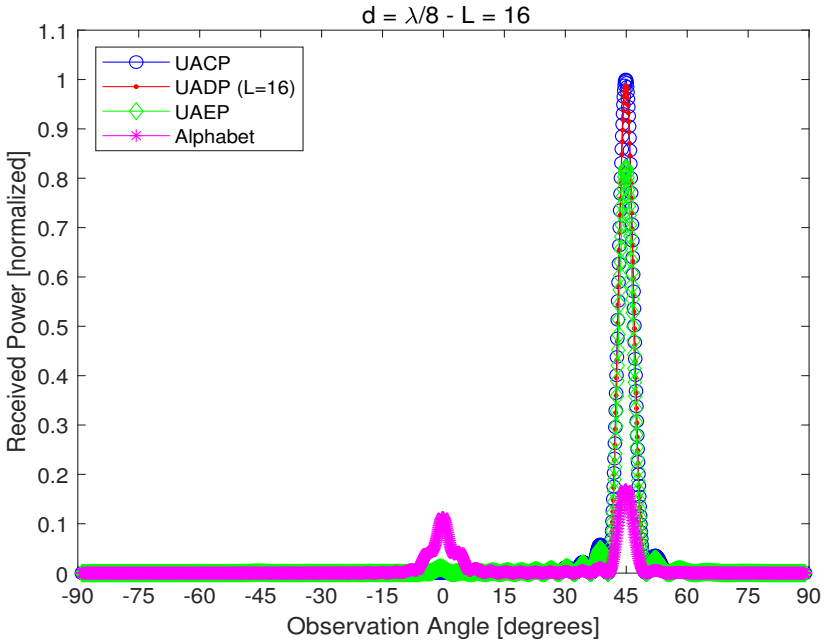

Figure 3.82: Received power as a function of the angle of observation (near-field case with the receiver located 5 meters far from the RIS). The RIS alphabet is [11], the desired angle of reflection is 45 degrees, and the inter-distance is $d = \lambda/8$.

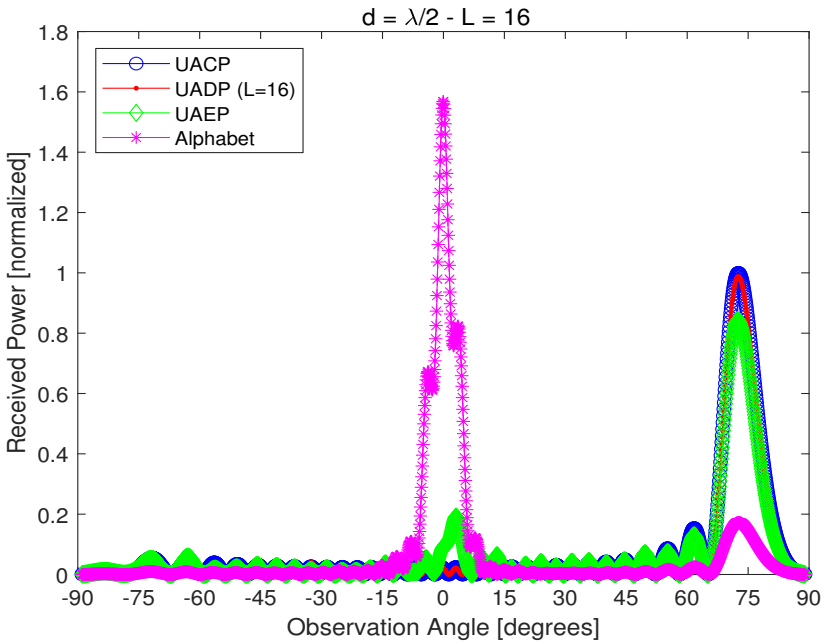

Figure 3.83: Received power as a function of the angle of observation (near-field case with the receiver located 5 meters far from the RIS). The RIS alphabet is [11], the desired angle of reflection is 75 degrees, and the inter-distance is $d = \lambda/2$.

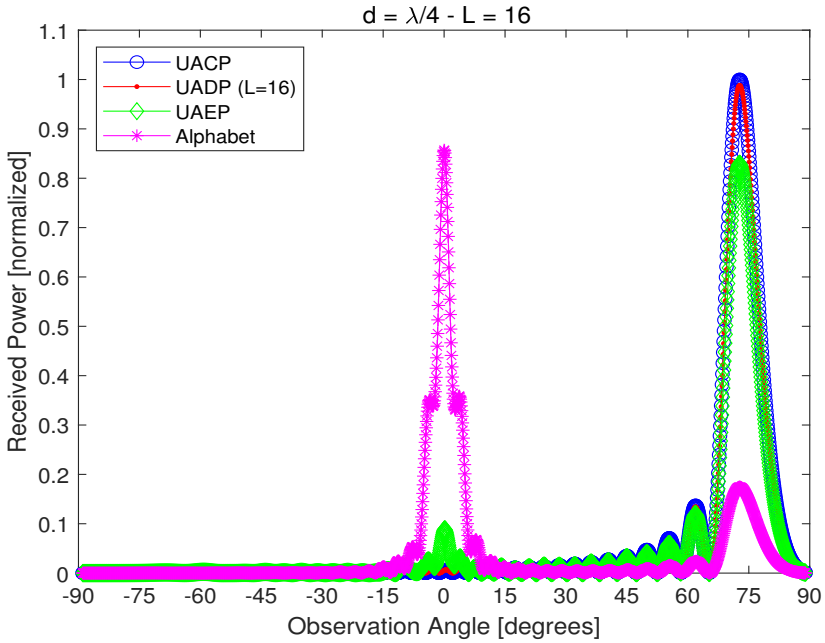

Figure 3.84: Received power as a function of the angle of observation (near-field case with the receiver located 5 meters far from the RIS). The RIS alphabet is [11], the desired angle of reflection is 75 degrees, and the inter-distance is $d = \lambda/4$.

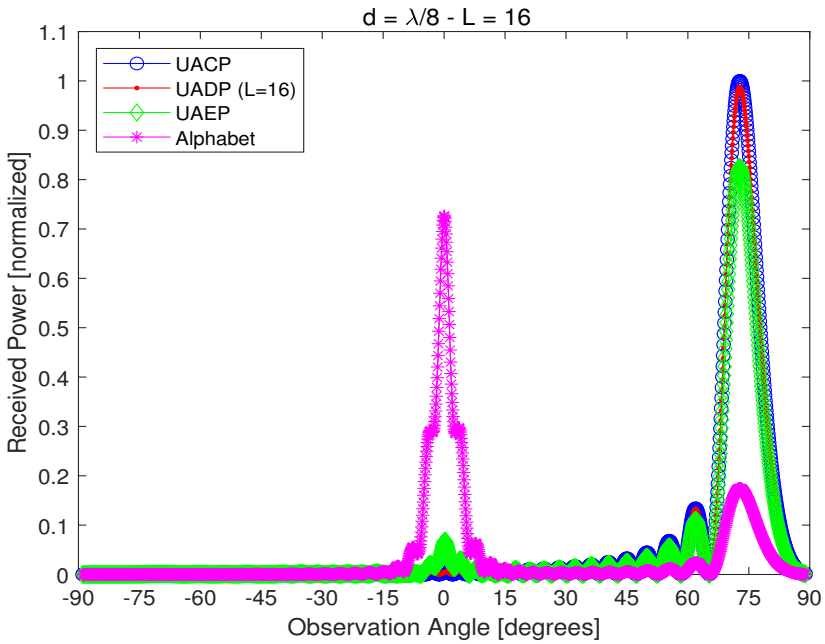

Figure 3.85: Received power as a function of the angle of observation (near-field case with the receiver located 5 meters far from the RIS). The RIS alphabet is [11], the desired angle of reflection is 75 degrees, and the inter-distance is $d = \lambda/8$.

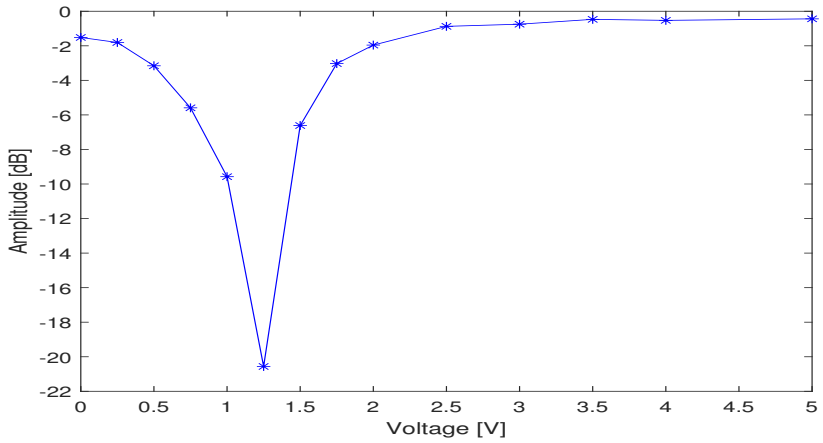

Figure 3.86: Amplitude of the RIS alphabet in Table 3.2.

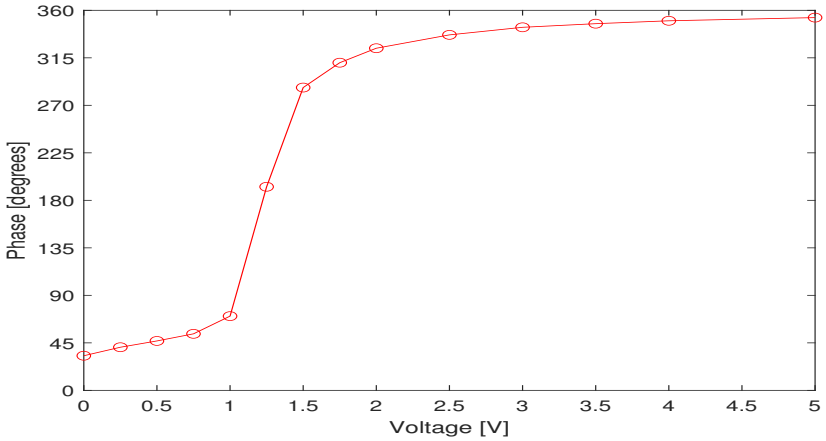

Figure 3.87: Phase of the RIS alphabet in Table 3.2.

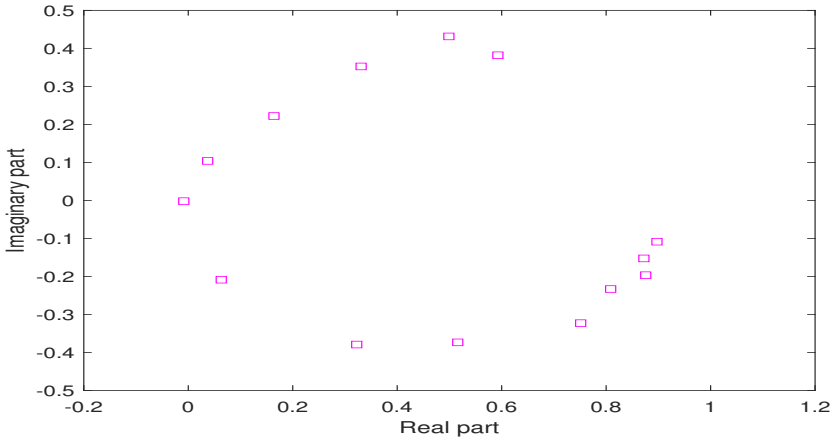

Figure 3.88: Representation in the complex plane of the RIS alphabet in Table 3.2.

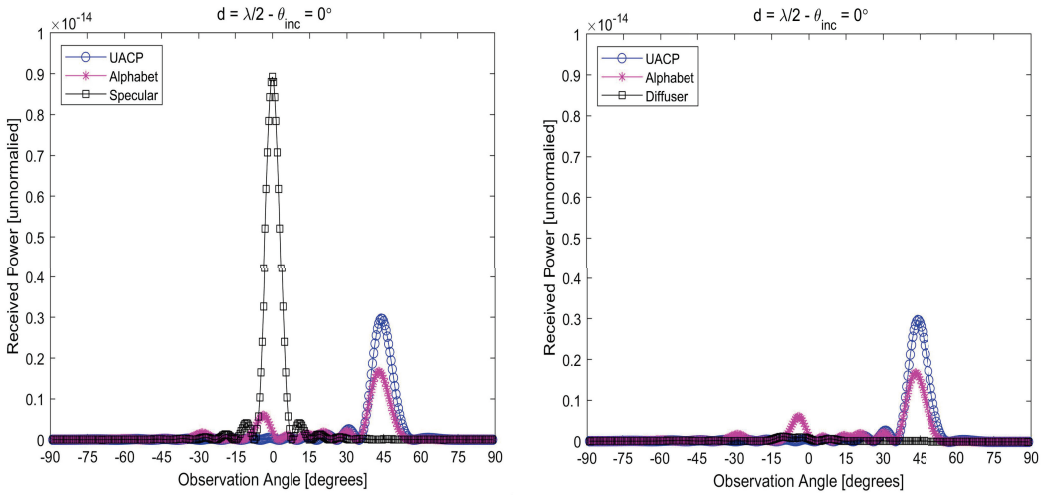

Figure 3.89: Received power as a function of the angle of observation (intended user). The RIS alphabet is [8], the desired angle of reflection is 45 degrees, and the inter-distance is $d = \lambda/2$.

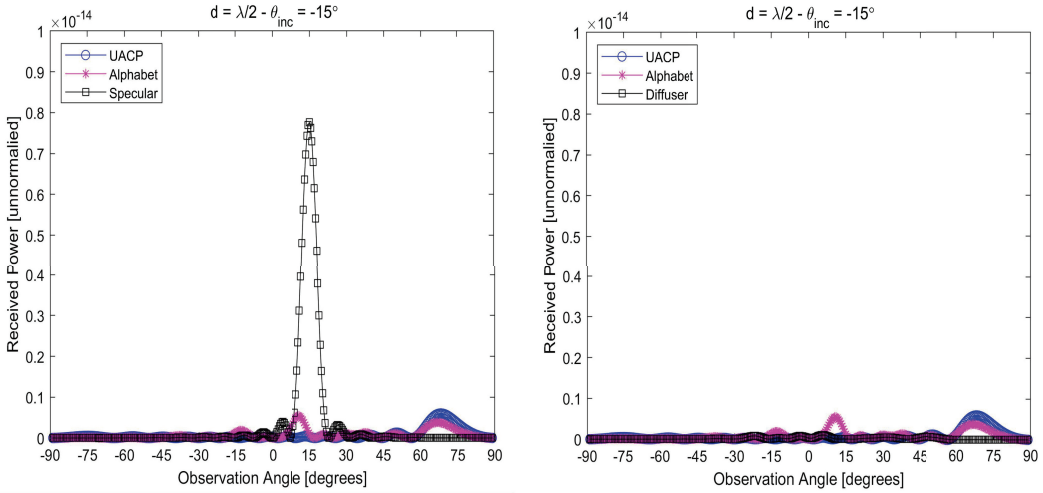

Figure 3.90: Received power as a function of the angle of observation (interferer at $\theta_{\text{inc}} = -15$ degrees). The RIS alphabet is [8], the desired angle of reflection is 45 degrees, and the inter-distance is $d = \lambda/2$.

3.5 Conclusions

In this chapter, we have reported a comprehensive numerical study of the reradiation properties of RISs that are modeled as digital metasurfaces. The considered RISs are characterized by realistic alphabets that are obtained from full-wave simulations and from existing experimental testbeds at different operating frequencies. We have shown that the size and the inter-distance between the RIS reconfigurable elements, and the quantization of the amplitudes and phases of the reflection coefficients both determine the quality of the reradiated pattern. More specifically, it is usually convenient to design an RIS with an inter-distance and a size of the RIS reconfigurable elements smaller than half of the wavelength if the reflection

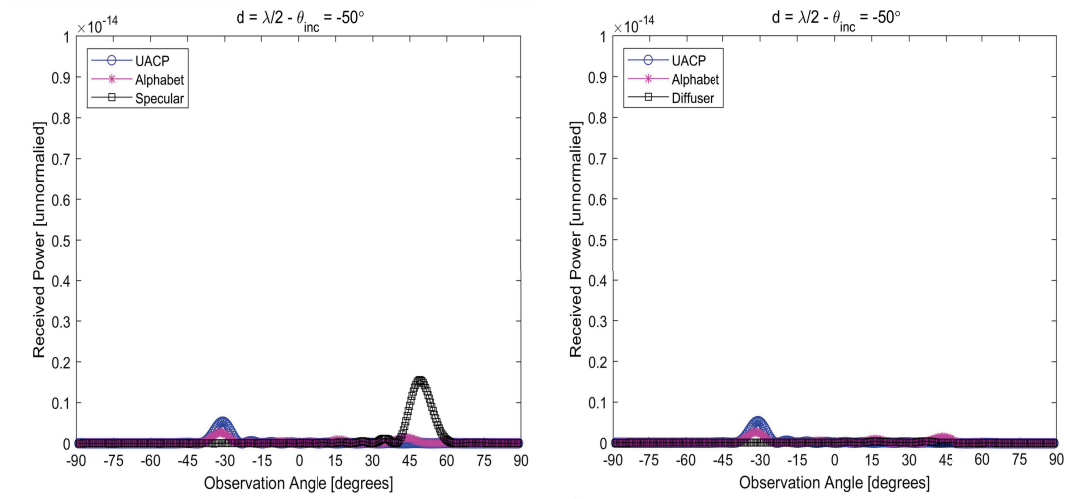

Figure 3.91: Received power as a function of the angle of observation (interferer at $\theta_{\text{inc}} = -50$ degrees). The RIS alphabet is [8], the desired angle of reflection is 45 degrees, and the inter-distance is $d = \lambda/2$.

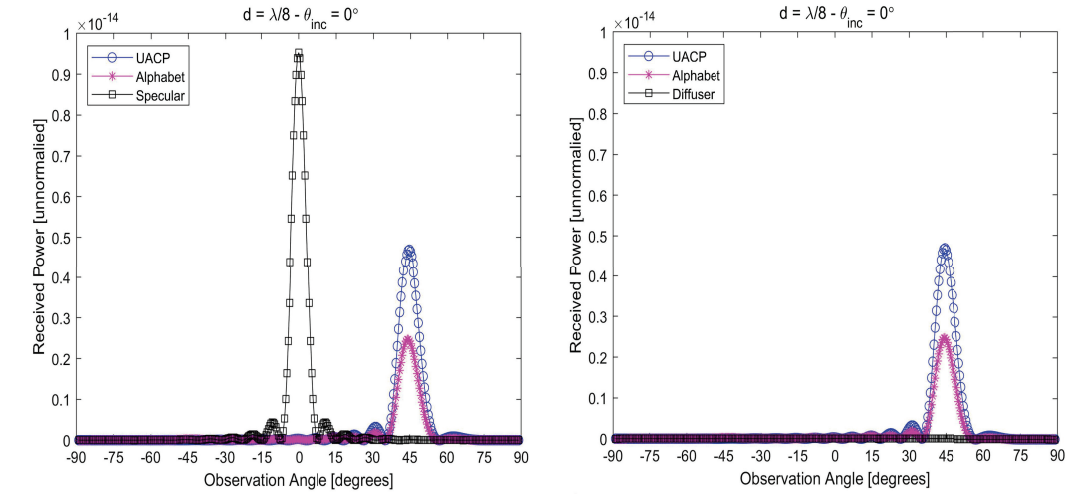

Figure 3.92: Received power as a function of the angle of observation (intended user). The RIS alphabet is [8], the desired angle of reflection is 45 degrees, and the inter-distance is $d = \lambda/8$.

coefficients cannot be continuously adjusted. If the reflection coefficients can be continuously adjusted, on the other hand, the advantage of using sub-wavelength RISs may be negligible in the considered case studies of RISs optimized according to a locally optimum design criterion. The use of binary RIS usually results in the presence of strong unwanted beams towards the direction that is symmetric with respect to the nominal direction of reradiation. This effect is, however, less evident in the near-field region of the RIS. Similarly, RISs that are characterized by alphabets in which the amplitude and the phase are not independent of each other and in which there are strong variations of the amplitude with the phase may result in strong reradiated beams towards other directions. The considered example has revealed the presence of a

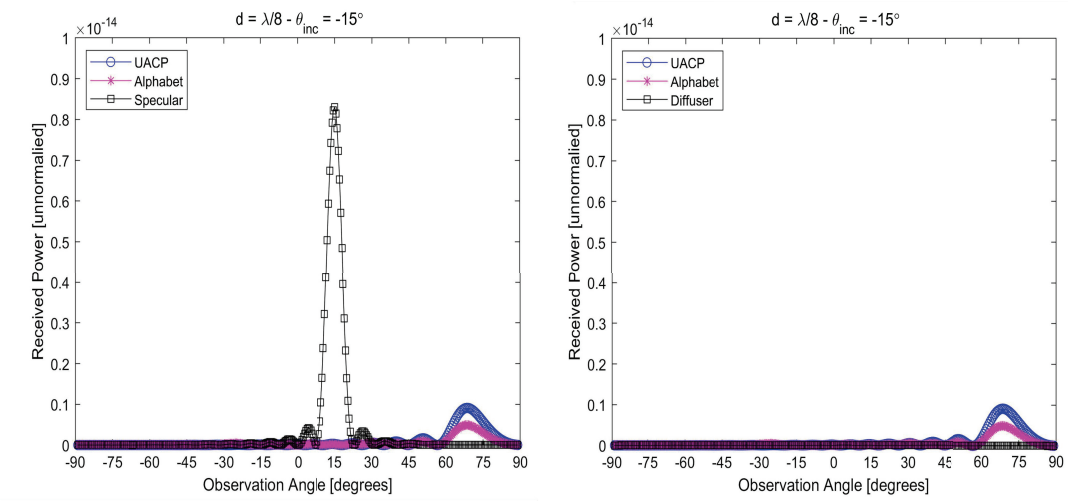

Figure 3.93: Received power as a function of the angle of observation (interferer at $\theta_{\text{inc}} = -15$ degrees). The RIS alphabet is [8], the desired angle of reflection is 45 degrees, and the inter-distance is $d = \lambda/8$.

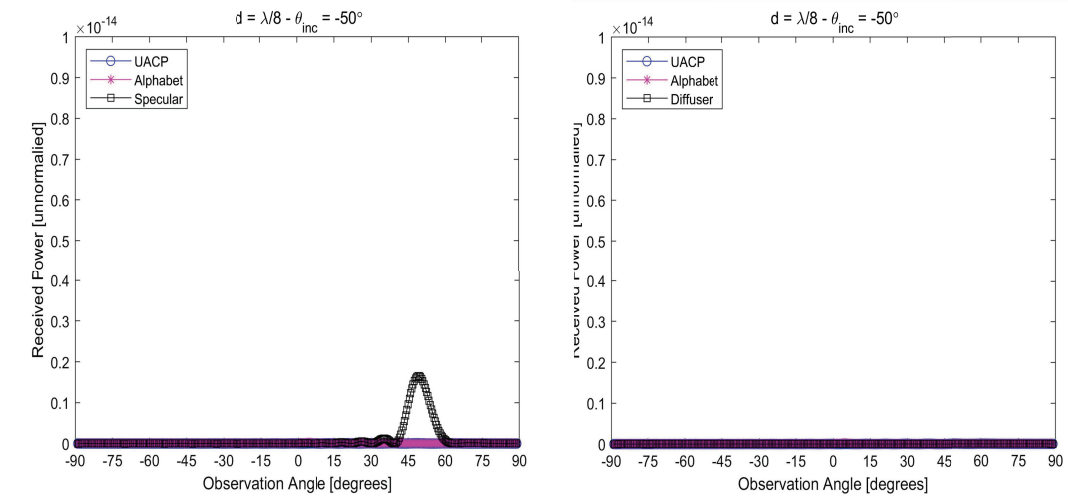

Figure 3.94: Received power as a function of the angle of observation (interferer at $\theta_{\text{inc}} = -50$ degrees). The RIS alphabet is [8], the desired angle of reflection is 45 degrees, and the inter-distance is $d = \lambda/8$.

strong specular reflection. Furthermore, we have shown that the main peak of the reradiated pattern may not be perfectly steered towards the nominal direction of reradiation for large angles of deflection. Finally, we have analyzed the reradiation characteristics of RISs in the presence of electromagnetic interference, and have shown that an RIS inherently filters out the interference towards the desired direction of reradiation, provided that the interfering electromagnetic waves originate from directions that are sufficiently different from the direction of incidence of the intended user. However, the interfering electromagnetic waves may be steered towards other directions, and, therefore, their impact needs to be accounted for in

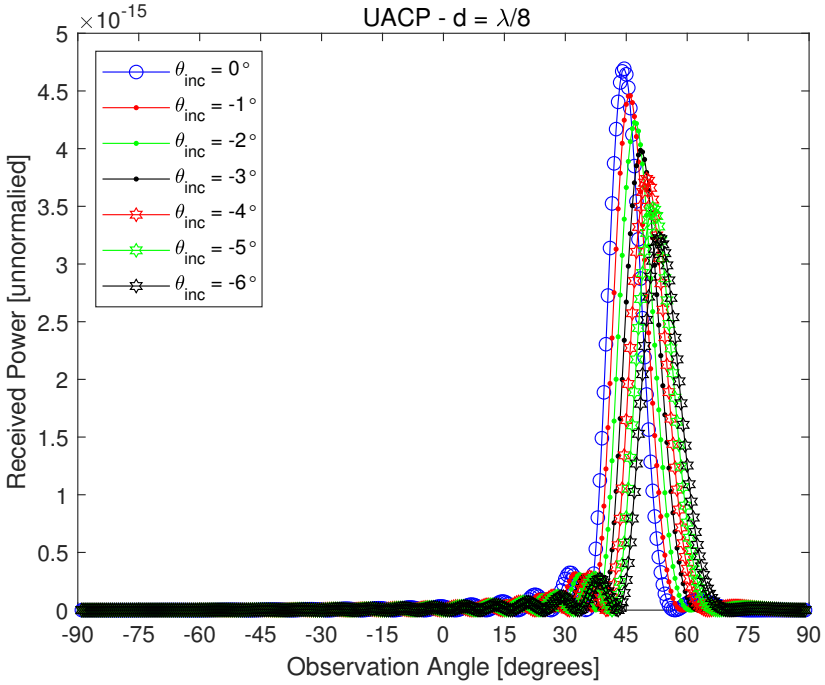

Figure 3.95: Received power as a function of the angle of observation (intended user and interferer from $\theta_{\text{inc}} = -6$ to $\theta_{\text{inc}} = -1$ degrees). The RIS alphabet is UACP, the desired angle of reflection is 45 degrees, and the inter-distance is $d = \lambda/8$.

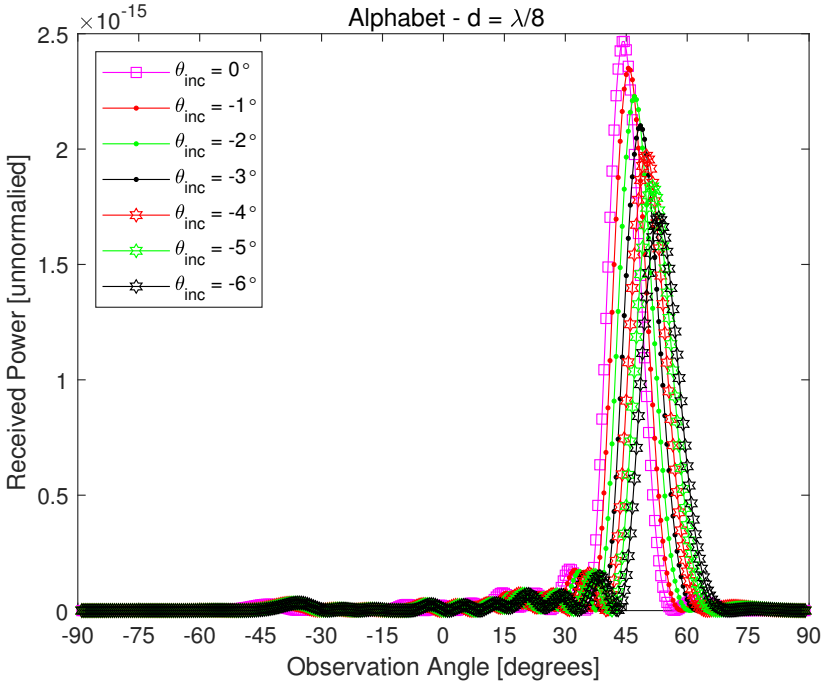

Figure 3.96: Received power as a function of the angle of observation (intended user and interferer from $\theta_{\text{inc}} = -6$ to $\theta_{\text{inc}} = -1$ degrees). The RIS alphabet is [8], the desired angle of reflection is 45 degrees, and the inter-distance is $d = \lambda/8$.

the context of network-level studies.

In summary, the study conducted in this chapter allows us to conclude that RISs have so far been designed to maximize some objective functions for specific user locations. However, the presence of reradiated beams towards directions different from the nominal ones and the impact of interfering signals have usually been ignored at the design stage. Implementation constraints, such as the need of using quantized reflection coefficients or the inherent interplay between the phase and the amplitude of the reflection coefficients, may result in unwanted reradiated beams and interfering signals that need to be kept under control at the design stage. It is therefore important to optimize an RIS by taking into account the entire reradiation pattern. If large angles of deflection need to be realized, non-local design criteria may need to be applied in order to ensure that the reradiated beam is directed towards the desired direction of reradiation.

4 Bi-objective Optimization of Information Rate and Harvested Power in RIS-aided SWIPT Systems

Chapter 4. Bi-objective Optimization of Information Rate and Harvested Power in RIS-aided SWIPT Systems

In this chapter, the problem of simultaneously optimizing the information rate and the harvested power in a reconfigurable intelligent surface (RIS)-aided multiple-input single-output downlink wireless network with simultaneous wireless information and power transfer (SWIPT) is addressed. The beamforming vectors, RIS reflection coefficients, and power split ratios are jointly optimized subject to maximum power constraints, minimum harvested power constraints, and realistic constraints on the RIS reflection coefficients. A practical algorithm is developed through an interplay of alternating optimization, sequential optimization, and pricing-based methods. Numerical results show that the deployment of RISs can significantly improve the information rate and the amount of harvested power.

This chapter is organized as follows. In *Section 4.1*, we introduce the background of RIS-aided SWIPT Systems, the related works to our work and our contribution. The system model and Problem formulation are introduced in *Section 4.2*. In *Section 4.3*, we provide an iterative algorithm for solving the optimization problem. In *Section 4.4*, numerical results are illustrated in order to quantitatively compare the impact of different network design parameters that are presented in the previous sections; besides, the computational complexity of the proposed algorithm is discussed. Finally, *Section 4.5* concludes this chapter.

4.1 Introduction

Reconfigurable Intelligent Surfaces (RISs) have emerged as a promising technology for sustainable sixth-generation (6G) networks [132, 14]. Thanks to their ability of reflecting and refracting electromagnetic signals in a reconfigurable fashion and with limited energy requirements, RISs can drastically reduce the energy consumptions in wireless networks[18]. In this context, RISs have also been studied in conjunction with simultaneous wireless information and power transfer (SWIPT), which is another key technology to improve the energy sustainability of future wireless networks.

Several studies show that the deployment of RISs can improve both the information and power transfer. In [133], the problem of transmit power minimization subject to quality of service (QoS) constraints and minimum energy harvesting requirements is addressed. The optimization problem is tackled by means of a penalty-based algorithm coupled with the alternating optimization technique. In [134], the problem of transmit power minimization for an RIS-assisted SWIPT non-orthogonal multiple-access (NOMA) network is investigated. A two-stage optimization algorithm is proposed to jointly optimize the transmit beamforming vector, the power-split ratio, and the RIS phase shifts under QoS constraints. Semidefinite relaxation coupled with alternating and sequential optimization methods are employed. In [135], the problem of maximizing the weighted sum-rate is investigated in a SWIPT-based multi-user multiple-input multiple-output (MIMO) downlink system, subject to minimum harvested energy constraints. Alternating optimization is used in conjunction with sequential optimization and pricing methods. In [136], the authors study the problem of resource allocation in RIS-aided SWIPT-based systems, in which a large RIS is split into several tiles that are designed for reducing the computational complexity. A globally optimal algorithm and a practical approach are developed by means of branch-and-bound and sequential methods. In [137], the trade-off between sum-rate maximization and total harvested power is investigated. The $\epsilon-$method coupled with alternating optimization is used to tackle the resulting multi-objective problem. In [138], the data rate maximization problem in an RIS-aided system in which multiple receivers perform information decoding and wireless power reception is analyzed. The problem is tackled by alternating optimization, sequential optimization, and sub-gradient searches.

This work considers a network in which a multiple-antenna access point (AP) serves single-antenna users with the aid of an RIS. Each receiver jointly performs information decoding and wireless power harvesting by means of power splitting. Unlike previous works, the following contributions are made.

1) We consider the novel bi-objective simultaneous maximization of the information rate and harvested power, subject to minimum downlink rate, minimum harvested power, and maximum transmit power constraints. The resulting non-convex problem is tackled by an interplay of alternating maximization, sequential optimization, and penalty-based methods. Since the receivers perform both information decoding and wireless power harvesting, the

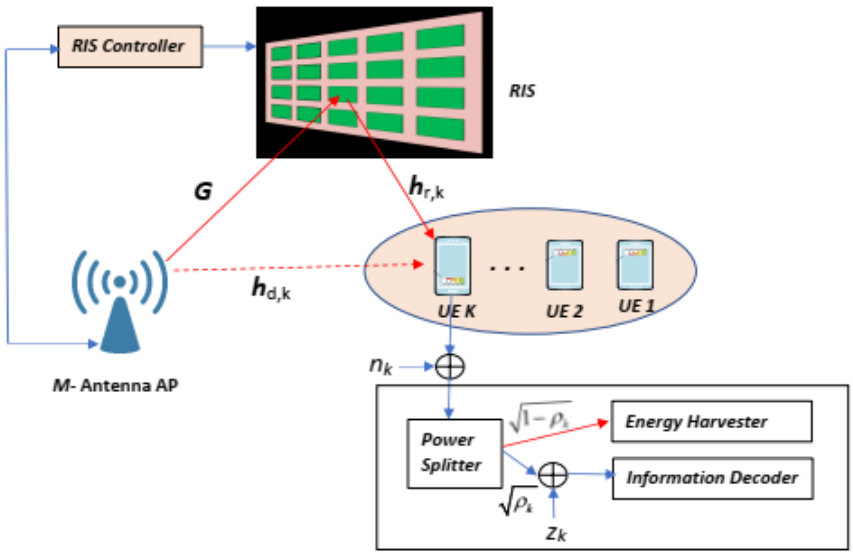

Figure 4.1: Illustration of the MISO RIS-assisted SWIPT system model.

optimization of the power split ratio is needed, which is a novel feature compared to most related works on RIS-aided and SWIPT-based systems.

2) We consider the realistic case in which the phases and moduli of the RIS reflection coefficients are not independent of one another, but are coupled by a deterministic function. This further complicates the scenario, making it challenging to find performing resource allocations at an affordable complexity.

3) Numerical results confirm the effectiveness of the proposed algorithm compared to traditional approaches. It is found, in particular, that increasing the number of RIS elements allows harvesting enough power, while at the same time supporting satisfactory sum-rate levels.

Among previous works, [137] and [138] are the most closely-related to our work. However, [137] investigates the rate and harvested energy trade-off for separated information and power receivers, i.e., each receiver performs either information decoding or wireless power harvesting. Also, independent phases and moduli are assumed for the RIS reflection coefficients. In addition, [138] considers integrated information and power receivers, but it focuses on maximizing only the information rate, without considering power harvesting and the relation between the phase and amplitude of the RIS reflection coefficients.

4.2 System Model and Problem Formulation

We consider an RIS-based multi-user multiple-input single-output (MISO) downlink indoor scenario in which an access point (AP) equipped with M antennas serves K single-antenna user equipment (UEs) employing SWIPT. The k-th UE employs a fraction ρ_k of the received

power for information decoding (ID), while the rest is used for power harvesting (PH). The channels from the AP to the RIS, from the AP to the k-th user, and from the RIS to the k-th user are denoted by $\mathbf{G} \in \mathbb{C}^{N\times M}$, $\mathbf{h}_{d,k} \in \mathbb{C}^{1\times M}$, and $\mathbf{h}_{r,k} \in \mathbb{C}^{1\times N}$, respectively, and are assumed to follow the Rician fading model. The reflection coefficient vector of the RIS is denoted by $\mathbf{v} = [v_1, ..., v_n] \in \mathbb{C}^{N\times 1}$, where $v_n = f_n(\theta_n)e^{j\theta_n}$ is the reflection coefficient of the n-th reflecting element of the RIS, with $-\pi \leq \theta_n \leq \pi$ and, e.g., $f_n(\theta_n) = f_{\min} + (1 - f_{\min})\left(\frac{\sin(\theta_n-\phi)+1}{2}\right)^{\alpha}$ is a function that relates the phase of the reflection coefficient to its modulus, where $f_{\min} \geqslant 0$, $\alpha \geqslant 0, \phi \geqslant 0$ are circuit implementation constants [139]. The proposed approach can be applied to any continuous and differentiable function $f_n(\theta_n)$. Given this notation and defining $\mathbf{H}_{r,k} = \text{diag}(\mathbf{h}_{\mathbf{r},\mathbf{k}})\mathbf{G}$, the sum-rate is:

$$R^{ID} = \sum_{k=1}^{K} \log\left(1 + \frac{\left|\left(\mathbf{h}_{d,k} + \mathbf{v}^H\mathbf{H}_{r,k}\right)\mathbf{w}_k\right|^2}{\sum\limits_{i=1,i\neq k}^{K}\left|\left(\mathbf{h}_{d,k}+\mathbf{v}^H\mathbf{H}_{r,k}\right)\mathbf{w}_i\right|^2+\sigma_k^2+\frac{\delta_k^2}{\rho_k}}\right) \tag{4.1}$$

wherein $\mathbf{w}_k \in \mathbb{C}^{M\times 1}$ is the transmit beamforming vector, and σ_k^2 and δ_k^2 model the power of the thermal noise and of the noise due to the conversion of the RF signal to the baseband. Furthermore, considering a linear harvesting model, the power harvested by the k-th UE is $P_{H,k} = \eta_k(1-\rho_k)\sum_{i=1}^{K}\left|(\mathbf{h}_{d,k} + \mathbf{v}^H\mathbf{H}_{r,k})\mathbf{w}_i\right|^2$, where $\eta_k \in [0,1]$ is the efficiency of the power harvesting circuit. Similar to [140], we consider the associated rate function:

$$R^{PH} = \sum_{k=1}^{K} \log\left(1 + \frac{\xi_k\eta_k(1-\rho_k)}{\sigma_k^2}\sum_{i=1}^{K}\left|(\mathbf{h}_{d,k} + \mathbf{v}^H\mathbf{H}_{r,k})\mathbf{w}_i\right|^2\right) \tag{4.2}$$

where $\xi_k \in [0,1]$ is the efficiency of the conversion from baseband power to RF power.

The goal of this work is to maximize a weighted sum of R^{ID} and R^{PH}, namely:

$$R_{sum}^{Eq}(\rho, \mathbf{w}, \mathbf{v}, \{\theta_n\}) = R^{ID} + \bar{\lambda}R^{PH} \tag{4.3}$$

where $\bar{\lambda}$ is a parameter to be tuned by the network operator according to the priorities granted to ID and PH [140].

Defining $\mathbf{h}_k = \mathbf{h}_{d,k} + \mathbf{v}^H\mathbf{H}_{r,k}$, the problem to be tackled in the rest of this work is formulated as:

$$\mathscr{P}_{\mathscr{A}}: \quad \max_{\rho,\mathbf{w},\mathbf{v},\{\theta_n\}} R_{sum}^{Eq}(\rho, \mathbf{w}, \mathbf{v}, \{\theta_n\}) \tag{4.4}$$

$$\text{s.t.C1: } \frac{|\mathbf{h}_k\mathbf{w}_k|^2}{\sum\limits_{i\neq k}^{K}|\mathbf{h}_k\mathbf{w}_i|^2+\sigma_k^2+\frac{\delta_k^2}{\rho_k}} \geq \gamma_{min},\ k = 1, \ldots, K \tag{4.5}$$

$$\text{C2: } \eta_k(1-\rho_k)\sum_{i=1}^{K}|\mathbf{h}_k\mathbf{w}_i|^2 \geq P_{min},\ k = 1, \ldots, K \tag{4.6}$$

$$\text{C3: } \sum_{k=1}^{K}\|\mathbf{w}_k\|^2 \leq P_T, ,\ \ 0 \leq \rho_k \leq 1 \tag{4.7}$$

$$\text{C4: } v_n = f_n(\theta_n)e^{j\theta_n}, \quad n = 1,\dots,N \tag{4.8}$$

$$\text{C5: } -\pi \le \theta_n \le \pi, \quad n = 1,\dots,N \tag{4.9}$$

It can be seen that $\mathscr{P}_{\mathscr{A}}$ is a non-convex problem due to the non-concavity of both the objective function and the constraints C1, C2, C4. Thus, traditional methods do not apply.

4.3 Proposed Approach

To tackle $\mathscr{P}_{\mathscr{A}}$, we first reformulate the sum of logarithms into a more tractable form by applying the method from [141] to each sum in the objective function. This yields:

$$\begin{aligned} \overline{\mathscr{P}_{\mathscr{A}}}: & \max_{\alpha_{\mathrm{I}},\beta_{\mathrm{I}},\alpha_{\mathrm{E}},\beta_{\mathrm{E}},\rho,\mathbf{w},\mathbf{v},\{\theta_{\mathrm{n}}\}} f_{\mathscr{A}}(\alpha_{\mathrm{I}},\beta_{\mathrm{I}},\alpha_{\mathrm{E}},\beta_{\mathrm{E}},\rho,\mathbf{w},\mathbf{v},\{\theta_{\mathrm{n}}\}) \\ & \text{s.t (C1), (C2), (C3), (C4), (C5)} \end{aligned} \tag{4.10}$$

wherein $f_{\mathscr{A}}$ is shown in (4.11), with $\bar{\eta}_k = \xi_k \eta_k$ and $\Re$ being the real part operator.

$$\begin{aligned} f_{\mathscr{A}}(\alpha_{\mathrm{I}},\beta_{\mathrm{I}},\alpha_{\mathrm{E}},\beta_{\mathrm{E}},\rho,\mathbf{w},\mathbf{v},\{\theta_{\mathrm{n}}\}) &= \sum_{k=1}^{K} \log(1+\alpha_{I,k}) + \bar{\lambda}\log(1+\alpha_{E,k}) - \left(\alpha_{I,k} + \bar{\lambda}\alpha_{E,k}\right) \\ &+ \sum_{k=1}^{K}\left(2\sqrt{\rho_k(1+\alpha_{I,k})}\Re(\beta_{I,k}^{*}\mathbf{h}_k\mathbf{w}_k)\right) - \sum_{k=1}^{K}\left(\left|\beta_{I,k}\right|^2\left(\sum_{i=1}^{K}\rho_k|\mathbf{h}_k\mathbf{w}_i|^2 + \rho_k{\sigma_k}^2 + \delta_k^2\right)\right) \\ &+ \sum_{k=1}^{K}\left(2\bar{\lambda}\sqrt{\bar{\eta}_k(1-\rho_k)(1+\alpha_{E,k})}\Re(\beta_{E,k}^{*}\sum_{i=1}^{K}\mathbf{h}_k\mathbf{w}_i)\right) - \sum_{k=1}^{K}\left(\bar{\lambda}\left|\beta_{E,k}\right|^2\left(\xi_k\eta_k(1-\rho_k)\sum_{i=1}^{K}|\mathbf{h}_k\mathbf{w}_i|^2 + {\sigma_k}^2\right)\right) \end{aligned} \tag{4.11}$$

In order to tackle (4.10), the first step is to embed (C4) into the objective, resorting to a penalty-based approach, which yields:

$$\begin{aligned} \overline{\mathscr{P}_{\mathscr{B}}}: & \max_{\alpha_{\mathrm{I}},\beta_{\mathrm{I}},\alpha_{\mathrm{E}},\beta_{\mathrm{E}},\rho,\mathbf{w},\mathbf{v},\{\theta_{\mathrm{n}}\}} f_{\mathscr{A}} - \Gamma\sum_{n=1}^{N}\left|v_n - f_n(\theta_n)e^{j\theta_n}\right|^2 \\ & \text{s.t (C1), (C2), (C3), (C5)} \end{aligned} \tag{4.12}$$

wherein Γ represents the penalty coefficient used for penalizing the violation of the equality constraint (C4). If $\Gamma \to \infty$, the solution of the original problem is obtained. Problem (4.12) will be tackled by alternating optimization, as explained next.

4.3.1 Optimization of $\alpha_{I,k}, \alpha_{E,k}, \beta_{Ik}, \beta_{Ek}, \rho_k$

The optimal $\alpha_{I,k}, \alpha_{E,k}, \beta_{Ik}, \beta_{Ek}$ are found by setting the gradient of the objective to zero, which yields:

$$\alpha_{I,k} = \frac{r^2 + r\sqrt{r^2+4}}{2} \tag{4.13}$$

$$\alpha_{E,k} = \frac{\tilde{r}^2 + \tilde{r}\sqrt{\tilde{r}^2+4}}{2} \tag{4.14}$$

$$\beta_{I,k} = \frac{\sqrt{\rho_k(1+\alpha_{Ik})}(\mathbf{h}_k\mathbf{w}_k)}{\sum\limits_{i=1}^{K} \rho_k|\mathbf{h}_k\mathbf{w}_i|^2 + \rho_k{\sigma_k}^2 + \delta_k^2} \tag{4.15}$$

$$\beta_{E,k} = \frac{\sqrt{\bar{\eta}_k(1-\rho_k)(1+\alpha_{Ek})}\sum\limits_{i=1}^{K}\mathbf{h}_k\mathbf{w}_i}{\bar{\eta}_k(1-\rho_k)\sum\limits_{i=1}^{K}|\mathbf{h}_k\mathbf{w}_i|^2 + {\sigma_k}^2} \tag{4.16}$$

with $\tilde{r} = \sqrt{\bar{\eta}(1-\rho_k)}\Re\left\{\beta_{E,k}^* \sum\limits_{i=1}\mathbf{h}_k\mathbf{w}_i\right\}$, $\quad r = \sqrt{\rho_k}\Re\left\{\beta_{I,k}^*\mathbf{h}_k\mathbf{w}_k\right\}$.

The optimization with respect to the coefficients $\{\rho_k\}$ is performed as follows. With respect to $\{\rho_k\}$, the objective function is strictly concave and the constraints (C1), (C2) are affine. Moreover, (C1) can be rewritten in a linear form as follows, for any $k = 1, \ldots, K$:

$$\rho_k|\mathbf{h}_k\mathbf{w}_k|^2 - \gamma_{min}\left(\rho_k\sum_{i=1,i\neq k}^{K}|\mathbf{h}_k\mathbf{w}_i|^2 + \rho_k\sigma_k^2 + \delta_k^2\right) \geq 0 \tag{4.17}$$

Thus, with respect to $\{\rho_k\}$, the problem is convex and can be solved by standard convex optimization algorithms [142]. Moreover, The PS should satisfy the minimum SINR (γ_{min}) and energy harvesting(E_{min}) requirement for each UE and $\rho_k^{min} \leqslant \rho_k^{\circ} \leqslant \rho_k^{max}$. From (C1) and (C2), we can find the minimum and maximum boundary values of the power splitting ratio to satisfy these constraints as follows:

$$\rho_k^{\min} \geqslant \frac{\gamma_{min}\delta_k^2}{\left|\hat{\mathbf{h}}_k\hat{\mathbf{w}}_k\right|^2 - \gamma_{min}\left(\sum\limits_{i=1,i\neq k}^{K}\left|\hat{\mathbf{h}}_k\hat{\mathbf{w}}_i\right|^2 + \sigma_k^2\right)} > 0, \tag{4.18}$$

$$\rho_k^{\max} \leqslant 1 - \frac{E_{min}}{\eta_k \sum_{i=1}^{K} \left|\hat{\mathbf{h}}_k \hat{\mathbf{w}}_i\right|^2} < 1 \tag{4.19}$$

Then, we can update the optimum value of PS using the following criteria:

$$\rho_k^{\circ} = \begin{cases} \rho_k^{min}, & \rho_k^{\bullet} < \rho_k^{min} \\ \rho_k^{\bullet}, & \rho_k^{min} \leqslant \rho_k^{\bullet} \leqslant \rho_k^{max} \\ \rho_k^{max}, & \rho_k^{\bullet}\rho_k > \rho_k^{max}. \end{cases} \tag{4.20}$$

4.3.2 Optimization of $\mathbf{w}_k$

When all the other variables are fixed, the objective function is a concave function in the transmit beamforming vectors $\mathbf{w}_k$. However, constraints (C1) and (C2) are still not convex. To deal with them, we use the successive convex approximation (SCA) method [135],[143]. Specifically, the convex term $|\mathbf{h}_k \mathbf{w}_k|^2$ is upper-bounded by its first-order Taylor expansion as follows:

$$\mathbf{w}_k^H \mathbf{h}_k^H \mathbf{h}_k \mathbf{w}_k \geq 2\Re\left(\mathbf{w}_k^{(t)H} \mathbf{h}_k^H \mathbf{h}_k \mathbf{w}_k\right) - \left(\mathbf{w}_k^{(t)H} \mathbf{h}_k^H \mathbf{h}_k \mathbf{w}_k^{(t)}\right) \tag{4.21}$$

wherein $\mathbf{w}_k^{(t)}, \forall k$ is the solution from the previous iteration. Thus, defining $d_k^{(w)} = \mathbf{w}_k^{(t)H} \mathbf{h}_k^H \mathbf{h}_k \mathbf{w}_k^{(t)}$, exploiting (4.21) and elaborating, (C1) can be recast as:

$$\gamma_{\min}\left(\sum_{i \neq k} |\mathbf{h}_k \mathbf{w}_i|^2 + \sigma_k^2 + \frac{\delta_k^2}{\rho_k}\right) + d_k^{(w)} - 2\Re\left(\mathbf{w}_k^{(t)H} \mathbf{h}_k^H \mathbf{h}_k \mathbf{w}_k\right) \leq 0$$

Similarly, (C2) can be reformulated as follows:

$$\eta_k (1-\rho_k) \sum_{k=1}^{K} 2\Re\left(\mathbf{w}_i^{(t)H} \mathbf{h}_k^H \mathbf{h}_k \mathbf{w}_i\right) - \mathbf{w}_i^{(t)H} \mathbf{h}_k^H \mathbf{h}_k \mathbf{w}_i^{(t)} \geq P_{min}$$

By replacing (C1) and (C2) with their reformulated versions, we obtain the convex surrogate problem to be solved in each iteration of the SCA method for optimizing $\mathbf{w}_k$.

4.3.3 Optimization of $\mathbf{v}$

The approach is similar to that used for the optimization of $\mathbf{w}_k$. In fact, the objective is concave in $\mathbf{v}$, while the constraints (C1) and (C2) can be handled by the SCA method. Specifically, (C1)

can be replaced by the convex constraint:

$$\gamma_{\min}\left(\sum_{i\neq k}^{K}|(\mathbf{h}_{d,k}+\mathbf{v}^{H}\mathbf{H}_{r,k})\mathbf{w}_i|^2+\sigma_k^2+\frac{\delta_k^2}{\rho_k}\right) \tag{4.22}$$
$$+(\mathbf{h}_{d,k}+\mathbf{v}^{(t)H}\mathbf{H}_{r,k})\mathbf{w}_k\mathbf{w}_k^H(\mathbf{h}_{d,k}+\mathbf{v}^{(t)H}\mathbf{H}_{r,k})^H$$
$$-2\Re\{(\mathbf{h}_{d,k}+\mathbf{v}^{(t)H}\mathbf{H}_{r,k})\mathbf{w}_k\mathbf{w}_k^H(\mathbf{h}_{d,k}+\mathbf{v}^{H}\mathbf{H}_{r,k})^H\}\leq 0$$

and (C2) by the convex constraint

$$\eta_k(1-\rho_k)\sum_{i=1}^{K}(\mathbf{h}_{d,k}+\mathbf{v}^{(t)H}\mathbf{H}_{r,k})\mathbf{w}_i\mathbf{w}_i^H(\mathbf{h}_{d,k}+\mathbf{v}^{(t)H}\mathbf{H}_{r,k})^H-$$
$$2\Re\{(\mathbf{h}_{d,k}+\mathbf{v}^{(t)H}\mathbf{H}_{r,k})\mathbf{w}_i\mathbf{w}_i^H(\mathbf{h}_{d,k}+\mathbf{v}^{H}\mathbf{H}_{r,k})^H\}\geq P_{min} \tag{4.23}$$

By replacing the constraints (C1) and (C2) with (4.22) and (4.23), we obtain the convex surrogate problem to be solved in each iteration of the SCA method for optimizing $\mathbf{v}$.

4.3.4 Updating θ_n

The RIS phase shifts are the solutions of the problem:

$$\max_{\{\theta_n\}}-\sum_{n=1}^{N}\left|v_n-f_n(\theta_n)e^{j\theta_n}\right|^2,\ \mathtt{s.t.}-\pi\leq\theta_n\leq\pi \tag{4.24}$$

It can be seen that the problem is separable over n, i.e., each summand can be optimized separately. Thus, defining $\varphi_n=\arg(v_n)$, the optimal θ_n is the solution of the problem:

$$\max_{\theta_n\in[-\pi,\pi]}2f_n(\theta_n)|v_n|\cos(\varphi_n-\theta_n)-f_n^2(\theta_n) \tag{4.25}$$

which can be solved by standard numerical methods.

4.3.5 Convergence and Complexity

Finally, the overall algorithm to solve the optimization problem is obtained by iteratively optimizing the different optimization variables as indicated in algorithm (2). Each iteration monotonically increases the objective value, which guarantees convergence. Moreover, the computational complexity is polynomial in the number of variables, since only the solution of convex problems is required[1]. Thus, the complexity of optimizing $\{\rho_k\}$ is $\mathcal{O}(K^{\eta_k})$, while the complexity of optimizing $\{\mathbf{w}_k\}$ and $\mathbf{v}$ are $\mathcal{O}(I_w(MK)^{\eta_w})$, and $\mathcal{O}(I_vN^{\eta_v})$, respectively, with I_w and I_v being the number of iterations of the SCA methods used to optimize $\mathbf{w}$ and $\mathbf{v}$.

[1]We recall that a convex problem can be solved with a complexity $\mathscr{C}=\mathcal{O}(L^{\eta})$, where L is the number of variables and $1\leq\eta\leq 4$ [144].

Algorithm 2 Penalty based Algorithm

Initialize $\rho, \mathbf{w}, \mathbf{v}, \{\theta_n\}_{n=1}^N$ and $\Gamma > 0$ with a feasible values; set ε_1 and ε_2 as the stopping conditions;
Set $t \leftarrow 0$
while The constraint violation is below a threshold $\varepsilon_2 > 0$ **do**
  Update the Penalty coefficient $\Gamma \leftarrow c\Gamma$
  while The stopping criteria does not meet **do**
    Update the reflection coefficient.
    Update the phase shift vector.
    Update $\boldsymbol{\alpha}_I, \boldsymbol{\alpha}_E, \boldsymbol{\beta}_I, \boldsymbol{\beta}_E$.
    Update transmit beamforming.
    Update Power Splitting vector.
  end while
end while
return $\rho, \mathbf{w}, \mathbf{v}, \{\theta_n\}_{n=1}^N$

On the other hand, the optimal $\{\alpha_{I,k}, \alpha_{E,k}, \beta_{Ik}, \beta_{Ek}\}$ are available in closed-form in (4.13), (4.14),(4.15), (4.16) and thus the complexity required for their computation can be neglected. Similarly, the complexity of Problem (4.24) can also be neglected, as it is linear in N. In fact, the problem can be decoupled over the N optimization variables, and, for each N, the optimal θ_n is obtain by solving (4.25). Thus, the overall complexity of the proposed method is given by $\mathscr{C} = I(\mathscr{O}(K^{\eta_k}) + \mathscr{O}(I_w(MK)^{\eta_w}) + \mathscr{O}(I_v N^{\eta_v}))$, where I is the number of alternating optimization iterations to be run until convergence. The exponents of the polynomial are not available in closed-form, but it is known that they are upper-bounded by 4 [144]. A typical value is 3.5, which comes up when interior-point methods are used [142].

4.4 Numerical Results

We consider an RIS-assisted MISO communication system in a typical indoor scenario, in which $M = 32$ transmit antennas are arranged in a uniform linear array, and each antenna has 6 dBi gain. Unless stated otherwise, we set $K = 4$ UEs and $N = 400$ RIS elements. The UEs are randomly and uniformly distributed within a disk of 2 m radius centered at (10 m, 10 m). An N-element RIS is located at (0 m, 5 m). All the channels are modeled as $X = L_x\left(\sqrt{\frac{\epsilon}{1+\epsilon}}\bar{X}^{LOS} + \sqrt{\frac{1}{1+\epsilon}}\bar{X}^{NLOS}\right)$, where $\bar{X}^{LOS}$ and $\bar{X}^{NLOS}$ are the line-of-sight (LOS) and non-LOS (NLOS) components, and X is either $\mathbf{G}$, $\mathbf{h}_{r,k}$, or $\mathbf{h}_{d,k}$. The NLOS component follows the Rayleigh fading model, while the LOS component is $\bar{X}^{LOS} = \mathbf{a}_N(\theta^{AoA})\mathbf{a}_M^H(\theta^{AoD})$, with:

$$\mathbf{a}_N(\theta^{AoA}) = [1, e^{j\frac{2\pi d}{\lambda}\sin(\theta^{AoA})}, \ldots, e^{j\frac{2\pi d}{\lambda}(N-1)\sin(\theta^{AoA})}]^T \tag{4.26a}$$

$$\mathbf{a}_M(\theta^{AoD}) = [1, e^{j\frac{2\pi d}{\lambda}\sin(\theta^{AoD})}, \ldots, e^{j\frac{2\pi d}{\lambda}(M-1)\sin(\theta^{AoD})}]^T \tag{4.26b}$$

where d and λ are the inter-antenna distance and the wavelength, respectively. We assume $d/\lambda = 1/2$. The path-loss is $L = C_0\left(\frac{r}{D_0}\right)^{-x_l}$, where r is the link distance and $D_0 = 1$ is the

Table 4.1: Simulation parameters.

Parameters	Values
Number of RIS elements / UEs	400 / K = 4
Maximum transmission power	P_T = 40 dBm
Path-loss exponent - RIS-aided channels	$x_l = 2.2$
Path-loss exponent - Direct channel	$x_l = 3.6$
Rician factor	$\epsilon = 5$ dB
Power conversion noise	$\delta_k^2 = \delta^2 = -50$ dBm
Thermal noise power	$\sigma_k^2 = \sigma^2 = -40$ dBm
Minimum harvested power	$P_{min} = -20$ dBm
Minimum SINR requirement	$\gamma_{\min}$ =0 dB
Power conversion efficiency	$\eta_k = \eta = 0.7$
Combining weight	$\bar{\lambda} = [0 : 0.2 : 1]$
Conversion efficiency (uplink) ξ_k	0.001

reference distance at which the reference path-loss $C_0 = -30$ dB is defined, x_l is the path-loss exponent. Other simulation parameters are given in Table 1 and are in agreement with [138]. For comparison, we evaluate the performance gain obtained by the proposed algorithm against the "No-RIS" scenario, where no RIS is deployed in the network.

Figure 4.2 depicts the relation between the number of RIS elements versus the sum-rate and the harvested power. We see that employing more RIS elements leads to a monotonic growth of the amount of harvested power and sum-rate. The figure reveals the effectiveness of the proposed algorithm compared to the "No RIS" case (denoted by "w/o RIS"). This monotonic gain is due to the appropriate design of the phase shifts of the RIS elements, which results in strong virtual LOS paths between the AP and the UEs. Also, the figure shows two special cases in which we optimize only the achievable rate, i.e., $\bar{\lambda} = 0$, and only the harvested power, i.e., $\bar{\lambda} \to \infty$. The proposed bi-objective optimization problem allows us to obtain the desired trade-off between sum-rate and harvested power by varying $\bar{\lambda}$, and it can be utilized to optimize only the sum-rate or the harvested power as two special cases.

In Fig. 4.3, we explore the trade-off between the sum-rate and harvested power as a function of the number of RIS elements. The case without RIS is reported for comparison. We observe that employing more RIS elements enhances the sum-rate and harvested power, and the proposed algorithm outperforms the "No RIS" scenario. Moreover, the figure highlights the impact of the parameter $\bar{\lambda}$, which is utilized to determine the service priority between optimizing the sum-rate (i.e., low values of $\bar{\lambda}$) or optimizing the harvested power (i.e., high values of $\bar{\lambda}$). When the system prioritizes the power harvesting, the proposed algorithm allocates more power to the power harvesting receiver, and thus the sum-rate decreases. Similarly, reducing the value of $\bar{\lambda}$ gives higher priority to the information decoding receiver. The figure shows the trade-off between the sum-rate and harvested power for any values of $\bar{\lambda}$. The extreme points to the left and to the right of the curves correspond to the single-objective sum-rate maximization and to the single-objective harvested power maximization, respectively.

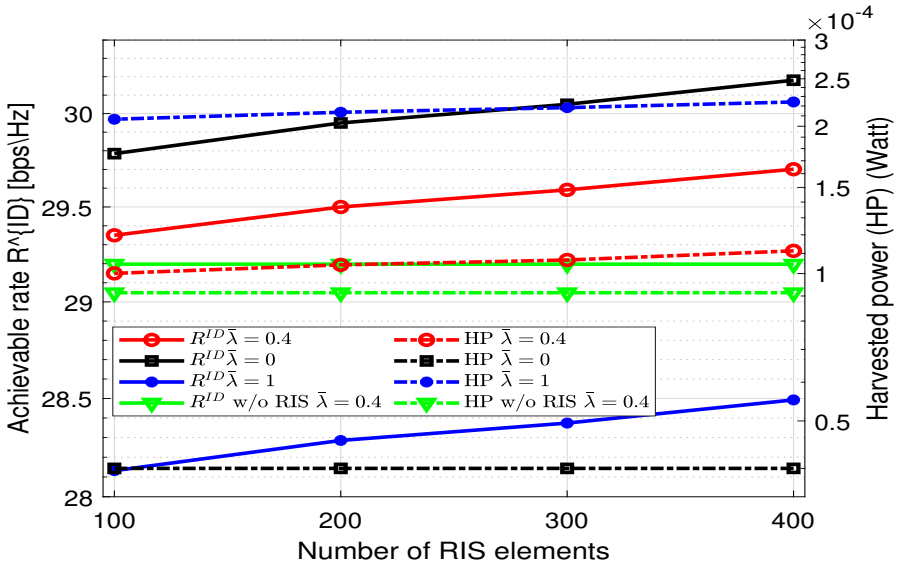

Figure 4.2: Sum-rate and harvested power versus the number of RIS elements for different values of $\bar{\lambda}$ ($K=4$).

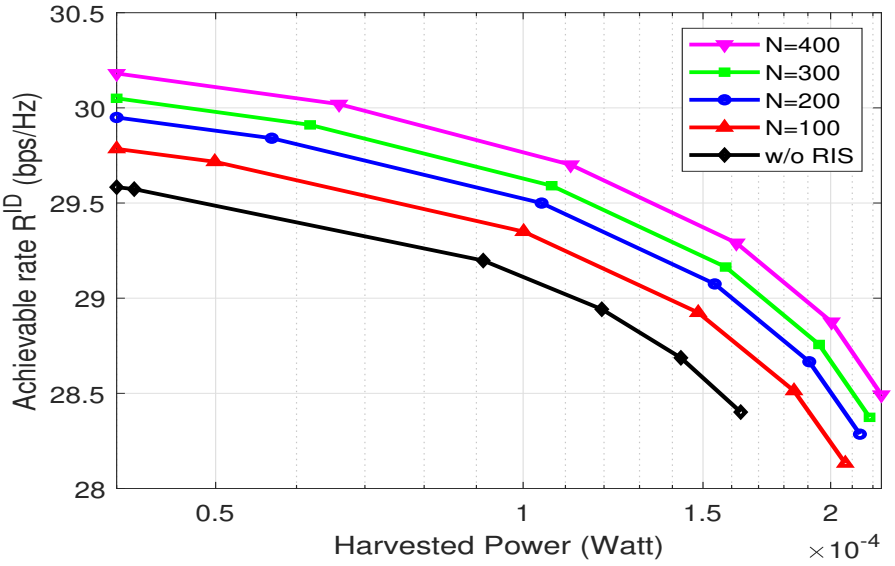

Figure 4.3: Trade-off between the sum-rate and harvested power with the number of RIS elements ($K=4$).

In Fig. 4.4, we examine the trade-off between the sum-rate and harvested power with the minimum value of the amplitude of the reflection coefficient f_{min} of the RIS elements. We see that the sum-rate and harvested power increase with f_{min}, with $f_{min}=1$ corresponding to the ideal case for an RIS.

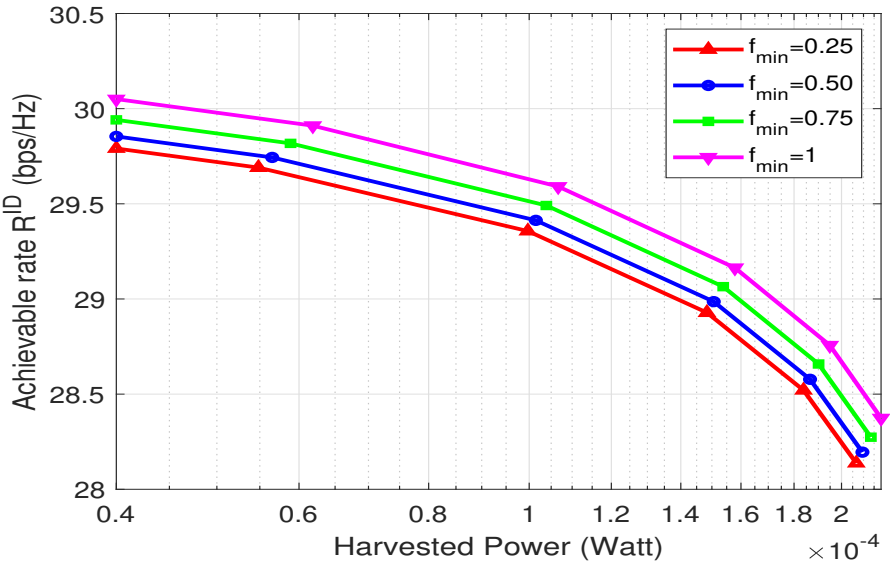

Figure 4.4: Trade-off between the sum-rate and harvested power with f_{min} ($N = 300$).

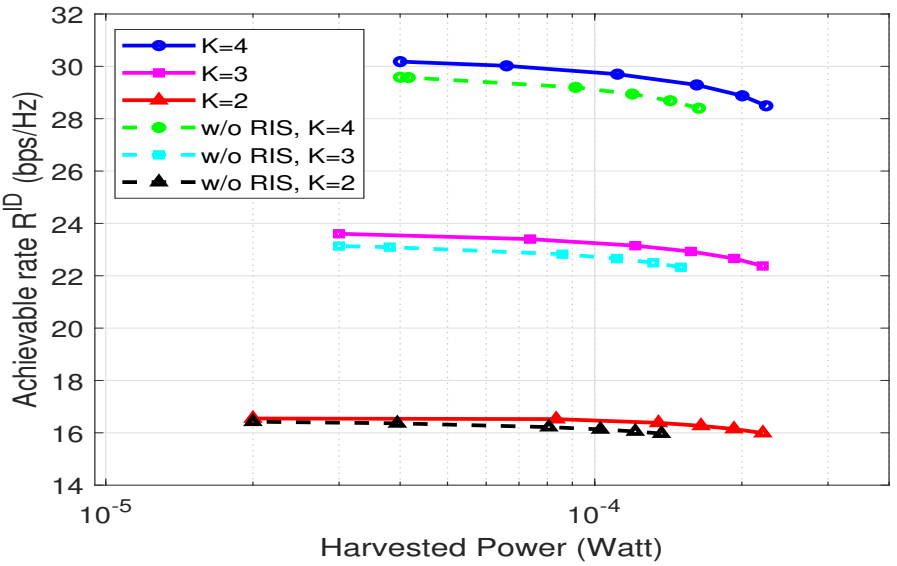

Figure 4.5: Trade-off between the sum-rate and harvested power with the number of UEs ($N = 400$).

In Fig. 4.5, finally, we investigate the trade-off between the sum-rate and harvested power as a function of the number of UEs. We see that the Pareto region is characterized by a larger excursion of the harvested power as the priority parameter $\bar{\lambda}$ varies, while the sum-rate shows a less significant variation. This is due to the stringent requirement that we imposed on the minimum harvested energy, which forces the optimization algorithm to allocate more resources for power harvesting, which inevitably leads to a lower sum-rate. Higher values of sum-rate can be obtained by reducing the value of the minimum acceptable harvested power. Nevertheless, satisfactory values of both the sum-rate and harvested power can be obtained

by deploying a sufficient number of RIS elements. Compared with the "No RIS" case, we see, e.g., that the harvested power increases from 0.11 mW to 0.19 mW while guaranteeing the same sum-rate of 29 bps/Hz if $K = 4$ and $N = 400$. The sum-rate and the harvested power can be further increased by deploying larger RISs.

4.5 Conclusion

We have investigated the trade-off between the sum-rate and harvested power in a multi-user RIS-aided downlink MISO system with SWIPT. Enforcing QoS constraints and practical phase shift constraints, the beamforming vector, the power splitting ratio, and the RIS reflection coefficients are jointly optimized by a two-layer penalty-based algorithm. Simulation results show that the proposed algorithm significantly outperforms conventional approaches in the absence of RISs.

5 Intelligent Omni-Surfaces (IOSs) for the MIMO Broadcast Channel

In this chapter, we consider intelligent omni-surfaces (IOSs), which are capable of simultaneously reflecting and refracting electromagnetic waves. We focus our attention on the multiple-input multiple-output (MIMO) broadcast channel, and we introduce an algorithm for jointly optimizing the covariance matrix at the base station, the matrix of reflection and transmission coefficients at the IOS, and the amount of power that is reflected and refracted from the IOS. The distinguishable feature of this work lies in taking into account that the reflection and transmission coefficients of an IOS are tightly coupled. Simulation results are illustrated to show the convergence of the proposed algorithm and the benefits of using surfaces with simultaneous reflection and refraction capabilities.

This chapter is organized as follows. In *Section 5.2*, we present the system model for the IOS-aided MIMO broadcast channel. In Section 5.3, we formulate the optimization problem to maximize the achievable sum-rate. In *Section 5.4*, we describe the optimization algorithm to solve the optimization problem. In *Section 5.5*, we provide simulation results that illustrate the achievable sum-rate. Conclusions are drawn in Section *5.6*.

5.1 Introduction

Reconfigurable intelligent surfaces (RISs) have emerged as a promising approach to improve the wireless communication channel quality and to extend the network coverage [145, 146]. However, the vast majority of works consider surfaces that can only reflect the incident signals, which limits the coverage capabilities offered by RISs [147, 148]. To tackle this problem, the recently proposed concept of intelligent omni-surface (IOS) provides 360° coverage thanks to surfaces that can simultaneously reflect and refract the incident signals [149]. The reflection and refraction capabilities of the incident electromagnetic waves are controlled through the optimization of two interlinked sets of reflection and transmission coefficients. In general, in other words, it is not possible to control the reflection and transmission coefficients independently.

Recently, a few research works have analyzed the performance of IOSs. In [150], the authors investigate the weighted sum-rate maximization under quality of service requirements and unit modulus constraints for the IOS elements, by utilizing the successive convex approximation method. In [151], the energy efficiency maximization problem is studied, and an optimization algorithm is proposed for jointly optimizing the transmit power and the passive beamforming at the IOS. In [152], the weighted sum-rate of an IOS-aided multiple-input multiple-output (MIMO) system is maximized by using the alternating optimization method. The precoding matrices are obtained by the Lagrange dual method, while the reflection and transmission coefficients are obtained by the penalty concave-convex method. Interested readers can consult [153], [154], [155], [156] for further information on IOSs.

In contrast to the available works, we focus our attention on optimizing the IOS in the MIMO broadcast channel. Also, for the first time, we explicitly take into account the dependence between the reflection and transmission coefficients, based on a recently implemented IOS prototype [157]. Specifically, the main contributions of this chapter are as follows:

- We utilize the duality between the broadcast channel and the multiple access channel to maximize the achievable sum-rate. We formulate a joint optimization problem for the users' covariance matrices, the reflection and transmission coefficients, and the power ratio between the reflected and transmitted power. We analyze the case studies with continuous-valued and discrete-valued phase shifts for the reflection and transmission coefficients, and we assume that they are not independent of each other.

- Due to the non-convexity of the formulated optimization problem, and the coupling between the optimization variables in the objective function, we propose an alternating optimization algorithm to solve the aforementioned problem. The optimal users' covariance matrices are obtained by applying the dual decomposition and the block coordinate maximization (BCM) method, while the optimal phase shifts of the reflection and transmission coefficients of the IOS elements are formulated in a simple expression. In addition, the power ratio between the reflected and refracted power is computed

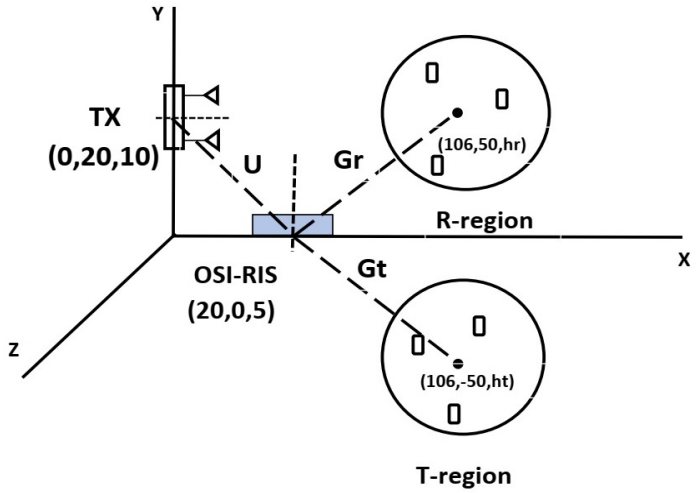

Figure 5.1: Aerial view of the considered communication system.

iteratively by utilizing the gradient ascent method.

- Simulation results show that the proposed algorithm converges relatively fast (i.e., within a few iterations) to a local optima. Moreover, we quantify the impact of discretizing the reflection and transmission coefficients for a two-state IOS testbed platform.

5.2 System Model

We consider an IOS-assisted multi-user MIMO broadcast channel, where a multi-antenna BS with N_t antennas communicate with K users, and each user is equipped with N_r antennas. The total number of users in the reflection and transmission sides of the IOS are denoted by KR and KT, respectively, with $K = KR + KT$. We assume that the BS and the users' antennas form a uniform linear array (ULA), and the inter-antenna separations are s_t and s_r, respectively. In addition, we assume that the IOS comprises N elements that can simultaneously reflect and refract the incident signals. Since the users can be located either in the reflection or the transmission sides of the IOS, a single user receives either the signal reflected or the signal refracted from the IOS.

To serve the users located in the reflection and transmission sides simultaneously, each element of the IOS applies a complex-valued reflection and transmission coefficient. The matrix of N reflection or transmission coefficients is denoted by $\mathbf{F}(\boldsymbol{\theta}) = \text{diag}(\boldsymbol{\theta}) \in \mathbb{C}^{N\times N}$, where $\boldsymbol{\theta} = \{\boldsymbol{\theta}^r, \boldsymbol{\theta}^t\}$, and $\boldsymbol{\theta^r} = \sqrt{\rho}\left[\tilde{\beta}_1^r, \tilde{\beta}_2^r, \ldots, \tilde{\beta}_N^r\right]^T \in \mathbb{C}^{N\times 1}$ and $\boldsymbol{\theta^t} = \sqrt{1-\rho}\left[\tilde{\beta}_1^t, \tilde{\beta}_2^t, \ldots, \tilde{\beta}_N^t\right]^T \in \mathbb{C}^{N\times 1}$. Specifically, the parameter $\rho \in [0,1]$ is an optimization variable that accounts for the amount of power that the IOS directs towards the users in the reflection side ($1-\rho$ is the amount of power directed towards the transmission side). Also, $\tilde{\beta}_n^r$ and $\tilde{\beta}_n^t$ are the reflection and transmission coefficients of the IOS. These reflection and transmission coefficients are interlinked and are optimized in pairs for each IOS element, i.e., $\{\tilde{\beta}_n^r, \tilde{\beta}_n^t\} \in \left\{(\tilde{\beta}_{s1}^r, \tilde{\beta}_{s1}^t), (\tilde{\beta}_{s2}^r, \tilde{\beta}_{s2}^t), \ldots, (\tilde{\beta}_{sQ}^r, \tilde{\beta}_{sQ}^t)\right\} =$

Ψ, where Q is the number of (reflection, transmission) coefficient pairs.

Due to the presence of the IOS, the end-to-end channel for the $k_r \in [1,\dots KR]$-user located in the reflection side is:

$$\begin{aligned}\mathbf{H}_{k_r} &= \mathbf{D}_{k_r} + \mathbf{G}_{k_r}\mathbf{F}(\boldsymbol{\theta}^r)\mathbf{U} \\ &= \mathbf{D}_{k_r} + \mathbf{G}_{k_r}\sqrt{\rho}\,\mathrm{diag}\left(\tilde{\beta}_1^r, \tilde{\beta}_2^r, ..., \tilde{\beta}_N^r\right)\mathbf{U} \\ &= \mathbf{D}_{k_r} + \sqrt{\rho}\sum_{n=1}^{N}\tilde{\beta}_n^r\mathbf{g}_{n,k_r}\mathbf{u}_n\end{aligned} \tag{5.1}$$

and the end-to-end channel for the $k_t \in [1,\dots KT]$-user located in the transmission side is:

$$\begin{aligned}\mathbf{H}_{k_t} &= \mathbf{D}_{k_t} + \mathbf{G}_{k_t}\mathbf{F}(\boldsymbol{\theta}^t)\mathbf{U} \\ &= \mathbf{D}_{k_t} + \mathbf{G}_{k_t}\sqrt{1-\rho}\,\mathrm{diag}\left(\tilde{\beta}_1^t, \tilde{\beta}_2^t, ..., \tilde{\beta}_N^t\right)\mathbf{U} \\ &= \mathbf{D}_{k_t} + \sqrt{1-\rho}\sum_{n=1}^{N}\tilde{\beta}_n^t\mathbf{g}_{n,k_t}\mathbf{u}_n\end{aligned} \tag{5.2}$$

In a compact form, we have:

$$\mathbf{H}_k(\boldsymbol{\theta}) = \mathbf{D}_k + \mathbf{G}_k\mathbf{F}(\boldsymbol{\theta})\mathbf{U} \tag{5.3}$$

where $\mathbf{D}_k \in \mathbb{C}^{N_r \times N_t}$ denotes the channel matrix between the BS and the k-th user, $\mathbf{U} \in \mathbb{C}^{N \times N_t}$ denotes the channel matrix between the BS and the IOS, and $\mathbf{G}_k \in \mathbb{C}^{N_r \times N}$ denotes the channel matrix between the IOS and the k-th user.

To simplify the notation, we write $\mathbf{H}_k$ instead of $\mathbf{H}_k(\boldsymbol{\theta})$, where the dependence on $\boldsymbol{\theta}$ is implicit. Thus, the received signal at the k-th user is written as:

$$\mathbf{y}_k = \mathbf{H}_k\mathbf{x}_k + \textstyle\sum_{j=1, j\neq k}^{K}\mathbf{H}_k\mathbf{x}_j + \mathbf{n}_k \tag{5.4}$$

where $\mathbf{H}_k \in \mathbb{C}^{N_r \times N_t}$ is the channel matrix for the k-th user, $\mathbf{x}_k \in \mathbb{C}^{N_t \times 1}$ is the transmitted signal intended for the k-th user, and $\mathbf{x}_j \in \mathbb{C}^{N_t \times 1}$ for $j \neq k$ are the transmitted signals intended for other users, which act as interference for the detection of $\mathbf{x}_k$. The noise vector $\mathbf{n}_k \in \mathbb{C}^{N_r \times 1}$ consists of independent and identically distributed (i.i.d.) elements whose distribution is $\mathscr{CN}(0, N_0)$, where N_0 is the noise variance.

5.3 Problem Formulation

We are interested in maximizing the achievable sum-rate of the considered IOS-aided wireless communication system. To accomplish this, we exploit the fact that the achievable rate region of a Gaussian MIMO broadcast channel can be achieved by dirty paper coding (DPC) [158]. DPC enables us to reduce the interference in a communication system, i.e., to perfectly eliminate the interference term $\sum_{j<k}\mathbf{H}_k\mathbf{x}_j$ for the k-th user. In this regard, the ordering of the

users clearly matters. Let π be an ordering of users, i.e., a permutation of the set $\{1,2,\ldots,K\}$. Then, for this ordering, the achievable rate for the k-th user can be computed as [159, Eq. (3)]:

$$R_{\pi(k)} = \log_2 \frac{\left|\mathbf{I} + \mathbf{H}_{\pi(k)}\left(\sum_{j\geq k}\mathbf{S}_{\pi(j)}\right)\mathbf{H}_{\pi(k)}^H\right|}{\left|\mathbf{I} + \mathbf{H}_{\pi(k)}\left(\sum_{j>k}\mathbf{S}_{\pi(j)}\right)\mathbf{H}_{\pi(k)}^H\right|} \tag{5.5}$$

where $\mathbf{S}_k = \mathbb{E}\{\mathbf{x}_k\mathbf{x}_k^H\} \succeq \mathbf{0}$ is the input covariance matrix of user k. We assume a sum-power constraint at the BS, i.e.:

$$\sum_{k=1}^K \mathrm{Tr}(\mathbf{S}_k) \leq P \tag{5.6}$$

where P is the maximum total power at the BS. Therefore, the achievable sum-rate optimization problem for the IOSs-assisted MIMO broadcast channel can be expressed as:

$$\max_{\mathbf{s},\tilde{\boldsymbol{\beta}}^l,\rho} \sum_{k=1}^K \log_2 \frac{\left|\mathbf{I} + \mathbf{H}_{\pi(k)}\left(\sum_{j\geq k}\mathbf{S}_{\pi(j)}\right)\mathbf{H}_{\pi(k)}^H\right|}{\left|\mathbf{I} + \mathbf{H}_{\pi(k)}\left(\sum_{j>k}\mathbf{S}_{\pi(j)}\right)\mathbf{H}_{\pi(k)}^H\right|} \tag{5.7a}$$

$$\text{s.t. } \sum_{k=1}^K \mathrm{Tr}(\mathbf{S}_k) \leq P; \mathbf{S}_k \succeq \mathbf{0}, \forall k, \tag{5.7b}$$

$$\{\tilde{\beta}_n^r, \tilde{\beta}_n^t\} \in \Psi; \quad \forall n \in [1,2,\ldots,N], \tag{5.7c}$$

$$0 \leq \rho \leq 1 \tag{5.7d}$$

where $\tilde{\boldsymbol{\beta}}^l = \{\tilde{\boldsymbol{\beta}}^r, \tilde{\boldsymbol{\beta}}^t\}$ and $l \in \{r,t\}$.

To solve this problem, we exploit the duality between the MIMO broadcast channel and the multiple access channel, as recently done in [160]. Accordingly, we reformulate the optimization problem in (5.7) as follows:

$$\begin{aligned} \max_{\bar{\mathbf{s}},\tilde{\boldsymbol{\beta}}^l,\rho} \quad & f(\bar{\mathbf{S}},\tilde{\boldsymbol{\beta}},\rho) = \log_2\left|\mathbf{I} + \sum_{k=1}^K \mathbf{H}_k^H\bar{\mathbf{S}}\mathbf{H}_k\right| \\ \text{s.t.} \quad & \sum_{k=1}^K \mathrm{Tr}(\bar{\mathbf{S}}_k) \leq P; \bar{\mathbf{S}}_k \succeq \mathbf{0}, \forall k, \\ & \{\tilde{\beta}_n^r, \tilde{\beta}_n^t\} \in \Psi; \quad \forall n \in [1,2,\ldots,N], \\ & 0 \leq \rho \leq 1, \end{aligned} \tag{5.8}$$

where $\mathbf{H}_k^H$ represents the dual multiple access channel corresponding to $\mathbf{H}_k$ and $\bar{\mathbf{S}}_\mathbf{k}$ is the dual multiple access input covariance matrix of the k-th user. Once the input covariance matrices $(\bar{\mathbf{S}}_k)_{k=1}^K$ in the dual multiple access channel are found, the corresponding covariance matrices $(\mathbf{S}_k)_{k=1}^K$ in the broadcast channel are obtained from [159, Eq. (11)], as:

$$\mathbf{S}_k = \mathbf{B}_k^{-1/2}\mathbf{F}_k\mathbf{G}_k^H\mathbf{A}_k^{1/2}\bar{\mathbf{S}}_k\mathbf{A}_k^{1/2}\mathbf{G}_k\mathbf{F}_k^H\mathbf{B}_k^{-1/2} \tag{5.9}$$

where $\mathbf{A}_k = \mathbf{I} + \mathbf{H}_k(\sum_{i=1}^{k-1}\mathbf{S}_i)\mathbf{H}_k^H$, $\mathbf{B}_k = \mathbf{I} + \sum_{i=k+1}^K \mathbf{H}_i^H\bar{\mathbf{S}}_i\mathbf{H}_i$, and $\mathbf{F}_k\boldsymbol{\Lambda}_k\mathbf{G}_k^H$ is the singular value decomposition of $\mathbf{B}_k^{-1/2}\mathbf{H}_k^H\mathbf{A}_k^{-1/2}$.

5.4 Proposed Optimization Method

To solve the formulated problem, we propose an alternating optimization method. The users' covariance matrices are optimized by exploiting the dual decomposition method in [160]. The reflection and transmission coefficients of the IOS are obtained by generalizing the method in [161], which is applicable to reflecting surfaces, under the assumption of continuous-valued coefficients. The corresponding discrete-valued reflection and transmission coefficients are obtained by projecting the obtained solutions onto the feasible set of possible discrete values. Moreover, we present a gradient-based method for optimizing the power ratio.

5.4.1 Covariance Matrix Optimization

For given values of the power ratio and the reflection and transmission coefficients, the achievable sum-rate optimization problem in (5.8) is simplified as follows:

$$\max_{\bar{\mathbf{S}}} \quad \log_2\left|\mathbf{I}+\sum_{k=1}^{K}\mathbf{H}_k^H\bar{\mathbf{S}}_k\mathbf{H}_k\right| \tag{5.10a}$$

$$\text{s.t.} \quad \bar{\mathbf{S}}\in\mathscr{S} \tag{5.10b}$$

where $\bar{\mathbf{S}}\triangleq(\bar{\mathbf{S}}_k)_{k=1}^K$ for $\mathscr{S}=\{\bar{\mathbf{S}}\mid\sum_{k=1}^K\mathrm{Tr}(\bar{\mathbf{S}}_k)\le P;\bar{\mathbf{S}}_k\succeq\mathbf{0}\,\forall k\}$. As described in [160, 90], the optimization problem in (10) is solved by using the dual decomposition Lagrangian and the accelerated block coordinate maximization methods.

To proceed further, we first form the partial Lagrangian function of (5.10) as [90]

$$\mathscr{L}(\mu,\bar{\mathbf{S}})=\ln\left|\mathbf{I}+\sum_{k=1}^{K}\mathbf{H}_k^H\bar{\mathbf{S}}_k\mathbf{H}_k\right|-\mu\left[\sum_{k=1}^{K}\mathrm{Tr}(\bar{\mathbf{S}}_k)-P\right] \tag{5.11}$$

where μ is the Lagrangian multiplier for the constraint (5.10b). For mathematical convenience, we use the natural logarithm in (5.11) without affecting the optimality of (5.10). For a given μ, the dual function is given as

$$g(\mu)=\max_{\bar{\mathbf{S}}\succeq\mathbf{0}}\mathscr{L}(\mu,\bar{\mathbf{S}}) \tag{5.12}$$

where the constraint $\bar{\mathbf{S}}\succeq\mathbf{0}$ is understood as $\bar{\mathbf{S}}_k\succeq\mathbf{0}$, $\forall k$. To evaluate $g(\mu)$, in [160] we have presented a cyclic block maximization method which cyclically optimizes each $\bar{\mathbf{S}}_k$ while keeping the other $\bar{\mathbf{S}}_j$ ($j\neq k$) fixed, and which was first applied in [162] to a system without an RIS. For the purpose of exposition, let us define $\bar{\mathbf{S}}^{(n)}\triangleq(\bar{\mathbf{S}}_1^{(n)},\ldots,\bar{\mathbf{S}}_{k-1}^{(n)},\bar{\mathbf{S}}_k^{(n)},\bar{\mathbf{S}}_{k+1}^{(n)},\ldots,\bar{\mathbf{S}}_K^{(n)})$ which represents the current iterate. The k-th element $\bar{\mathbf{S}}_k$ of the next iterate is found to be the optimal solution of the following problem:

$$\max_{\bar{\mathbf{S}}_k\succeq\mathbf{0}} \quad \ln\left|\mathbf{I}+\bar{\mathbf{H}}_k^{-1/2}\mathbf{H}_k^H\bar{\mathbf{S}}_k\mathbf{H}_k\bar{\mathbf{H}}_k^{-1/2}\right|-\mu\,\mathrm{Tr}(\bar{\mathbf{S}}_k) \tag{5.13}$$

where

$$\bar{\mathbf{H}}_k = \mathbf{I} + \sum_{j=1, j\neq k}^{K} \mathbf{H}_j^H \bar{\mathbf{S}}_j \mathbf{H}_j. \tag{5.14}$$

It can be seen that the optimal solution to (5.13) is given by [162]

$$\bar{\mathbf{S}}_k^{\star} = \mathbf{V}_k \operatorname{diag}\Big(\Big[\big(\frac{1}{\mu} - \frac{1}{\sigma_1}\big)_+, \big(\frac{1}{\mu} - \frac{1}{\sigma_2}\big)_+, \ldots, \big(\frac{1}{\mu} - \frac{1}{\sigma_r}\big)_+\Big]^{\mathsf{T}}\Big)\mathbf{V}_k^H \tag{5.15}$$

and $\mathbf{H}_k \bar{\mathbf{H}}_k^{-1} \mathbf{H}_k^H = \mathbf{V}_k \operatorname{diag}\Big(\sigma_1, \sigma_2, \ldots, \sigma_r\Big)\mathbf{V}_k^H$ is the eigenvalue decomposition (EVD) of $\mathbf{H}_k \bar{\mathbf{H}}_k^{-1} \mathbf{H}_k^H$ and $r = \operatorname{rank}(\mathbf{H}_k) \leq \min(N_t, n_r)$.

5.4.2 IOS Optimization

For given $\{\bar{S}_k\}_{k=1}^K$ and ρ, the optimization problem in (5.8) with respect to $\tilde{\beta}_n^l$, $l \in \{r, t\}$, can be written as follows:

$$\begin{aligned} \max_{\tilde{\beta}_n^l} \quad & f(\tilde{\beta}_n^l) = \log_2 \Big| \mathbf{I} + \sum_{k=1}^{K} \mathbf{H}_k^H \bar{\mathbf{S}} \mathbf{H}_k \Big| \\ \text{s.t.} \quad & \{\tilde{\beta}_n^r, \tilde{\beta}_n^t\} \in \Psi; \quad \forall n \in [1, 2, \ldots, N] \end{aligned} \tag{5.16}$$

To tackle this problem, we first optimize both $\tilde{\beta}_n^r$ and $\tilde{\beta}^t$ by assuming that they are continuous-valued and independent coefficients, and we then project the obtained solutions onto the set of feasible discrete phase shifts, by taking into account that the reflection and transmission coefficients are interlinked.

For ease of writing, we define the variables $\mathbf{G}_k = [\mathbf{g}_1, \ldots, \mathbf{g}_n]$, $\mathbf{U} = [\mathbf{u}_1^T, ..., \mathbf{u}_n^T]^T$, and

$$\bar{\mathbf{D}}_k = \begin{cases} \mathbf{D}_i^r & \forall i \in \{1, ..., KR\} \\ \mathbf{D}_j^t & \forall j \in \{1, ..., KT\} \end{cases} \tag{5.17}$$

$$\bar{\mathbf{g}}_{n,k} = \begin{cases} \mathbf{g}_{n,i}^r & \forall i \in \{1, ..., KR\} \\ \mathbf{g}_{n,j}^t & \forall j \in \{1, ..., KT\} \end{cases} \tag{5.18}$$

Under the assumption that $\tilde{\beta}_n^r$ and $\tilde{\beta}_n^t$ can be optimized independently (this is removed next by projecting on the feasible set),the objective function can be rewritten as follows:

$$f(\tilde{\beta}_n^l) = \log_2 \left| \begin{array}{l} \mathbf{I} + \left(\begin{array}{l} \sum_{k=1}^{KR} \left(\bar{\mathbf{D}}_k + \sum_{n=1}^{N} \sqrt{\rho} \tilde{\beta}_n^r \bar{\mathbf{g}}_{n,k} \mathbf{u}_n \right)^H \\ \times \overline{\mathbf{S}}_k \left(\bar{\mathbf{D}}_k + \sum_{n=1}^{N} \sqrt{\rho} \tilde{\beta}_n^r \bar{\mathbf{g}}_{n,k} \mathbf{u}_n \right) \end{array} \right) \\ + \left(\begin{array}{l} \sum_{k=1}^{KT} \left(\bar{\mathbf{D}}_k + \sum_{n=1}^{N} \sqrt{1-\rho} \tilde{\beta}_n^t \bar{\mathbf{g}}_{n,k} \mathbf{u}_n \right)^H \\ \times \overline{\mathbf{S}}_k \left(\bar{\mathbf{D}}_k + \sum_{n=1}^{N} \sqrt{1-\rho} \tilde{\beta}_n^t \bar{\mathbf{g}}_{n,k} \mathbf{u}_n \right) \end{array} \right) \end{array} \right| \tag{5.19}$$

Thus, for optimizing $\tilde{\beta}_n^r$, we have:

$$f(\tilde{\beta}_n^r) = \log_2 \left| \mathbf{A}_n^r + \tilde{\beta}_n^r \mathbf{B}_n^r + \tilde{\beta}_n^{r*} \mathbf{B}_n^{rH} \right| \tag{5.20}$$

and, for optimizing $\tilde{\beta}_n^t$, we have:

$$f(\tilde{\beta}_n^t) = \log_2 \left| \mathbf{A}_n^t + \tilde{\beta}_n^t \mathbf{B}_n^t + \tilde{\beta}_n^{t*} \mathbf{B}_n^{tH} \right| \tag{5.21}$$

where:

$$\mathbf{B}_n^r = \sqrt{\rho} \sum_{k=1}^{KR} (\bar{\mathbf{D}}_k^H + \sum_{l=1, n \neq l}^{N} \sqrt{\rho} \tilde{\beta}_l^{r*} \mathbf{u}_l^H \bar{\mathbf{g}}_{l,k}^H) \overline{\mathbf{S}}_k \bar{\mathbf{g}}_{n,k} \mathbf{u}_n \tag{5.22}$$

$$\mathbf{B}_n^t = \sum_{k=1}^{KT} (\sqrt{1-\rho} \bar{\mathbf{D}}_k^H + \sum_{n \neq l}^{N} (1-\rho) \tilde{\beta}_l^{t*} \mathbf{u}_l^H \bar{\mathbf{g}}_{l,k}^H) \overline{\mathbf{S}}_k \bar{\mathbf{g}}_{n,k} \mathbf{u}_n \tag{5.23}$$

$$\begin{aligned} \mathbf{A}_n^r = \mathbf{I} &+ \sum_{k=1}^{KT} (\bar{\mathbf{D}}_k + \sum_{n=1}^{N} \sqrt{1-\rho} \tilde{\beta}_n^t \bar{\mathbf{g}}_{n,k} \mathbf{u}_n)^H \overline{\mathbf{S}}_k (\bar{\mathbf{D}}_k + \sum_{n=1}^{N} \sqrt{1-\rho} \tilde{\beta}_n^t \bar{\mathbf{g}}_{n,k} \mathbf{u}_n) \\ &+ \sum_{k=1}^{KR} (\bar{\mathbf{D}}_k^H + \sum_{l=1, n \neq l}^{N} \sqrt{\rho} \tilde{\beta}_l^{r*} \mathbf{u}_l^H \bar{\mathbf{g}}_{l,k}^H) \overline{\mathbf{S}}_k (\bar{\mathbf{D}}_k + \sum_{l=1, n \neq l}^{N} \sqrt{\rho} \tilde{\beta}_l^r \bar{\mathbf{g}}_{l,k} \mathbf{u}_l) \\ &+ \sum_{k=1}^{KR} \rho \mathbf{u}_n^H \bar{\mathbf{g}}_{n,k}^H \overline{\mathbf{S}}_k \bar{\mathbf{g}}_{n,k} \mathbf{u}_n \end{aligned} \tag{5.24}$$

$$\begin{aligned} \mathbf{A}_n^t = \mathbf{I} &+ \sum_{k=1}^{KR} (\bar{\mathbf{D}}_k + \sum_{n=1}^{N} \sqrt{\rho} \tilde{\beta}_n^r \bar{\mathbf{g}}_{n,k} \mathbf{u}_n)^H \overline{\mathbf{S}}_k (\bar{\mathbf{D}}_k + \sum_{n=1}^{N} \sqrt{\rho} \tilde{\beta}_n^r \bar{\mathbf{g}}_{n,k} \mathbf{u}_n) \\ &+ \sum_{k=1}^{KT} (\bar{\mathbf{D}}_k^H + \sum_{l=1, n \neq l}^{N} \sqrt{1-\rho} \tilde{\beta}_l^{t*} \mathbf{u}_l^H \bar{\mathbf{g}}_{l,k}^H) \overline{\mathbf{S}}_k (\bar{\mathbf{D}}_k + \sum_{l=1, n \neq l}^{N} \sqrt{1-\rho} \tilde{\beta}_l^t \bar{\mathbf{g}}_{l,k} \mathbf{u}_l) \\ &+ \sum_{k=1}^{KT} (1-\rho) \mathbf{u}_n^H \bar{\mathbf{g}}_{n,k}^H \overline{\mathbf{S}}_k \bar{\mathbf{g}}_{n,k} \mathbf{u}_n \end{aligned} \tag{5.25}$$

Algorithm 3 AO algorithm to solve (5.8)

Initialize $\bar{\mathbf{S}}^{(0)}$, $\{\tilde{\beta}^{r(0)}, \tilde{\beta}^{t(0)}\}$ and $\rho^{(0)}$ with feasible values;
Set $i \leftarrow 0$
while a stopping criterion is not met **do**
  Compute $(\bar{\mathbf{S}}_k^{(i+1)})_{k=1}^K$ according to **Algorithm 2** in [163]
  for $n = 1, 2, \ldots, N_{\text{ris}}$ **do**
    $\tilde{\beta}_n^{*(i+1)} = \exp(-j \arg(\sigma_n))$ using ((5.26))
    Apply the phase shift projection procedure, if required, based on (5.27)
  end for
  $\rho^{(i+1)} = \mathbb{P}_D\left(\rho^{(i)} + \upsilon^{(i)} \nabla_\rho f(\rho)|_{\rho=\rho^{(i)}}\right)$
end while
return $\mathbf{S}^\bullet = \mathbf{S}^{(i)}$, $\rho^\bullet = \rho^{(i)}$ and $\{\tilde{\beta}^{r\bullet(i)}, \tilde{\beta}^{t\bullet(i)}\}$

The optimal solution of the optimization problem in (5.19) is then given by [160]:

$$\tilde{\beta}_n^{*r} = \exp(-j \arg(\sigma_n^r)) \tag{5.26a}$$

$$\tilde{\beta}_n^{*t} = \exp(-j \arg(\sigma_n^t)) \tag{5.26b}$$

where σ_n^r and σ_n^t are the only non-zero eigenvalues of $\left(\mathbf{A}_n^r\right)^{-1}\mathbf{B}_n^r$ and $\left(\mathbf{A}_n^t\right)^{-1}\mathbf{B}_n^t$, respectively.

The obtained continuous-valued solution of the reflection and transmission coefficients is denoted by $\{\tilde{\beta}_n^{*r}, \tilde{\beta}_n^{*t}\} = SC$. The corresponding discrete-valued solution in the considered feasible set is obtained by projecting SC on the discrete set Ψ. As a case study, we consider the IOS prototype in [157], where each IOS element can be configured in two states, where each state is identified by a pair of reflection and transmission coefficients, i.e., $\{(\tilde{\beta}_{S1}^r, \tilde{\beta}_{S1}^t), (\tilde{\beta}_{S2}^r, \tilde{\beta}_{S2}^t)\} = \{S1, S2\} = \Psi$.

In this case, the projection can be formulated as follows:

$$\{\tilde{\beta}^{r\bullet}, \tilde{\beta}^{t\bullet}\} = \begin{cases} \left(\beta_{S1}^r, \beta_{S1}^t\right), \|SC - S1\|_2 < \|SC - S2\|_2 \\ \left(\beta_{S2}^r, \beta_{S2}^t\right), \quad \text{otherwise} \end{cases} \tag{5.27}$$

where $\{\tilde{\beta}^{r\bullet}, \tilde{\beta}^{t\bullet}\}$ denotes the reflection and transmission coefficients that minimize the distance between the solution of the continuous-valued case and the feasible discrete set.

5.4.3 Power Ratio Optimization

For given values of $\{\bar{S}_k^*\}_{k=1}^K$ and $\{\tilde{\beta}^{r\bullet}, \tilde{\beta}^{t\bullet}\}$, the optimization problem in (5.8) can be explicitly rewritten as:

$$\max_{\rho} \quad f(\rho) = \log_2\left|\mathbf{I} + \sum_{k=1}^{K} \mathbf{H}_k^H \bar{\mathbf{S}}_k \mathbf{H}_k\right| \tag{5.28a}$$

$$\text{s.t.} \quad 0 \le \rho \le 1 \tag{5.28b}$$

The objective function $f(\rho)$ can be rewritten as:

$$f(\rho) = \log_2 \left| \mathbf{I} + \sum_{k=1}^{K} \mathbf{H}_k^H \overline{\mathbf{S}}_k \mathbf{H}_k \right| \tag{5.29}$$

$$= \log_2 \left| \mathbf{I} + \sum_{i=1}^{KR} \mathbf{H}_i \overline{\mathbf{S}}_i \mathbf{H}_i^H + \sum_{j=1}^{KT} \mathbf{H}_j \overline{\mathbf{S}}_j \mathbf{H}_j^H \right| \tag{5.30}$$

$$= \log_2 \left| \begin{array}{l} \mathbf{I} + 2\sqrt{\rho} \sum\limits_{k=1}^{KR} \sum\limits_{n=1}^{N} \tilde{\beta}_n^{r*} \mathbf{u}_n^H \bar{\mathbf{g}}_{n,k}^H \overline{\mathbf{S}}_k \bar{\mathbf{D}}_k \\ +2\sqrt{1-\rho} \sum\limits_{k=1}^{KT} \sum\limits_{n=1}^{N} \tilde{\beta}_n^{t*} \mathbf{u}_n^H \bar{\mathbf{g}}_{n,k}^H \overline{\mathbf{S}}_k \bar{\mathbf{D}}_k \\ + \sum\limits_{k=1}^{KR} \left(\begin{array}{l} \sum\limits_{n=1}^{N} \sum\limits_{n=1}^{N} \rho \tilde{\beta}_n^{r*} \tilde{\beta}_n^{r} \mathbf{u}_n^H \bar{\mathbf{g}}_{n,k}^H \overline{\mathbf{S}}_k \bar{\mathbf{g}}_{n,k} \mathbf{u}_n \\ +\bar{\mathbf{D}}_k^H \overline{\mathbf{S}}_k \bar{\mathbf{D}}_k \end{array} \right) \\ + \sum\limits_{k=1}^{KT} \left(\begin{array}{l} \sum\limits_{n=1}^{N} \sum\limits_{n=1}^{N} (1-\rho) \tilde{\beta}_n^{t*} \tilde{\beta}_n^{t} \mathbf{u}_n^H \bar{\mathbf{g}}_{n,k}^H \overline{\mathbf{S}}_k \bar{\mathbf{g}}_{n,k} \mathbf{u}_n \\ +\bar{\mathbf{D}}_k^H \overline{\mathbf{S}}_k \bar{\mathbf{D}}_k \end{array} \right) \end{array} \right| \tag{5.31}$$

In order to find the optimal value of the power ratio ρ, we solve the equation $f^{'}(\rho) = 0$, where $f^{'}(\rho)$ is the first-order derivative of $f(\rho)$. For ease of notation, let us define:

$$\mathbf{X_1} = \sum_{k=1}^{KR} \sum_{n=1}^{N} \tilde{\beta}_n^{r*} \mathbf{u}_n^H \bar{\mathbf{g}}_{n,k}^H \overline{\mathbf{S}}_k \bar{\mathbf{D}}_k \tag{5.32}$$

$$\mathbf{X_2} = \sum_{k=1}^{KT} \sum_{n=1}^{N} \tilde{\beta}_n^{t*} \mathbf{u}_n^H \bar{\mathbf{g}}_{n,k}^H \overline{\mathbf{S}}_k \bar{\mathbf{D}}_k \tag{5.33}$$

$$\mathbf{Y_1} = \sum_{k=1}^{KR} \sum_{n=1}^{N} \sum_{n=1}^{N} \tilde{\beta}_n^{r*} \tilde{\beta}_n^{r} \mathbf{u}_n^H \bar{\mathbf{g}}_{n,k}^H \overline{\mathbf{S}}_k \bar{\mathbf{g}}_{n,k} \mathbf{u}_n \tag{5.34}$$

$$\mathbf{Y}_2 = \sum_{k=1}^{KT} \sum_{n=1}^{N} \sum_{n=1}^{N} \tilde{\beta}_n^{t*} \tilde{\beta}_n^{t} \mathbf{u}_n^H \bar{\mathbf{g}}_{n,k}^H \overline{\mathbf{S}}_k \bar{\mathbf{g}}_{n,k} \mathbf{u}_n \tag{5.35}$$

$$\bar{\mathbf{X}} = \mathbf{I} + \sum_{i=1}^{KR} \mathbf{H}_i \overline{\mathbf{S}}_i \mathbf{H}_i^H + \sum_{j=1}^{KT} \mathbf{H}_j \overline{\mathbf{S}}_j \mathbf{H}_j^H \tag{5.36}$$

The first-order and second-order derivatives, $f^{'}(\rho)$ and $f^{''}(\rho)$, respectively, can be formulated

as:

$$f'(\rho) = \nabla_\rho f(\rho) = \mathrm{Tr}\left(\bar{\mathbf{X}}^{-1}\left(\left(\frac{\mathbf{X}_1}{\sqrt{\rho}} - \frac{\mathbf{X}_2}{\sqrt{1-\rho}}\right) + (\mathbf{Y}_1 - \mathbf{Y}_2)\right)\right) \tag{5.37}$$

$$f''(\rho) = -\frac{1}{\ln 2}\left(INV(\bar{\mathbf{X}})\right)^2 \left(\begin{array}{l} 0.5\left(\sqrt[-3/2]{\rho}\mathbf{X_1} + \sqrt[-3/2]{1-\rho}\mathbf{X_2}\right)\bar{\mathbf{X}} \\ +\left(\left(\frac{\mathbf{X}_1}{\sqrt{\rho}} - \frac{\mathbf{X}_2}{\sqrt{1-\rho}}\right) + (\mathbf{Y}_1 - \mathbf{Y}_2)\right)^2 \end{array}\right) \tag{5.38}$$

where $\nabla_\rho f(\rho)$ is the gradient of $f(\rho)$ with respect to ρ.

The objective function in (5.28a) is a concave function with respect to ρ, since the second derivative in (5.38) is no greater than zero. Therefore, the optimization problem in (5.28a) has a single optimum value. However, it is hard to find a closed-form solution by solving $f^{'}(\rho) = 0$. Thus, we utilize the projected gradient (PG) method. Specifically, ρ in the $(i+1)$-th iteration is updated as follows:

$$\rho^{i+1} = \mathbb{P}_D\left(\rho^i + \upsilon^i \nabla_\rho f(\rho)|_{\rho=\rho^i}\right) \tag{5.39}$$

where υ^i in (5.39) is the step size that is updated by using the backtracking line search method in [160], and the projection operator $\mathbb{P}_D$ is defined as:

$$\hat{\rho} = \mathbb{P}_D(\rho) = \begin{cases} \rho^{min} & \rho^\bullet < \rho^{min} \\ \rho^\bullet & \rho^{min} \leqslant \rho^\bullet \leqslant \rho^{max} \\ \rho^{max} & \rho > \rho^{max} \end{cases} \tag{5.40}$$

where $\rho^\bullet$ and $\hat{\rho}$ are the solutions obtained before and after implementing the projection, and ρ^{min} and ρ^{max} are the minimum and maximum values for ρ, respectively.

5.5 Simulation Results

In this section, we evaluate the achievable sum-rate of the proposed algorithms with the aid of Monte Carlo simulations. Specifically, we compare the sum-rates under the assumption that the reflection and transmission coefficients are continuous-valued and independent values, and under the assumption that they are interlinked and belong to a discrete set.

The simulation setup is the following: the carrier frequency is $f = 2\,\mathrm{GHz}$ (the wavelength is $\lambda = 15\,\mathrm{cm}$), $s_t = s_r = s_{\mathrm{ris}} = \lambda/2 = 7.5\,\mathrm{cm}$, the network topology is given in Fig. 1, $N_t = 8$, $P = 1\,\mathrm{W}$, and $N_0 = -110\,\mathrm{dB}$. The IOS consists of $N_{\mathrm{ris}} = 15 \times 15 = 225$ elements placed in a 15×15 square formation. The users are equipped with $N_r = 2$ antennas and are randomly distributed within the disks shown in Fig. 1. The results are averaged over 100 independent channel realizations.

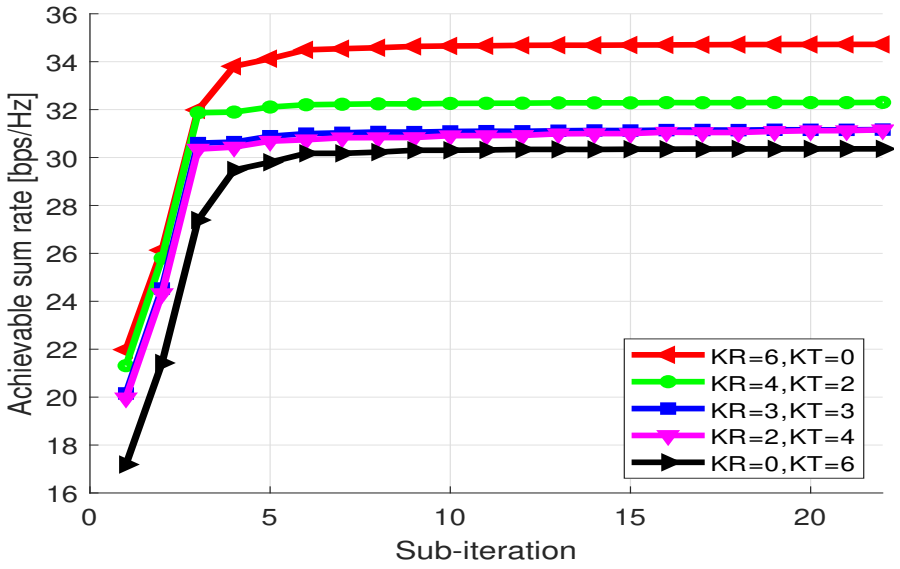

Figure 5.2: Continuous-valued coefficients.

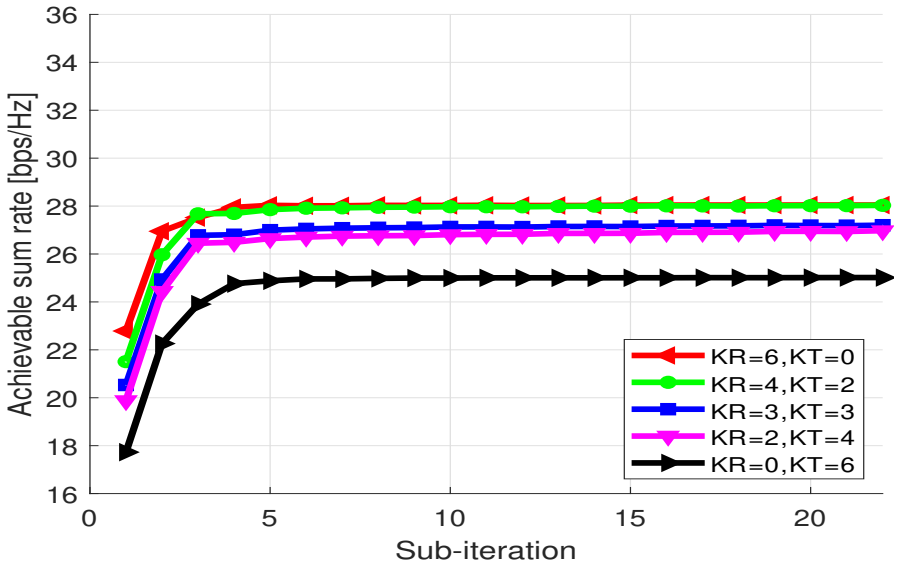

Figure 5.3: Discrete-valued coefficients.

The achievable sum-rate results for the continuous case are shown in Fig. 5.2. We assume that each iteration of Algorithms 1 consists of three sub-iterations, so that in each sub-iteration we optimize all of the users' covariance matrices or all of the RIS phase shifts or the power ratio. Hence, the achievable sum-rate in Figs. 5.2 is computed after every sub-iteration. As it can be noticed, all the curves converge within 10 sub-iterations. Due to the assumed geometry, the R-users should in most cases be located closer to the BS than the T-users. Therefore, the largest rate is obtained when all the users are in the R-region and the lowest when all the users are located in the T-region.

The achievable sum-rate results for the discrete case are shown in Fig. **??**. Discretization values for the RIS reflection/refraction coefficients are provided in Table 1 in [157], which contains only two states. Besides, the reflection coefficient amplitude in that table is much weaker than the refraction coefficient amplitude. The convergence rate for all curve is around 5-6 bit/s/Hz lower than in the continuous case. In the discrete case, the achievable sum-rate when the users are distributed between the R- and the T-region are comparable to the case when all of the users are placed in the R-zone. In general, the use of IOS-RIS can help us to "reach" all the user no matter if they are in the R- or the T-region and on that way provide the largest achievable sum-rate.

5.6 Conclusion

In this chapter, we have proposed optimization algorithms for maximizing the sum-rate in IOS-aided MIMO broadcast channels. We have optimized the covariance matrices at the transmitter, the reflection and transmission coefficients of the IOS, and the ratio between the reflected and refracted power. The simulations results demonstrate that the presented algorithm provides a rapid convergence rate in a few iterations.

6 Conclusion

This chapter highlights conclusions of the thesis and discusses possible directions for future work.

6.1 Summary

In general, this thesis provides contributions on: (i) the performance of RISs based on accurate and realistic electromagnetic reradiation models. Moreover, it provides some of optimization frameworks for enhancing the communication system performance on the following two use case: (i) To jointly improves the information rate and the amount of harvested power in a RIS-aided MISO downlink multiuser wireless network. (ii) enhancing spectral efficiency for large number of users located on cell edge or on the other side of the RIS by utilizing the intelligent omni-surfaces (IOSs).

The thesis starts by introducing, in Chapter 1, the challenges of fulfilling the tough requirements of of 6G networks. To proceed further, it introduces the concept of smart radio environments (SRE) and RISs as one of the enabling technologies, through highlighting its properties, functionalities, and benefits compared to the existing technologies. Then it summarizes some of the potential applications of RIS in 6G networks.

Chapter 2 also introduces the state-of-art optimization techniques developed for RIS-aided systems. Firstly, it introduces the system models of RIS-aided MIMO systems and then investigates the reflection principle of RISs. In addition, it introduces the Optimization techniques challenges of RIS-assisted systems. Also, The proposed optimization techniques for designing the continuous and discrete phase shifts are presented in detail.

Chapter 3 studies the impact of realistic reradiation models for RISs as a function of the sub-wavelength inter-distance between nearby elements of the RIS, the quantization levels of the reflection coefficients, the interplay between the amplitude and phase of the reflection coefficients, and the presence of electromagnetic interference. Furthermore, it investigates both case studies on the far-field and near-field regions of a RIS. In conclusion, our study shows that, due to design constraints, such as the need to use quantized reflection coefficients or the inherent interplay between the phase and the amplitude of the reflection coefficients, a RIS may reradiate power towards unwanted directions that depend on the intended and interfering electromagnetic waves. Furthermore, we have shown that the prominent peak of the reradiated pattern may not be perfectly steered towards the nominal direction of reradiation for large angles of deflection. Therefore, it is, in general, essential to optimize a RIS by taking into account the entire reradiation pattern by design in order to maximize the reradiated power towards the desired directions of reradiation while keeping the power reradiated towards other unwanted directions at a low level. Among the considered designs for RISs, our study shows that a 2-bit digitally controllable RIS with an almost constant reflection amplitude as a function of the applied phase shift, and whose scattering elements have a size and an inter-distance between $(1/8)$-th and $(1/4)$-th of the signal wavelength may be a good trade-off between performance, implementation complexity, and cost.

Chapter 4 considers the problem of simultaneously optimizing the information rate and the harvested power in a reconfigurable intelligent surface (RIS)-aided multiple-input single-output downlink multiuser wireless network with simultaneous wireless information, and

power transfer (SWIPT) is addressed. The beamforming vectors, RIS reflection coefficients, and power split ratios are jointly optimized subject to maximum power constraints, minimum harvested power constraints, and realistic constraints on the RIS reflection coefficients. A practical algorithm is developed through an interplay of alternating optimization, sequential optimization, and pricing-based methods. Moreover, it considered the realistic case in which a deterministic function couples the phases and moduli of the RIS reflection coefficients. In addition, the optimization of the power split ratio at the receiver, which is a novel feature compared to most related works on RIS-aided and SWIPT-based systems.

Chapter 5 proposes an optimization algorithm that has a rapid convergence rate in a few iterations for maximizing the sum rate in IOS-aided MIMO broadcast channels, which can be exploited to serve the cell-edge user and enhance network coverage. The optimization algorithm is applied to optimize the covariance matrix at the base station, the reflection and transmission coefficients matrix at the IOS, and the amount of power that is reflected and refracted from the IOS. This work's distinguishable feature lies in considering that the reflection and transmission coefficients of an IOS are tightly coupled. Finally, Chapter 6 summarizes the main findings of the thesis and discusses possible future directions that are worth investigating to unlock the full potential of RIS and bring it into practice. In addition, we have to consider that the results presented in Chapter 3, are done under some assumption that needs to be modified to study a more practical consideration and constraints such as the mutual coupling between the reflecting elements especially for smaller inter-distance between the RIS-elements (i.e., (1/32)th of wavelength).

To summarize, in the general context of wireless communications, the results obtained in this thesis reveals that one should always design optimization techniques taking into account not only the realistic reradiation models but also the hardware design constraints

6.2 Future Work

Regarding the road ahead, there are several fundamental and open research issues that deserve attention. In this section, we summarize some open research directions in the context of RIS-aided wireless systems.

6.2.1 Active RIS

Nearly Passive RIS architectures have attracted significant attention due to their low hardware cost and energy consumption. Nevertheless, they have their limitations. Since the signals received at the receiver suffer form the dual path loss and attenuation especially if the receiver is located in the far-field region. Consequently, the received power is relatively small compared with the power received form the direct links, especially when the direct links are strong. To overcome this issue, Utilizing an active RIS architecture is a promising solution [164, 165, 166, 167]. The active RISs are capable of simultaneously amplifying the magnitude of the reflected

signals by using an additional power supply. Therefore, more dedicated beamforming at the BS and phase shifts at the RIS should be designed to balance the performance and energy consumption. Besides, defining the optimal deployment of the active RISs is still an open question.

6.2.2 Double/multi-RIS

Most of the existing works have considered the deployment of a single RIS however, it may be suitable to implement multiple RISs, in some scenarios, in order to direct the signals and bypass the blocking objects in a smart manner [146]. Thus, double/multiple RISs may be utilized to realize a blockage-free communication network via multiple signal reflections. However, this new architecture require highly accurate CSI, which is challenging to obtain due to the coupling of the different reflected signal links and more channel coefficients to be estimated [168, 169, 170]. Finally, the analysis and design of multi-RIS communications at high frequency bands and the impact of the secondary reflections among the RISs are an open research issues.

6.2.3 Near-Field Channel

Since the current nearly passive RIS architecture is utilizing the radio waves existed in the environment to operate, the RIS planar array should have typically large aperture to compensate the absence of power amplifiers and digital signal processing units for regenerating the signals and to ensure a sufficiently large coverage. Depending on the size of the RIS, the operating frequency, and its distance from the transmitter and the receiver, it may be necessary to utilize a near-field communication model [171, 172, 173, 174]. Since the near-field communication models are less understood it is essential to examine accurate channel models to reveal the fundamental performance limits and the scaling laws of RISs in this context.

6.2.4 Mobility

Since the most existing works focus on quasi-static scenarios where the users and the RISs are assumed to be nearly stationary, it is inevitable to investigate scenarios with mobility [175, 176, 177, 178, 179], such as wireless systems where the RISs may even be mobile as they may be carried by UAVs or they may be deployed in trains. More advanced channel estimation methods are needed to quickly and accurately track the rapidly time-varying channels for accurate phase shifts design at the RIS and to be updated more frequently. In high-mobility scenarios, it is imperative to design efficient signal processing schemes to avoid a expensive high overhead which deserves further research in more practical scenarios.

6.2.5 Electromagnetically Consistent Signal Processing

Since the current signal processing methods for RIS-aided systems are based on RIS and channel that adhere to the "signals and systems" perspective. In this context, the electromagnetic aspects of the design of RISs are abstracted and simplified, however, the RIS is a sophisticated device that does not operate as an ideal mirror. Depending on the specific design, an RIS may reradiate signals towards undesired directions (grating lobes), which need to be kept under control in order to avoid wasting power towards unwanted directions and to create interference[180]. It is inevitable and important to develop electromagnetically consistent models and the corresponding signal processing algorithms that take them into account. Furthermore, these signal processing algorithms need to account for the electromagnetic interference produced by RISs and the spatial correlation due to the mutual coupling that may originate from closely spaced scattering elements.

Bibliography

[1] W. Jiang, B. Han, M. A. Habibi, and H. D. Schotten, "The road towards 6g: A comprehensive survey," *IEEE Open Journal of the Communications Society*, vol. 2, pp. 334–366, 2021.

[2] M. Di Renzo, M. Debbah, D.-T. Phan-Huy, A. Zappone, M.-S. Alouini, C. Yuen, V. Sciancalepore, G. C. Alexandropoulos, J. Hoydis, H. Gacanin *et al.*, "Smart radio environments empowered by reconfigurable AI meta-surfaces: An idea whose time has come," *EURASIP Journal on Wireless Communications and Networking*, vol. 2019, no. 1, pp. 1–20, 2019.

[3] Q. Wu and R. Zhang, "Towards smart and reconfigurable environment: Intelligent reflecting surface aided wireless network," *IEEE Communications Magazine*, vol. 58, no. 1, pp. 106–112, 2019.

[4] M. Di Renzo, K. Ntontin, J. Song, F. H. Danufane, X. Qian, F. Lazarakis, J. De Rosny, D.-T. Phan-Huy, O. Simeone, R. Zhang, M. Debbah, G. Lerosey, M. Fink, S. Tretyakov, and S. Shamai, "Reconfigurable intelligent surfaces vs. relaying: Differences, similarities, and performance comparison," *IEEE Open Journal of the Communications Society*, vol. 1, pp. 798–807, 2020.

[5] Q. Wu, S. Zhang, B. Zheng, C. You, and R. Zhang, "Intelligent reflecting surface-aided wireless communications: A tutorial," *IEEE Transactions on Communications*, vol. 69, no. 5, pp. 3313–3351, 2021.

[6] Y.-C. Liang, J. Chen, R. Long, Z.-Q. He, X. Lin, C. Huang, S. Liu, X. S. Shen, and M. Di Renzo, "Reconfigurable intelligent surfaces for smart wireless environments: channel estimation, system design and applications in 6G networks," *Science China Information Sciences*, vol. 64, no. 10, pp. 1–21, 2021.

[7] S. Abeywickrama, R. Zhang, Q. Wu, and C. Yuen, "Intelligent reflecting surface: Practical phase shift model and beamforming optimization," *IEEE Transactions on Communications*, vol. 68, no. 9, pp. 5849–5863, 2020.

[8] L. Dai, B. Wang, M. Wang, X. Yang, J. Tan, S. Bi, S. Xu, F. Yang, Z. Chen, M. Di Renzo, C.-B. Chae, and L. Hanzo, "Reconfigurable intelligent surface-based wireless communica-

tions: Antenna design, prototyping, and experimental results," *IEEE Access*, vol. 8, pp. 45 913–45 923, 2020.

[9] H. Zhang, S. Zeng, B. Di, Y. Tan, M. Di Renzo, M. Debbah, Z. Han, H. V. Poor, and L. Song, "Intelligent omni-surfaces for full-dimensional wireless communications: Principles, technology, and implementation," *IEEE Communications Magazine*, vol. 60, no. 2, pp. 39–45, 2022.

[10] W. Tang, X. Chen, M. Z. Chen, J. Y. Dai, Y. Han, M. Di Renzo, S. Jin, Q. Cheng, and T. J. Cui, "Path loss modeling and measurements for reconfigurable intelligent surfaces in the millimeter-wave frequency band," *CoRR*, vol. abs/2101.08607, 2021. [Online]. Available: https://arxiv.org/abs/2101.08607

[11] R. Fara, P. Ratajczak, D.-T. Phan-Huy, A. Ourir, M. Di Renzo, and J. de Rosny, "A prototype of reconfigurable intelligent surface with continuous control of the reflection phase," *IEEE Wireless Communications*, vol. 29, no. 1, pp. 70–77, 2022.

[12] S. Nayak and R. Patgiri, "6G communication: Envisioning the key issues and challenges," *arXiv preprint arXiv:2004.04024*, 2020.

[13] M. D. Renzo, M. Debbah, D. T. Phan-Huy, A. Zappone, M. S. Alouini, C. Yuen, V. Sciancalepore, G. C. Alexandropoulos, J. Hoydis, H. Gacanin, J. de Rosny, A. Bounceur, G. Lerosey, and M. Fink, "Smart radio environments empowered by reconfigurable AI meta-surfaces: an idea whose time has come," *Eurasip Journal on Wireless Communications and Networking*, vol. 2019, no. 1, 2019.

[14] Q. Wu and R. Zhang, "Towards smart and reconfigurable environment: Intelligent reflecting surface aided wireless network," *IEEE Commun. Mag.*, vol. 58, no. 1, pp. 106–112, 2020.

[15] V. S. Asadchy, M. Albooyeh, S. N. Tcvetkova, A. Díaz-Rubio, Y. Ra'di, and S. A. Tretyakov, "Perfect control of reflection and refraction using spatially dispersive metasurfaces," *Phys. Rev. B*, vol. 94, p. 075142, Aug 2016. [Online]. Available: https://link.aps.org/doi/10.1103/PhysRevB.94.075142

[16] A. Díaz-Rubio, V. S. Asadchy, A. Elsakka, and S. A. Tretyakov, "From the generalized reflection law to the realization of perfect anomalous reflectors," *Science Advances*, vol. 3, no. 8, 2017. [Online]. Available: https://advances.sciencemag.org/content/3/8/e1602714

[17] E. Basar, M. Di Renzo, J. De Rosny, M. Debbah, M.-S. Alouini, and R. Zhang, "Wireless Communications Through Reconfigurable Intelligent Surfaces," *IEEE Access*, vol. 7, no. June 2018, pp. 116 753–116 773, 2019.

[18] C. Huang, S. Hu, G. C. Alexandropoulos, A. Zappone, C. Yuen, R. Zhang, M. D. Renzo, and M. Debbah, "Holographic MIMO surfaces for 6g wireless networks: Opportunities, challenges, and trends," *IEEE Wireless Commun.*, vol. 27, no. 5, pp. 118–125, 2020.

[19] J. Zhao, "A survey of intelligent reflecting surfaces (irss): Towards 6g wireless communication networks," *arXiv preprint arXiv:1907.04789*, 2019.

[20] S. Hu, F. Rusek, and O. Edfors, "Beyond massive-mimo: The potential of data-transmission with large intelligent surfaces," *IEEE Transactions on Acoustics, Speech, and Signal Processing*, vol. 66, no. 10, pp. 2746–2758, 5 2018.

[21] I. Yildirim, A. Uyrus, and E. Basar, "Modeling and analysis of reconfigurable intelligent surfaces for indoor and outdoor applications in future wireless networks," *IEEE Transactions on Communications*, vol. 69, no. 2, pp. 1290–1301, 2021.

[22] G. Lavigne, K. Achouri, V. S. Asadchy, S. A. Tretyakov, and C. Caloz, "Susceptibility derivation and experimental demonstration of refracting metasurfaces without spurious diffraction," *IEEE Transactions on Antennas and Propagation*, vol. 66, no. 3, pp. 1321–1330, 2018.

[23] N. Yu, P. Genevet, M. A. Kats, F. Aieta, J.-P. Tetienne, F. Capasso, and Z. Gaburro, "Light propagation with phase discontinuities: generalized laws of reflection and refraction," *science*, vol. 334, no. 6054, pp. 333–337, 2011.

[24] S. Xia, Y. Shi, Y. Zhou, and X. Yuan, "Reconfigurable intelligent surface for massive connectivity: Joint activity detection and channel estimation," *IEEE Transactions on Signal Processing*, vol. 69, pp. 5693–5707, 2021.

[25] Y. Lu and L. Dai, "Reconfigurable intelligent surface based hybrid precoding for THz communications," *arXiv preprint arXiv:2012.06261*, 2020.

[26] B. Ning, Z. Chen, W. Chen, and Y. Du, "Channel estimation and transmission for intelligent reflecting surface assisted THz communications," in *ICC 2020-2020 IEEE International Conference on Communications (ICC)*. IEEE, 2020, pp. 1–7.

[27] K. Tekbıyık, G. Karabulut Kurt, A. Rıza Ekti, A. Görçin, and H. Yanikomeroglu, "Reconfigurable intelligent surface empowered terahertz communication for LEO satellite networks," *arXiv e-prints*, pp. arXiv–2007, 2020.

[28] X. Shao, C. You, W. Ma, X. Chen, and R. Zhang, "Target sensing with intelligent reflecting surface: Architecture and performance," *IEEE Journal on Selected Areas in Communications*, vol. 40, no. 7, pp. 2070–2084, 2022.

[29] Y. Tang, G. Ma, H. Xie, J. Xu, and X. Han, "Joint transmit and reflective beamforming design for irs-assisted multiuser miso swipt systems," in *ICC 2020 - 2020 IEEE International Conference on Communications (ICC)*, 2020, pp. 1–6.

[30] T. Bai, C. Pan, C. Han, and L. Hanzo, "Empowering mobile edge computing by exploiting reconfigurable intelligent surface," *arXiv preprint arXiv:2102.02569*, 2021.

[31] X. Hu, C. Masouros, and K.-K. Wong, "Reconfigurable intelligent surface aided mobile edge computing: From optimization-based to location-only learning-based solutions," *IEEE Transactions on Communications*, 2021.

[32] H. Hashida, Y. Kawamoto, and N. Kato, "Intelligent reflecting surface placement optimization in air-ground communication networks toward 6G," *IEEE Wireless Communications*, vol. 27, no. 6, pp. 146–151, 2020.

[33] L. Ge, P. Dong, H. Zhang, J.-B. Wang, and X. You, "Joint beamforming and trajectory optimization for intelligent reflecting surfaces-assisted UAV communications," *IEEE Access*, vol. 8, pp. 78 702–78 712, 2020.

[34] C. Pan, G. Zhou, K. Zhi, S. Hong, T. Wu, Y. Pan, H. Ren, M. Di Renzo, A. L. Swindlehurst, R. Zhang, and A. Y. Zhang, "An overview of signal processing techniques for ris/irs-aided wireless systems," 2021. [Online]. Available: https://arxiv.org/abs/2112.05989

[35] D. M. Pozar, *Microwave engineering*. John wiley & sons, 2011.

[36] Y. Yang, S. Zhang, and R. Zhang, "IRS-enhanced OFDMA: Joint resource allocation and passive beamforming optimization," *IEEE Wireless Commun. Lett.*, vol. 9, no. 6, pp. 760–764, Jun. 2020.

[37] Z. Zhang and L. Dai, "A joint precoding framework for wideband reconfigurable intelligent surface-aided cell-free network," *IEEE Trans. Signal Process.*, vol. 69, pp. 4085–4101, Jun. 2021.

[38] T. Bai, C. Pan, H. Ren, Y. Deng, M. Elkashlan, and A. Nallanathan, "Resource allocation for intelligent reflecting surface aided wireless powered mobile edge computing in OFDM systems," *IEEE Trans. Wireless Commun.*, vol. 20, no. 8, pp. 5389–5407, Aug. 2021.

[39] S. Abeywickrama, R. Zhang, Q. Wu, and C. Yuen, "Intelligent reflecting surface: Practical phase shift model and beamforming optimization," *IEEE Trans. Commun.*, vol. 68, no. 9, pp. 5849–5863, Sept. 2020.

[40] W. Cai, H. Li, M. Li, and Q. Liu, "Practical modeling and beamforming for intelligent reflecting surface aided wideband systems," *IEEE Commun. Lett.*, vol. 24, no. 7, pp. 1568–1571, Jul. 2020.

[41] H. Li, W. Cai, Y. Liu, M. Li, Q. Liu, and Q. Wu, "Intelligent reflecting surface enhanced wideband MIMO-OFDM communications: From practical model to reflection optimization," *IEEE Trans. Commun.*, vol. 69, no. 7, pp. 4807–4820, Jul. 2021.

[42] B. Feng, J. Gao, Y. Wu, W. Zhang, X.-G. Xia, and C. Xiao, "Optimization techniques in reconfigurable intelligent surface aided networks," *IEEE Wireless Communications*, vol. 28, no. 6, pp. 87–93, 2021.

[43] Q. Wu and R. Zhang, "Intelligent reflecting surface enhanced wireless network via joint active and passive beamforming," *IEEE Transactions on Wireless Communications*, vol. 18, no. 11, pp. 5394–5409, 2019.

[44] X. Yu, D. Xu, D. W. K. Ng, and R. Schober, "Irs-assisted green communication systems: Provable convergence and robust optimization," *IEEE Transactions on Communications*, vol. 69, no. 9, pp. 6313–6329, 2021.

[45] K. Shen and W. Yu, "Fractional programming for communication systems - part I: Power control and beamforming," *IEEE Trans. Signal Process.*, vol. 66, no. 10, pp. 2616–2630, May 2018.

[46] Q. Shi, M. Razaviyayn, Z.-Q. Luo, and C. He, "An iteratively weighted MMSE approach to distributed sum-utility maximization for a MIMO interfering broadcast channel," *IEEE Trans. Signal Process.*, vol. 59, no. 9, pp. 4331–4340, Sept. 2011.

[47] J. Chen, Y.-C. Liang, Y. Pei, and H. Guo, "Intelligent reflecting surface: A programmable wireless environment for physical layer security," *IEEE Access*, vol. 7, pp. 82 599–82 612, Jun. 2019.

[48] G. Zhou, C. Pan, H. Ren, K. Wang, M. Elkashlan, and M. Di Renzo, "Stochastic learning-based robust beamforming design for RIS-aided millimeter-wave systems in the presence of random blockages," *IEEE Trans. Veh. Technol.*, vol. 70, no. 1, pp. 1057–1061, Jan. 2021.

[49] Y. Zhang, C. Zhong, Z. Zhang, and W. Lu, "Sum rate optimization for two way communications with intelligent reflecting surface," *IEEE Commun. Lett.*, vol. 24, no. 5, pp. 1090–1094, May 2020.

[50] X. Yu, D. Xu, and R. Schober, "Enabling secure wireless communications via intelligent reflecting surfaces," in *Proc. IEEE Global Commun. Conf. (Globecom)*, Dec. 2019, pp. 1–6.

[51] S. Zhang and R. Zhang, "Capacity characterization for intelligent reflecting surface aided MIMO communication," *IEEE J. Sel. Areas Commun.*, vol. 38, no. 8, pp. 1823–1838, Aug. 2020.

[52] Q. Wu and R. Zhang, "Joint active and passive beamforming optimization for intelligent reflecting surface assisted SWIPT under QoS constraints," *IEEE J. Sel. Areas Commun.*, vol. 38, no. 8, pp. 1735–1748, Aug. 2020.

[53] Y. Omid, S. M. Shahabi, C. Pan, Y. Deng, and A. Nallanathan, "Low-complexity robust beamforming design for IRS-aided MISO systems with imperfect channels," *IEEE Commun. Lett.*, vol. 25, no. 5, pp. 1697–1701, May 2021.

[54] Q. Wu and R. Zhang, "Intelligent reflecting surface enhanced wireless network via joint active and passive beamforming," *IEEE Trans. Wireless Commun.*, vol. 18, no. 11, pp. 5394–5409, Nov. 2019.

[55] M. Cui, G. Zhang, and R. Zhang, "Secure wireless communication via intelligent reflecting surface," *IEEE Wireless Commun. Lett.*, vol. 8, no. 5, pp. 1410–1414, Oct. 2019.

[56] Z. Chu, W. Hao, P. Xiao, and J. Shi, "Intelligent reflecting surface aided multi-antenna secure transmission," *IEEE Wireless Commun. Lett.*, vol. 9, no. 1, pp. 108–112, Jan. 2020.

[57] P. Wang, J. Fang, X. Yuan, Z. Chen, and H. Li, "Intelligent reflecting surface-assisted millimeter wave communications: Joint active and passive precoding design," *IEEE Trans. Veh. Technol.*, vol. 69, no. 12, pp. 14 960–14 973, Dec. 2020.

[58] G. Yang, X. Xu, Y.-C. Liang, and M. Di Renzo, "Reconfigurable intelligent surface-assisted non-orthogonal multiple access," *IEEE Trans. Wireless Commun.*, vol. 20, no. 5, pp. 3137–3151, May 2021.

[59] G. Zhou, C. Pan, H. Ren, K. Wang, and Z. Peng, "Secure wireless communication in RIS-aided MISO system with hardware impairments," *IEEE Wireless Commun. Lett.*, vol. 10, no. 6, pp. 1309–1313, Jun. 2021.

[60] M. Zeng, X. Li, G. Li, W. Hao, and O. A. Dobre, "Sum rate maximization for IRS-assisted uplink NOMA," *IEEE Commun. Lett.*, vol. 25, no. 1, pp. 234–238, Jan. 2021.

[61] M. Grant and S. Boyd, "CVX: Matlab software for disciplined convex programming, version 2.1," 2014.

[62] N. Sidiropoulos, T. Davidson, and Z.-Q. Luo, "Transmit beamforming for physical-layer multicasting," *IEEE Trans. Signal Process.*, vol. 54, no. 6, pp. 2239–2251, Jan. 2006.

[63] M. Fu, Y. Zhou, and Y. Shi, "Intelligent reflecting surface for downlink non-orthogonal multiple access networks," in *Proc. IEEE Global Commun. Conf. Workshops (GC Wkshps)*, Dec. 2019, pp. 1–6.

[64] X. Hu, C. Masouros, and K.-K. Wong, "Reconfigurable intelligent surface aided mobile edge computing: From optimization-based to location-only learning-based solutions," *IEEE Trans. Commun.*, vol. 69, no. 6, pp. 3709–3725, Jun. 2021.

[65] C. Huang, A. Zappone, G. C. Alexandropoulos, M. Debbah, and C. Yuen, "Reconfigurable intelligent surfaces for energy efficiency in wireless communication," *IEEE Trans. Wireless Commun.*, vol. 18, no. 8, pp. 4157–4170, Aug. 2019.

[66] G. Zhou, C. Pan, H. Ren, K. Wang, and A. Nallanathan, "Intelligent reflecting surface aided multigroup multicast MISO communication systems," *IEEE Trans. Signal Process.*, vol. 68, pp. 3236–3251, Apr. 2020.

[67] H. Shen, W. Xu, S. Gong, Z. He, and C. Zhao, "Secrecy rate maximization for intelligent reflecting surface assisted multi-antenna communications," *IEEE Commun. Lett.*, vol. 23, no. 9, pp. 1488–1492, Sept. 2019.

[68] L. Dong and H.-M. Wang, "Secure MIMO transmission via intelligent reflecting surface," *IEEE Wireless Commun. Lett.*, vol. 9, no. 6, pp. 787–790, Jun. 2020.

[69] C. Pan, H. Ren, K. Wang, M. Elkashlan, A. Nallanathan, J. Wang, and L. Hanzo, "Intelligent reflecting surface aided MIMO broadcasting for simultaneous wireless information and power transfer," *IEEE J. Sel. Areas Commun.*, vol. 38, no. 8, pp. 1719–1734, Aug. 2020.

[70] Z. Peng, Z. Zhang, C. Pan, L. Li, and A. L. Swindlehurst, "Multiuser full-duplex two-way communications via intelligent reflecting surface," *IEEE Trans. Signal Process.*, vol. 69, pp. 837–851, Jan. 2021.

[71] C. Pan, H. Ren, K. Wang, W. Xu, M. Elkashlan, A. Nallanathan, and L. Hanzo, "Multicell MIMO communications relying on intelligent reflecting surfaces," *IEEE Trans. Wireless Commun.*, vol. 19, no. 8, pp. 5218–5233, Aug. 2020.

[72] X. Yu, D. Xu, and R. Schober, "MISO wireless communication systems via intelligent reflecting surfaces: (invited paper)," in *Proc. IEEE/CIC Int. Conf. Commun. China (ICCC)*, Aug. 2019, pp. 735–740.

[73] P. Wang, J. Fang, L. Dai, and H. Li, "Joint transceiver and large intelligent surface design for massive MIMO mmWave systems," *IEEE Trans. Wireless Commun.*, vol. 20, no. 2, pp. 1052–1064, Feb. 2021.

[74] H.-M. Wang, J. Bai, and L. Dong, "Intelligent reflecting surfaces assisted secure transmission without eavesdropper's CSI," *IEEE Signal Process. Lett.*, vol. 27, pp. 1300–1304, Jul. 2020.

[75] H. Guo, Y.-C. Liang, J. Chen, and E. G. Larsson, "Weighted sum-rate maximization for reconfigurable intelligent surface aided wireless networks," *IEEE Trans. Wireless Commun.*, vol. 19, no. 5, pp. 3064–3076, May 2020.

[76] Y. Li, M. Jiang, Q. Zhang, and J. Qin, "Joint beamforming design in multi-cluster MISO NOMA reconfigurable intelligent surface-aided downlink communication networks," *IEEE Trans. Commun.*, vol. 69, no. 1, pp. 664–674, Jan. 2021.

[77] H. Yang, X. Yuan, J. Fang, and Y.-C. Liang, "Reconfigurable intelligent surface aided constant-envelope wireless power transfer," *IEEE Trans. Signal Process.*, vol. 69, pp. 1347–1361, Feb. 2021.

[78] G. Zhou, C. Pan, H. Ren, K. Wang, and A. Nallanathan, "A framework of robust transmission design for IRS-aided MISO communications with imperfect cascaded channels," *IEEE Trans. Signal Process.*, vol. 68, pp. 5092–5106, Aug. 2020.

[79] L. Zhang, C. Pan, Y. Wang, H. Ren, and K. Wang, "Robust beamforming design for intelligent reflecting surface aided cognitive radio systems with imperfect cascaded CSI," *early access in IEEE Trans. Cogn. Commun. Netw.*, pp. 1–1, 2021.

[80] Y. Chen, Y. Wang, and L. Jiao, "Robust transmission for reconfigurable intelligent surface aided millimeter wave vehicular communications with statistical CSI," *early access in IEEE Trans. Wireless Commun.*, pp. 1–1, 2021.

[81] J. Ye, S. Guo, and M.-S. Alouini, "Joint reflecting and precoding designs for SER minimization in reconfigurable intelligent surfaces assisted MIMO systems," *IEEE Trans. Wireless Commun.*, vol. 19, no. 8, pp. 5561–5574, Aug. 2020.

[82] X. Hu, C. Zhong, and Z. Zhang, "Angle-domain intelligent reflecting surface systems: Design and analysis," *IEEE Trans. Commun.*, vol. 69, no. 6, pp. 4202–4215, Jun. 2021.

[83] K. Zhi, C. Pan, H. Ren, and K. Wang, "Ergodic rate analysis of reconfigurable intelligent surface-aided massive MIMO systems with ZF detectors," *early access in IEEE Commun. Lett.*, 2021.

[84] A. Papazafeiropoulos, C. Pan, P. Kourtessis, S. Chatzinotas, and J. M. Senior, "Intelligent reflecting surface-assisted MU-MISO systems with imperfect hardware: Channel estimation and beamforming design," *early access in IEEE Trans. Wireless Commun.*, pp. 1–1, 2021.

[85] N. S. Perovic, L.-N. Tran, M. Di Renzo, and M. F. Flanagan, "Achievable rate optimization for MIMO systems with reconfigurable intelligent surfaces," *IEEE Trans. Wireless Commun.*, vol. 20, no. 6, pp. 3865–3882, 2021.

[86] M. Shao, Q. Li, and W.-K. Ma, "Minimum symbol-error probability symbol-level precoding with intelligent reflecting surface," *IEEE Wireless Commun. Lett.*, vol. 9, no. 10, pp. 1601–1605, Oct. 2020.

[87] S. Wang, Q. Li, and M. Shao, "One-bit symbol-level precoding for MU-MISO downlink with intelligent reflecting surface," *IEEE Signal Process. Lett.*, vol. 27, pp. 1784–1788, Sept. 2020.

[88] N. S. Perović, M. Di Renzo, and M. F. Flanagan, "Channel capacity optimization using reconfigurable intelligent surfaces in indoor mmwave environments," in *Proc. IEEE Int. Conf. Commun. (ICC)*, 2020, pp. 1–7.

[89] N. S. Perović, L.-N. Tran, M. Di Renzo, and M. F. Flanagan, "Optimization of RIS-aided MIMO systems via the cutoff rate," *IEEE Wireless Commun. Lett.*, vol. 10, no. 8, pp. 1692–1696, Aug. 2021.

[90] N. S. Perović, L.-N. Tran, M. Di Renzo, and M. F. Flanagan, "On the maximum achievable sum-rate of the RIS-aided MIMO broadcast channel," *arXiv:2110.01700*, 2021.

[91] A. Beck and M. Teboulle, "A fast iterative shrinkage-thresholding algorithm for linear inverse problems," *SIAM journal on imaging sciences*, vol. 2, no. 1, pp. 183–202, 2009.

[92] K. Zhi, C. Pan, H. Ren, and K. Wang, "Power scaling law analysis and phase shift optimization of RIS-aided massive MIMO systems with statistical CSI," 2020. [Online]. Available: https://arxiv.org/abs/2010.13525

[93] ——, "Statistical CSI-based design for reconfigurable intelligent surface-aided massive MIMO systems with direct links," *IEEE Wireless Commun. Lett.*, vol. 10, no. 5, pp. 1128–1132, May 2021.

[94] K. Zhi, C. Pan, H. Ren, K. Wang, M. Elkashlan, M. Di Renzo, R. Schober, H. V. Poor, J. Wang, and L. Han, "Two-timescale design for reconfigurable intelligent surface-aided massive MIMO systems with imperfect CSI," 2021. [Online]. Available: https://arxiv.org/abs/2108.07622

[95] J. Dai, Y. Wang, C. Pan, K. Zhi, H. Ren, and K. Wang, "Reconfigurable intelligent surface aided massive MIMO systems with low-resolution DACs," *IEEE Commun. Lett.*, vol. 25, no. 9, pp. 3124–3128, Sept. 2021.

[96] C. Huang, R. Mo, and C. Yuen, "Reconfigurable intelligent surface assisted multiuser MISO systems exploiting deep reinforcement learning," *IEEE J. Sel. Areas Commun.*, vol. 38, no. 8, pp. 1839–1850, Aug. 2020.

[97] K. Feng, Q. Wang, X. Li, and C.-K. Wen, "Deep reinforcement learning based intelligent reflecting surface optimization for MISO communication systems," *IEEE Wireless Commun. Lett.*, vol. 9, no. 5, pp. 745–749, May 2020.

[98] H. Yang, Z. Xiong, J. Zhao, D. Niyato, L. Xiao, and Q. Wu, "Deep reinforcement learning-based intelligent reflecting surface for secure wireless communications," *IEEE Trans. Wireless Commun.*, vol. 20, no. 1, pp. 375–388, Jan. 2021.

[99] Q. Wu and R. Zhang, "Beamforming optimization for wireless network aided by intelligent reflecting surface with discrete phase shifts," *IEEE Trans. Commun.*, vol. 68, no. 3, pp. 1838–1851, Mar. 2020.

[100] M.-M. Zhao, Q. Wu, M.-J. Zhao, and R. Zhang, "Intelligent reflecting surface enhanced wireless networks: Two-timescale beamforming optimization," *IEEE Trans. Wireless Commun.*, vol. 20, no. 1, pp. 2–17, Jan. 2021.

[101] J. Yuan, Y.-C. Liang, J. Joung, G. Feng, and E. G. Larsson, "Intelligent reflecting surface-assisted cognitive radio system," *IEEE Trans. Commun.*, vol. 69, no. 1, pp. 675–687, Jan. 2021.

[102] S. Hu, Z. Wei, Y. Cai, C. Liu, D. W. K. Ng, and J. Yuan, "Robust and secure sum-rate maximization for multiuser MISO downlink systems with self-sustainable IRS," *IEEE Trans. Commun.*, vol. 69, no. 10, pp. 7032–7049, Oct. 2021.

[103] M. Shao, Q. Li, W.-K. Ma, and A. M.-C. So, "A framework for one-bit and constant-envelope precoding over multiuser massive MISO channels," *IEEE Trans. Signal Process.*, vol. 67, no. 20, pp. 5309–5324, Oct. 2019.

[104] L. You, J. Xiong, D. W. K. Ng, C. Yuen, W. Wang, and X. Gao, "Energy efficiency and spectral efficiency tradeoff in RIS-aided multiuser MIMO uplink transmission," *IEEE Trans. Signal Process.*, vol. 69, pp. 1407–1421, Jan. 2021.

[105] Q. Wu and R. Zhang, "Towards smart and reconfigurable environment: Intelligent reflecting surface aided wireless network," *IEEE Commun. Mag.*, vol. 58, no. 1, pp. 106–112, 2020.

[106] C. Liaskos, A. Tsioliaridou, A. Pitsillides, S. Ioannidis, and I. F. Akyildiz, "Using any surface to realize a new paradigm for wireless communications," *Commun. ACM*, vol. 61, no. 11, pp. 30–33, 2018.

[107] M. Di Renzo, K. Ntontin, J. Song, F. H. Danufane, X. Qian, F. I. Lazarakis, J. de Rosny, D. Phan-Huy, O. Simeone, R. Zhang, M. Debbah, G. Lerosey, M. Fink, S. A. Tretyakov, and S. Shamai, "Reconfigurable intelligent surfaces vs. relaying: Differences, similarities, and performance comparison," *IEEE Open J. Commun. Soc.*, vol. 1, pp. 798–807, 2020.

[108] C. Pan, H. Ren, K. Wang, J. F. Kolb, M. Elkashlan, M. Chen, M. Di Renzo, Y. Hao, J. Wang, A. L. Swindlehurst, X. You, and L. Hanzo, "Reconfigurable intelligent surfaces for 6g systems: Principles, applications, and research directions," *IEEE Commun. Mag.*, vol. 59, no. 6, pp. 14–20, 2021.

[109] G. Gradoni, M. Di Renzo, A. Diaz-Rubio, S. Tretyakov, C. Caloz, Z. Peng, A. Alu, G. Lerosey, M. Fink, V. Galdi, T. J. Cui, B. Frazier, S. Anlage, M. Salucci, A. Massa, Q. Cheng, J. Wang, S. Jin, D. Dardari, N. Decarli, O. Yurduseven, M. Matthaiou, M. Kenney, G. Gordon, O. Georgiou, C. L. Nguyen, E. Martini, S. Maci, H. Wakatsuchi, and S. Phang, "Smart radio environments," 2021. [Online]. Available: https://arxiv.org/abs/2111.08676

[110] T. J. Cui, M. Q. Qi, X. Wan, J. Zhao, and Q. Cheng, "Coding metamaterials, digital metamaterials and programmable metamaterials," *Light Sci. Appl.*, vol. e218, no. 3, 2014.

[111] M. Di Renzo, A. Zappone, M. Debbah, M.-S. Alouini, C. Yuen, J. De Rosny, and S. Tretyakov, "Smart radio environments empowered by reconfigurable intelligent surfaces: How it works, state of research, and the road ahead," *IEEE Journal on Selected Areas in Communications*, vol. 38, no. 11, pp. 2450–2525, 2020.

[112] "European Telecommunications Standards Institute – Industry Specification Group (ISG) on Reconfigurable Intelligent Surfaces (RIS)." [Online]. Available: https://www.etsi.org/committee/1966-ris

[113] W. Tang, M. Z. Chen, J. Y. Dai, Y. Zeng, X. Zhao, S. Jin, Q. Cheng, and T. J. Cui, "Wireless communications with programmable metasurface: New paradigms, opportunities, and challenges on transceiver design," *IEEE Wireless Communications*, vol. 27, no. 2, pp. 180–187, 2020.

[114] N. Shlezinger, G. C. Alexandropoulos, M. F. Imani, Y. C. Eldar, and D. R. Smith, "Dynamic metasurface antennas for 6g extreme massive mimo communications," *IEEE Wireless Communications*, vol. 28, no. 2, pp. 106–113, 2021.

[115] C. Huang, S. Hu, G. C. Alexandropoulos, A. Zappone, C. Yuen, R. Zhang, M. Di Renzo, and M. Debbah, "Holographic MIMO surfaces for 6g wireless networks: Opportunities, challenges, and trends," *IEEE Wireless Commun.*, vol. 27, no. 5, pp. 118–125, 2020.

[116] D. Dardari, "Communicating with large intelligent surfaces: Fundamental limits and models," *IEEE Journal on Selected Areas in Communications*, vol. 38, no. 11, pp. 2526–2537, 2020.

[117] D. Dardari and N. Decarli, "Holographic communication using intelligent surfaces," *IEEE Communications Magazine*, vol. 59, no. 6, pp. 35–41, 2021.

[118] S. Phang, M. T. Ivrlač, G. Gradoni, S. C. Creagh, G. Tanner, and J. A. Nossek, "Near-field mimo communication links," *IEEE Transactions on Circuits and Systems I: Regular Papers*, vol. 65, no. 9, pp. 3027–3036, 2018.

[119] G. Gradoni and M. Di Renzo, "End-to-end mutual coupling aware communication model for reconfigurable intelligent surfaces: An electromagnetic-compliant approach based on mutual impedances," *IEEE Wireless Commun. Lett.*, vol. 10, no. 5, pp. 938–942, 2021.

[120] X. Qian and M. Di Renzo, "Mutual coupling and unit cell aware optimization for reconfigurable intelligent surfaces," *IEEE Wireless Commun. Lett.*, vol. 10, no. 6, pp. 1183–1187, 2021.

[121] A. Abrardo, D. Dardari, M. Di Renzo, and X. Qian, "Mimo interference channels assisted by reconfigurable intelligent surfaces: Mutual coupling aware sum-rate optimization based on a mutual impedance channel model," *IEEE Wireless Communications Letters*, vol. 10, no. 12, pp. 2624–2628, 2021.

[122] R. J. Williams, P. Ramírez-Espinosa, J. Yuan, and E. De Carvalho, "Electromagnetic based communication model for dynamic metasurface antennas," *IEEE Transactions on Wireless Communications*, pp. 1–1, 2022.

[123] M. Di Renzo, F. H. Danufane, and S. Tretyakov, "Communication models for reconfigurable intelligent surfaces: From surface electromagnetics to wireless networks optimization," 2021. [Online]. Available: https://arxiv.org/abs/2110.00833

[124] M. Moccia, S. Liu, R. Y. Wu, G. Castaldi, A. Andreone, T. J. Cui, and V. Galdi, "Coding metasurfaces for diffuse scattering: Scaling laws, bounds, and suboptimal design," *Advanced Optical Materials*, vol. 5, no. 19, p. 1700455, 2017. [Online]. Available: https://onlinelibrary.wiley.com/doi/abs/10.1002/adom.201700455

[125] A. Díaz-Rubio and S. Tretyakov, "Macroscopic modeling of anomalously reflecting metasurfaces: Angular response and far-field scattering," *IEEE Trans. Antennas Propag.*, pp. 1–1, 2021.

[126] V. Degli-Esposti, E. M. Vitucci, M. Di Renzo, and S. A. Tretyakov, "Reradiation and scattering from a reconfigurable intelligent surface: A general macroscopic model," *CoRR*, vol. abs/2107.12773, 2021. [Online]. Available: https://arxiv.org/abs/2107.12773

[127] J. C. Liang, Q. Cheng, Y. Gao, C. Xiao, S. Gao, L. Zhang, S. Jin, and T. J. Cui, "An angle-insensitive 3-bit reconfigurable intelligent surface," *IEEE Transactions on Antennas and Propagation*, pp. 1–1, 2021.

[128] S. Abeywickrama, R. Zhang, Q. Wu, and C. Yuen, "Intelligent reflecting surface: Practical phase shift model and beamforming optimization," *IEEE Transactions on Communications*, vol. 68, no. 9, pp. 5849–5863, 2020.

[129] J.-B. Gros, V. Popov, M. A. Odit, V. Lenets, and G. Lerosey, "A reconfigurable intelligent surface at mmwave based on a binary phase tunable metasurface," *IEEE Open Journal of the Communications Society*, vol. 2, pp. 1055–1064, 2021.

[130] W. Tang, M. Z. Chen, X. Chen, J. Y. Dai, Y. Han, M. Di Renzo, Y. Zeng, S. Jin, Q. Cheng, and T. J. Cui, "Wireless communications with reconfigurable intelligent surface: Path loss modeling and experimental measurement," *IEEE Trans. Wireless Commun.*, vol. 20, no. 1, pp. 421–439, 2021.

[131] D. Bertsekas, *Nonlinear Programming*. Athena Scientific, 1999.

[132] M. Di Renzo *et al.*, "Smart radio environments empowered by reconfigurable intelligent surfaces: How it works, state of research, and the road ahead," *IEEE J. Sel. Areas Commun.*, vol. 38, no. 11, pp. 2450–2525, 2020.

[133] Q. Wu and R. Zhang, "Joint active and passive beamforming optimization for intelligent reflecting surface assisted SWIPT under QoS constraints," *IEEE J. Sel. Areas Commun.*, vol. 38, no. 8, pp. 1735–1748, 2020.

[134] Z. Li, W. Chen, Q. Wu, K. Wang, and J. Li, "Joint beamforming design and power splitting optimization in IRS-assisted SWIPT NOMA networks," *IEEE Trans. Wireless Commun.*, vol. 21, no. 3, pp. 2019–2033, 2022.

[135] C. Pan, H. Ren, K. Wang, M. Elkashlan, A. Nallanathan, J. Wang, and L. Hanzo, "Intelligent reflecting surface aided MIMO broadcasting for simultaneous wireless information and power transfer," *IEEE J. Sel. Areas Commun.*, vol. 38, no. 8, pp. 1719–1734, 2020.

[136] D. Xu, V. Jamali, X. Yu, D. W. K. Ng, and R. Schober, "Optimal resource allocation design for large IRS-assisted SWIPT systems: A scalable optimization framework," *IEEE Trans. Commun*, vol. 70, no. 2, pp. 1423–1441, 2022.

[137] A. Khalili, S. Zargari, Q. Wu, D. W. K. Ng, and R. Zhang, "Multi-objective resource allocation for IRS-aided SWIPT," *IEEE Commun. Lett.*, vol. 10, no. 6, pp. 1324–1328, 2021.

[138] C. He, X. Xie, K. Yang, and Z. J. Wang, "A joint power splitting, active and passive beamforming optimization framework for IRS assisted MIMO SWIPT system," *arXiv preprint arXiv:2105.14545*, 2021.

[139] S. Abeywickrama, R. Zhang, Q. Wu, and C. Yuen, "Intelligent reflecting surface: Practical phase shift model and beamforming optimization," *IEEE Trans. Commun*, vol. 68, no. 9, pp. 5849–5863, 2020.

[140] J. Tang, Y. Yu, M. Liu, D. K. C. So, X. Zhang, Z. Li, and K.-K. Wong, "Joint power allocation and splitting control for SWIPT-enabled NOMA systems," *IEEE Trans. Wireless Commun.*, vol. 19, no. 1, pp. 120–133, 2020.

[141] K. Shen and W. Yu, "Fractional programming for communication systems—part ii: Uplink scheduling via matching," *IEEE Trans. Signal Process.*, vol. 66, no. 10, pp. 2631–2644, 2018.

[142] S. Boyd and L. Vandenberghe, *Convex optimization*. Cambridge university press, 2004.

[143] C. Pan, H. Ren, M. Elkashlan, A. Nallanathan, and L. Hanzo, "Robust beamforming design for ultra-dense user-centric C-RAN in the face of realistic pilot contamination and limited feedback," *IEEE Trans. Wireless Commun.*, vol. 18, no. 2, pp. 780–795, 2019.

[144] A. Ben-Tal and A. Nemirovski, *Lectures on Modern Convex Optimization: Analysis, Algorithms, Engineering Applications*. MPS-SIAM Series on Optimization, SIAM, 2001.

[145] M. Di Renzo, A. Zappone, M. Debbah, M.-S. Alouini, C. Yuen, J. de Rosny, and S. Tretyakov, "Smart radio environments empowered by reconfigurable intelligent surfaces: How it works, state of research, and road ahead," vol. 38, no. 11, pp. 2450–2525, Nov. 2020.

[146] M. Di Renzo, M. Debbah, D.-T. Phan-Huy, A. Zappone, M.-S. Alouini, C. Yuen, V. Sciancalepore, G. C. Alexandropoulos, J. Hoydis, H. Gacanin *et al.*, "Smart radio environments empowered by reconfigurable AI meta-surfaces: An idea whose time has come," *EURASIP J. Wireless Commun. and Netw.*, vol. 2019, no. 1, pp. 1–20, 2019.

[147] Q. Wu and R. Zhang, "Intelligent reflecting surface enhanced wireless network via joint active and passive beamforming," *IEEE Transactions on Wireless Communications*, vol. 18, no. 11, pp. 5394–5409, 2019.

[148] C. Huang, A. Zappone, G. C. Alexandropoulos, M. Debbah, and C. Yuen, "Reconfigurable intelligent surfaces for energy efficiency in wireless communication," vol. 18, no. 8, pp. 4157–4170, 2019.

[149] S. Zhang, H. Zhang, B. Di, Y. Tan, M. Di Renzo, Z. Han, H. Vincent Poor, and L. Song, "Intelligent omni-surfaces: Ubiquitous wireless transmission by reflective-refractive metasurfaces," vol. 21, no. 1, pp. 219–233, 2022.

[150] P. P. Perera, V. G. Warnasooriya, D. Kudathanthirige, and H. A. Suraweera, "Sum rate maximization in STAR-RIS assisted full-duplex communication systems," *arXiv:2203.04709*, 2022.

[151] Z. Yang, M. Chen, W. Saad, W. Xu, M. Shikh-Bahaei, H. Poor, and S. Cui, "Energy-efficient wireless communications with distributed reconfigurable intelligent surfaces," vol. 21, no. 1, pp. 665–679, 2022.

[152] H. Niu, Z. Chu, F. Zhou, P. Xiao, and N. Al-Dhahir, "Simultaneous transmission and reflection reconfigurable intelligent surface assisted MIMO systems," *arXiv:2106.09450*, 2021.

[153] J. Xu, Y. Liu, X. Mu, and O. A. Dobre, "STAR-RISs: Simultaneous transmitting and reflecting reconfigurable intelligent surfaces," *IEEE Commun. Lett.*, vol. 25, no. 9, pp. 3134–3138, 2021.

[154] Y. Liu, X. Mu, J. Xu, R. Schober, Y. Hao, H. V. Poor, and L. Hanzo, "STAR: Simultaneous transmission and reflection for 360° coverage by intelligent surfaces," *IEEE Wirel. Commun.*, vol. 28, no. 6, pp. 102–109, 2021.

[155] X. Mu, Y. Liu, L. Guo, J. Lin, and R. Schober, "Simultaneously transmitting and reflecting (star) ris aided wireless communications," *IEEE Trans. Wireless Commun.*, vol. 21, no. 5, pp. 3083–3098, 2022.

[156] J. Xu, Y. Liu, X. Mu, J. T. Zhou, L. Song, H. V. Poor, and L. Hanzo, "Simultaneously transmitting and reflecting intelligent omni-surfaces: Modeling and implementation," *IEEE Vehicular Technology Magazine*, vol. 17, no. 2, pp. 46–54, 2022.

[157] H. Zhang, S. Zeng, B. Di, Y. Tan, M. Di Renzo, M. Debbah, Z. Han, H. V. Poor, and L. Song, "Intelligent omni-surfaces for full-dimensional wireless communications: Principles, technology, and implementation," *IEEE Commun. Mag.*, vol. 60, no. 2, pp. 39–45, 2022.

[158] H. Weingarten, Y. Steinberg, and S. Shamai, "The capacity region of the Gaussian multiple-input multiple-output broadcast channel," vol. 52, no. 9, pp. 3936–3964, Sep. 2006.

[159] S. Vishwanath, N. Jindal, and A. Goldsmith, "Duality, achievable rates and sum-rate capacity of Gaussian MIMO broadcast channels," vol. 49, no. 10, pp. 2658–2668, Oct. 2003.

[160] N. S. Perović, L.-N. Tran, M. Di Renzo, and M. F. Flanagan, "Achievable rate optimization for MIMO systems with reconfigurable intelligent surfaces," *IEEE Transactions on Wireless Communications*, 2021.

[161] S. Zhang and R. Zhang, "Capacity characterization for intelligent reflecting surface aided MIMO communication," vol. 38, no. 8, pp. 1823–1838, Aug. 2020.

[162] W. Yu, "Sum-capacity computation for the Gaussian vector broadcast channel via dual decomposition," vol. 52, no. 2, pp. 754 –759, Feb. 2006.

[163] N. S. Perović, L.-N. Tran, M. Di Renzo, and M. F. Flanagan, "On the achievable sum-rate of the ris-aided mimo broadcast channel : Invited paper," in *2021 IEEE 22nd International Workshop on Signal Processing Advances in Wireless Communications (SPAWC)*, 2021, pp. 571–575.

[164] Z. Zhang, L. Dai, X. Chen, C. Liu, F. Yang, R. Schober, and H. V. Poor, "Active RIS vs. passive RIS: Which will prevail in 6G?" 2021. [Online]. Available: https://arxiv.org/abs/2103.15154

[165] D. Xu, X. Yu, D. W. K. Ng, and R. Schober, "Resource allocation for active IRS-assisted multiuser communication systems," 2021. [Online]. Available: https://arxiv.org/abs/2108.13033

[166] C. You and R. Zhang, "Wireless communication aided by intelligent reflecting surface: Active or passive?" *early access in IEEE Wireless Commun. Lett.*, 2021.

[167] M. H. Khoshafa, T. M. N. Ngatched, M. H. Ahmed, and A. R. Ndjiongue, "Active reconfigurable intelligent surfaces-aided wireless communication system," *early access in IEEE Commun.Lett.*, 2021.

[168] C. You, B. Zheng, and R. Zhang, "Wireless communication via double IRS: Channel estimation and passive beamforming designs," *IEEE Wireless Commun. Lett.*, vol. 10, no. 2, pp. 431–435, Feb. 2021.

[169] B. Zheng, C. You, and R. Zhang, "Uplink channel estimation for double-IRS assisted multi-user MIMO," in *IEEE Int. Conf. Commun. (ICC), Montreal, Canada*, Jun. 2021, pp. 1–6.

[170] ——, "Efficient channel estimation for double-IRS aided multi-user MIMO system," *IEEE Trans. Commun.*, vol. 69, no. 6, pp. 3818–3832, Jun. 2021.

[171] E. Björnson and L. Sanguinetti, "Power scaling laws and near-field behaviors of massive MIMO and intelligent reflecting surfaces," *IEEE Open Journal of the Commun. Society*, vol. 1, pp. 1306–1324, Sept. 2020.

[172] C. Feng, H. Lu, Y. Zeng, S. Jin, and R. Zhang, "Wireless communication with extremely large-scale intelligent reflecting surface," in *Proc. IEEE/CIC Int. Conf. Commun. China (ICCC Workshops)*, Sept. 2021, pp. 165–170.

[173] E. Björnson, Ö. T. Demir, and L. Sanguinetti, "A primer on near-field beamforming for arrays and reconfigurable intelligent surfaces," 2021. [Online]. Available: https://arxiv.org/abs/2110.06661

[174] X. Wei, L. Dai, Y. Zhao, G. Yu, and X. Duan, "Codebook design and beam training for extremely large-scale RIS: Far-field or near-field?" 2021. [Online]. Available: https://arxiv.org/abs/2109.10143

[175] Z. Mao, M. Peng, and X. Liu, "Channel estimation for reconfigurable intelligent surface assisted wireless communication systems in mobility scenarios," *China Commun.*, vol. 18, no. 3, pp. 29–38, Mar. 2021.

[176] S. Sun and H. Yan, "Channel estimation for reconfigurable intelligent surface-assisted wireless communications considering doppler effect," *IEEE Wireless Commun. Lett.*, vol. 10, no. 4, pp. 790–794, Apr. 2021.

[177] B. Matthiesen, E. Björnson, E. De Carvalho, and P. Popovski, "Intelligent reflecting surface operation under predictable receiver mobility: A continuous time propagation model," *IEEE Wireless Commun. Lett.*, vol. 10, no. 2, pp. 216–220, Feb. 2021.

[178] Z. Huang, B. Zheng, and R. Zhang, "Transforming fading channel from fast to slow: Intelligent refracting surface aided high-mobility communication," 2021. [Online]. Available: https://arxiv.org/abs/2106.02274

[179] S. E. Zegrar, L. Afeef, and H. Arslan, "A general framework for RIS-aided mmWave communication networks: Channel estimation and mobile user tracking," 2020. [Online]. Available: https://arxiv.org/abs/2009.01180

[180] M. Di Renzo, F. H. Danufane, and S. Tretyakov, "Communication models for reconfigurable intelligent surfaces: From surface electromagnetics to wireless networks optimization," 2021. [Online]. Available: https://arxiv.org/abs/2110.00833